

Abstract

Behbehani, Mark Kian Study of Phase separation and Ordering in InGaN and AlInGaN: Experimental and Computer Modeling. (Under the direction of Nadia El-Masry and Donald Brenner)

A comprehensive study examines the phase behaviour of InGaN and AlInGaN including growth characterization and computer modeling. InGaN alloys were grown with up to 50% InGaN and studied for phase separation and ordering. The AlInGaN system has been studied with discovery of the Self Assembled Super-Lattice (SASL) and the Strain Equilibrium Indium (In) Incorporation Effect. Computer modeling was performed using a strain based Valence Force Field (VFF) model combined with a Monte Carlo method to study both the composition pulling and the Strain Equilibrium In Incorporation Effect

In the InGaN system, both phase separation and ordering behaviour in the InGaN system was studied extensively. Using Transmission Electron Microscopy, the presence of simultaneous phase separation and (0002) ordering was confirmed. The composition pulling effect was also studied in the InGaN system. VFF computer modeling was successfully used to predict the composition of highly strained InGaN films based on the bulk composition.

In the AlInGaN system, the SASL effect was discovered using Transmission Electron Microscopy. In addition the Strain Equilibrium In Incorporation Effect was discovered using a combination of Transmission Electron Microscopy and X-ray diffraction.

Using a VFF Metropolis Monte Carlo algorithm, the Strain Equilibrium In Incorporation Effect has been studied. The computer model has been able to predict the In incorporation behaviour of highly strained films in the AlInGaN system and has confirmed that the strain energy is the primary factor determining the In composition in strained AlInGaN films.

Study of Phase Separation and Ordering in InGaN and AlInGaN: Experimental and Computer Modeling

By

Mark K Behbehani

A dissertation submitted to the Graduate Faculty of North Carolina State University in partial fulfillment of the requirements for the Degree of Doctor of Philosophy

Materials Science and Engineering

Raleigh

2004

APPROVED BY:

Chair of Advisory Committee

Co-chair of Advisory Committee

Biography

Mark Behbehani was born in North Tonawanda NY and grew up in Cincinnati. He graduated with a BS in Materials Science and Engineering in 1993 from North Carolina State University and has been working on his PhD since that time. Along the way, Mark completed a commercial pilots licence, a masters degree in Computer Science and a battle with cancer.

Acknowledgements

Special Thanks to Mason and Meredith Reed for helping me all these many years and to Oliver Luen and Peter Larmey for helping me when it counted the most. I would also like to thank my parents who have never given up hope that I might graduate one day. I have receive great guidance and learning from the many graduate students who have graduated before me especially Eddie Piner who taught me how to grow GaN.

Table of Contents

List of Tables	vi
List of Figures	vii
Chapter One: Introduction	1
1.1 Growth of GaN InGaN and AlGaN	1
1.2 GaN based electronic devices	2
1.3 GaN based optical devices	2
1.4 Laser Diodes	3
1.5 Quantum Dots in InGaN	3
1.6 References	5
Chapter Two: Experimental Methods	8
2.1 Metal Organic Chemical Vapour Deposition (MOCVD)/ALE System	8
2.1.1 Gas delivery system	8
2.1.2 Growth chamber design	9
2.2 Thomas Swan MOCVD System	10
2.3 Growth of GaN and development of ALE and MOCVD buffer layers	11
2.4 Hall measurements	14
2.5 Photoluminescence	16
2.6 $\theta - 2\theta$ x-ray analysis.	17
2.7 Double crystal XRD	17
2.8 TEM Analysis	18
2.9 SIMS Analysis	19
Chapter Three: Development of GaN Buffer Layer	26
3.1 Introduction to the nitride buffer layer.	26
3.2 Growth of The ALE Buffer layer	28
3.3 Development of chamber design	29
3.4 AlN Buffer Layers	32
3.5 Hybrid AlN/GaN Buffer Layer	33
3.6 GaN Buffer Layer	33
3.7 References	39
Chapter Four: Growth and Ordering of InGaN	42
4.1 InGaN Growth	42
4.2 Detection of phase separation	44
4.3 Discovery of Ordering in InGaN	46
4.4 Confirming the Origin of the Extra Spots	49
4.5 References	52
Chapter Five: Growth of AlInGaN and the Strain Equilibrium In Incorporation Effect.	85
5.1 Advantages of AlInGaN	85
5.2 Growth of AlInGaN	86
5.3 SASL Effect	88
5.4 Strain Equilibrium In incorporation Effect	90
5.5 The Role of Strain in AlInGaN	92

5.6	The composition pulling effect in InGaN and its relation to the Strain Equilibrium In incorporation effect	93
5.7	Initial two-dimensional VFF model	95
5.8	References	96
Chapter Six: Modeling Introduction and Background		117
6.1	Development of strain energy modeling	121
6.2	References	125
Chapter Seven: Description of Model and Results		138
7.1	Development of Model from Takayama	138
7.2	Development of Computer Model	139
7.3	Implementing Strain	141
7.4	Debugging the VFF Computer Model	143
7.5	Comparison to Published Values	145
7.6	Optimizing performance of VFF model	145
7.7	Calculating Phase Diagrams with the VFF Model	146
7.8	Using VFF to Study the Compositional Pulling Effect	149
7.9	Monte Carlo Method	151
7.10	Testing Metropolis Monte Carlo Simulation for Correctness	155
7.11	Preferential Lattice Sites for In and Al	158
7.12	Temperature Effects on the Metropolis Monte Carlo Simulation	159
7.13	VFF Metropolis Monte Carlo Method for AlInGaN	161
7.14	References	168
Chapter Eight: Conclusions		221
Chapter Nine: Future Work		222

List of Tables

Table 5-1 Intensity of 50% InGaN peak with increasing Al	92
Table 7-1 Strain energies for various crystal sizes.	144
Table 7-2 Comparison of Current Model to Published Results.....	145

List of Figures

Figure 1-1 Diagram showing the relative lattice parameter and bandgap of the nitride system.	7
Figure 2-1 Schematic of the ALE/MOCVD system (Parker).....	20
Figure 2-2 Schematic of the ALE Reactor Layout (Parker)	21
Figure 2-3 Schematic for ALE Growth Mode (Piner)	22
Figure 2-4 MOCVD Growth Mode (Piner)	23
Figure 2-5 Schematic representation of Swan MOCVD system (Aumer)	24
Figure 2-6 MOCVD Growth Chamber for Swan (Aumer).....	25
Figure 3-1 Diagram of modified MOCVD Setup (Parker).....	41
Figure 4-1 Growth structure for InGaN study. The InGaN layers studied were grown on a 1 μ m GaN film acting as a base layer. The buffer layer was the ALE AlN at 700°C followed by an AlGaN grading layer.....	55
Figure 4-2 Curve showing the effect of Growth temperature on In incorporation. Samples were grown under all N ₂ conditions at an In:Ga ratio of 1:1. (Piner)	56
Figure 4-3 Graph showing In composition from θ -2 θ for different V/III ratios. Conditions for the runs were: In:Ga ratio of 1:1 temperature of 780°C and 50sccm of H ₂ on column III side. Notice that the In composition levels out for V/III ratios greater than 10,000. (Piner).....	57
Figure 4-4 Graph of In composition vs. temperature for different H ₂ flows. Growth conditions were 27,500 V/III and In:Ga ratio 1:1. Thickness of the films	

increased with increasing In, indicating that the In incorporation rate was the limiting factor.....58

Figure 4-5 Graph showing evolution of θ - 2θ XRD scans as In composition increases in InGaN alloys. InGaN peak shifts to lower angles as In content increases. Notice the additional peak at 31.5 degrees due to phase separation in the 40 and 49% In scans. Graph from Piner59

Figure 4-6 θ - 2θ scan for 20%In InGaN alloy. Peaks are present for InGaN, GaN and AlN (from the buffer layer). No additional peaks are seen.....60

Figure 4-7 θ - 2θ scan for 49% In InGaN alloy. Second curve is fitting curve made up of independent Gaussians to determine compositions present in the film. Note the presence of both higher and lower In compositions indicating phase separation of 49% In composition. (Piner)61

Figure 4-8 TEM – SAD image showing 10% In InGaN alloy. TEM pattern shows [2-1-10] zone axis. Notice how spots are clearly defined without any additional spots.62

Figure 4-9 TEM – SAD image showing 49% In InGaN alloy. TEM pattern shows [2-1-10] zone axis. Notice how the spots are split for higher indexes indicating phase separation of the InGaN alloy. Vertical smears in the c-axis (vertical direction) are stacking faults.....63

Figure 4-10 Behaviour of different InGaN alloys compared with predicted solubility. Compositions below the spinodal curve are all single phase, whereas compositions above the spinodal point are multiple phases (showing phase separation). Spinodal point is limiting factor for solubility. (Ho et al. APL 1996)..64

Figure 4-11 Cross-sectional TEM image of 20% InGaN film. No phase separation is observed. The arrows indicate the ordered regions. Both 1:1 and 1:3 In:Ga ordered regions are observed.....	65
Figure 4-12 Cross-sectional TEM image of 49% InGaN showing both phase separation and ordering. Dark regions are high In phase, while arrows indicate ordered regions.....	66
Figure 4-13 TEM-SAD image of 20% InGaN film showing extra spots due to both 1:1 (50%) and 1:3 (25%) ordering. Inset shows magnified view of extra spots.....	67
Figure 4-14 TEM-SAD image of 49% InGaN film showing extra spots due to 1:3 (25%) ordering. Inset shows magnified view of extra spots.....	68
Figure 4-15 Schematic diagram showing the ordering structures for 1:1 and 1:3 In:Ga ordering along the c-axis.....	69
Figure 4-16 Summary of runs checked by TEM for ordering	70
Figure 4-17 Cross-sectional TEM image of 20% InGaN showing ordered region near edge of crystal domain. Arrow indicates threading dislocation. The right image shows magnified view of ordered region. Both 1:1 and 1:3 In:Ga ordering are present.....	71
Figure 4-18 Computer generated theoretical TEM-SAD pattern for perfect 1:1 ordering of InGaN crystal. Smaller spots are extra spots due to ordering.....	72
Figure 4-19 Computer generated theoretical TEM-SAD pattern for perfect 1:3 ordering of InGaN crystal. Smaller spots are extra spots due to ordering.....	73
Figure 4-20 TEM-SAD image of 14% AlGaN showing 3:1 Ga:Al ordering along the (0001) plane. (Korakakis APL 1997).....	74

Figure 4-21 Simulated diffraction pattern for [2-1-10] zone axis.....	75
Figure 4-22 Schematic of a twin plane.	76
Figure 4-23 Wuff net construction for generating virtual twin plane for [2-1-11] twin. The dark line indicates where reverse twin of image plane would be located. Circles represent spots that can be twinned to image plane.....	77
Figure 4-24 Computer generated simulated TEM-SAD image with additional spots added from Wuff net construction for [2-1-11] twin represented by a 35° rotation around [01-10]. The extra spots from the twin are indicated by hollow circles.	78
Figure 4-25 Wuff net construction for generating virtual twin plane for [2-112] and [- 1012] twins. Lines indicate where reverse twins of image plane would be located. Circles represent spots that can be twinned to image plane.	79
Figure 4-26 Computer generated simulated TEM-SAD image with additional spots added from Wuff net construction for [2-1-12] twin represented by a 65° rotation around [01-10]. The extra spots from the twin are indicated by hollow circles.	80
Figure 4-27 Computer generated simulated TEM-SAD image with additional spots added from Wuff net construction for [-1012] twin represented by rotation around the [1-210]. The extra spots from the twin are indicated by hollow circles.	81
Figure 4-28 Computer generated simulated TEM-SAD image with additional spots for [0-112] twin represented by a rotation around [2-1-10]. Since twin identity involves rotation around zone axis, no Wuff net construction is necessary. The extra spots from the twin are indicated by hollow circles.	82

Figure 4-29 TEM image compared with same region imaged using extra ordering spots. Ordered regions are enhanced, showing that extra spots are coming from ordered regions indicated by arrows	83
Figure 4-30 Simulated diffraction pattern using Fourier transform of TEM image of 20% InGaN alloy. Fourier transform of the image gives same pattern as TEM-SAD.....	84
Figure 5-1 Structure for AlInGaN Growth using GaN buffer layer	99
Figure 5-2 Plot of growth flux required for 10% InGaN at various temperatures. In:Ga ratio was held constant at 10:1 while V/III ratio was 100,000:1 (Aumer)	100
Figure 5-3 Cross-sectional TEM of the self-assembled superlattice (SASL) in AlInGaN. The SASL consists of high-In, high-Al regions alternating with lower-Al, lower-In regions. The arrows are pointing to the bright layers with high-Al and high-In content.....	101
Figure 5-4 SIMS data for SASL shows increase in both In and Al during SASL effect. In increases from 6-9% while Al increases from 8-23%. Temperature and Growth conditions are constant.	102
Figure 5-5 Quantum well structure exhibiting SASL effect. Quantum well is 6nm InGaN while cladding layers are AlInGaN with SASL.....	103
Figure 5-6 Graph shows actual and predicted 0002 lattice spacing for constant In incorporation and Strain Equilibrium In incorporation at 790°C. In:Al ratio for Strain Equilibrium. Effect is approximately 1:4.5 for growth on GaN. The datapoint closely follows Strain Equilibrium Effect curve.....	104

Figure 5-7 Graph shows actual and predicted 0002 lattice spacing for constant In incorporation and Strain Equilibrium In incorporation at 810°C. In:Al ratio for Strain Equilibrium Effect is approximately 1: 4.5 for growth on GaN. The datapoints closely follow Strain Equilibrium Effect curve.....	105
Figure 5-8 Graph shows actual and predicted 0002 lattice spacing for constant In incorporation and Strain Equilibrium In incorporation at 830°C. In:Al ratio for Strain Equilibrium Effect is approximately 1: 4.5 for growth on GaN. The datapoints closely follow Strain Equilibrium Effect curve.....	106
Figure 5-9 Graph shows actual and predicted 0002 lattice spacing for constant In incorporation and Strain Equilibrium In incorporation for 857°C. In:Al ratio for Strain Equilibrium Effect is approximately 1: 4.5 for growth on GaN. The datapoints closely follow Constant In incorporation curve.	107
Figure 5-10 Plot shows suppression of phase separation with increasing Al content. The strain from Al cancels strain from In reducing the strain and the driving force for phase separation.	108
Figure 5-11 Structure for critical layer thickness study. Thin InGaN layers are grown on 1μm GaN bulk layer. Buffer layer is GaN buffer layer.	109
Figure 5-12 Results for critical layer study showing the critical layer thickness for different InGaN compositions.....	110
Figure 5-13 Reciprocal lattice maps for InGaN samples. Maps show main layers at 28% and 40% InGaN respectively plus strained layers of different composition. Initial strained layers are 16% for 28% InGaN and 20% for 40% InGaN (Robbins).....	111

Figure 5-14 Double crystal X-ray analysis of 11-24 off axis peak to determine composition. 25 minute film shows composition of 4.2% InGaN (Reed).....	112
Figure 5-15 Double crystal X-ray analysis of 11-24 off axis peak to determine composition. 105 minute film shows composition of 6.2% InGaN(Reed).....	113
Figure 5-16 Results from Gong, et al., showing the increase of Al composition for AlGaN grown on AlN layer compared with AlGaN grown on a GaN layer. Shows similar composition pulling effect in AlGaN (Gong)	114
Figure 5-17 Two-dimensional Valence Force Field Model showing $\text{In}_1\text{Al}_1\text{Ga}_{62}\text{N}$ crystal atom positions are distorted by the strain fields surrounding the In and Al atoms. The total strain Energy of the crystal is 20.01 arbitrary units.	115
Figure 5-18 Two-dimensional VFF model of same $\text{In}_1\text{Al}_1\text{Ga}_{62}\text{N}$ crystal as before but with the In and Al atoms moved closer together. The strain fields from the In and Al atoms cancel out leaving the surrounding atoms relatively undistorted. The total strain for the crystal is 15.32 arbitrary units.	116
Figure 6-1 Calculation of phase diagram using the regular solution model. Ω used is Stringfellows value of 5.98 kcal/mol. Upper curve represents the strain energy H. Lower curve represents the entropy term TS.	127
Figure 6-2 Calculation of phase diagram using the regular solution model. Ω used is Stringfellows value of 5.98 kcal/mol. Upper curve is the free energy diagram. Lower curve is the derivative of the free energy.	128
Figure 6-3 Predicted phase diagram for InGaN from Ho and Stringfellow (APL 69 1996)	129

Figure 6-4 Formula for Delta Lattice Parameter model with table of interaction parameters for III-V alloys.....	130
Figure 6-5 Limiting cases for the VFF model. The VCA approximation represents fixed bond angles, while the CRA approximation represents fixed bond lengths. The minimum energy VFF model is a combination of the two but is closer to the CRA model	131
Figure 6-6 Figure showing the actual bond lengths for the InGaN crystal system. The upper and lower lines represent the CRA crystal approximation and the middle line represents the VCA approximation. Figure from Jeffs N.J., Mater. Res. Soc. Symp. Proc. No 512, p.519.....	132
Figure 6-7 Diagram of the stretching and bending moments for the GaN tetrahedra used in the VFF model. α represents the bond stretching energy and β represents the bond angle distortion	133
Figure 6-8 Formula for the VFF model in the zinc-blende crystal system. The r_{ij} represent the vectors between the pairs of atoms in the tetrahedra. The atom position is relocated to get a minimum total energy U	134
Figure 6-9 Elemental clusters used for the CVM method. The cluster variation method statistically combines the elemental clusters and was used extensively in the zinc-blende crystal structure as the basis for the DLP model	135
Figure 6-10 The cluster variation method has drawbacks however. If alloy is 25% overall, 0%, 50%, 75% and 100% tetrahedral will all be strained leaving only 25% relaxed. This error tends to overestimate the strain in the crystal.	136

Figure 6-11 Phase diagram for the AlInGaN system showing isotherms from 0-3000C	
Figure from Matsuoka T., Apl. Phy. Lett. 71 (1) 1997	137
Figure 7-1 Diagram of the stretching and bending moments for the wurtzite GaN tetrahedra. Note that the distances in the <i>a</i> and <i>c</i> directions are not equal. Likewise, the angles between the a-a and a-c bonds are not equal either. This makes the calculations more difficult. Figure from Takayama.	170
Figure 7-2 Formula for the total energy for the wurtzite VFF model. Notice that the <i>c</i> axis components and <i>a</i> axis components have be calculated separately. This is essentially the algorithm used for the current model; however, the axis have been transformed to a orthogonal axis system to allow the use of dot products instead of the slower cos() functions. Figure from Takayama.....	171
Figure 7-3 Comparison of the current model to the data from Takayama. The values are in agreement to less than 5%. Because both models are randomly generated, perfect agreement is unlikely	172
Figure 7-4 Showing the convergence of the strain energy with iterations for 25% InGaN alloy using the VFF model. Bottom plot is same curve on a magnified scale.....	173
Figure 7-5 Showing strain energy vs. number of iterations for 25% InGaN alloy. Notice that the final converged value is not the minimum. This is due to the greedy algorithm being non-optimal.....	174
Figure 7-6 Table showing the final values of strain energy for different threshold values. Notice the slight difference between the final converged value and the minimum. Threshold for all simulations was set at 1E-5.	175

Figure 7-7 Plot of Ω vs. composition for the wurtzite VFF model. Adding In to a GaN matrix is more difficult than adding Ga to an InN matrix due to the larger strain energy for GaN.....	176
Figure 7-8 Free energy curves using variable Ω . Notice once again the lower solubility of In in the GaN matrix.....	177
Figure 7-9 Calculation of phase diagram using the regular solution model. Stringfellow's value for Ω of 5.98 kcal/mol is used. Upper curve is the free energy diagram. Lower curve is the derivative of the free energy.	178
Figure 7-10 Unstable mixing region calculation for AlInGaN from Takayama.	179
Figure 7-11 Calculated Spinodal for AlInGaN from Matsuoka	180
Figure 7-12 Free energy curves, for the relaxed crystal, generated using the VFF calculation at every point. Model used code from Monte Carlo algorithm, but with random swaps. Values for InGaN (0 Al) curve are consistent with Ω calculations. Notice the decrease in In solubility with increasing Al.....	181
Figure 7-13 Derivative of the free energy curve for relaxed crystal. Notice the decrease (x axis intercept) of the equilibrium In composition. Spinodal point (maximum) is relatively unaffected.	182
Figure 7-14 Free energy curves for strained InGaN and AlInGaN on GaN generated using the VFF calculation for every point. Model used code from Monte Carlo algorithm, but with random swaps. Notice that unlike the relaxed curves the solubility of In is not affected by the increasing Al.....	183

Figure 7-15 Derivative of the free energy curve for strained InGaN and AlInGaN alloys. The equilibrium In composition increases slightly with increasing Al.	184
Figure 7-16 Data from Hiramatsu showing the increase in In composition with layer thickness.....	185
Figure 7-17 Diagram of the growth of 20% InGaN on a AlGaN layer. The initial layers are strained to the underlying substrate and are of lower composition than the relaxed bulk film.	186
Figure 7-18 Method for testing the Monte Carlo In incorporation hypothesis. The two films are compared using the VFF model. The model compares the energy to add an In atom into each film using the relationship	187
Figure 7-19 Calculations for composition pulling of 20% InGaN on GaN	188
Figure 7-20 11-24 off-axis DCXRD scan of InGaN Showing 4.2% In.....	189
Figure 7-21 11-24 off-axis DCXRD scan of InGaN Showing 6.2% In.....	190
Figure 7-22 Composition pulling calculations of 6.2% InGaN on GaN.....	191
Figure 7-23 Showing the standard deviation for ten runs with the Boltzmann probability applied to the addition of In atoms only. The deviations using this method are large enough to mask the Strain equilibrium In incorporation effect. ..	192
Figure 7-24 Start the Monte Carlo algorithm by calculating the strain energy of the crystal.....	193
Figure 7-25 Select two random column III sites that are different atoms and exchange positions.....	194
Figure 7-26 Recalculate strain energy with the new atom positions.	195

Figure 7-27 If the energy is less, the swap always occurs. If the energy is greater then the probability is given by the formula $P = \text{Exp}(-(\text{Energy change})/kT)$. Unfavourable transitions are still possible but with a Boltzmann distribution of probability.....	196
Figure 7-28 Monte Carlo simulation for $\text{Al}_1\text{In}_1\text{Ga}_{126}\text{N}$ showing the final number of atoms per lattice site vs. strain energy of that lattice site. Simulations are run for various numbers of sweeps.....	197
Figure 7-29 Monte Carlo simulation showing the final number of atoms per lattice site vs. strain energy of that lattice site. Simulations are run for various numbers of sweeps.....	198
Figure 7-30 Monte Carlo simulation showing the final number of atoms per lattice site vs. strain energy of that lattice site. Simulations are run for various numbers of sweeps.....	199
Figure 7-31 Monte Carlo simulation showing the final number of atoms per lattice site vs. strain energy of that lattice site. Simulations are run for various numbers of sweeps.....	200
Figure 7-32 Plot of the correlation coefficient R to the ideal Boltzmann distribution. Curve is essentially flat above 32 sweeps. Curve bends over between 16 and 32 sweeps. Therefore all simulations will be run at least 25 sweeps.....	201
Figure 7-33 The minimum energy location has a path of two bonds between the In and Al atoms. The maximum energy locations have three paths of three bonds each for a total of ten bonds.....	202

Figure 7-34 Curves showing Monte Carlo simulation of Al ₁ In ₁ Ga ₁₂₆ N crystal at 300K and 300°C. The number of atoms per lattice site is plotted vs. strain energy of lattice site.....	203
Figure 7-35 Curves showing Monte Carlo simulation of Al ₁ In ₁ Ga ₁₂₆ N crystal at 500°C and 700°C. The number of atoms per lattice site is plotted vs. strain energy of lattice site.....	204
Figure 7-36 Curves showing Monte Carlo simulation of Al ₁ In ₁ Ga ₁₂₆ N crystal at 800°C and 900°C. The number of atoms per lattice site is plotted vs. strain energy of lattice site.....	205
Figure 7-37Curves showing Monte Carlo simulation of Al ₁ In ₁ Ga ₁₂₆ N crystal at 1000°C and 1200°C. The number of atoms per lattice site is plotted vs. strain energy of lattice site.....	206
Figure 7-38 Curves showing Monte Carlo simulation of Al ₁ In ₁ Ga ₁₂₆ N crystal at 1400°C. The number of atoms per lattice site is plotted vs. strain energy of lattice site. Notice how the curve fits the Boltzmann less and less at high temperatures.....	207
Figure 7-39 Plot of correlation coefficient of the data to the ideal Boltzmann distribution. Note the second order transformation between 800°C – 900°C. This is most likely due to the increase in thermal energy allowing the atoms to hop “uphill” against the strain field.....	208
Figure 7-40 Curve showing strain energy and integrated differential strain energy for the Monte Carlo simulation of a 25In 25Al 78Ga N alloy. Convergence is indicated when the integrated differential strain oscillates around zero.....	209

Figure 7-41 Curve showing strain energy and integrated differential strain energy for
5In 5Al 118Ga N alloy. Notice the much faster convergence than the 25In 25Al
alloy.....210

Figure 7-42 Free energy curve for Monte Carlo simulation for 128 atom AlInGaN
crystal strained to GaN at three different compositions of Al. Simulation was
run at 800C for 25 sweeps. The equilibrium In composition increases with
increasing Al. Simulation runs took approx. 20hr.....211

Figure 7-43 Derivative free energy for Monte Carlo simulation of 128 atom AlInGaN
crystal strained to GaN. Equilibrium In composition shifts from 2.5In to 7In
with the addition of 25Al atoms. This is in complete agreement with the strain
equilibrium In incorporation effect.....212

Figure 7-44 Monte Carlo simulation for 1024 atom crystal strained to GaN at three
different compositions of Al. Simulation was run at 800C for 10 sweeps. The
equilibrium In composition increases with increasing Al, but not as large an
effect as for 128 atoms. Simulation runs took approx. 20 days.....213

Figure 7-45 Derivative free energy for Monte Carlo simulation for 1024 atoms
strained to GaN. Equilibrium In composition shifts from 22In to 44In with the
addition of 200Al atoms. The expected shift would be 40In. The discrepancy
between the actual and expected shift is due to the limited number of sweeps.....214

Figure 7-46 Set of Monte Carlo runs for 25Al curve. Monte Carlo simulations were
performed using Boltzmann probability addition only, 5 sweeps and 25sweeps.
The 25 sweep curve matches the result for the 128 atom simulation while the 5
sweep is closer to the results from the 1024 atom crystal. This would indicate

that the discrepancies for the 1024 atom crystal are from an insufficient number
of sweeps.....215

Figure 7-47 Derivative free energy for Monte Carlo simulation for 25Al curve. The
25 sweep curve matches the results for the 128 atom simulation while the 5
sweep is in close agreement with the 1024. This would indicate that the
discrepancies for the 1024 atom crystal are from an insufficient number of
sweeps.....216

Figure 7-48 Free energy curves from Monte Carlo simulation for 128 atoms strained
to GaN at 1000°C and 25 sweeps. The equilibrium In composition changes from
5In to 10In. While the equilibrium In compositions are higher, the strain
equilibrium effect is unchanged.....217

Figure 7-49 Derivative free energy for Monte Carlo simulation at 1000°C.
Equilibrium In composition shifts from 5In to 10In. All equilibrium In
compositions are shifted higher.....218

Figure 7-50 Plot of desorption rate vs. temperature for different H₂ flows using the
data from the InGaN runs for the H₂ study. All fitting curves are normalized to a
Do value corresponding to the Debye frequency for GaN. Resulting activation
energy for 0 sccm H₂ is 2.6eV.....219

Figure 7-51 The ratio of diffusion events to desorption events is plotted using the
activation energy for desorption combined with the activation energy for In
surface diffusion from Neugebauer. The curve is normalized for 1000 diffusion
events/ desorption event at 800°C. The number of diffusion events per
desorption decreases from 1000 to 140 from 800°C – 900°C.....220

Chapter One: Introduction

The GaN AlN InN crystal system is a direct bandgap system covering the entire visible spectrum (Figure 1-1). The bandgaps range from 0.8 eV for InN[1] to 3.4 eV for GaN and up to 6.4 eV for AlN[2]. In addition to the optical properties of the nitride materials system, it also has excellent electrical properties. The direct bandgap, a high dielectric strength and good thermal conductivity make the Nitride system ideal for high frequency high power devices. InGaN/GaN Light Emitting Diodes (LEDs) have been commercialized with excellent efficiency in the blue and green[3], allowing for solid-state displays with excellent brightness and contrast. With their 80% electrical power reduction and 1000% lifetime increase over filtered light bulbs, green LEDs are making their way into every stoplight[4]. With the commercialization of GaN based lasers the capacity of optical storage is set to make a giant leap over existing 670nm lasers for DVD.

1.1 Growth of GaN InGaN and AlGaN

The first GaN research was undertaken by Pankove in the early 1970's[5]. While the devices were grown polycrystalline and had only n-type doping, Pankove was able to achieve detectable light emission using a Metal Insulator Semiconductor structure[6]. A resurgence in the GaN field occurred in 1986 when Amano et al. were able to grow GaN single crystals on Sapphire using a low temperature buffer layer[7]. This led to a burst of research characterizing the GaN/AlN/InN system. The last hurdle was jumped when Asaki discovered that electron beam annealing could activate Mg doped GaN and make it p-type[8]. With the ability to p-type dope GaN, the first LEDs were produced in less than three years[9].

The research effort into III-nitride materials exploded during the 1990's culminating in the last few years with several companies achieving commercial success marketing optoelectronic devices based on this material system.

1.2 GaN based electronic devices

The combination of high bandgap and high saturation velocity are ideal for high-speed transistors and FETS. The mobility of GaN increases as the layer thickness decreases reaching peak mobility of $600 \text{ cm}^2/\text{Vs}$ at 200\AA [4]. To take advantage of this property, Heterojunction Field Effect Transistors (HFETs) are used. Using this structure, room temperature mobilities of $1650 \text{ cm}^2/\text{V s}$ have been achieved. Using the High Electron Mobility Transistor (HEMT) structure two-Dimensional electron gas mobilities of $2200 \text{ cm}^2/\text{Vs}$ have been achieved[10]. GaN HEMT have been demonstrated with cut-off frequencies of 140GHz [11]. GaN/AlGaN Heterojunction Bipolar Transistors (HBTs) have been demonstrated with power densities of 270kW/cm^2 [12].

1.3 GaN based optical devices

Before the advent of GaN based LEDs the colors commonly available for LEDs were bright red, bright yellow, and a pale yellowish green. While efficiencies of red and yellow LEDs were pushing 40% efficiency, the green LEDs based on GaAsP were not able to get above 0.1% efficiency in the 530nm green range, the wavelength for the eyes peak sensitivity. This is due to the GaAsP semiconductor becoming indirect at those wavelengths. As disappointing as that might sound, it was great compared to the only commercially available blue LED based on a transition level in SiC. The SiC based LEDs (not to be confused with the GaN LED grown on SiC which are extremely efficient) cost several dollars apiece and had an efficiency of 0.02%[4]!

With the advent of InGaN/GaN based LEDs this has changed dramatically. In the space of less than 10 years, the efficiency for green LEDs has jumped from 0.1% to 35% quantum efficiency[13]. For the blue LEDs, efficiency has jumped from 0.02% to 35% quantum efficiency[14]. This has truly been a revolution in solid-state lighting. Combined

with existing highly efficient red and yellow LEDs, whole new applications using solid-state lighting are now possible.

1.4 Laser Diodes

The emergence of commercially viable blue Laser Diodes (LD) opened up a whole new era in optical storage. While the CD standard used GaAs based LD at 800nm to store 700MB of information on an optical disk, InGaAsP LD at 670nm can store 4.7 GB on the same sized optical disk. With the introduction of InGaN based LD at 405nm, the blue-ray optical disks are expected to make a similar leap in capacity. In fact, the improvement in areal density combined with closer track spacing and multiple layers has led to the development of optical drives holding 100GB on a single CD.

Current GaN based LD are operating at threshold currents of $2000\text{A}/\text{cm}^2$ with quantum efficiencies of 35%[15]. Compare these numbers to the current red and infrared LD with $500\text{A}/\text{cm}^2$ [16] and 80% quantum efficiency. While the blue lasers might not appear in walkmans anytime soon, they have reached the power, efficiency, and reliability to be a commercial success.

1.5 Quantum Dots in InGaN

When the first InGaN LEDs appeared, there was surprise in the solid-state community that devices with dislocation densities of 10^{10} cm^{-2} could work at all[17]. This compares to dislocation densities in the GaAs system in the 10^4 cm^{-2} range. Not only did the InGaN LEDs work, they were comparable in efficiency to GaAs LEDs with six orders of magnitude lower dislocation density. The lack of understanding about how the devices could be so efficient in such a highly defective crystal did not prevent Nichia and others from making them[18]. The reason for this efficiency turned out to be one advantage of the lattice mismatch between InN and GaN. During growth, the In atoms can cluster to reduce the strain in the crystal. The

clustering of In forms quantum dots that confine the carriers. This quantum confinement of the carriers enhances recombination at the quantum dots and prevents recombination at the dislocations. The quantum dot effect is so strong that even when low dislocation density material became available, the better quality material did not significantly improve the quantum efficiency of LEDs, especially at lower currents[17]. The effect of the lower dislocation density was proportional to the increased active volume. This compares to the GaAs system where each dislocation acts as a short across the active junction and has a large detrimental effect on device performance. Because the phase behaviour of the InGaN material is so critical to the device performance, the study of the InGaN system has great research and commercial importance.

1.6 References

1. Wu, J., et al., *Unusual properties of the fundamental band gap of InN*. Applied Physics Letters, 2002. **80**(21): p. 3967-3969.
2. Morkoc, H., et al., *Large-Band-Gap Sic, Iii-V Nitride, and Ii-Vi Znse-Based Semiconductor-Device Technologies*. Journal of Applied Physics, 1994. **76**(3): p. 1363-1398.
3. Nakamura, S., et al., *Characteristics of InGaN multi-quantum-well-structure laser diodes*. Applied Physics Letters, 1996. **68**(23): p. 3269-3271.
4. Nakamura, S., *The blue laser Diode*. 1997: Springer.
5. Pankove, J.I., et al., *Luminescent Properties of Gan*. Solid State Communications, 1970. **8**(13): p. 1051-&.
6. Pankove, J.I., E.A. Miller, and Berkeyhe.Je, *Gan Electroluminescent Diodes*. Rca Review, 1971. **32**(3): p. 383-&.
7. Amano, H., et al., *Metalorganic Vapor-Phase Epitaxial-Growth of a High-Quality Gan Film Using an Ain Buffer Layer*. Applied Physics Letters, 1986. **48**(5): p. 353-355.
8. Amano, H., et al., *P-Type Conduction in Mg-Doped Gan Treated with Low-Energy Electron-Beam Irradiation (Leebi)*. Japanese Journal of Applied Physics Part 2-Letters, 1989. **28**(12): p. L2112-L2114.
9. Nakamura, S., *Zn-Doped Ingnn Growth and Ingan/Algan Double-Heterostructure Blue-Light-Emitting Diodes*. Journal of Crystal Growth, 1994. **145**(1-4): p. 911-917.
10. Demchuk, A., et al. *MOCVD AlGaN/GaN HFET's Material Optimization and Devices Characterization*. in *2003 FALL MEETING PROCEEDINGS*. 2003.
11. Parikh, P., et al., *Record power-added-efficiency, low-voltage GOI (GaAs on insulator) MESFET technology for wireless applications*. Ieee Transactions on Microwave Theory and Techniques, 1998. **46**(12): p. 2202-2207.

12. Makimoto, T., Y. Yamauchi, and K. Kumakura, *High-power characteristics of GaN/InGaN double heterojunction bipolar transistors*. Applied Physics Letters, 2004. **84**(11): p. 1964-1966.
13. Barsky, F., *Cree Expands Green LED Product Family*. 2004, Cree.
14. Barsky, F., *Cree Expands Product Line With Introduction of XThinTM LED Products*. 2003, Cree.
15. Hansen, M., et al., *Higher efficiency InGaN laser diodes with an improved quantum well capping configuration*. Applied Physics Letters, 2002. **81**(22): p. 4275-4277.
16. Li, W., et al., *Low-threshold-current 1.32-mu m GaInNAs/GaAs single-quantum-well lasers grown by molecular-beam epitaxy*. Applied Physics Letters, 2001. **79**(21): p. 3386-3388.
17. Chichibu, S.F., et al., *Emission mechanisms of bulk GaN and InGaN quantum wells prepared by lateral epitaxial overgrowth*. Applied Physics Letters, 1999. **74**(10): p. 1460-1462.
18. Nakamura, S., *Ingan/Algan Blue-Light-Emitting Diodes*. Journal of Vacuum Science & Technology a-Vacuum Surfaces and Films, 1995. **13**(3): p. 705-710.

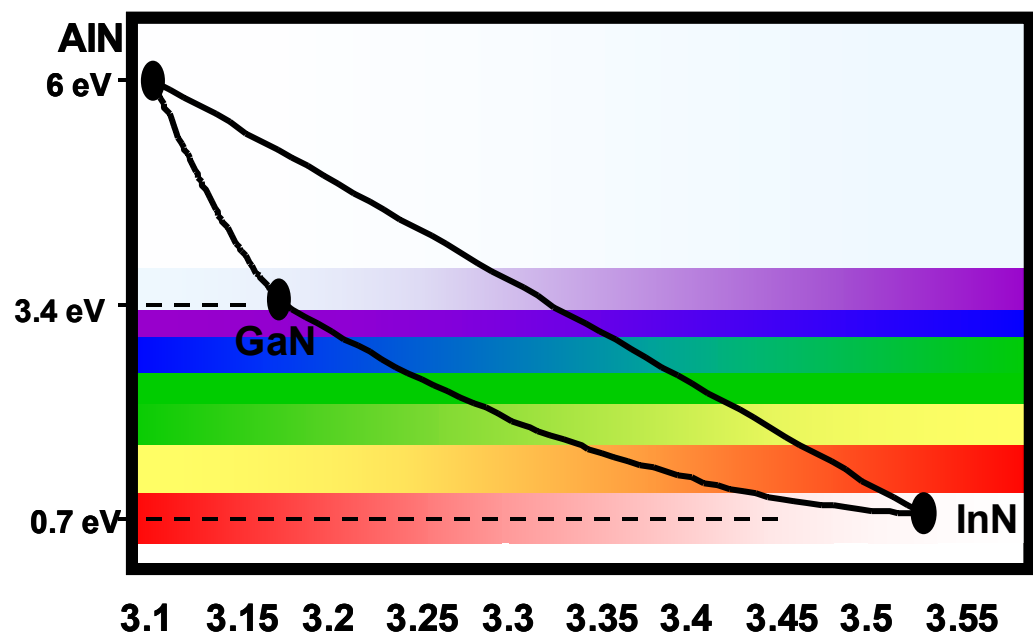


Figure 1-1 Diagram showing the relative lattice parameter and bandgap of the nitride system.

Chapter Two: Experimental Methods

2.1 Metal Organic Chemical Vapour Deposition (MOCVD)/ALE System

MOCVD growth consists of Chemical Vapour Deposition, a chemical reaction of the component gasses on the surface of the growing film, using metalorganics as the precursor gasses. In MOCVD, the liquid metalorganics are delivered to the gas stream by passing the carrier gas through a bubbler and carrying the carrier gas / metalorganic vapour to the growth surface along with gaseous ammonia. In our reactor design, the Ga, Al, In, and Mg sources are liquid metalorganics in bubblers. The column V sources ammonia (for N) and silane (for Si doping) are delivered by pressurized cylinders of high purity gas.

MOCVD is popular in industry because of its (relatively) low cost and high throughput. Because the MOCVD is grown at pressures ranging from 100 torr – 750 torr, the chamber does not need to be pumped to high vacuum. The disadvantages of MOCVD are that the incomplete pyrolysis of the metal-organics leads to carbon contamination in the growing films. While having the proper gas conditions during growth can minimize carbon incorporation, it will not totally eliminate it.

2.1.1 Gas delivery system

In the MOCVD/ALE system (**Figure 2-1**), the flow of the column III gases can be controlled by changing the pressure of the lines leading to the bubblers and by changing the temperatures of the bubbler baths. The vapour pressure of the metalorganics changes with temperature while the overall percentage is a function of the total pressure. The temperature of the bubblers is controlled by the temperature of the water baths that they sit in and the pressures are controlled by the pressure of the run line. Individual Mass Flow Controllers (MFCs) give a constant flow of each carrier gas through the bubblers. Bypass valves around

each bubbler allow for constant flows through the MFC when the bubblers are switched to flowing from bypassed. All of the column III flows and column V gasses are delivered into the run/vent manifold through MFCs at a constant pressure.

The run/vent manifold output runs to two main lines that travel to the chamber and to the vent manifold. For each input gas, there is a pair of pneumatic valves attached to these two main lines. This series of valves (one pair for each incoming gas) switch each flow to either the run or vent line. This allows the gas flows to be stabilized by flowing to the vent line before they are switched. The pressure in the run manifold is determined by a needle valve in the lines leading to the chamber, while the pressure in the vent line can be controlled by either a needle valve or by changing the N flow into the vent manifold. Pressure gauges are mounted at each of the bubblers and in the run and vent manifolds. The pressure of the main growth chamber is controlled by a MKS pressure controller that holds the chamber at a constant pressure by automatically operating a throttle valve at the output of the growth chamber. Since the vacuum pump is always running the chamber pressure can be controlled from very low pressure (limited by the pumping capacity and the growth flows) to above atmospheric (by almost closing the valve).

The system is supplied by ultra high purity N₂ that is run through a Nanochem purifier. The NH₃ is supplied from a tank and then run through another Nanochem filter. Finally, the H₂ source is also supplied from a high-pressure cylinder and then run through a third Nanochem purifier. Each Nanochem purifier is designed for its specific gas. A series of pneumatically controlled three-way valves control the different gas flows leading to the chamber. By operating these valves from the control panel, the outputs of the run line can be switched to the various different inputs on the chamber for the ALE and MOCVD growth modes.

2.1.2 Growth chamber design

In the MOCVD/ALE system, the growth chamber (**Figure 2-2**) is constructed of quartz and stainless steel. The main section of the chamber is quartz to allow for Radio Frequency (RF) heating while the top plate and bottom flange are stainless steel. The quartz is sealed to the stainless steel using a double o-ring seal, with a small vacuum pump evacuating the volume between the o-rings. Large clips are used to hold the quartz tube to the endcap and the flange. The various gas lines are plumbed into the system through the stainless steel top plate. The column III, column V, centerline, and the auxiliary line are all separately controlled, allowing for a large degree of flexibility. The graphite susceptor sits inside another smaller quartz chamber that seals the reaction gasses further from the rest of the chamber.

The heart of the MOCVD/ALE reactor is the ALE susceptor. An illustration of the susceptor, showing the gas flows, is given in **Figure 2-3**. The design of the susceptor is critical to the growth process. The susceptor is constructed of graphite and coated with SiC to protect it from the growth environment. The graphite serves as an inductive load to heat the sample from the RF coils. The susceptor also has to control the flow of gasses in the ALE mode to keep the column III and column V flows separated. The susceptor is constructed in three pieces. The top plate serves mainly to separate and direct the gas flows. The rotating piece has to both heat and rotate the sample between the column III and column V sides of the growth chamber. Finally, the base of the susceptor has to support the susceptor in the chamber, mount the thermocouple for temperature measurement, and serve as a bearing surface for the rotating piece. At the bottom of the chamber, a magnetic feed-through is used to rotate the sample, while a bellows is used to allow for raising and lowering the susceptor.

2.2 Thomas Swan MOCVD System

As a commercial system, the Thomas Swan has a very well designed gas manifold (**Figure 2-5**). Because the main principles are the same as the ALE/MOCVD reactor above,

only the changes in design will be given here. For growth of optical devices, abrupt interfaces are very important. The Thomas Swan reactor has many features that are designed for the instantaneous changes in precursor flux needed for abrupt layers. Because the volume of a valve limits its switching speed, the Thomas Swan run/vent switching block is constructed of custom valves with very small static volumes.

Another problem encountered when growing abrupt interfaces is the changes in pressure when gas flows are changed from the vent line to the run line. This problem is fixed by an extra set of make up lines flowing the carrier gas. The make up lines are controlled by the computer to flow an amount of gas corresponding to the switch in flows between the run line and the vent line. If a TMIn line flowing 300 sccm is switched from run to vent, then the vent makeup line will flow 300 sccm and switch from vent to run. The make-up lines, along with the pressure controlled vent MFC keep the pressures in the vent and run line equal under all conditions.

The chamber design for the Thomas Swan (**Figure 2-6**) reactor is a copy of the final MOCVD chamber design, with the only difference being the input tube. In the ALE/MOCVD reactor the inlet tube consists of a hollow tube with a quartz divider plate, while in the Swan MOCVD the inlet tube consists of two concentric tubes with the smaller inner tube flowing into column III and the larger outer tube flowing into column V gasses.

2.3 Growth of GaN and development of ALE and MOCVD buffer layers

GaN crystals were grown using a combination of the ALE growth mode and the MOCVD growth mode. The experiments utilized an ALE buffer layer and an MOCVD bulk layer. These procedures were used for both the InGaN growth study and the AlInGaN growth study.

The preparation of the sapphire samples prior to GaN growth is similar to the procedures for other MOCVD processes. The sapphire starts out as 2-inch wafer with c-plane orientation miscut to (11-20). The samples are cut up into 15mm x15mm squares for use in the MOCVD reactor. This has two purposes, it uses up less sapphire and it also makes the growth uniformity less critical. Growth uniformity varied considerably among the various chamber configurations. The 15mm x 15mm samples were cleaned in batches of seven samples, which correspond to the number of samples from one two inch sapphire wafer. The samples were cleaned in boiling hexane, acetone, and methanol and then dried with clean N₂ from a GP45 liquid cylinder. The cleaned samples were then placed in a dry box under flowing N₂ until they are ready for growth.

The preparation of the growth chamber consisted of a cycle purge that involved opening the throttle valve to pull to the lowest pressure allowed and then setting the pressure to 100 torr (later 150 torr). This process was repeated 10 times using a relatively high flow of N₂. This cycle purge was performed right after the sample was loaded before the growth run was started. If the prior run were an InGaN run, the chamber would be coated with In from the previous run. This required a bake-out run without a sample present to remove some of the In from the walls of the chamber. The bake-out run was performed at 1000°C and maximum flow of H₂.

In the initial stages of the growth run, after the cycle purge, but before any of the reactant gasses were flowed, a preclean step was performed using 1050°C and 15 minutes of maximum H₂ flow. This served to remove any organic material from the surface of the sapphire wafer. This preclean step was eventually performed at 1100°C as the susceptor/RF coupling was improved to allow higher temperatures. After the preclean step, the sample is ready for growth.

The buffer layer step is the most critical step for the quality of the GaN film. This is where most of the work was done to optimize growth conditions. Initially an ALE buffer

layer growth process was used. This involved a passivation step introducing NH₃ at high temperature for a short period of time (typically 1 min).

After the passivation step, the AlN buffer layer is grown using the system in the ALE growth mode (**Figure 2-3**). This configuration consisted of the susceptor utilizing a rotating and stationary component. This allowed both MOCVD and ALE growth with the same susceptor. In the ALE mode, the sample is mounted on a rotating portion of the susceptor and then gasses are flowed such that the column III gases consisting of TMAl with a N₂ carrier gas are flowed in at the front of the susceptor, the column V gasses consisting of NH₃ and a N₂ carrier gas are flowed in the back of the susceptor, and a centerline flow is run in the center three tubes to separate the column III and column V gas flows. The sample is rotated at 30 RPM so that the sample alternates between the column III and column V gas flows every two seconds. Combined with the c-plane orientation of the sample, this has the effect of growing one monolayer at a time on the growth surface. The ALE growth is continued for 500 Al-N monolayers.

After the ALE film, the reactor is changed from ALE mode to MOCVD mode (**Figure 2-4**). This is done by changing the centerline flow from the carrier gases to the column V gases. The susceptor is shaped such that the flow from the centerline is carried down the offset ramp to where the column III gas is flowing. This sets up two flow conditions with the column III impinging vertically on the sample and the column V coming in horizontally along the ramp. The rotating piece of the susceptor is held stationary under the column III flow. After the ALE AlN layer, a 10-minute AlN bulk layer is grown using the MOCVD configuration. After this AlN layer is grown, a transition layer consisting of a graded AlGaN layer is grown to help relax the mismatch between the AlN layer and the bulk GaN layer grown above. The AlGaN layer is grown starting at 25% AlGaN and then grading to GaN over 10 minutes. At the end of this step, the sample is ready for the growth of the GaN main layer.

For growth utilizing the MOCVD GaN buffer layer, the thermal clean and passivation steps are performed the same as for the ALE buffer layer. After the passivation step, the sample is cooled to the GaN buffer layer growth temperature. Growth temperatures from 500°C to 600°C were used in the study to improve GaN buffer layer quality. The sample is allowed to rest at the GaN buffer temperature and then, when the temperatures have stabilized, the GaN buffer layer is grown. The GaN buffer layer is grown at GaN flow rates from 3.5 – 5.0 sccm to give a thickness ranging from 3.0 – 6.0 Å per second. NH₃ flows ranged from 1.0 - 1.25 l/m, giving a V/III ratio of 4000 to 7200. The thickness and temperature of the buffer layer were changed in an effort to improve the properties of the final GaN film.

After the growth of the GaN buffer layer, the sample was heated up to the growth temperature for the main GaN growth layer. The combination of gas flow conditions and ramp rate were important factors for the quality of the bulk GaN film that was grown afterwards. The growth conditions for the bulk GaN layer were changed from the buffer layer. The growth flux was lowered to 1.0 – 3.0 sccm, resulting in a V/III ratio of 6700 to 25000.

If the sample is grown too thick, the sample may crack during cool-down due to the thermal mismatch. The thickness at which cracking occurs depends on the combination of the composition and thickness of the bulk film. Even identical compositions vary in the susceptibility to cracking depending on the growth quality of the film. Films that have a finely nucleated buffer layer and high dislocation density are more susceptible to cracking than the films that were grown with a sparsely nucleated buffer and lower dislocation density.

2.4 Hall measurements

One of the best measurements of crystal quality both chemically and structurally is the Hall measurement. The Hall measurement setup consists of a large electromagnet controlled manually combined with computer controlled digital multi-meter and programmable current source. The samples are cleaved into a 5mm by 5mm square pieces and then cleaned in acetone and methanol. The contacts consisted of In dots that had been carefully cut from a block of In using a fresh razor blade and then chemically cleaned in HCl for 30 seconds to remove any impurities. The In dots are then rinsed with de-ionized water and methanol and then stored in a beaker filled with methanol.

The GaN samples were mounted in a temperature controlled mounting stage. The stage can be either heated resistively or cooled using adiabatic expansion of high pressure N₂. The temperature range for the Dewar was 77K to 373K. The sample was connected to Keithly instruments that were under computer control. The computer program used the Van der Pauw technique to calculate the sheet resistance, resistivity, carrier concentration, and the mobility of the sample.

The background concentration of the samples gave a good indication of the quality of the crystal. The samples grown with insufficiently thick buffer layers exhibited poor crystal quality. In addition to the poor double crystal XRD full width half maximum, these samples had background concentrations above 10^{18} and mobilities less than $100 \text{ cm}^2/\text{V s}$. Samples grown with optimized buffer layers had carrier concentrations in the low 10^{17} and mobilities of almost $290 \text{ cm}^2/\text{V s}$. Later work by Mason Reed with GaN buffer layers optimized for H₂ carrier gas resulted in mobilities of almost $400 \text{ cm}^2/\text{V s}$.

The buffer layers that are too thin undergo densely nucleated three-dimensional growth and the resulting numerous low angle grain boundaries result in numerous scattering sites and low carrier mobilities. In addition, the boundaries between nucleation sites also serve to create background carriers due to the high dislocation density. On the other hand, properly grown GaN buffer layers with sparsely nucleated grains give large regions of relatively good GaN with fewer structural defects to scatter carriers and lower carrier concentrations.

2.5 Photoluminescence

Photoluminescence (PL) was used to determine the optical properties of the material. While Hall mobility is affected by all kinds of defects, PL mainly responds to optically active defects. For poor quality (either chemically or structurally) crystals, the photoluminescence is weak and corresponds to a deep level with the photon energy below the bandgap. These deep levels result from optically active impurities. A good example of this is the weak yellow emission from InGaN containing carbon impurities. This yellow deep level peak is present due to the incomplete reaction of the metalorganics from low temperature, low H₂ partial pressure or a combination of both. The presence of optically active defects is very important to the operation of optical devices. In our experiments, PL is mainly used to characterize InGaN and AlGaN layers used in LED structures. For the InGaN layers, PL can give the optical bandgap of the material, which may, or may not, be at the band edge. By looking at the intensity and line width of the InGaN peak, it is possible to determine the optical quality of the films. PL is usually combined with θ-2θ x-ray analysis to determine the composition of InGaN films.

PL can also be performed on AlGaN/InGaN/AlGaN quantum well structures to determine the quality of the quantum well. Quantum wells are very sensitive to the barrier height and well width, therefore it is necessary to optimize these conditions to get an efficient device. By comparing quantum wells with identical structures grown at earlier times it is possible to check the system for contaminants that would affect optical devices. Because the quantum well concentrates the carriers in a small region, the output from quantum wells is much more susceptible to optically active defects than the bulk crystal.

The PL setup consisted of the pump laser, the optical mirrors to direct the beam, the diffractometer, and the amplifier to amplify the luminescence signal. The pump laser consisted of a He-Cd laser that emitted at 325nm. The pump laser beam was routed through

a chopper that pulses the beam in sync with a lock-in amplifier. The chopped beam is focused to hit the sample at an angle, allowing both the reflected and transmitted beam of the pump laser to be blocked. The spot at which the pump laser strikes the sample is imaged by a second set of optics to image the luminance from the sample. The luminance signal is filtered to block any scattered light from the pump laser. The luminance signal is then run through a motorized diffractometer. Slits at the input and output of the diffractometer determine the sensitivity when output to the photomultiplier tube. By measuring samples with consistent slit settings and photomultiplier voltages, it was possible to compare the relative intensity of different quantum wells.

2.6 θ – 2θ x-ray analysis.

The θ - 2θ x-ray was used to determine the InGaN and GaN (0002) peaks. The θ - 2θ x-ray machine is a Rigaku system set up for Cu K α radiation ($\lambda = 1.54058$) at 35kV and 25mA of beam current. Samples were scanned from $15^\circ < 2\theta < 80^\circ$ at 0.02 degrees per second. For higher sensitivity, when looking at thin films or looking for forbidden peaks, a longer count time was used. The samples were calibrated to the c-plane (0006) sapphire peak located at $2\theta = 41.685^\circ$. The GaN and InGaN peaks are indexed from the sapphire reflection and Vegards law is used to determine the In composition in bulk layers. The Rigaku can also be used to detect phase separation by detecting secondary phases and to detect ordering by the appearance of forbidden peaks. The Rigaku is limited when evaluating strained films due to the (0002) dimension being distorted by the biaxial strain.

2.7 Double crystal XRD

The Double Crystal X-Ray Diffraction (DCXRD) system is a lower resolution system than the θ - 2θ that has a Si (111) monochromater crystal and independently steppable θ

measurement. The resolution of the θ stepper motor is one arcsecond. The DCXRD is used for estimation of crystal quality by measuring the Full Width Half Max (FWHM) of the resulting films. Since the detector is wide open and has no slits, it does not have the resolution to measure composition; however, it can give an indication of the film thickness from the area under the curve. The stage is also motorized to move parallel to the crystal surface allowing a scan over the entire sample to determine film uniformity. These scans were critically important when developing the reactor configuration, as they were the only reliable gauge of growth uniformity. Both on-axis scans and off-axis scans are possible using the DCXRD. By looking at higher order on-axis and off-axis scans, it is possible to determine the compositions of strained thin films. The on-axis DCXRD is not sensitive to threading dislocations that are perpendicular to the surface, while the off axis DCXRD is sensitive to threading dislocations. The off axis measurement is significantly more difficult to perform, limiting its everyday use.

2.8 TEM Analysis

Transmission Electron Microscopy (TEM) was used to characterize the structural quality of the films via high-resolution imaging. TEM was also used to gather crystallographic information from small regions of the sample using selected area diffraction (SAD). TEM required that the films be prepared to make them thin enough to transmit electrons. A Topcon EMB002 transmission electron microscope at 200kV was used for the TEM studies using two-beam bright and dark field imaging and SAD. Bright-field imaging is performed by collecting information only from the central beam using the objective aperture, while dark-field imaging involves selecting one of the diffracted beams as a source. For high resolution TEM (HRTEM), the primary beam is recombined with a diffracted beam, allowing for distinction between the diffracting planes.

2.9 SIMS Analysis

Secondary Ion Mass Spectrometry (SIMS) was utilized to measure the elemental concentration as a function of depth. This is a mass spectrometry technique that involves sputtering material by bombarding the surface with energetic Ce ions, then measuring the secondary ions for the number of atoms of the target element as a function of sputtering depth. Since sputtering rates differ widely a sample of a similar compound of known concentration is needed as a standard. Even with the limitation of having a suitable standard, SIMS is applicable to all materials and is even capable of detecting isotopes and molecules. The main advantage of SIMS is its sensitivity. SIMS is capable of measuring concentrations as low as 10^{15} atoms/cm³, which corresponds to parts per billion total concentration.

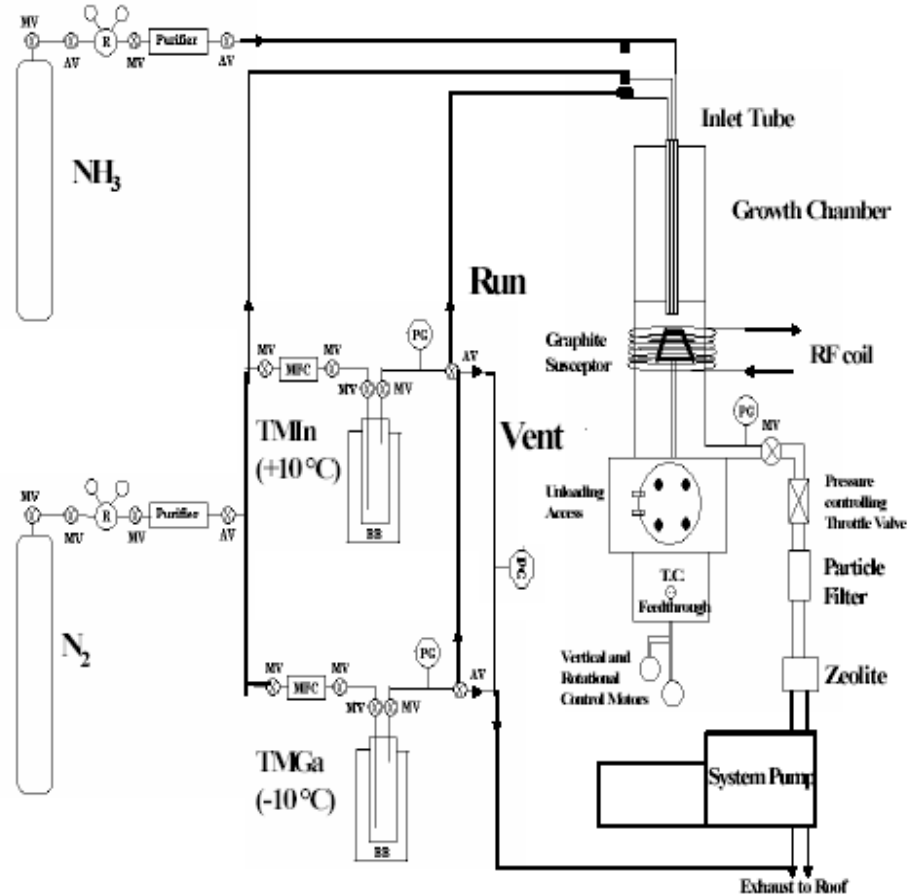


Figure 2-1 Schematic of the ALE/MOCVD system (Parker)

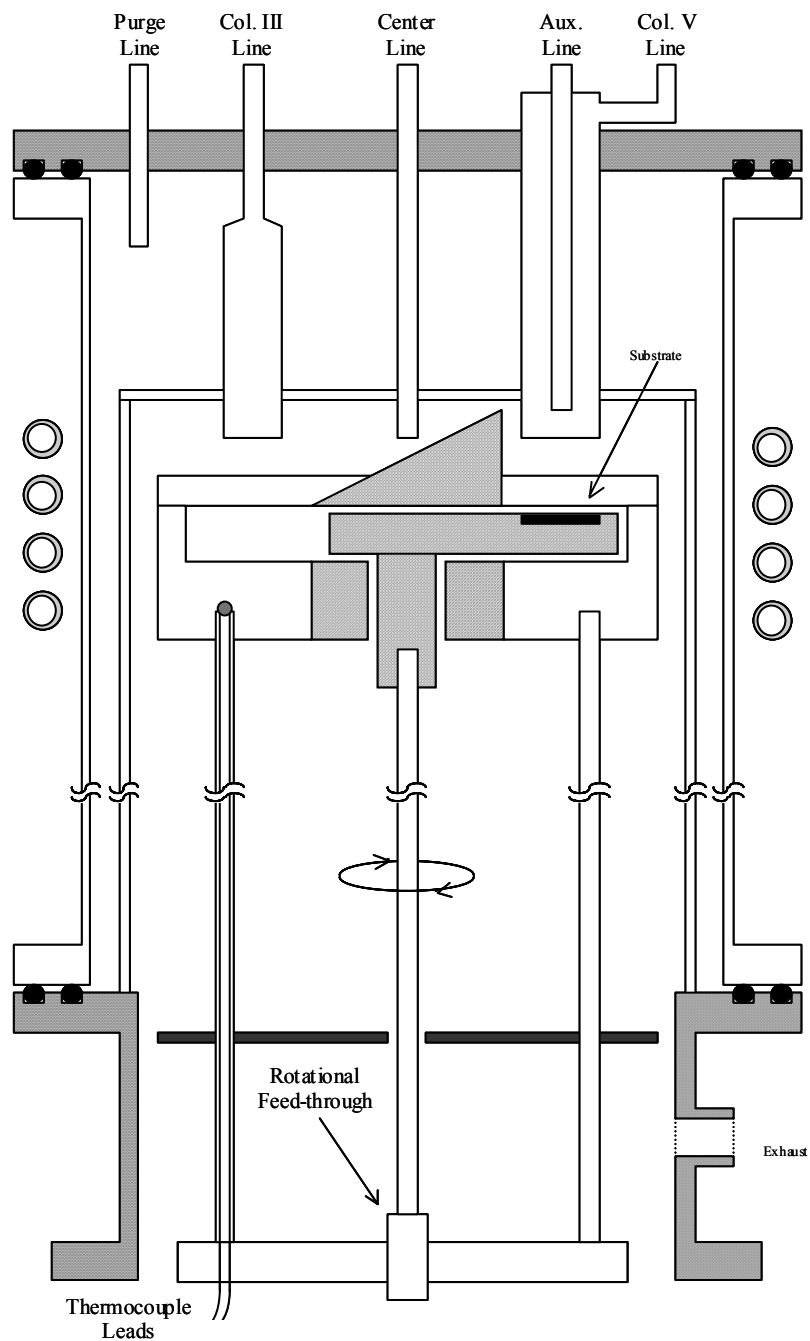


Figure 2-2 Schematic of the ALE Reactor Layout (Parker)

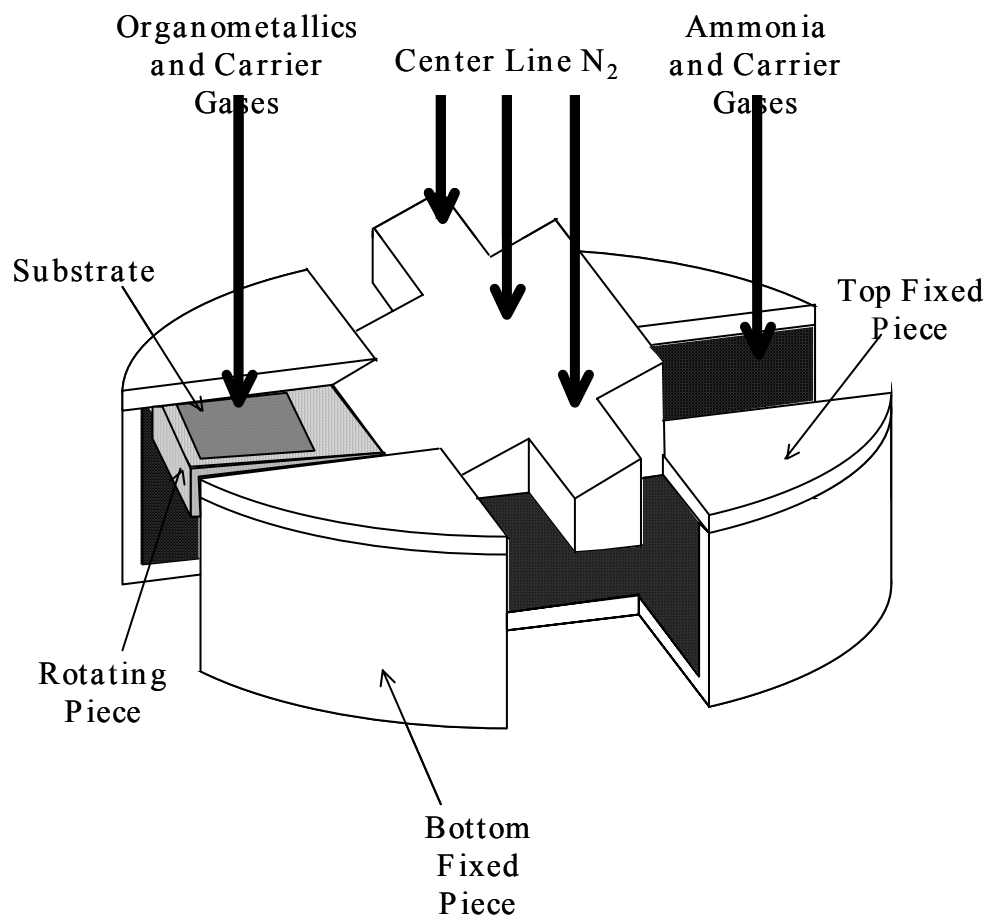


Figure 2-3 Schematic for ALE Growth Mode (Piner)

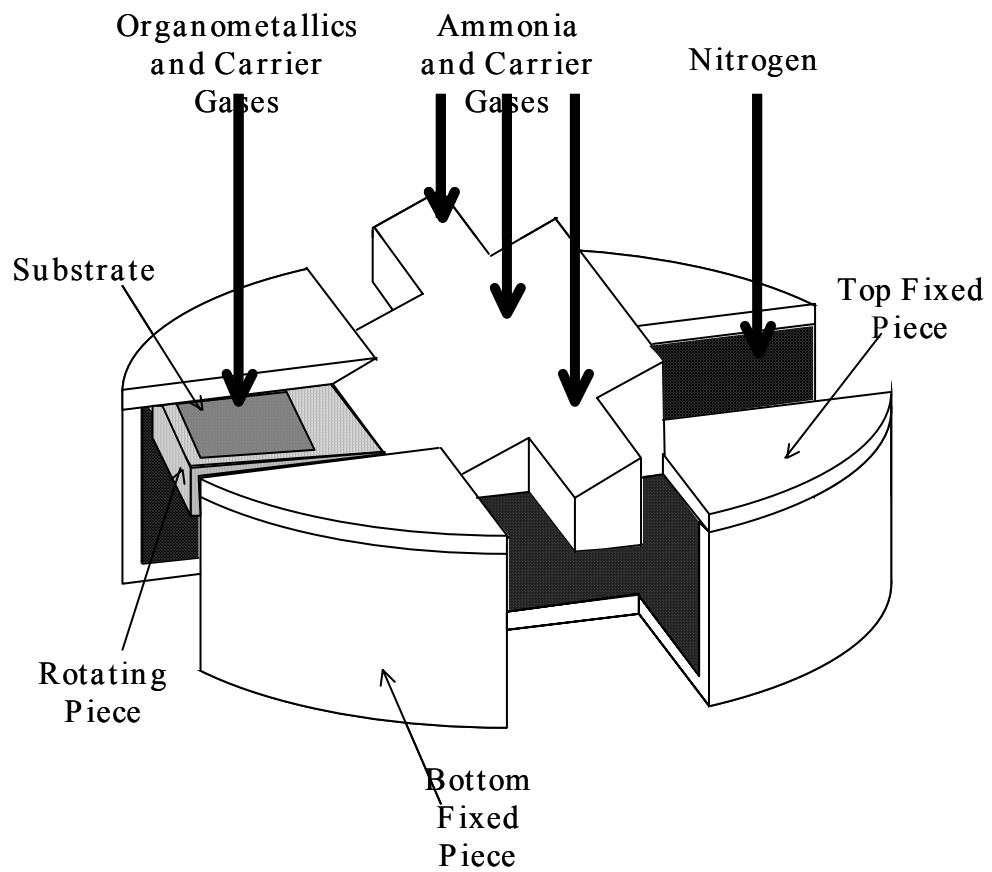


Figure 2-4 MOCVD Growth Mode (Piner)

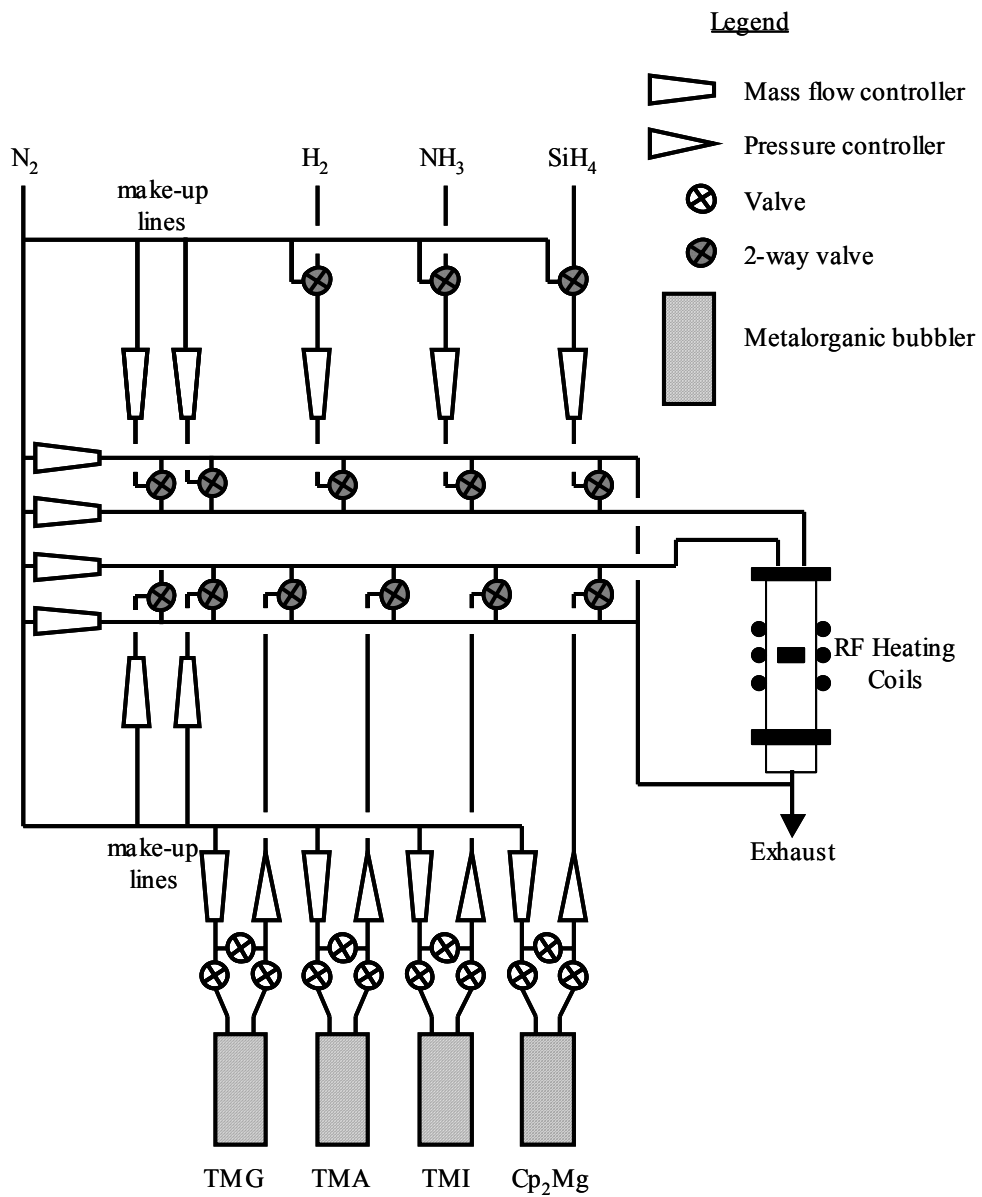


Figure 2-5 Schematic representation of Swan MOCVD system (Aumer)

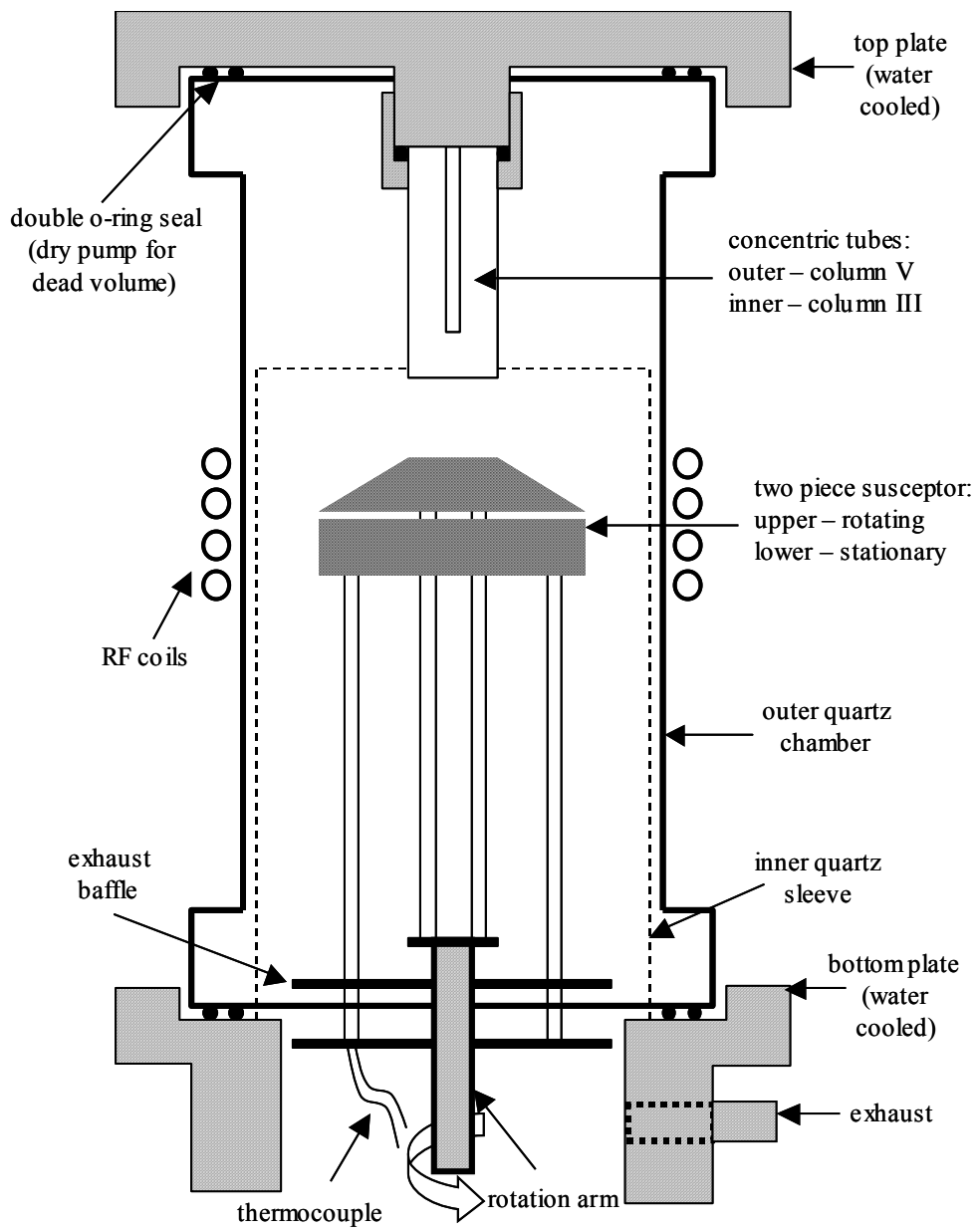


Figure 2-6 MOCVD Growth Chamber for Swan (Aumer)

Chapter Three:Development of GaN Buffer Layer

3.1 Introduction to the nitride buffer layer.

Buffer layers were developed to allow for the growth of single crystal GaN on sapphire. Sapphire has a lattice mismatch of 15% with GaN, making the growth of a single crystal film very difficult. The solution to this problem is to grow a low-temperature buffer layer that can accommodate some of the mismatch between the sapphire and the single crystal GaN film grown on top of the buffer layer. Growth of GaN on sapphire without a buffer layer results in polycrystalline films that are inferior for electronic and optical devices.

The first buffer layers for GaN grown on sapphire were developed by Amano et al. [1] in 1986. This AlN buffer layer allowed for the growth of single crystal GaN on sapphire. Prior to this point all of the GaN grown had been polycrystalline. The ability to grow single crystal on an inexpensive, readily available substrate gave a significant boost to nitride research and represents one of the milestones in GaN development. With the successful development of the low temperature buffer layer, GaN has been successfully grown on SiC[2], Si[3], and spinel ($MgAl_2O_4$)[4]. Growth of GaN on Si represents the lowest possible cost, but the crystal quality of the resulting GaN film is much poorer than the other substrates. The growth of GaN on $MgAl_2O_4$ is mainly to take advantage of the cleave planes for making Laser Diodes (LD). The growth of GaN on SiC has been used commercially for many years for LED production. Although the SiC is very expensive compared to sapphire the advantages in processing and packaging from having a conductive substrate more than made up for the cost of the SiC wafers.

The low temperature buffer layer is grown in several stages. These consist of the nitrogen passivation step, the buffer layer growth step, ramp step, anneal step, and the initial high temperature GaN layer. During the nitrogen passivation step the Al_2O_3 surface is converted into AlN to allow for the growth of either an AlN or a GaN low temperature layer.

Vennegues et al. [5] showed that this AlN layer extended up to 10 monolayers into the sapphire substrate. After the surface of the sapphire has been passivated, the low temperature buffer layer is grown at between 400°C and 600°C. Growing the buffer layer at a low temperature results in a highly defective thin film. The crystal defects in the buffer layer serve two purposes. First, they accommodate the mismatch between the GaN and the sapphire. Second, they represent a high-energy crystal state that can recrystallize under annealing. The ramp and anneal step give the low temperature buffer layer time to undergo recrystallization. Finally, the initial growth of the high temperature GaN film is not smooth, but is made up of three-dimensional islands that slowly coalesce into a smooth film.

The quality of the buffer is critical, because the buffer layer determines the polarity of the film, density of stacking faults and mixed polarities, and the dislocation density for all of the films grown afterwards. Traditionally, Ga polar films grow on AlN buffers while N polar films grow on GaN buffers. However, it is possible to get either type of polarity by varying the growth rate of the film[6, 7]. While good quality material has been grown with either polarity, initial buffer layer growth can contain a mixture of both polarities. If the mixture of polarities is not annealed to one or the other, stacking faults will be widespread, thereby reducing crystal quality. The size of the domains in the bulk GaN layer depends on the structure of the underlying buffer layer. Fine domain sizes increase the defect density and reduce the mobility of carriers in the films. Bridger et al. [8] found that the carrier diffusion lengths were proportional to the size of the growth domains. Their data strongly suggest that recombination due to defects at growth domain boundaries is the limiting factor for carrier lifetimes.

Initially, thin AlN buffers were used for the growth of GaN on sapphire. The AlN buffer layers were developed to the point where mobilities of $430 \text{ cm}^2/\text{V s}$ at 300K with the mobility increasing to $500 \text{ cm}^2/\text{V s}$ at 77K were achieved. Background carrier concentrations as low as $2 * 10^{17}$ had been achieved with AlN buffer layers[1]. GaN buffer layers were not developed initially due their narrow window for optimum performance. However, the GaN buffer layers were soon developed to the point that they began to exceed their AlN

competition. The GaN buffer layers had slightly better mobilities at room temperature ($450 \text{ cm}_2/\text{V s}$) than AlN buffer layers[9]. At 77K however, the GaN buffer layers have mobilities of $900 \text{ cm}_2/\text{V s}$. The background carrier concentration is also much lower for GaN buffer layers than for AlN buffer layers. Carrier concentrations as low as $4 * 10^{16}$ have been achieved in GaN on GaN buffer layers[10].

Epitaxial Lateral Overgrowth (ELO) was developed to allow for increased buffer layer performance by laterally growing GaN over a SiO_2 mask where the GaN only contacts the sapphire through openings in the mask[11]. Because the laterally overgrown GaN does not contact the sapphire and is incoherent to the SiO_2 , the areas of lateral overgrowth have vastly reduced threading dislocation densities. This gives excellent crystal quality, but with geometrical limitations due to the masking step. The excellent areas of ELO are in the region between the mask openings and the merger of the two overgrowing layers from the adjacent mask openings. While this structure makes it difficult to generate large area devices, it is ideal for LD as they have a stripe geometry that perfectly matches the geometry of the low defect areas of the ELO Grown Films.

3.2 Growth of The ALE Buffer layer

During my tenure on the MOCVD system, we had grown materials ranging from ALE quantum wells to bulk GaN based on a GaN buffer layer. The first six months on the system were spent with the ALE buffer layer configuration. Most of the work at that time was for the study of H_2 on the growth of InGaN alloys. The ALE buffer layer gave good materials properties for the GaN and InGaN films.

A typical ALE growth run is started by annealing under H_2 for 15 minutes prior to passivation under NH_3 for one minute at 1050°C and 700 torr. The temperature is then dropped to 700°C and the pressure is dropped to 100 torr for the ALE growth. To convert

the reactor to ALE mode (Figure 2-3), several valves are operated to direct the gas flow to the separate V and III sides used for ALE. The ALE growth was run for 500 cycles with a rotational speed of 30 rpm. After the completion of the 500 cycles of ALE, the reactor is heated to 950°C and growth of MOCVD layers are initiated. During the heat up, the reactor is converted over to MOCVD mode (Figure 2-4). To do this, the column V flow is changed from the back tube to the center tubes that can flow down the ramp. The chamber pressure is increased back up to 700 torr and the sample is rotated and locked under the column III side. The MOCVD layers grown at 950°C consist of a 25% AlGaN layer that is graded to GaN over a period of 2.5 minutes. The AlGaN layer is followed by a GaN prelayer and then by the bulk GaN layer.

The ALE buffer layer had been in use for over a year and had proven to be very forgiving of varying growth conditions. The films were structurally good, with DCRXD linewidths of 40 arcseconds on-axis and 300 arcseconds off-axis. The only problem was that the Hall mobilities were limited to around $290\text{cm}^2/\text{Vs}$.

In an attempt to improve upon the ALE buffer layer, we embarked on a series of system modifications and growth experiments using MOCVD AlN and GaN low temperature buffer layers. Initial experiments utilized the ALE reactor configuration and an AlN buffer layer. Later a hybrid buffer layer utilizing an AlN layer followed by a grading layer to a GaN layer was used. Finally, a pure GaN low temperature buffer layer was used. An extensive series of system modifications were undertaken to transition the chamber from the ALE configuration, which was a compromise between the ALE and MOCVD modes, to a pure MOCVD configuration.

3.3 Development of chamber design

The majority of the system modifications were to address the gas flow dynamics in the reactor. The initial goal was to increase the gas flow velocity and decrease the residence

time of the reactants in flux to the growth surface. The initial design for the ALE system used a ramp that served as a divider for the column III and column V gasses in ALE mode and was converted to a guide to route the column V gasses to the growth surface. The problem with this design was that the column V gasses were heated and allowed to diffuse out and slow down as they went down the ramp. These effects increased the likelihood of gas phase reaction in the vicinity of the growth surface.

The initial modification of the system involved the replacement of the paddle for the sample holder with a round disk. This modification required that the ramp be offset to channel gasses from the column V side instead of the centerline. These modifications eliminated the possibility of growing ALE GaN, but allowed for sample rotation for better uniformity and also made the temperature of the sample much more controllable. Although these improvements were beneficial, they still allowed the column III and column V gasses to heat up and react. The best way to reduce this problem was to remove the ramp completely. This started a series of modifications using bent quartz tubes to channel the gas to the growth surface. Unlike the graphite/SiC ramp used previously, the quartz tubes were not heated by the RF field. This allowed the gasses to remain cooler and be separated until they were close to the sample surface. Unfortunately, we were not able to construct tubes that replicated the smooth transition between the ramp and the sample holder, resulting in turbulence that was detrimental to the film quality.

One of the more serious issues with the system that would cause problems throughout the development of the GaN buffer layer was a consistent “pepper” effect in the films. The “pepper” consisted of small crystals of GaN that were readily apparent by optical microscopy. At the time, it was decided that the pepper effect was the result of gas phase reaction depositing small crystallites of GaN onto the growing film.

To get rid of the “pepper,” we embarked on a series of system modifications to eliminate gas phase reactions. We also optimized the susceptor and reactor design for

MOCVD growth. Although most of the designs that were tried were unsuccessful, they led to the development of the current setup, which has excellent performance for MOCVD GaN.

The change to the quartz tubes for the column III and column V gasses significantly reduced the heating and intermixing of the reactant gasses, however the samples still exhibited the “pepper”. In addition, the system changes that had been implemented had completely changed the gas dynamics to where all of the previous optimizations were out the window. This resulted in sub-optimum films. In a final attempt to reduce the gas residence time, we modified the quartz tubes to include an additional end plate with dozens of small, laser drilled holes. These holes effectively reduced the cross-sectional area to the limit of the linear flow regime to reduce the gas residence time to the absolute minimum possible.

All of the studies for the optimum design of the column III and column V delivery tubes were done using similar GaN buffer layers. Changes to the growth rate and time had to be made to get consistent results, but the basic temperatures and conditions were held as constant as possible under the conditions. This allows, in a limited way, a comparison between the different gas delivery designs. This was interesting in that the design that had given the best crystal quality was a derivative of the original ALE setup. The optimal configuration had a sloped pyramid to deliver the column V gasses and a column III tube that had a plate with five medium sized holes in a baffle placed 2 cm from the end of the tube.

The absolute worst setup was the one with the quartz tubes that had laser drilled end caps. It is interesting to note that the design that was intended to have the highest permissible gas velocity to reduce gas phase interaction actually had one of the worst “pepper” surfaces of all of the designs. Hall mobility on the best sample from this design was only $9 \text{ cm}^2/\text{Vs}$.

The lesson learned in this series of experiments is that the turbulence from the high-speed jets impinging on each other negates any advantage from higher gas velocity. The best results occurred with a design that had slower moving, even flows of the column III and column V gasses with a smooth interface between the two flows. This lesson was

incorporated into the current design that uses a long rectangular tube that is at relatively low velocity and utilizes a quartz spacer running down the length of the tube. The current design does have problems with gas phase reaction. However, the solution to this problem was to reduce the chamber pressure, thereby increasing the gas velocity. This proved to be much more effective than using artificial constrictions that induced turbulence.

3.4 AlN Buffer Layers

AlN buffer layers were popular during the early days of GaN, but fell out of favour due to the superiority of the GaN buffer layer. The AlN buffer layer has some of the same advantages as the ALE buffer layer, namely that there is a wide range of conditions that result in good quality films with smooth specular surfaces. During the AlN buffer layer study, we experimented with buffer layer temperature, growth rate, growth time, and post buffer layer annealing. The optimum conditions that were arrived at were 3 sccm TMGa for 6 minutes with a 3 minute anneal. Unfortunately, the best AlN films that we grew did not have properties that were any better than the ALE buffer layer.

In fact, the MOCVD AlN buffer layer properties were in most cases worse than the ALE. This is an interesting development, as the nitrogen passivation, gas flow, V/III and bulk growth conditions were very similar between the ALE and MOCVD buffer layers. One possible explanation for this is the V/III ratio. Long after we completed the AlN buffer study, Ito et al. [12] reported that the V/III ratio of the AlN buffer layer was critical to the quality of the final film. V/III ratios of less than 1800 were found to give the best quality films. If the V/III ratio is too high, the film quality degrades significantly. Because our AlN buffer layer runs were using a V/III ratio ranging from 4000 to 7200, our conditions were well outside of the ideal range.

This conclusion would seem to be borne out by our results with double the normal NH₃ flow. These runs were of very poor quality and looked polycrystalline. The optimum

conditions for the AlN buffer we obtained were with lower NH₃ and higher growth rates. However, these results were still not as good as the best ALE films. With the ALE films alternately exposed to 100% column III followed by 100% column V, the Al atoms on the surface would have approximately 1 second per cycle under 0 V/III ratio to rearrange themselves on the surface. This could explain the improved film quality compared to MOCVD AlN buffer layers with similar gross gas chemistry.

3.5 Hybrid AlN/GaN Buffer Layer

The next buffer layer that was investigated was the hybrid AlN/GaN buffer layer. The AlN/GaN buffer layer consisted of a 2 minute AlN layer grown at 5 sccm followed by a grading layer to GaN with a capping layer of 1 minute of GaN. This hybrid nucleation layer was followed by a 3 minute anneal at high temperature prior to the growth of the GaN bulk layer. The hybrid layer gave results comparable with the ALE layer. During the time the hybrid layer was used, we repeated some of the ALE InGaN runs to check for repeatability of the system. The properties of the InGaN were unaffected by the change in the underlying nucleation layer from ALE AlN to MOCVD AlN/GaN. InGaN quantum wells were also grown using the hybrid AlN/GaN buffer. Although the results with the InGaN quantum wells were similar to the ALE buffer layers, they still lagged behind when compared with commercial InGaN grown on pure GaN low temperature buffer layers.

3.6 GaN Buffer Layer

The final buffer layer that was studied and that continues to be used currently in the system is the pure GaN buffer layer. This is the standard buffer layer used by most commercial GaN devices grown on sapphire. Although the GaN buffer layer has the best overall properties, it is very sensitive to growth variation. At the time that we were studying the GaN buffer layer, it was not well documented in the literature. This made it necessary to determine the optimal conditions by trial and error. The buffer layer process was also studied

as it related to the formation of the continuous film by optical microscopy. Our early attempts at a GaN buffer layer used this method to determine the optimal thickness of the buffer layer to get a smooth film. While this method as it relates to the buffer layer is flawed, it gave valuable insight into how to interpret the optical surface of the bulk layers.

Although the ALE reactor configuration was not optimal for the GaN MOCVD buffer, the initial results were promising. After calibrating the GaN buffer layer for temperature, growth rate, and thickness, we were able to get good mobilities approaching $280 \text{ cm}^2/\text{Vs}$. The high temperature annealing step was investigated using the AlN/GaN hybrid buffer and was determined to have little effect on the film quality. We did not further investigate the effect of annealing with the pure GaN buffer layer. The best results with the AlN/GaN buffer layer did not use a separate anneal stage, and we ended up not using an anneal step on the pure GaN buffer layer. This is unfortunate, as it was later discovered[13] that the anneal step is a critical factor in getting optimal quality GaN from pure GaN low temperature buffer layers.

The samples where we experimented with altering the annealing time were thicker GaN buffer layers and annealed under low partial pressures of H_2 . To get the best quality GaN buffer, it is necessary to carefully balance the annealing step with the thickness of the buffer layer. When the buffer layer forms initially, it has numerous three dimensional islands that are each oriented slightly differently to each other. Left alone, these islands would coalesce and form domains with a slight mismatch to each other. If you grow the buffer layer thick enough, the domains will coalesce during the buffer layer and lock in the mismatch domains (we studied this optically in a series of runs growing only the buffer layer). Unfortunately, the perfectly smooth looking buffer layer consists of densely nucleated domains while ideal buffer layers actually look very poor and rough under the optical microscope.

During this anneal, the buffer layer begins to desorb. If annealed for long enough, the buffer layer would desorb completely and the high temperature growth would start with bare

sapphire. However, when the GaN buffer layer desorbs, it does not do so uniformly. Some of the domains are more mismatched to the passivated sapphire than others. Because these mismatched domains have a higher energy, they are less stable and tend to desorb first. In addition, not all of the GaN that desorbs leaves the sample completely; some of the GaN redeposits elsewhere on the sample. During the anneal step the unstable domains tend to desorb completely, leaving the desorbed GaN to redeposit on the most stable domains which are closely aligned to the passivated sapphire underneath[14]. This gives a rough surface as the desorbed GaN redeposits on the stable islands. Halidou et al.[13] studied the annealing of the GaN buffer layer and its effect on the surface roughness. Using reflectivity measurements, he showed that H₂ enhances surface transport and leads to a three dimensional surface, thereby enhancing the transformation of GaN. We observed this roughening on some of the thin buffer layer only samples, but because we were looking to get smooth and specular samples, we thought that what we were seeing was undesirable. Although the ideal buffer layers are rough at this point, the roughness represents a sparsely nucleated array of stable islands. Growth on this film gives a bulk layer with large domains and relatively few domain boundaries to scatter carriers.

In addition to the annealing step selectively desorbing mismatched GaN domains, it also can selectively desorb different polarities of GaN. Sumiya et al.[15] showed that the V/III ratio affected the polarity of the low temperature GaN buffer layers and that upon annealing, the +c or Ga terminated surface remains after the N terminated surface is etched away. Under the V/III ratios that we were using, the samples had mixed polarity. Without a good annealing step to etch away the second polarity, the mix in polarities will lead to numerous stacking faults in both the buffer layer and the layers grown afterwards.

One problem that plagued the system throughout the study of optimum gas delivery was a lack of repeatability over time. The problem with repeatability became worse the longer a given configuration was in use. This had been noticed in the ALE setup and our understanding was that the rotating piece that held the sample and the fixed piece that contacted the controlling thermocouple would degrade over time and result in incorrect

temperatures. After a number of runs, the chamber was cleaned out, the quartz was etched (which took several days), and the calibration of the thermocouple to the sample checked with an optical pyrometer. Deviations of up to 35°C were not unusual. When the deviations became too large, the rotating piece and/or fixed piece would be replaced.

During the study of the GaN buffer layer, it was determined that the addition of H₂ in the bulk layer significantly improved the optical quality of the GaN. From that point on, all runs were conducted with maximum H₂ in the bulk layer. The improvement from H₂ is not unexpected, as the addition of H₂ in InGaN results in reductions in the incorporation of impurities, Piner et al. [16]. By adding H₂ to InGaN, impurities such as C and O can be reduced by over an order of magnitude. In the case of C impurities, this reduction in impurities can have an even greater effect than would be expected from scattering alone. The C atoms can act as amphoteric dopants resulting in highly compensated films. This compensation effect can significantly reduce mobilities in the GaN films.

Another effect that H₂ has on the growth of GaN is that it increases the surface mobility of adatoms on the growing film. This increase in mobility is partially due to the passivation of dangling bonds on the growth surface. These dangling bonds can impede the mobility of Ga adatoms during the growth process. The result of the improvements in surface mobility is seen as a beneficial change in surface morphology. In films grown with no H₂ in the carrier gas, the surface morphology will have the form of smoothed hexagons that are densely packed. These hexagons represent the different domains arising from the three dimensional islands that nucleated the film growth before coalescing into the growth surface. With the addition of H₂, these hexagonal features become much larger and much more sparse. Because the three-dimensional islands formed during the buffer layer have slightly different crystallographic orientations, the interfaces between these islands scatter the charge carriers, reducing the mobility. Higher Ga surface mobilities allow for larger domains of GaN. The larger domains are sparser, resulting in less scattering in the crystal from domain boundaries.

Unfortunately, the addition of H₂ during the bulk growth had an unintended side effect. The H₂ at high temperature greatly increased the speed at which the susceptors would degrade. As soon as the coating of SiC was compromised, the high temperature H₂ would etch away the underlying graphite at an alarming rate. Whereas before the susceptors would degrade slowly over time in a predictable manner, with the increased H₂ flows the susceptors would degrade at such a rate that the temperatures would change from run to run.

The degrading susceptors would also contaminate the system as the graphite was etched away. The exposure of the underlying graphite to the H₂ carrier gas would create a significant source of C impurities in the reactor. The film quality from a compromised susceptor was noticeably degraded compared to a fresh one. This effect would not always be apparent until the temperatures would start to drift. In one case, the problem was identified when the susceptor crumbled when the sample being loaded, leaving a hollow shell of SiC with nothing inside. During the times of active system modification the susceptors would not be in place long enough to degrade. However, when an optimal system configuration was decided on, the susceptor degradation became a much more serious problem.

The existing susceptor design was based on the ALE configuration. As such, it had intricate passages used for gas flow isolation during ALE mode growth. It also had to have clearance for the rotating piece to travel. During the time the ALE system was in use, the runs did not use H₂ except in the cleaning step prior to the buffer layer. Little consideration was given to the thermal stresses on the susceptor during the heating and cooling cycles. The ALE design contained numerous sharp angles that acted as stress concentrators where the SiC could be compromised. With these problems in mind, a new susceptor design was developed to have as smooth a shape as possible. In addition to the reduction in stress concentrations, the smooth susceptors were also less expensive to machine.

In all, over 400 growth runs were performed over a 15-month period. During this time, there were 38 system modifications. While most of the runs were not successful, the experience gained allowed for a gradual evolution of the reactor chamber from a purpose

built ALE reactor forced to grow MOCVD, to a dedicated MOCVD design. The final design of the reactor (Figure 3-1) used the long rectangular tube with the quartz spacer running down the length of the tube and the newly designed smooth susceptor. To cut down on gas phase reaction, the pressure was lowered and a water-cooled quartz sleeve was installed. The resulting system configuration produced GaN material that equalled the quality of some of the best GaN films.

3.7 References

1. Amano, H., et al., *Metalorganic Vapor-Phase Epitaxial-Growth of a High-Quality Gan Film Using an Ain Buffer Layer*. Applied Physics Letters, 1986. **48**(5): p. 353-355.
2. Fischer, S., et al., *Properties of GaN grown at high rates on sapphire and on 6H-SiC*. Applied Physics Letters, 1996. **69**(18): p. 2716-2718.
3. Watanabe, A., et al., *The Growth of Single Crystalline Gan on a Si Substrate Using Aln as an Intermediate Layer*. Journal of Crystal Growth, 1993. **128**(1-4): p. 391-396.
4. Kuramata, A., et al., *High-Quality Gan Epitaxial Layer Grown by Metalorganic Vapor-Phase Epitaxy on (111) MgAl₂O₄ Substrate*. Applied Physics Letters, 1995. **67**(17): p. 2521-2523.
5. Vennegues, P. and B. Beaumont, *Transmission electron microscopy study of the nitridation of the (0001) sapphire surface*. Applied Physics Letters, 1999. **75**(26): p. 4115-4117.
6. Huang, D., et al., *Dependence of GaN polarity on the parameters of the buffer layer grown by molecular beam epitaxy*. Applied Physics Letters, 2001. **78**(26): p. 4145-4147.
7. Huang, D., et al., *Polarity of GaN grown on sapphire by molecular beam epitaxy with different buffer layers*. Physica Status Solidi a-Applied Research, 2001. **188**(2): p. 571-574.
8. Bridger, P.M., et al., *Correlation between the surface defect distribution and minority carrier transport properties in GaN*. Applied Physics Letters, 1998. **73**(23): p. 3438-3440.
9. Akasaki, I., et al., *Effects of Ain Buffer Layer on Crystallographic Structure and on Electrical and Optical-Properties of Gan and Ga_{1-X}Al_Xn(0-Less-Than-X-Less-Than-or-Equal-to-0.4) Films Grown on Sapphire Substrate by Movpe*. Journal of Crystal Growth, 1989. **98**(1-2): p. 209-219.

10. Amano, H., et al., *P-Type Conduction in Mg-Doped Gan Treated with Low-Energy Electron-Beam Irradiation (Leebi)*. Japanese Journal of Applied Physics Part 2-Letters, 1989. **28**(12): p. L2112-L2114.
11. Nakamura, S., et al., *High-power, long-lifetime InGaN/GaN/AlGaN-based laser diodes grown on pure GaN substrates*. Japanese Journal of Applied Physics Part 2-Letters, 1998. **37**(3B): p. L309-L312.
12. Ito, T., et al., *Effect of AlN buffer layer deposition conditions on the properties of GaN layer*. Journal of Crystal Growth, 1999. **205**(1-2): p. 20-24.
13. Halidou, I., et al., *Annealing effect on GaN buffer layer surface*. Physica Status Solidi a-Applied Research, 2001. **184**(1): p. 263-271.
14. Lorenz, K., et al., *Comparative study of GaN and AlN nucleation layers and their role in growth of GaN on sapphire by metalorganic chemical vapor deposition*. Applied Physics Letters, 2000. **77**(21): p. 3391-3393.
15. Sumiya, M., et al., *Systematic analysis and control of low-temperature GaN buffer layers on sapphire substrates*. Journal of Applied Physics, 2003. **93**(2): p. 1311-1319.
16. Piner, E.L., et al., *Impurity dependence on hydrogen and ammonia flow rates in InGaN bulk films*. Applied Physics Letters, 1997. **71**(14): p. 2023-2025.

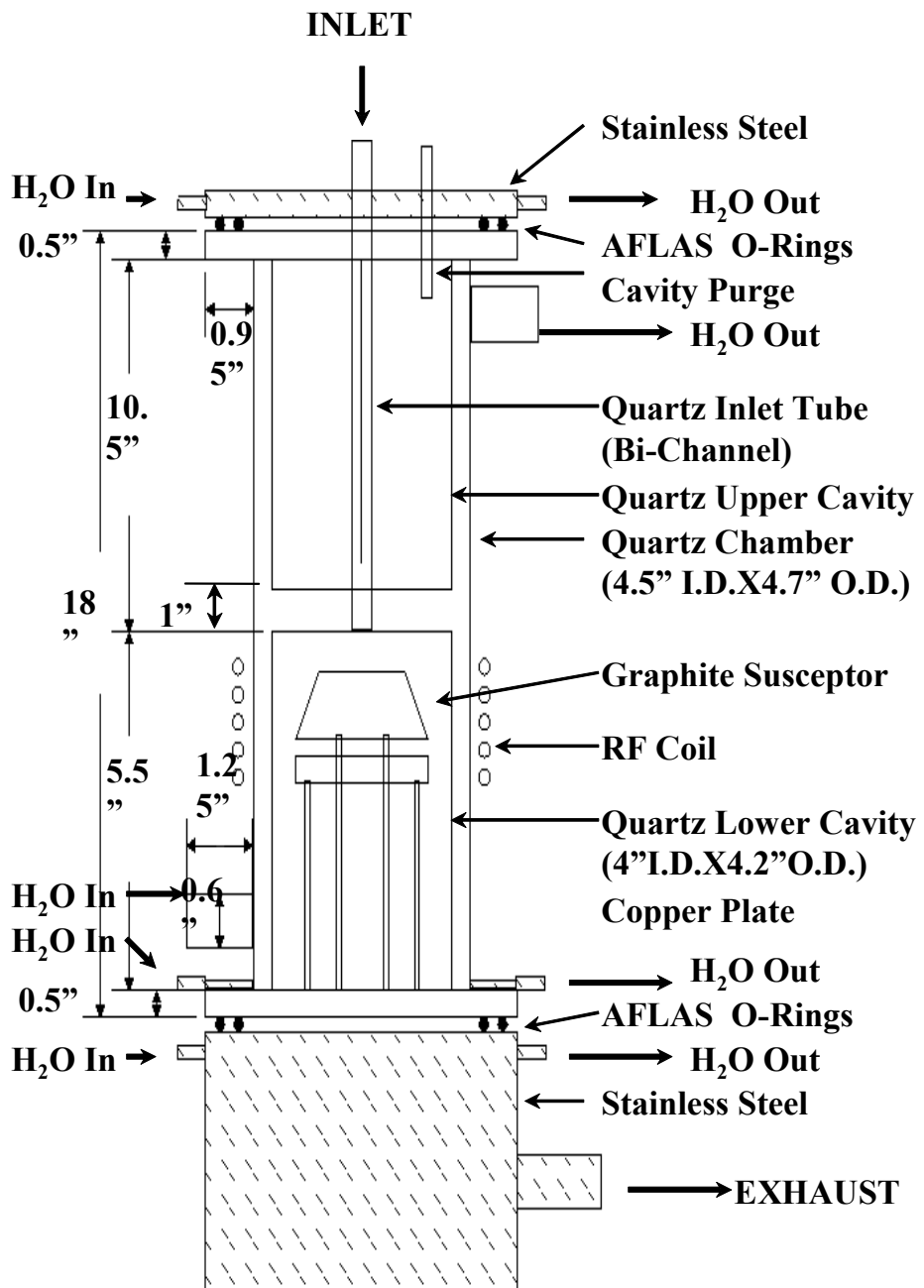


Figure 3-1 Diagram of modified MOCVD Setup (Parker)

Chapter Four: Growth and Ordering of InGaN

4.1 InGaN Growth

Structure for InGaN growth (given in Figure 4-1) consisted of an InGaN bulk layer on top of an ALE buffer layer followed by a GaN bulk layer (as shown in Figure 1). Studies [1] have shown that InGaN grown on a high temperature GaN bulk layer is of much better quality than InGaN grown directly on a low temperature buffer layer. The buffer layer used is the same ALE buffer layer used for the GaN growth discussed in Chapter 3. It consisted of an ALE buffer layer that was grown at 700°C followed by 15 minutes MOCVD AlGaN layer and 10 minutes GaN layer grown at 950°C. The growth sources consisted of an In source of ethyl-dimethyl-indium EDMIn at 10°C, a Ga source of TMGa at -10°C, and an Al source of TMAl at 18°C. NH₃ serves as the column V source. The initial growth conditions used are the same as for GaN on the ALE buffer layer, followed by the bulk InGaN layer.

Growth conditions for InGaN films consisted of: temperatures between 680°C and 780°C, TMGa flows of 1-10 µmol/min, and EDMIn flow of 1-6 µmol/min. Flows from the column III side were typically around 1 l/min. NH₃ flows ranged from 0.3 to 5 l/min, with the balance of the volume made up by N₂. Because InN has a higher N₂ partial pressure than GaN or AlN, InGaN films need to be grown at higher V/III ratios. The higher vapour pressure for InN is a direct result of the lower bond strength of 44 kcal/mol as compared to AlN and GaN, which have 66 kcal/mol and 51 kcal/mol respectively[2].

The resulting In compositions were a strong function of temperature as shown in Figure 4-2. The In composition, under identical growth conditions of 1:1 In:Ga ratio, decreased from 49% to 12% with an increase in growth temperature of 90°C. The thickness of the InGaN layers increased from 300 nm to 500 nm with increasing In content. This would indicate that the composition difference is from the additional incorporation of In, with Ga composition relatively constant.

The increase in In composition with an increase in In:Ga ratio was anywhere from almost linear at low temperatures, to very little effect at high temperatures. Increases in the TMG rate at a constant In:Ga ratio resulted in a higher In% in the films, indicating that higher growth rates increase the In incorporation. This is in agreement with previous studies on growth rate effects in InGaN[3]. To check that the decrease in InGaN composition with temperature was not due to the decrease in cracking efficiency of the NH₃, additional experiments were run to test the effect of V/III ratio on In incorporation (Figure 4-3). The In incorporation rate was constant above a critical V/III ratio of around 10,000. These results would indicate that the growth temperature is the dominant factor for the incorporation of In in InGaN films.

A strong effect was noted with the presence of H₂ during the growth of InGaN. InGaN runs with large amounts of H₂ showed almost no In incorporation [4]. It appeared that H₂ was preventing the incorporation of In in the InGaN alloy. To study this effect a set of runs was done with temperatures ranging from 690°C up to 780°C with varying flows of H₂ on the column III side from 0 to 100 sccm. For all of the runs, the In:Ga ratio was held constant at 1:1 and the V/III ratio was 27,500. The results of the study are given in Figure 4-4. At 710°C the amount of In decreased from 40% InGaN to 15% InGaN with the addition of 100sccm H₂. Thickness of the films increased with increasing In composition, indicating that the In incorporation rate was the limiting factor. Studies for the effect of H₂ on the growth and the impurity content of InGaN were published by Piner et al.[4, 5].

One difficultly with growing higher In composition films is the prevention of In metal droplets. If the In:Ga ratio is too high for growth at a lower temperature or with too low of a V/III ratio, In metal droplets will form on the surface. It has been demonstrated by Bedair et al. that when In metal droplets form on the surface of the growing film, they can effectively getter the In from that film, resulting in a dramatically reduced In composition in the film [6].

4.2 Detection of phase separation

The growth of InGaN compositions above 20% In becomes complicated by phase separation. Growing devices with In compositions higher than 20% can be achieved with thin InGaN films. This is due to the large strain difference between the GaN and InN alloys resulting in large strain energies for InGaN films grown on GaN. When the strain energy gets too high, it is possible to reduce the energy of the InGaN alloy by phase separating. This can occur in one of three ways: clustering, where the different atoms group on a small scale coherently strained to the rest of the crystal; ordering, where the different atoms separate into an ordered structure of alternating composition; and phase separation, where the different atoms separate into clusters that are not coherent to the rest of the crystal. Moon et al.[7] found that In segregation can take two forms. The first, surface segregation, forms as self-assembled quantum dot of In that acts to enhance radiative recombination. The second are regions formed in the InGaN film during the higher temperature growth for the capping layers of the device. These regions tend to act as non-radiative recombination centers.

Phase separation has been observed in both mixed cation and mixed anion crystal systems. The InGaAs[8], AlGaAs[9], InGaP[10], GaAsP[11], GaAsSb[12], and the InGaAsP[13] have all been shown to undergo phase separation. Phase separation in InGaN was first observed[14] during growth of polycrystalline samples. The phase separation in the polycrystalline InGaN was observed after long annealing at temperatures above 600°C. Because all of these studies rely on XRD to indirectly detect the phase separation, the structure of the phase-separated regions was not studied.

During the study of the effect of H₂ on InGaN growth conditions, XRD was routinely done to calculate the composition of the InGaN using the 0002 peak. In the samples that had In compositions over 40%, extra peaks were noticed with higher In compositions than the rest of the crystal, as shown in Figure 4-5. In addition to the extra peak in the high In region of the InGaN curve, an additional shoulder in the low In region also appeared. A typical XRD scan for InGaN is shown in Figure 4-6, while the scans with the additional peaks are

shown in Figure 4-7. The second curve is a fitting curve made up of independent Gaussians to determine compositions present in the film. Note the presence of both higher and lower In compositions indicating phase separation of 49% In composition. This pattern indicated that some of the InGaN was phase separating into a higher and lower In components.

Because these results strongly indicated the presence of phase separation, TEM analysis was performed on the InGaN samples. After the TEM cross-sectional samples were prepared, TEM analysis was done with a Topcon 002B Tunnelling Electron Microscope at an acceleration voltage of 200kV. Both normal and Selected Area Diffraction (SAD) modes were used. The compositions below 20% showed good crystal quality with no evidence of phase separation or ordering as shown in Figure 4-8. The samples at 28%, 40% and 49% all showed evidence of phase separation in the form of separated diffraction spots for the higher order indexes as shown in Figure 4-9. In addition, the 49% sample of the TEM image showed regions of spinodal decomposition. The discrepancy in the appearance of phase separation by TEM at much lower In compositions than by XRD is not unexpected given the superior sensitivity of the TEM.

Comparing the experimental data to the VFF model by Ho and Stringfellow et al., there is good agreement with the predicted spinodal curve (Figure 4-10). The spinodal point is predicted to be around 22% InGaN at a growth temperature of 800°C. When experimental data is superimposed on the Ho and Stringfellow curve, the spinodal curve delineates the InGaN without phase separation and the InGaN with phase separation. These experimental results demonstrate that it is relatively easy to get compositions above the equilibrium composition, but it is much more difficult to get single-phase material above the spinodal.

Growth of InGaN compositions above the equilibrium composition would help explain the gettering effect from In metal on the surface of the material. If the InGaN film were at the equilibrium composition, then the addition of an In source would not change the composition of the InGaN film. However, if the In composition was above the equilibrium value, it would take extra energy to force the In into solution. If another pathway for the In

became available by the appearance of In metal on the surface, the In would prefer the lower energy phase (In metal) and deposit there instead of the InGaN film. This would result in a decrease of the In content in the InGaN film.

4.3 Discovery of Ordering in InGaN

Another interesting discovery in the TEM images were regions of the InGaN that looked like an ordered structure. These regions were present in both the 20% InGaN sample (Figure 4-11) and the 49% InGaN sample (Figure 4-12). The suspicion of ordering was confirmed by the appearance of extra spots representing forbidden reflections in the SAD patterns for 20% (Figure 4-13) and 49% (Figure 4-14). These extra spots strongly suggest the presence of an ordered structure. Both 1:1 (50% InGaN) and 1:3 (25% InGaN) ordering can be seen in the SAD diffraction patterns for the 20% and 49% InGaN films. An overview of the samples studied shows the samples that exhibited ordering with their compositions (Figure 4-16).

GaN and related compounds have the Wurzite structure with space group P63mc. In this crystal, the Ga (or group III) atoms and N atoms occupy the 2b position with the Ga atoms at $(1/3, 2/3, 0 ; 2/3, 1/3, \frac{1}{2})$ and the N atoms at $(1/3, 2/3, 0.377 ; 2/3, 1/3, 0.877)$ positions. This structure has two Ga atoms and two N atoms per unit cell ($a = 3.189 \text{ \AA}$, $c = 5.185 \text{ \AA}$). InGaN compounds with compositions of 25% In and higher have the tendency to show both phase separation and ordering. By studying the possibilities of ordering in this type of crystal, the logical ordering will occur along the *c-axis* [0001]. This ordering can take place by stacking alternating layers of column III atoms (In and Ga) in the 2b location ($z = 0$ and $\frac{1}{2}$) of the space group P63mc. If the stacking occurs with the sequence In-Ga-In-Ga-...(1:1), the result is a crystal with 50% InGaN. This type of stacking will break the crystal symmetry to a lower one. The highest possible space group that will allow this stacking to occur is P3m1(#165). In this crystal, the unit cell has one Ga atom, one In atom, and two N atoms per unit cell ($a = 3.150 \text{ \AA}$, and $c = 5.081 \text{ \AA}$). The Ga, In, and N atoms will occupy the

1b and 1c positions, respectively (here, $z = 0$ and $\frac{1}{2}$). The Ga in 1b position at $(\frac{1}{3} \ 2/3 \ 0)$ and In at $(2/3, 1/3, \frac{1}{2})$. In this unit cell, the N atoms will occupy the 1b and 1c locations with $z = 0.377$ and 0.877 . The unit cell in this structure will have a *c-axis* value close to that of the disordered InGaN ($x = 0.5$). This primitive cell will result in the appearance of the forbidden reflections in the electron diffraction patterns such as (0001) , (0003) , ...etc.

In the case of the 25% InGaN composition, the crystal can have the tendency to order by stacking Ga and In atoms with the ratio of 3:1 along the *c-axis* (Ga-Ga-Ga-In-Ga-Ga-In-Ga-...). This stacking will also break the 6-fold symmetry in P63mc to the trigonal symmetry. The highest symmetry this crystal can have is also the space group P3m1. In this type of ordering, there will be three Ga atoms and one In atom per unit cell. These will have the following atomic positions:

1 Ga at 1b	$(\frac{1}{3}, \frac{2}{3}, 0)$
2 Ga at 1c	$(\frac{2}{3}, \frac{1}{3}, \frac{1}{4}); (\frac{2}{3}, \frac{1}{3}, \frac{3}{4})$
1 In at 1b	$(\frac{1}{3}, \frac{2}{3}, \frac{1}{2})$

With this stacking, the unit cell will be double that of the disordered $\text{Ga}_{0.75}\text{In}_{0.25}\text{N}$ along the *c-axis*. In this crystal, the N atoms will be shifted by 0.127 in the z value above each Group III atom in the unit cell. This ordering will result in the appearance of the super lattice reflections $(000\frac{1}{2})$ and (0001) in the original disordered diffraction pattern. Schematics for both of the ordered structures can be seen in Figure 4-15.

Ordering has been predicted for many III/V systems, including the III/V nitride system. Ordering in the GaInP system had been theoretically predicted as far back as 1985. Srivastava et al.[15] performed a local density first principles simulation and found that the ordered phase of InGaP was both thermodynamically stable and the lowest energy for the GaInP system. In 1986, Ichimura et al.[16] using a thermodynamic model that looked at the elastic strains in the crystal, also showed that ordering was a stable phase. Ordering was predicted for the InGaN system by Miller et al.[17]. Using electrostatic analysis of dipole energy, they found that the clustering of atoms along the [0001] direction is energetically

favourable, while the anti-clustering of In atoms on the [0001] planes is also energetically favourable. This would favour clustering/ordering along the [0001] direction.

Ordering has also been discovered experimentally in the nitride system. Ruterana et al.[18] discovered ordering in AlGaN grown using MOCVD. The ordering types occurring were 1:1 and 3:1 Al:Ga, occurring simultaneously. Doppalapudi et al.[19, 20] discovered that ordering occurred in InGaN grown on both *a*-plane and *c*-plane sapphire. They also discovered that the degree of ordering increased with the growth rate.

Several researchers have studied the effects of crystal strain on the formation of ordered structures. In the InGaP system, Zhang et al.[21] studied the effect of sub-surface strains on the formation of ordering using a VFF model. Teles et al.[22] studied ordering in InGaN using a cluster-based model utilizing first principles total energy calculations. They found that biaxial strain inhibits phase separation and acts as a driving force for ordering. Monte Carlo simulations showed that the crystals ordered into a 3,3 ordered structure. On the other hand, Northrup et al.[23] suggests that the number of bonds along the [10-11] facets surrounding dislocations control ordering in InGaN.

While the explanations from Northrup and Teles differ, they are both consistent concerning the locations of the ordered domains in this study. Although the samples do not display uniform ordering, small patches of ordered domains approximately 20 nm in size are seen in regions of the film. Figure 4-17 shows one of these regions right next to a threading dislocation leading up to a v-pit, which are commonly seen in InGaN. As the v-pit would provide a mechanism for the formation of the ordered region as predicted by Northrup, the strain field from the threading dislocation would provide the bi-axial strain for formation of ordering consistent with Teles. The idea that specific crystal conditions are necessary for ordering to occur in InGaN would explain why only a small volume of ordered material is present in the sample.

The samples in this study were analyzed by XRD for long count times in order to detect ordering by the appearance of the forbidden peaks. Unfortunately, none of the samples exhibited the extra peaks such as seen by Korakakis et al.[24] by XRD. This is most likely due to the very small domains and incomplete ordering that was observed in the TEM. XRD is not sensitive enough to detect the weak superlattice peak from the limited diffracted volume of the ordered domains.

The extra spots on the TEM-SAD images are consistent with the theoretical patterns from 1:1 (Figure 4-18) and 1:3 (Figure 4-19) In:Ga ordering. The extra spots are also similar to the TEM-SAD image for 1:3 Al:Ga ordering from Korekakis et al.[24] (Figure 4-20). Although the extra spots on the TEM-SAD images appeared to be ordering superlattice spots, they needed to be analyzed to confirm their origin. To be sure that the extra spots represented an ordered phase, all other possible causes must be ruled out.

4.4 Confirming the Origin of the Extra Spots

To calculate whether or not the extra spots were due to double diffraction, a TEM-SAD image was calculated using Photoshop. According to Edington[25], the double diffraction in the closely packed hexagonal system is a superposition of the zone axis on which the beam is imaging, plus the other zone axis that meet the Laue condition for the reflected beam from the initial zone axis. This calculation gives the pattern shown in Figure 4-21. Even though some of the spots from double diffraction correspond to the spots on the SAD films, they are not consistent with the TEM-SAD images. This makes it unlikely that double diffraction was responsible for the extra spots seen on the SAD-TEM image.

Another possible cause of extra spots is twinning. To determine if the extra spots are due to twinning, it is necessary to generate the simulated twinning patterns for all of the commonly seen twin planes in hexagonal closed packed (HCP) materials. A twin is simply a mirror inversion of the crystal structure across a mirror plane called the twin plane, as shown

in Figure 4-22. In the HCP systems, the commonly observed twin planes are $\langle 10\bar{1}2 \rangle$, $\langle -1122 \rangle$, and $\langle -11\bar{2}1 \rangle$. There is no easy way to represent mirror symmetry when calculating diffraction spots. Therefore, it is useful to use a crystallographic identity that converts the mirror plane into a rotation. In the case of twins, the twinning symmetry can be represented by a rotation around another plane that has the same effect as the mirror symmetry across the twin plane. The advantage of this is that rotations are easily calculated using a Wuff net.

The rotation identity for the $\langle 10\bar{1}2 \rangle$ twin plane is a 95° rotation around the $[-12\bar{1}0]$ axis. For the $\langle -1122 \rangle$ and $\langle -11\bar{2}1 \rangle$ twin planes, the rotations are 63.5° around the $[-1100]$ and 34.5° around the $[\bar{1}100]$. By following these identities, it is possible to determine the origin of a twin spot. Because in the SAD images the spots were fairly strong and the planes to which they indexed (when they indexed at all) were very weak, a different approach was used. In this approach, instead of starting with the twin spot and trying to find the origin, the image plane was run through the reverse operation of indexing the twin plane. This created a “virtual twin” plane that consisted of the location of all of the crystallographic directions that could possibly be twinned to lie on the image plane and appear in the TEM-SAD.

The starting point for the “virtual twin” is the $[0001]$ projection for the HCP system showing all of the major planes, as shown in Figure 4-23. The zone axis for the TEM-SAD is marked on the projection as a straight line representing the intersection of the image plane with the Wuff net. The virtual twin plane is formed by taking all of the major indexes on the image plane and operating the reverse twin operation of 35° around the $[0\bar{1}00]$ axis (opposite axis indicates reverse rotation). Once all of the major zone axis points have been “reverse twinned,” the points are connected with a smooth curve representing the “virtual twin” plane and all points that lie within $5^\circ - 10^\circ$ of the curve are considered possible twin spots.

Now that the possible twin spots are known, it is necessary to figure out where they will appear on the TEM-SAD image. There are two critical pieces of information here. The first is that the relative angle of the twin spot can be compared to the other major spots on the

“reverse twinned” zone axis. This means that if a twin reflection appears midway between the [0002] and the [01-10] directions, the twin spot will be at an angle midway between those spots on the TEM-SAD. The second piece of information is that the twin spots have to satisfy the Laue condition. This means that the distance from the origin can be predicted from the plane spacing of the origin of the twin spot. With the information of the angle relative to the other spots and the distance from the origin from the plane spacing, the possible twin spots can be plotted on the TEM-SAD image. The resulting predicted TEM-SAD image for the [2-1-11] twin plane is given in Figure 4-24.

Figure 4-25 shows the Wuff net for the [2-1-12] and [-1012] twins. The “virtual twin” planes are generated by rotating 65° around the [01-10] and the [1-210] planes, respectively. The resulting simulated twinning patterns are shown in Figures 26 and 27. For the [0-112] twin plane, the rotation was around the [2-1-10] plane. Because this plane is the same as the zone axis, no Wuff net construction is needed and the simulated image is a simple superposition of the TEM-SAD with a rotated version of itself (Figure 4-28). To eliminate twining as a possible source of the extra spots, all of the possible <11-20>, <11-21>, and <11-22> twin planes were simulated. As shown in the figures, the extra spots that arise from the twinning are not consistent with the extra spots from the original TEM-SAD images.

The final step in confirming the ordering in InGaN is to compare the TEM-SAD with the ordered regions seen in the cross-sectional TEM images. Starting from the TEM-SAD, it is possible to image the cross-sectional TEM image using the extra spots that appear from the ordering. This results in the image given in Figure 4-29. The ordered region on the cross-sectional TEM image is clearly enhanced from the original image on the left. This indicates that the ordered region on the cross-sectional TEM image is responsible for the extra spots in the TEM-SAD. Taking the opposite approach, it is possible to simulate a SAD from an image by using a Fourier transform. Figure 4-30 shows the resulting Fourier transform of the cross-sectional TEM image of the ordered region. The resulting pattern shows both the 1:1 and 1:3 extra spots and is very similar to the original TEM – SAD image.

4.5 References

1. Nakamura, S., et al., *In_xGa(1-X)N/In_yGa(1-Y)N Superlattices Grown on Gan Films*. Journal of Applied Physics, 1993. **74**(6): p. 3911-3915.
2. Harrison, W.A., *Electronic Structure and the Properties of Solids*. 1988: Dover.
3. Keller, S., et al., *Growth and characterization of bulk InGaN films and quantum wells*. Applied Physics Letters, 1996. **68**(22): p. 3147-3149.
4. Piner, E.L., et al., *Effect of hydrogen on the indium incorporation in InGaN epitaxial films*. Applied Physics Letters, 1997. **70**(4): p. 461-463.
5. Piner, E.L., et al., *Impurity dependence on hydrogen and ammonia flow rates in InGaN bulk films*. Applied Physics Letters, 1997. **71**(14): p. 2023-2025.
6. Bedair, S.M., et al., *Growth and characterization of In-based nitride compounds*. Journal of Crystal Growth, 1997. **178**(1-2): p. 32-44.
7. Moon, Y.T., et al., *Effects of thermal and hydrogen treatment on indium segregation in InGaN/GaN multiple quantum wells*. Journal of Applied Physics, 2001. **89**(11): p. 6514-6518.
8. Shahid, M.A., et al., *Atomic Ordering in Ga_{0.47}In_{0.53}As and Ga_xIn_{1-x}As_yP_{1-y} Alloy Semiconductors*. Physical Review Letters, 1987. **58**(24): p. 2567-2570.
9. Kuan, T.S., et al., *Long-Range Order in Al_xGa_{1-x}As*. Physical Review Letters, 1985. **54**(3): p. 201-204.
10. Gomyo, A., et al., *Evidence for the Existence of an Ordered State in Ga_{0.5}In_{0.5}p Grown by Metalorganic Vapor-Phase Epitaxy and Its Relation to Band-Gap Energy*. Applied Physics Letters, 1987. **50**(11): p. 673-675.
11. Jaw, D.H., G.S. Chen, and G.B. Stringfellow, *Atomic Ordering in InAs_{0.5}P_{0.5} Grown by Organometallic Vapor-Phase Epitaxy*. Applied Physics Letters, 1991. **59**(1): p. 114-116.
12. Jen, H.R., K.Y. Ma, and G.B. Stringfellow, *Long-Range Order in InAs_{sb}*. Applied Physics Letters, 1989. **54**(12): p. 1154-1156.

13. Henoc, P., et al., *Composition Modulation in Liquid-Phase Epitaxial In_xGa_{1-x}AsyP_{1-y} Layers Lattice Matched to InP Substrates*. Applied Physics Letters, 1982. **40**(11): p. 963-965.
14. Osamura, K., S. Naka, and Y. Murakami, *Preparation and Optical-Properties of Ga_{1-x}In_xn Thin-Films*. Journal of Applied Physics, 1975. **46**(8): p. 3432-3437.
15. Srivastava, G.P., J.L. Martins, and A. Zunger, *Atomic-Structure and Ordering in Semiconductor Alloys*. Physical Review B, 1985. **31**(4): p. 2561-2564.
16. Ichimura, M. and A. Sasaki, *Short-Range Order in III-V Ternary Alloy Semiconductors*. Journal of Applied Physics, 1986. **60**(11): p. 3850-3855.
17. Miller, E.J. and E.T. Yu, *Influence of the dipole interaction energy on clustering in In_xGa_{1-x}N alloys*. Applied Physics Letters, 2001. **78**(16): p. 2303-2305.
18. Ruterana, P., et al., *Evidence for multiple chemical ordering in AlGaN grown by metalorganic chemical vapor deposition*. Applied Physics Letters, 2001. **78**(3): p. 344-346.
19. Doppalapudi, D., et al., *Phase separation and ordering in InGaN alloys grown by molecular beam epitaxy*. Journal of Applied Physics, 1998. **84**(3): p. 1389-1395.
20. Doppalapudi, D., S.N. Basu, and T.D. Moustakas, *Domain structure in chemically ordered In_xGa_{1-x}N alloys grown by molecular beam epitaxy*. Journal of Applied Physics, 1999. **85**(2): p. 883-886.
21. Zhang, S.B., S. Froyen, and A. Zunger, *Surface Dimerization Induced Cuptb Versus Cupta Ordering of GaInP Alloys*. Applied Physics Letters, 1995. **67**(21): p. 3141-3143.
22. Teles, L.K., et al., *Strain-induced ordering in In_xGa_{1-x}N alloys*. Applied Physics Letters, 2003. **82**(24): p. 4274-4276.
23. Northrup, J.E., L.T. Romano, and J. Neugebauer, *Surface energetics, pit formation, and chemical ordering in InGaN alloys*. Applied Physics Letters, 1999. **74**(16): p. 2319-2321.
24. Korakakis, D., K.F. Ludwig, and T.D. Moustakas, *Long range order in Al_xGa_{1-x}N films grown by molecular beam epitaxy*. Applied Physics Letters, 1997. **71**(1): p. 72-74.

25. Edington, J.W., *Electron Diffraction in the Electron Microscope*. Practical Electron Microscopy. 1975: Macmillan.

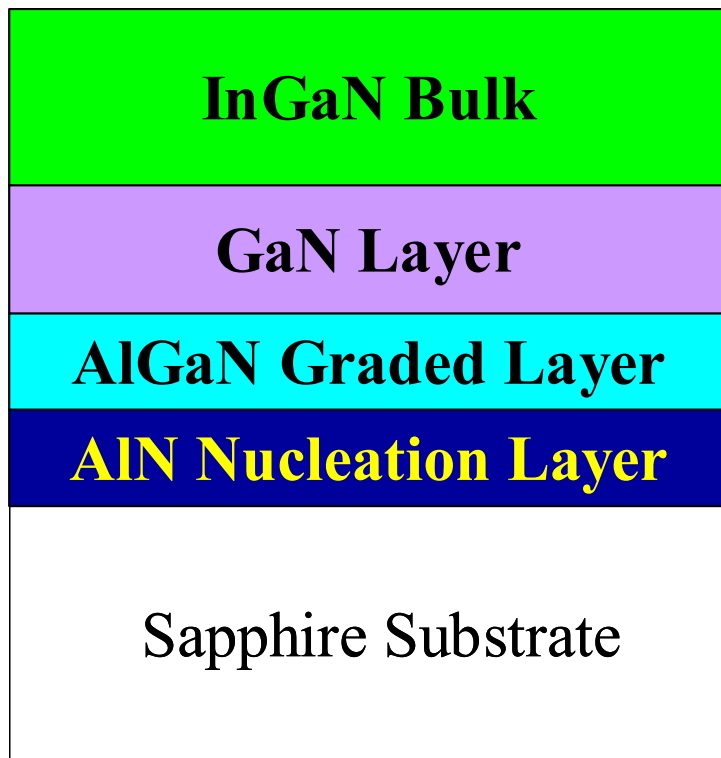


Figure 4-1 Growth structure for InGaN study. The InGaN layers studied were grown on a 1 μm GaN film acting as a base layer. The buffer layer was the ALE AlN at 700°C followed by an AlGaN grading layer.

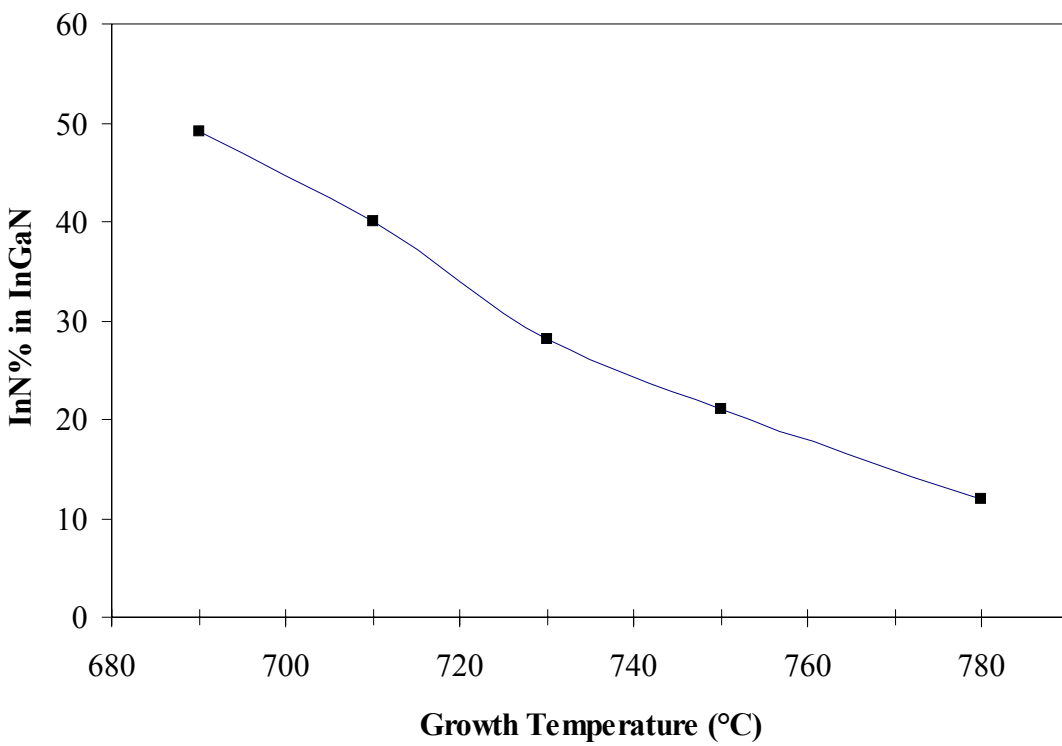


Figure 4-2 Curve showing the effect of Growth temperature on In incorporation. Samples were grown under all N₂ conditions at an In:Ga ratio of 1:1. (Piner)

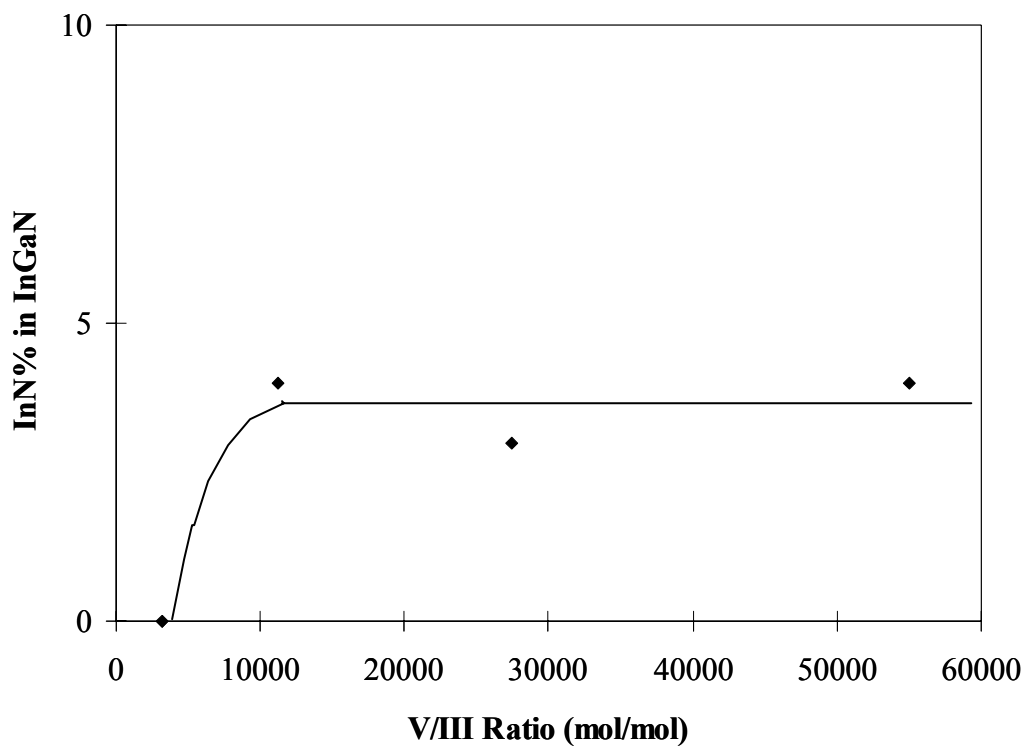


Figure 4-3 Graph showing In composition from θ - 2θ for different V/III ratios. Conditions for the runs were: In:Ga ratio of 1:1 temperature of 780°C and 50sccm of H_2 on column III side. Notice that the In composition levels out for V/III ratios greater than 10,000. (Piner)

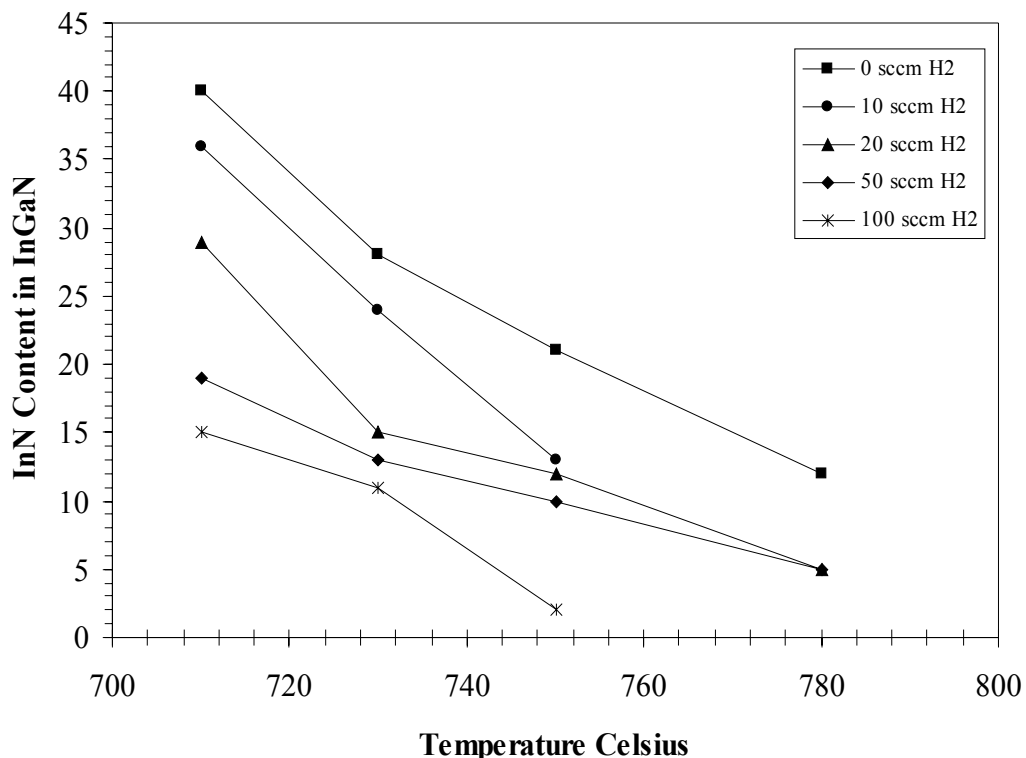


Figure 4-4 Graph of In composition vs. temperature for different H₂ flows. Growth conditions were 27,500 V/III and In:Ga ratio 1:1. Thickness of the films increased with increasing In, indicating that the In incorporation rate was the limiting factor.

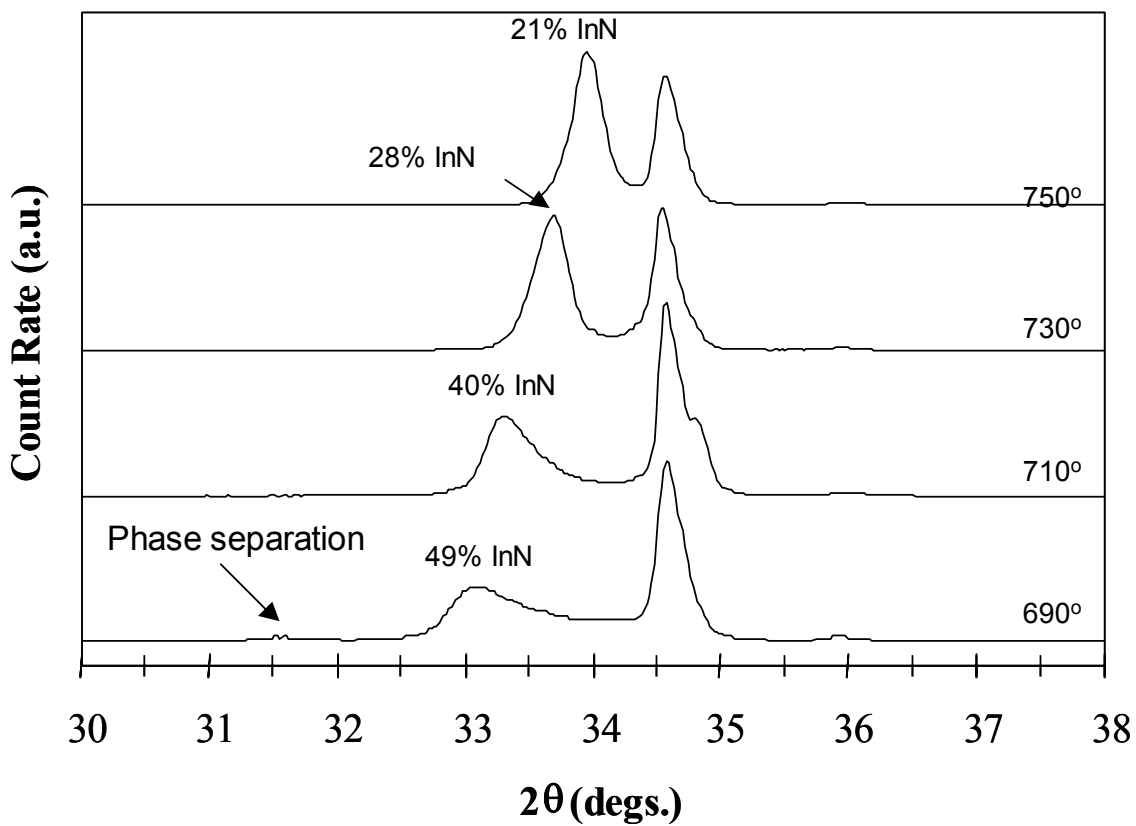


Figure 4-5 Graph showing evolution of θ - 2θ XRD scans as In composition increases in InGaN alloys. InGaN peak shifts to lower angles as In content increases. Notice the additional peak at 31.5 degrees due to phase separation in the 40 and 49% In scans. Graph from Piner

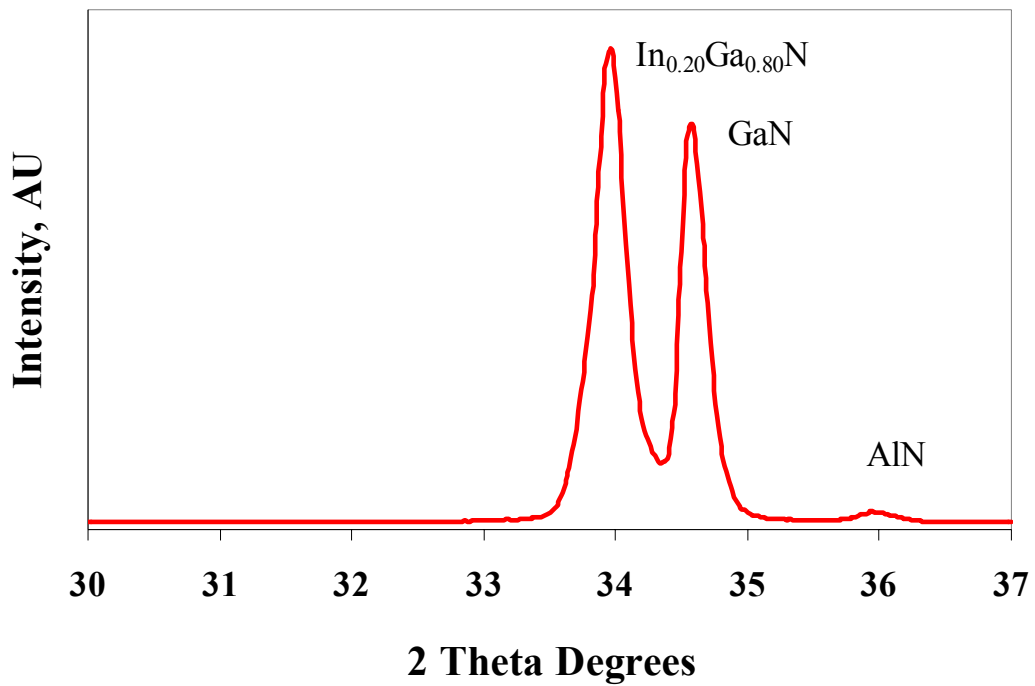


Figure 4-6 θ - 2θ scan for 20%In InGaN alloy. Peaks are present for InGaN, GaN and AlN (from the buffer layer). No additional peaks are seen.

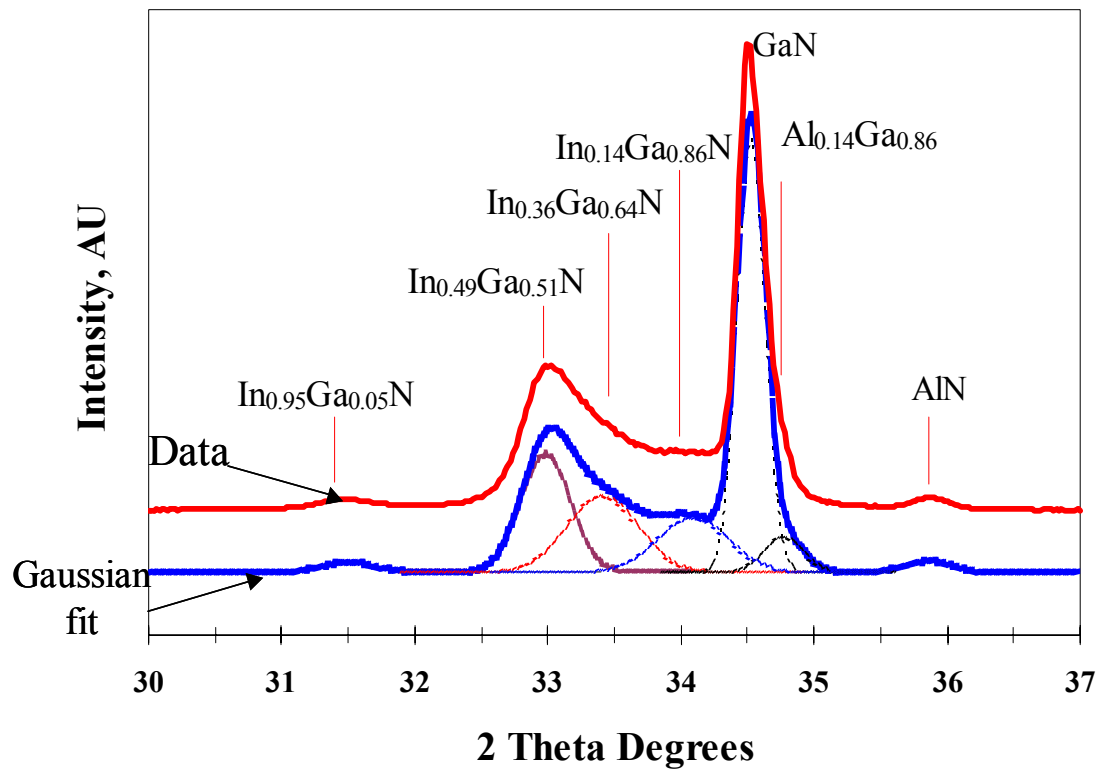


Figure 4-7 θ - 2θ scan for 49% In InGaN alloy. Second curve is fitting curve made up of independent Gaussians to determine compositions present in the film. Note the presence of both higher and lower In compositions indicating phase separation of 49% In composition.
(Piner)

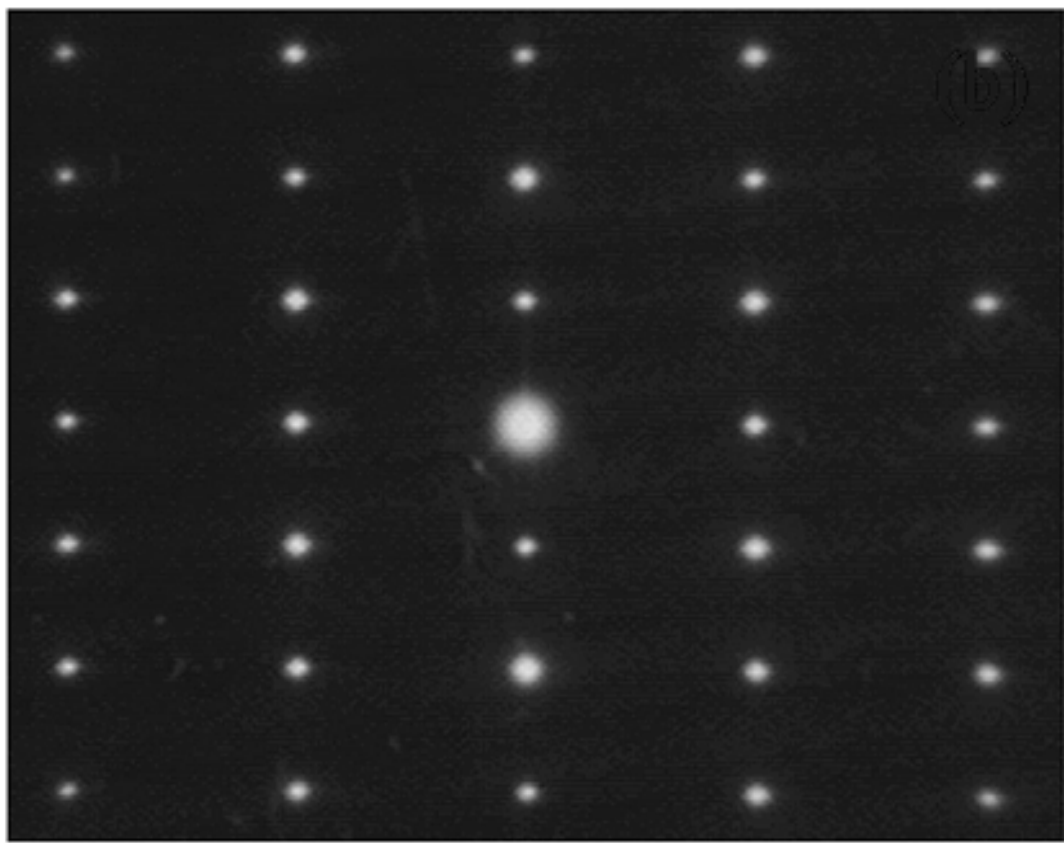


Figure 4-8 TEM – SAD image showing 10% In InGaN alloy. TEM pattern shows [2-1-10] zone axis. Notice how spots are clearly defined without any additional spots.

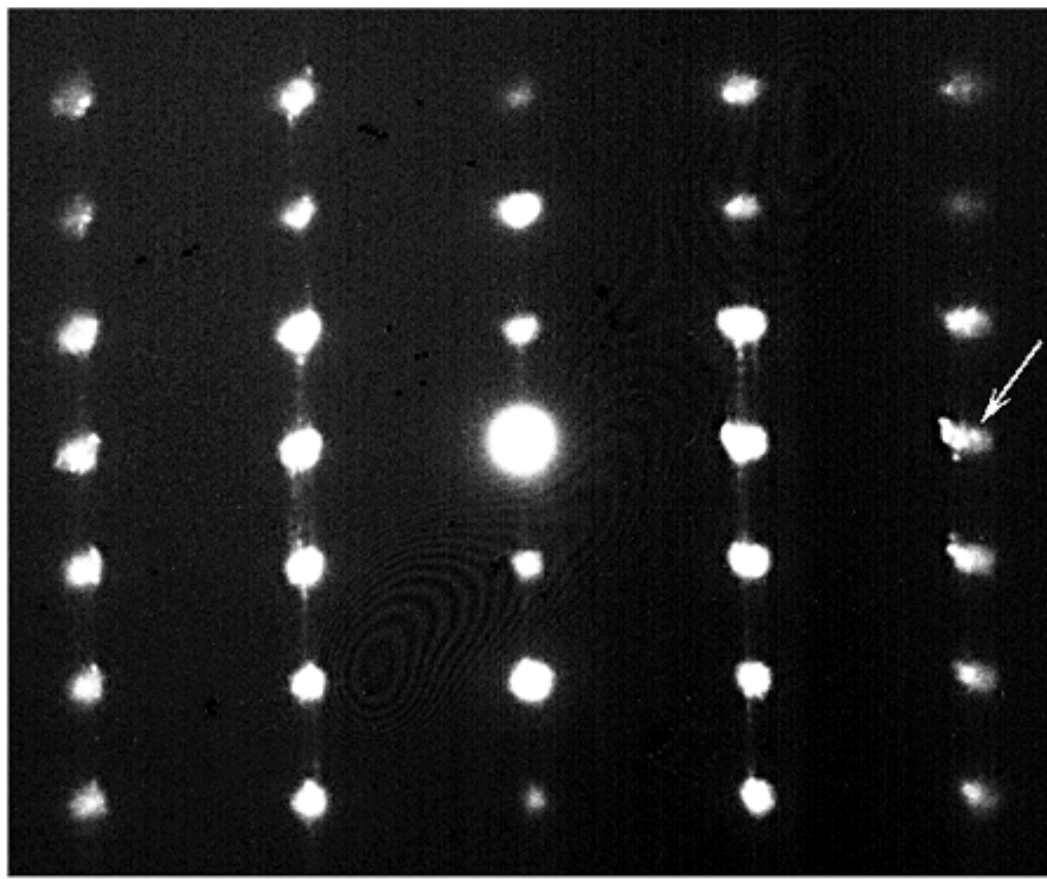


Figure 4-9 TEM – SAD image showing 49% In InGaN alloy. TEM pattern shows [2-1-10] zone axis. Notice how the spots are split for higher indexes indicating phase separation of the InGaN alloy. Vertical smears in the c-axis (vertical direction) are stacking faults

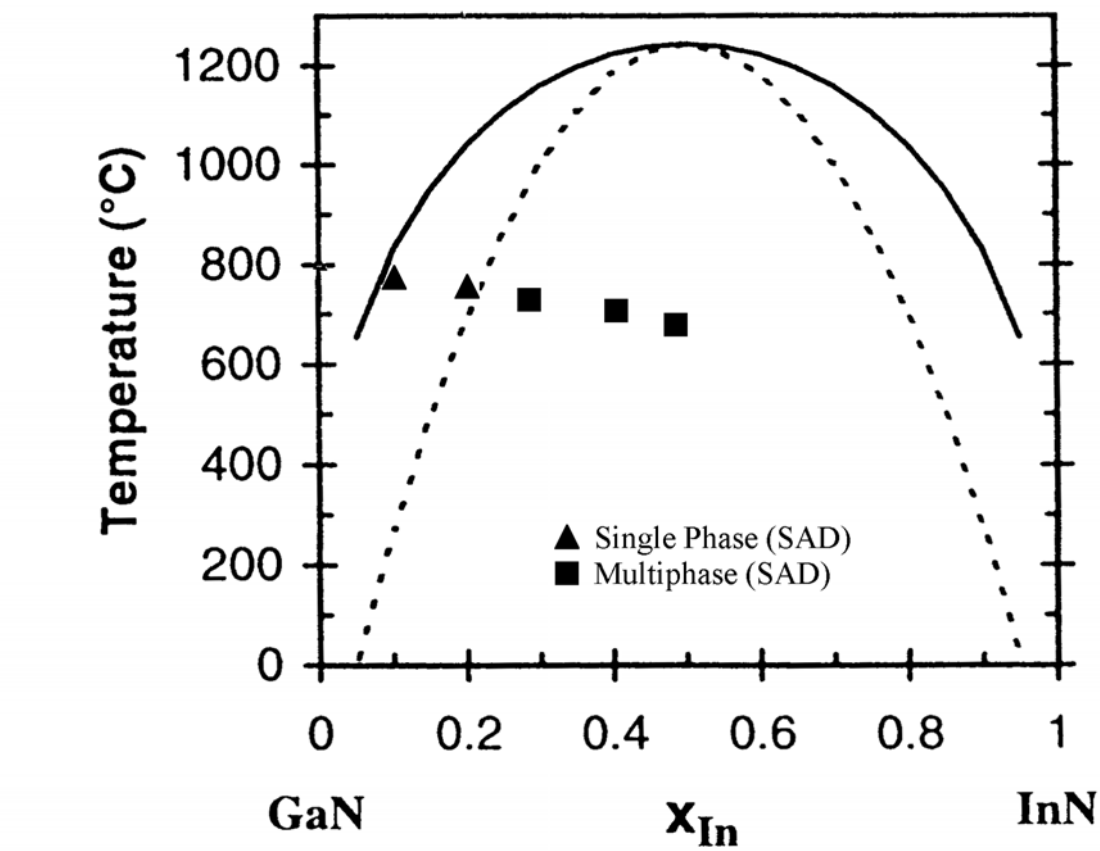


Figure 4-10 Behaviour of different InGaN alloys compared with predicted solubility. Compositions below the spinodal curve are all single phase, whereas compositions above the spinodal point are multiple phases (showing phase separation). Spinodal point is limiting factor for solubility. (Ho et al. APL 1996)

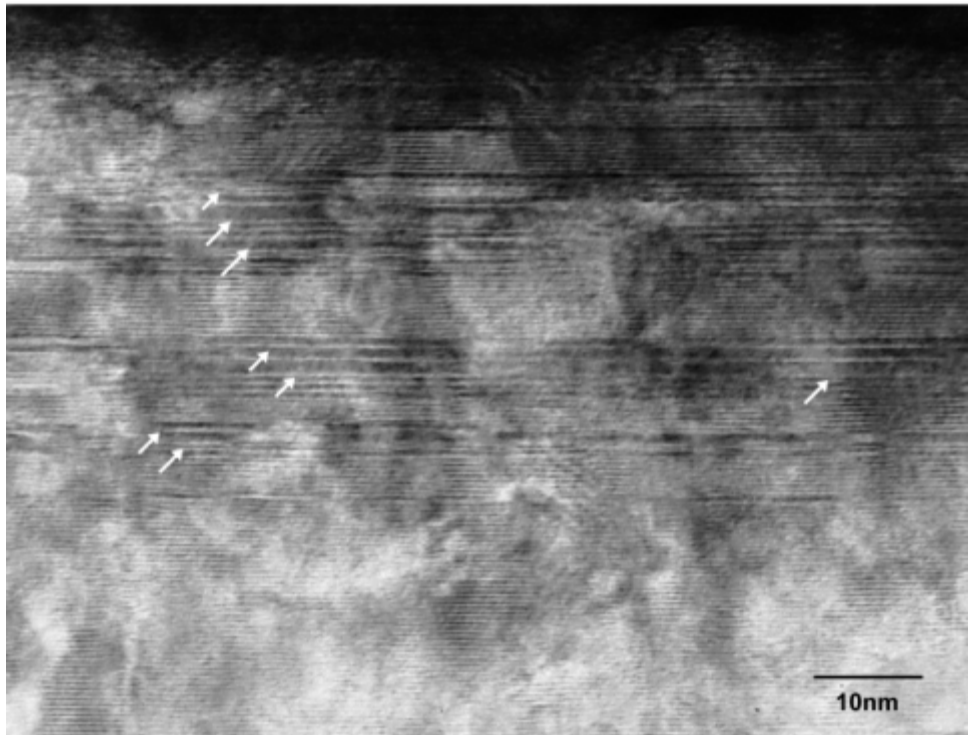


Figure 4-11 Cross-sectional TEM image of 20% InGaN film. No phase separation is observed. The arrows indicate the ordered regions. Both 1:1 and 1:3 In:Ga ordered regions are observed.

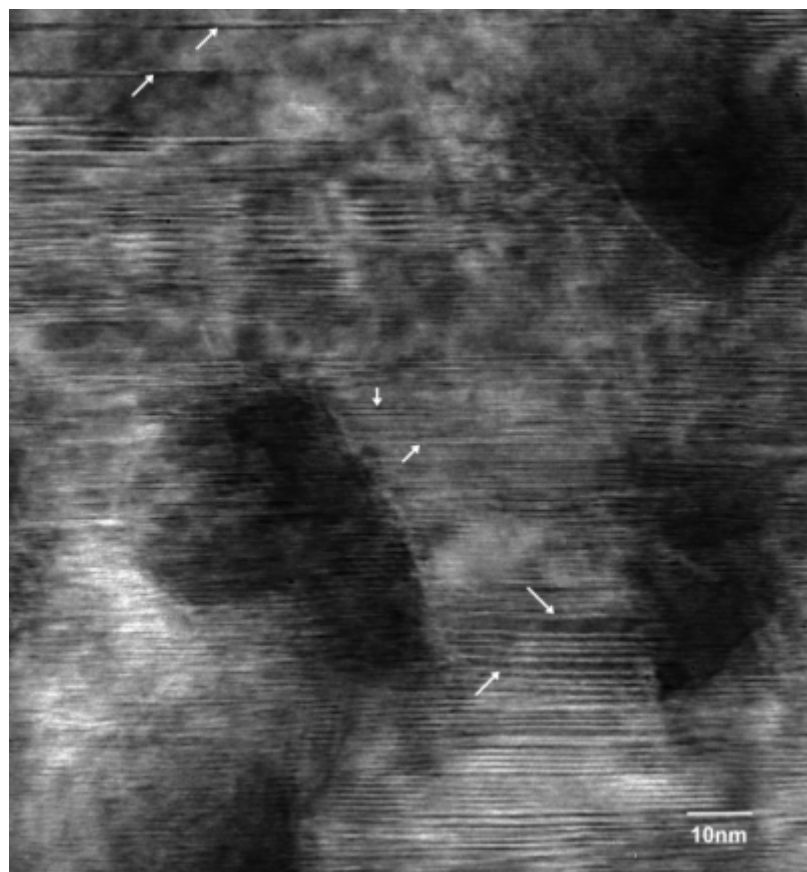


Figure 4-12 Cross-sectional TEM image of 49% InGaN showing both phase separation and ordering. Dark regions are high In phase, while arrows indicate ordered regions.

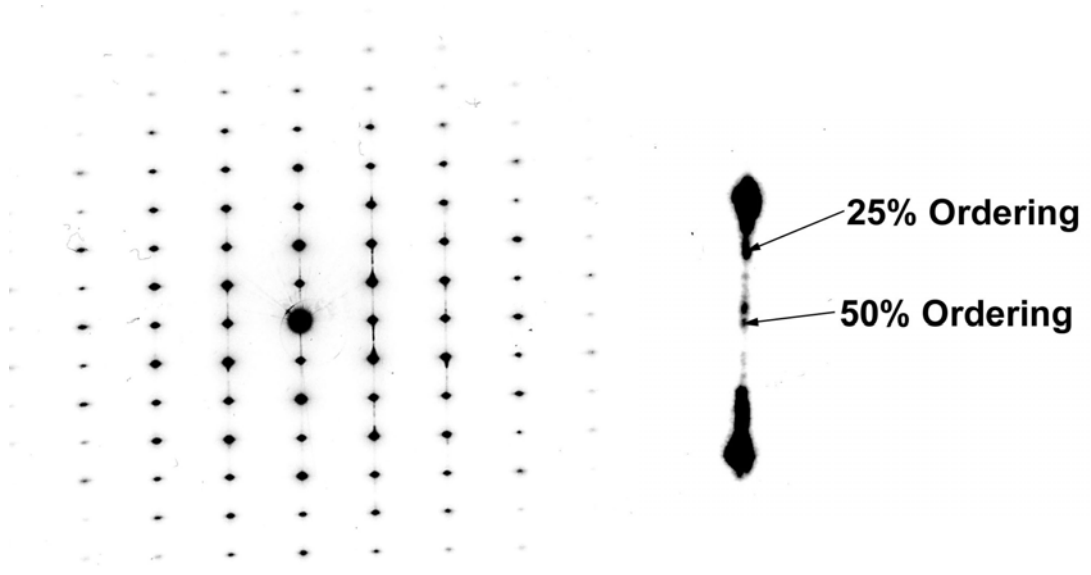
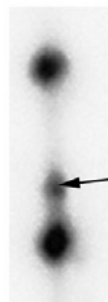
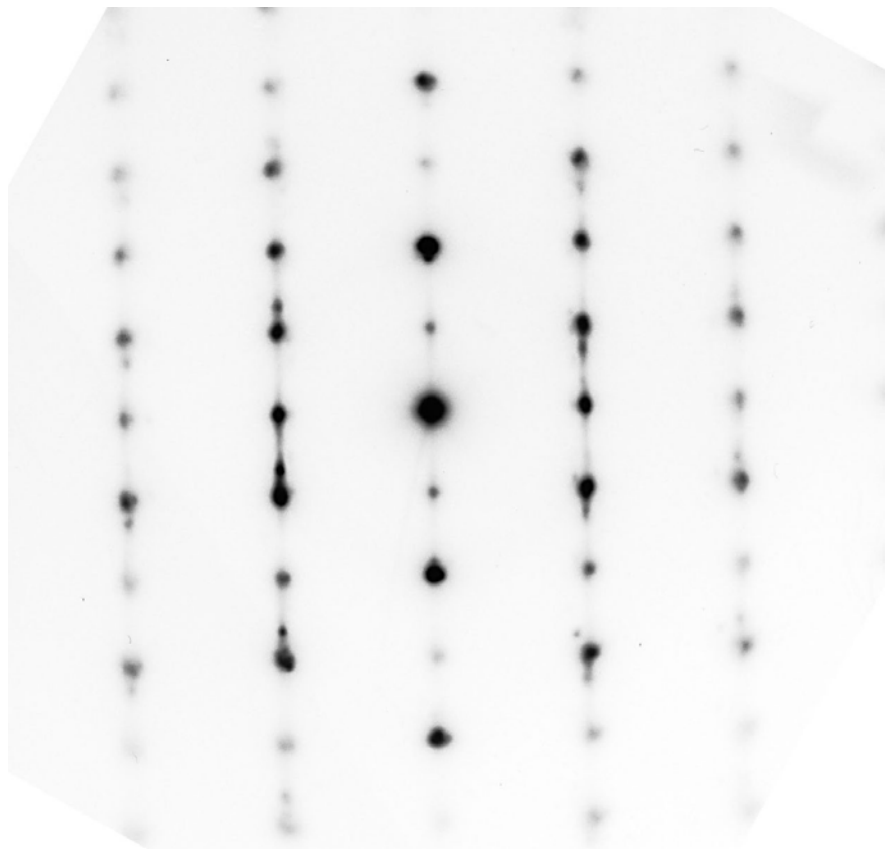


Figure 4-13 TEM-SAD image of 20% InGaN film showing extra spots due to both 1:1 (50%) and 1:3 (25%) ordering. Inset shows magnified view of extra spots.



25% Ordering

Figure 4-14 TEM-SAD image of 49% InGaN film showing extra spots due to 1:3 (25%) ordering. Inset shows magnified view of extra spots.

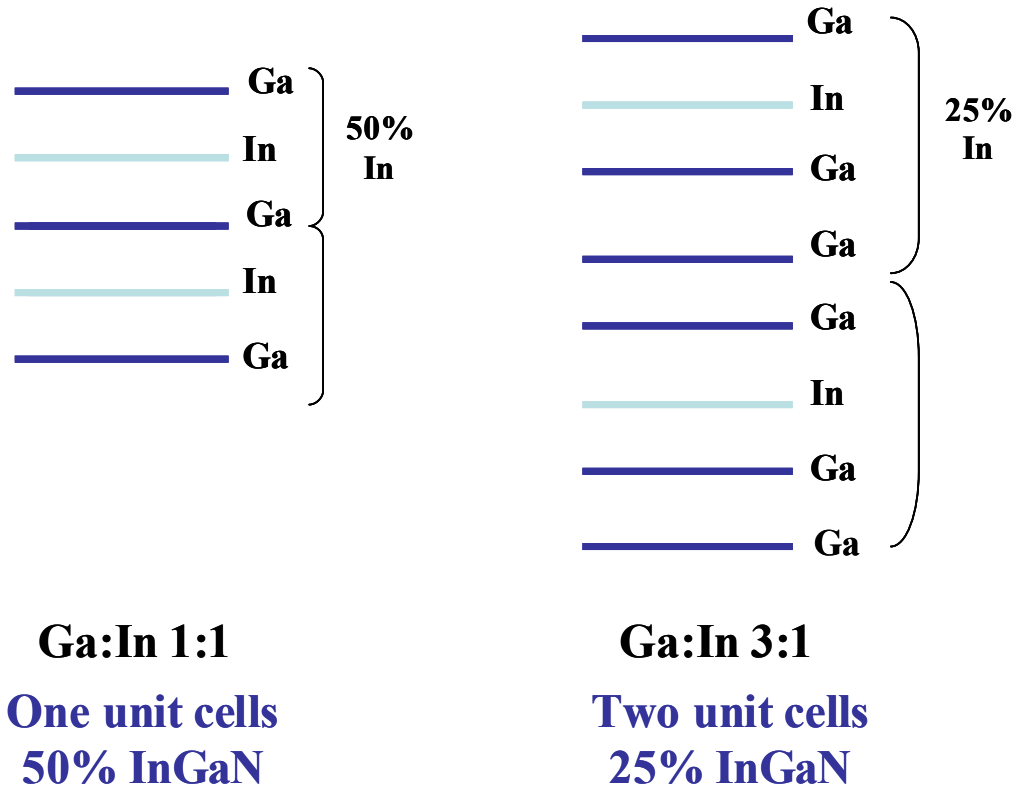


Figure 4-15 Schematic diagram showing the ordering structures for 1:1 and 1:3 In:Ga ordering along the c-axis.

Sample	Tg	ln%	ORDER
94	750	10	no
92	750	21	yes
99	730	28	no
118	710	29	no
105	710	36	yes
106	710	40	yes
107	690	43	yes
108	690	49	yes

Figure 4-16 Summary of runs checked by TEM for ordering

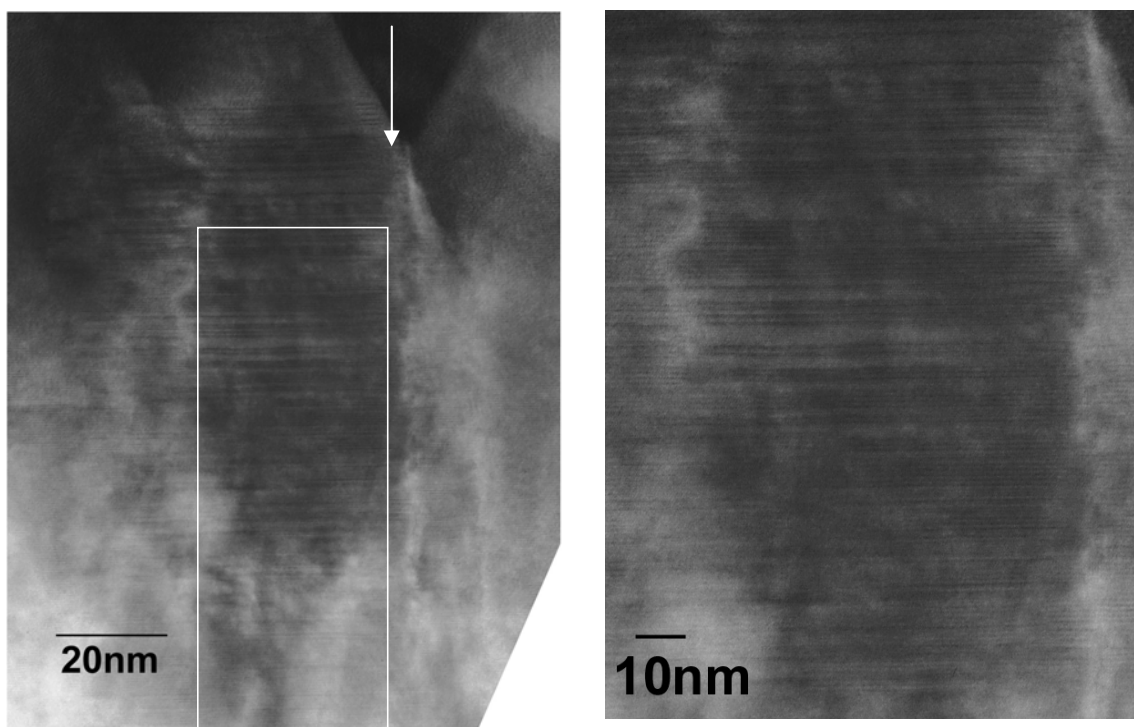


Figure 4-17 Cross-sectional TEM image of 20% InGaN showing ordered region near edge of crystal domain. Arrow indicates threading dislocation. The right image shows magnified view of ordered region. Both 1:1 and 1:3 In:Ga ordering are present.

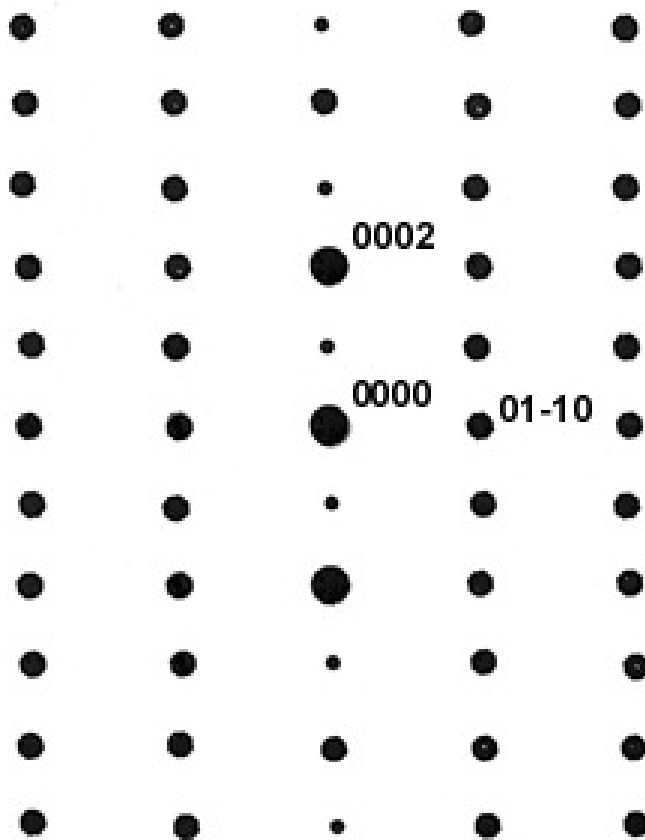


Figure 4-18 Computer generated theoretical TEM-SAD pattern for perfect 1:1 ordering of InGaN crystal. Smaller spots are extra spots due to ordering.

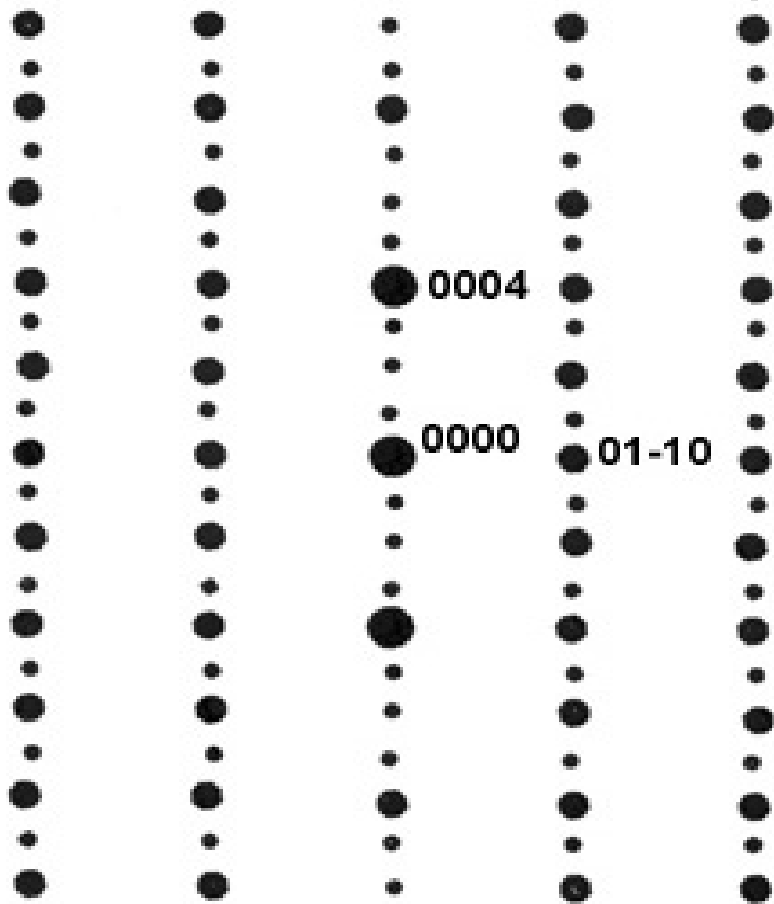


Figure 4-19 Computer generated theoretical TEM-SAD pattern for perfect 1:3 ordering of InGaN crystal. Smaller spots are extra spots due to ordering.

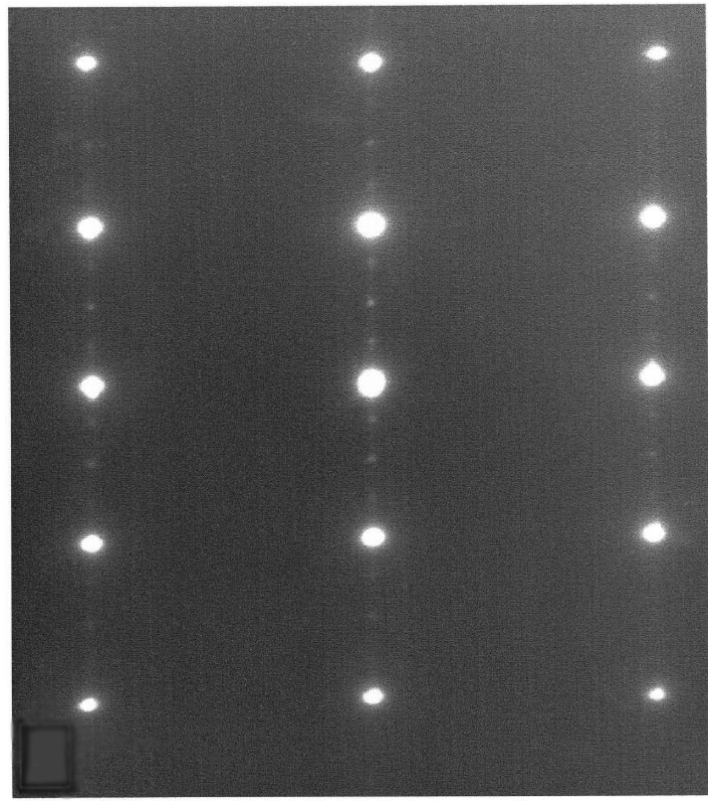


Figure 4-20 TEM-SAD image of 14% AlGaN showing 3:1 Ga:Al ordering along the (0001) plane. (Korakakis APL 1997)

Double Diffraction for 10-10

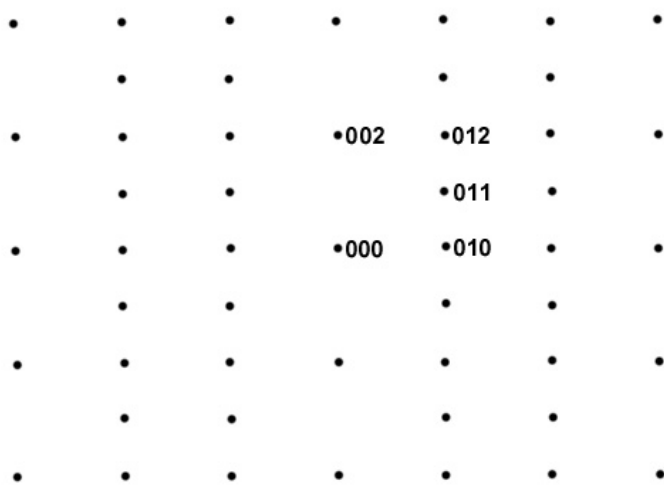


Figure 4-21 Simulated diffraction pattern for [2-1-10] zone axis.

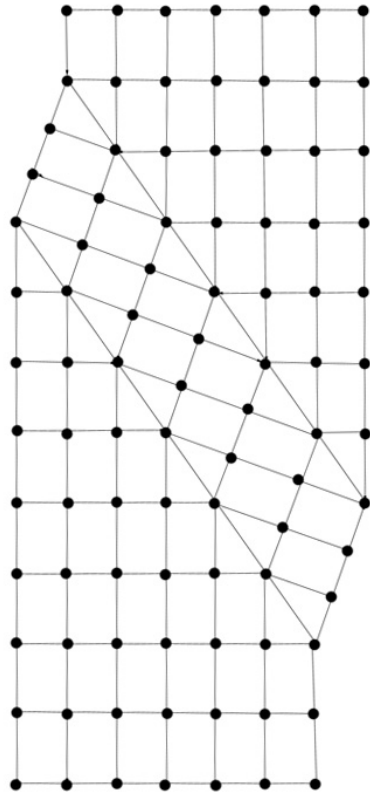


Figure 4-22 Schematic of a twin plane.

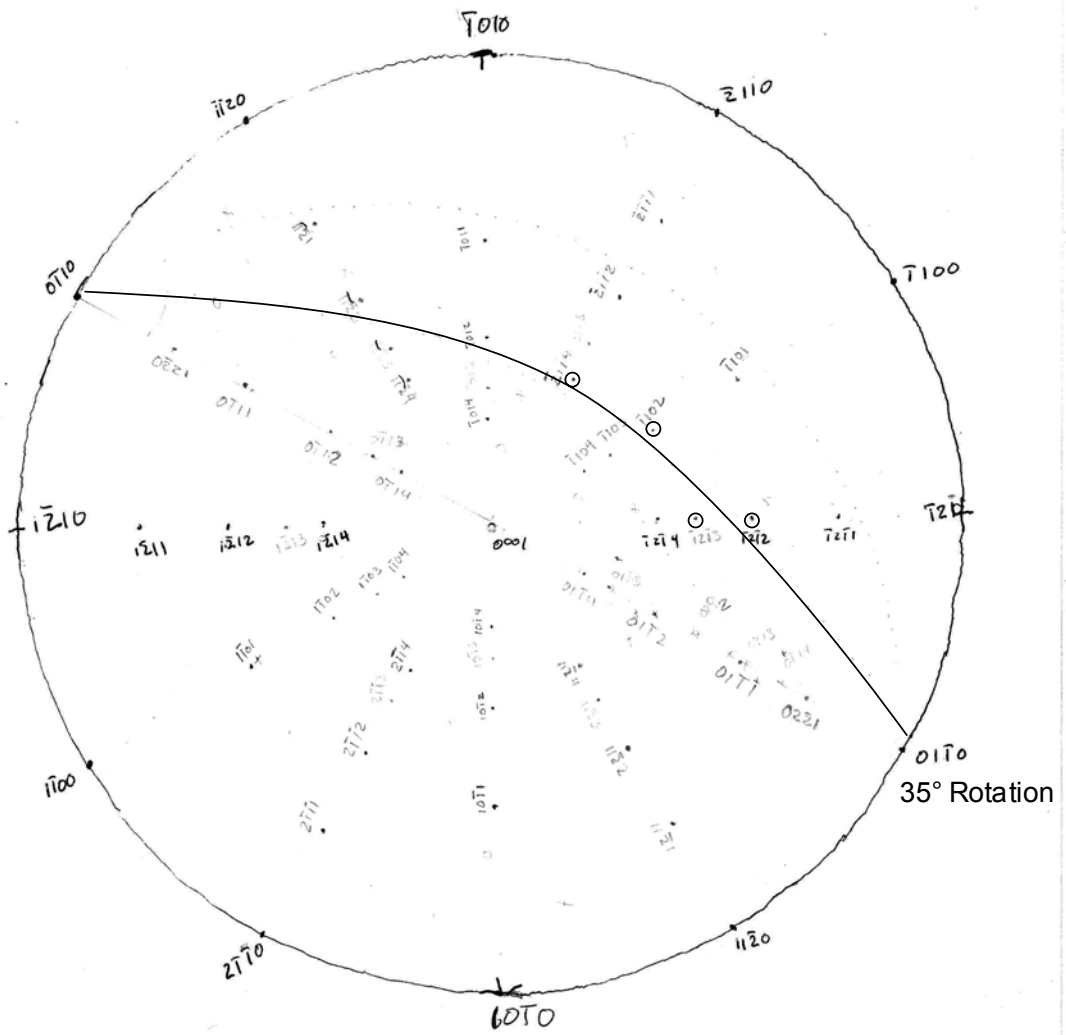


Figure 4-23 Wuff net construction for generating virtual twin plane for [2-1-11] twin. The dark line indicates where reverse twin of image plane would be located. Circles represent spots that can be twinned to image plane.

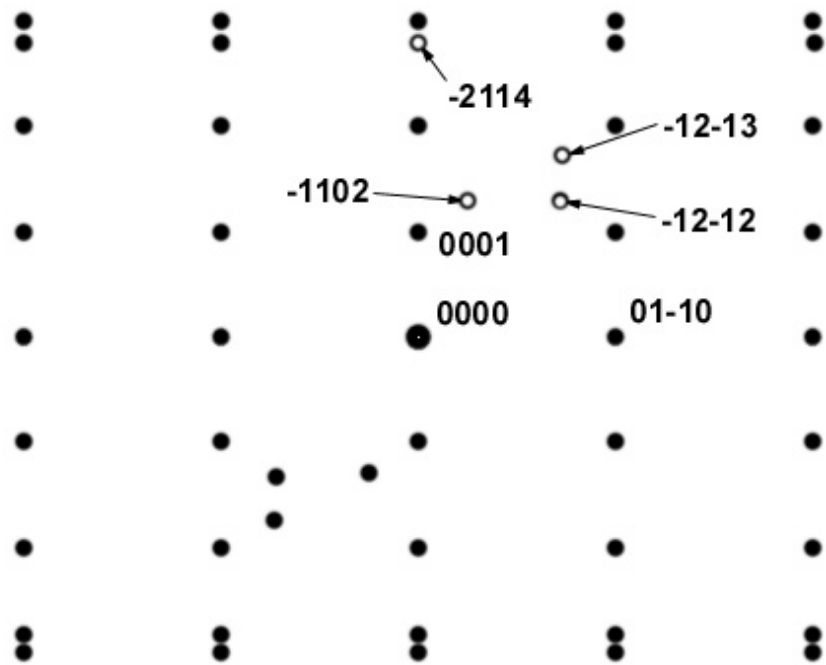


Figure 4-24 Computer generated simulated TEM-SAD image with additional spots added from Wulff net construction for [2-1-11] twin represented by a 35° rotation around [01-10]. The extra spots from the twin are indicated by hollow circles.

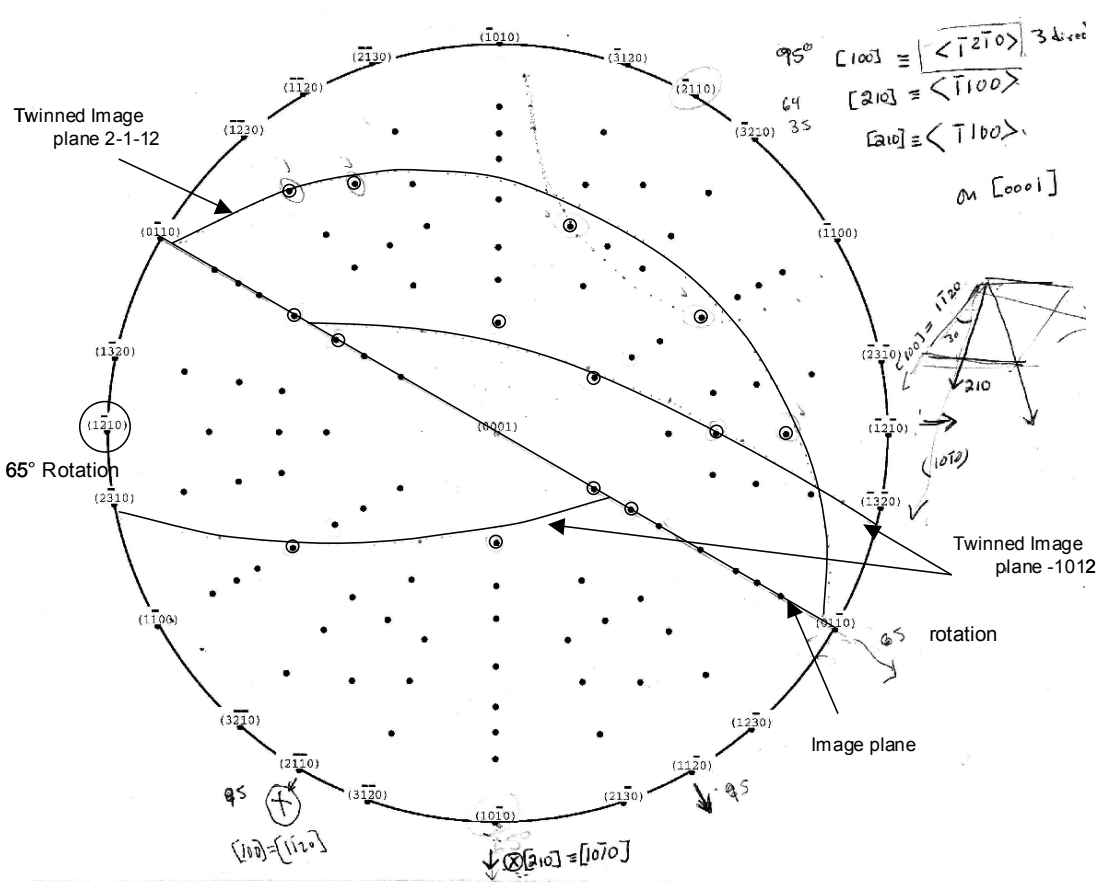


Figure 4-25 Wuff net construction for generating virtual twin plane for [2-112] and [-1012] twins. Lines indicate where reverse twins of image plane would be located. Circles represent spots that can be twinned to image plane.

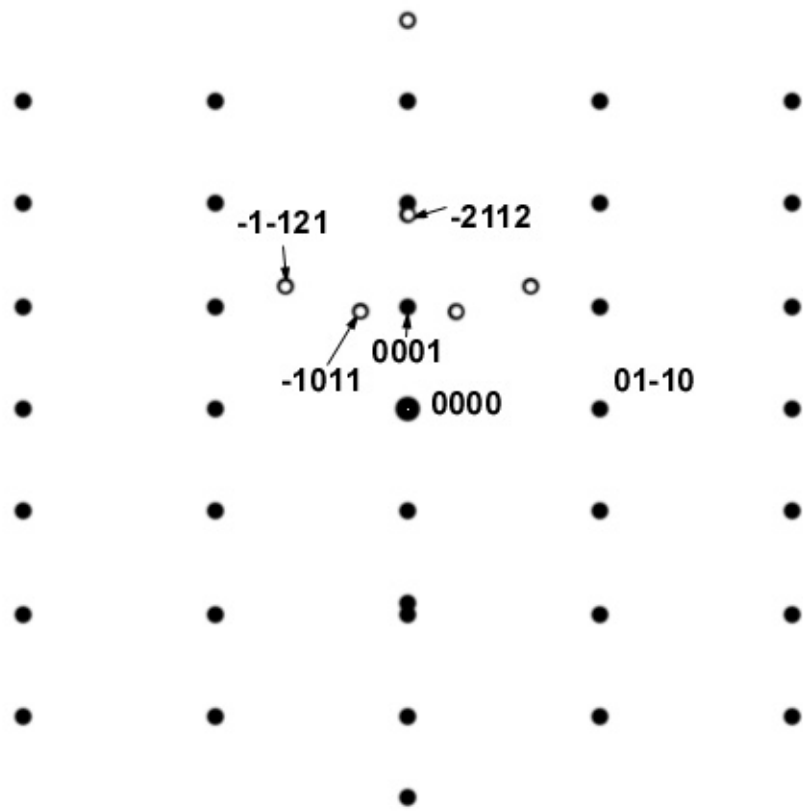


Figure 4-26 Computer generated simulated TEM-SAD image with additional spots added from Wulff net construction for [2-1-12] twin represented by a 65° rotation around [01-10].
The extra spots from the twin are indicated by hollow circles.

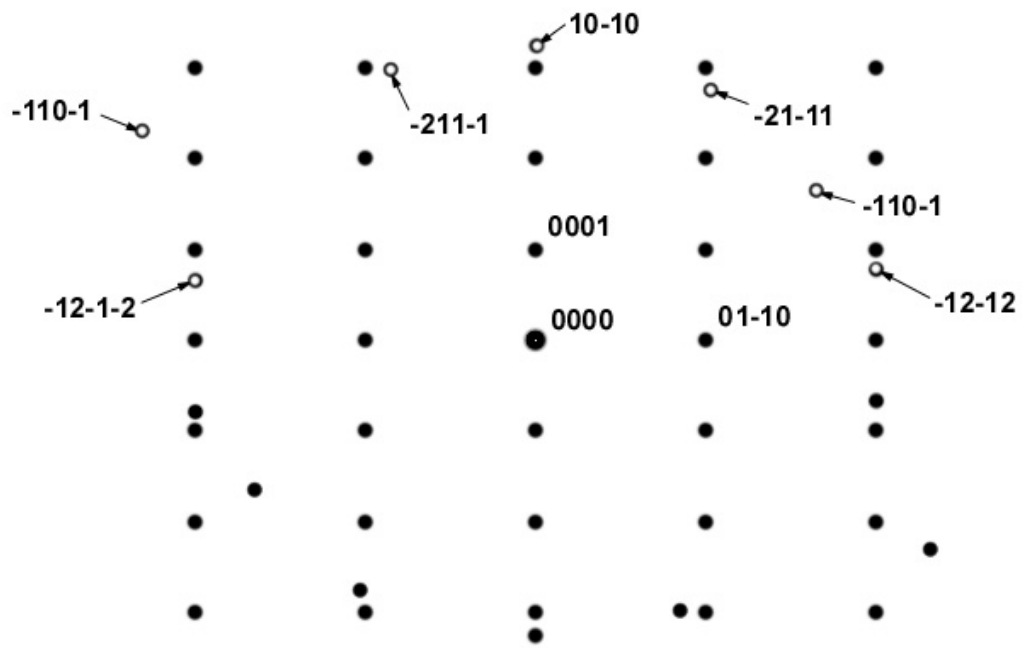


Figure 4-27 Computer generated simulated TEM-SAD image with additional spots added from Wulff net construction for [-1012] twin represented by rotation around the [1-210]. The extra spots from the twin are indicated by hollow circles.

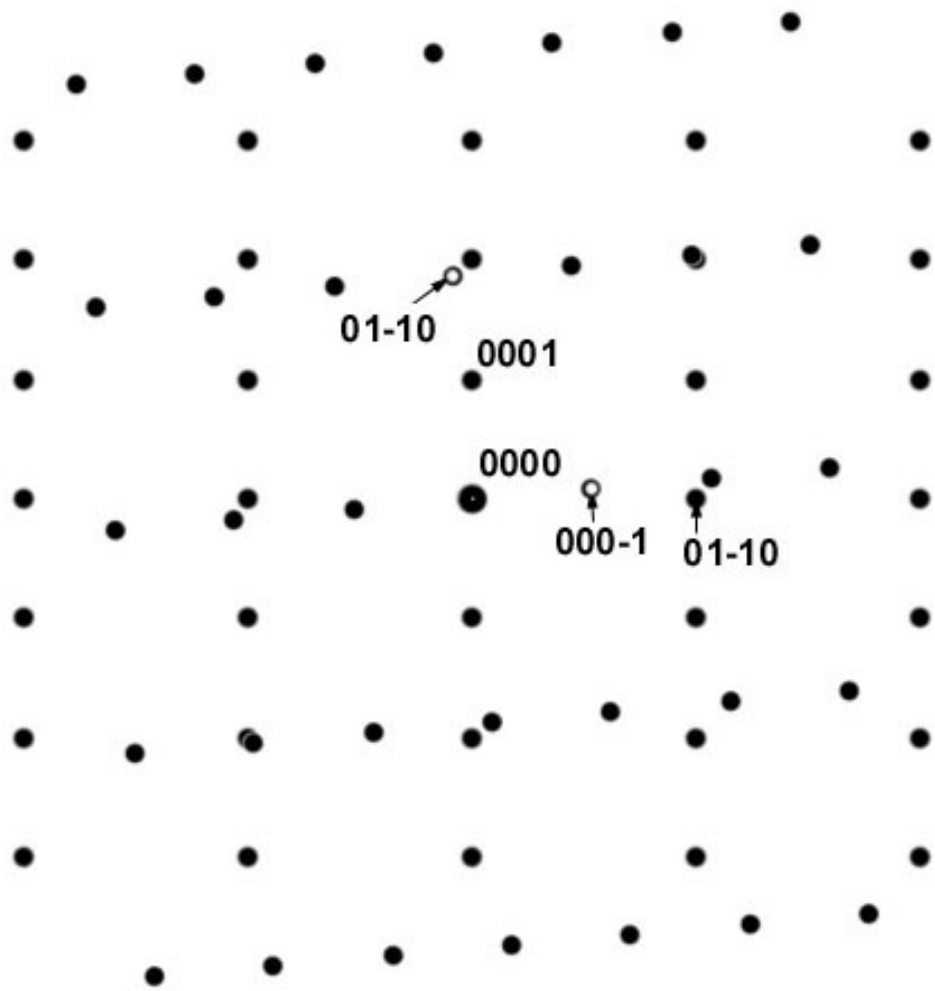


Figure 4-28 Computer generated simulated TEM-SAD image with additional spots for [0-112] twin represented by a rotation around [2-1-10]. Since twin identity involves rotation around zone axis, no Wulff net construction is necessary. The extra spots from the twin are indicated by hollow circles.

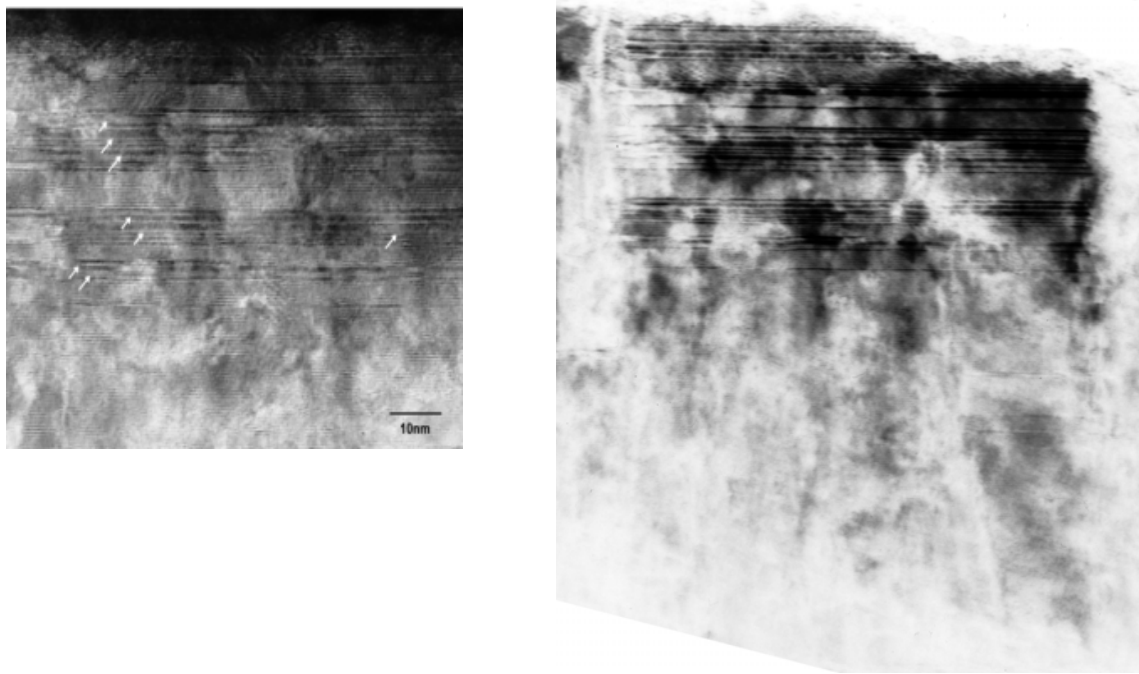


Figure 4-29 TEM image compared with same region imaged using extra ordering spots. Ordered regions are enhanced, showing that extra spots are coming from ordered regions indicated by arrows

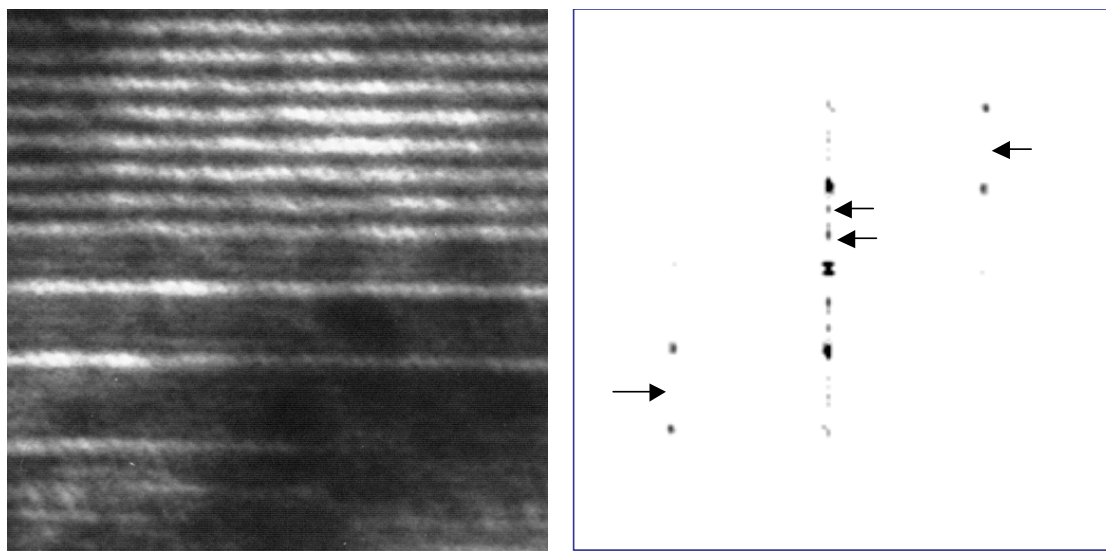


Figure 4-30 Simulated diffraction pattern using Fourier transform of TEM image of 20% InGaN alloy. Fourier transform of the image gives same pattern as TEM-SAD.

Chapter Five: Growth of AlInGaN and the Strain Equilibrium In Incorporation Effect.

5.1 Advantages of AlInGaN

The ternary InGaN system has been used to grow MOSFETS, LED, LD, photodetectors, and numerous other devices. However, the large lattice mismatch between InGaN, GaN, and AlGaN can limit layer selection in devices. It is not uncommon to have a device structure where you want a high bandgap cladding layer on a low bandgap InGaN layer. In these cases the InGaN film will be highly strained which will lead to many undesirable problems such as cracking, increased defect density, and piezoelectric strain effects. In the GaAs system, these effects can be mitigated by using a quaternary alloy such as InGaAsP. The quaternary alloy allows for independent control of lattice constant and bandgap, giving much greater flexibility in the design of devices. The advantages for quaternary alloys hold true in the nitride system also. In addition to the flexibility with regard to bandgap and lattice constant, the AlInGaN alloy has additional advantages for short wavelength LED's and LD's.

InGaN LED's and LD's have surprisingly good performance given the high level of defects in the crystals (excluding ELO grown crystals). Recently, it was hypothesized [1] that the In in the InGaN layers was clustering giving rise to quantum regions of high In. These high In regions, or quantum dots, have the useful property of confining the carriers spatially in the crystal. The confined carriers are more likely to recombine radiatively than they would in the bulk regions of a defect free crystal. In a crystal with a high defect density, the resulting improvements in optical output are truly impressive. The initial short wavelength LED's attempted to use GaN as a main layer with AlGaN cladding layers. The results of the devices were disappointing. However, with an AlInGaN alloy, you can add a

small amount of In to the alloy with the additional Al giving you the same lattice/bandgap properties of the GaN active layer. Hirayama et al.[2], discovered that the addition of just 3% - 5% In to AlGaN alloys can increase the PL emission by three orders of magnitude compared to the AlGaN layer with no In present. This increase is attributed to the In segregating into quantum dots. The resulting emission from the AlInGaN is almost as strong as the best quality InGaN. Chen et al.[3], also studied AlInGaN using Raman scattering and determined that the In in AlInGaN does indeed form quantum dots. Using AlInGaN gives the advantages of higher radiative emission from the quantum dots, but at a much shorter wavelength than possible with the InGaN alloys.

While quaternary devices in the InGaAsP system are more difficult to grow than simple InGaAs devices, the conditions for growth of the quaternary are similar to the corresponding ternary alloys, allowing them to be routinely grown in industry. In the nitride system, by comparison, the growth conditions for the InGaN ternary and AlGaN ternary are vastly different. While InN films can be grown at 500°C, AlN films are grown at temperatures of around 1100°C. This leaves any temperature used to grow an AlInGaN quaternary a compromise. To get good quality AlGaN requires growth at a high temperature, yet to get enough In incorporation requires much lower temperatures. This problem can be offset by growing at higher temperatures than normal for InGaN while using much higher than normal In:Ga ratios and higher growth rates as discussed in Chapter 3. However, this approach is limited by the formation of In metal droplets.

5.2 Growth of AlInGaN

The first step to getting AlInGaN growth is to achieve In incorporation at high temperatures. Under normal MOCVD conditions, the reactor is run in a diffusion-limited mode with the composition of the final film closely related to the composition of the gas stream. In InGaN growth, this is usually not the case as the In desorbs readily from the surface. The optimum conditions for InGaN growth with our reactor design was 700°C -

780°C with an In:Ga ratio of around 3:1. These conditions produce films up to 40% InGaN with good crystalline quality as measured by DCXRD and good optical quality as measured by PL. To get good quality Al in the AlInGaN alloy, the growth temperature needs to be almost 100°C higher than for InGaN. Under the normal flow conditions for InGaN, this would result in almost no measurable In incorporation. In previous InGaN studies, InGaN grown at 780°C contained only 5% In.

A series of InGaN samples were grown to determine optimum conditions for the growth of InGaN at elevated temperatures. The InGaN samples were grown on an MOCVD GaN buffer layer as described in Chapter 3 followed by the addition of a thick (2um) layer of bulk GaN (Figure 4-1). Due to the higher In:Ga ratio in the InGaN layer, the V/III gas ratio was increased to 100,000:1 to reduce the chance of In metal formation. N₂ was used as the carrier gas. Studies have shown that InGaN is unstable in the presence of low V/III and high partial pressures of H₂ [4]. The InGaN samples were grown at temperatures ranging from 770°C up to 895°C with In:Ga ratios ranging from 3:1 to 10:1. At lower temperatures, the higher In:Ga ratios resulted in In metal forming on the surface, whereas at higher temperatures, the lower In:Ga ratios resulted in no detectable In incorporation. The growth rate was also increased at higher temperatures to allow for increased In incorporation with the 10:1 In:Ga ratio[5]. The growth rate required for 10% In incorporation at different temperatures is given in Figure 5-2. The InGaN conditions selected for the AlInGaN study consisted of In:Ga ratios from 7:1 – 10:1 and temperatures ranging between 790°C and 870°C. These conditions resulted in acceptable InGaN films with good XRD and PL. Compositions of the InGaN alloys ranged from 20% In at 780°C to 0% In at 870°C.

During the AlInGaN study [6], quaternary alloys were grown at temperatures of 790°C, 810°C, 830°C, 842°C, 850°C and 870°C (**Figure 5-1**). For each temperature, an InGaN calibration run was used to calibrate the In desorption rate for the AlInGaN runs at that temperature. The assumption was that the In composition was determined by desorption of the In from the surface and was relatively constant regardless of the composition of the underlying layer. The AlInGaN runs were performed as a series of runs starting with the

InGaN run and then incrementally substituting Al for Ga while maintaining the same In:(Al+Ga) ratio. Assuming the In composition was constant, and that the Al:Ga ratio in the film is the same as the gas phase, the compositions of the AlInGaN alloys were predicted. The Al percentage in the quaternary alloys ranged from 5% Al to 56% Al; however, best crystal quality was achieved with the Al composition below 25% Al.

In addition to the bulk AlInGaN study, a separate study using the AlInGaN alloys to act as cladding layers for InGaN quantum wells[7] was run. The use of AlInGaN allowed quantum wells to be constructed with identical bandgap structures but under compressive, neutral, and tensile strains. Extensive PL was performed on these samples to determine the effect of strain on the optical properties of the InGaN quantum wells. This led to the discovery of the piezoelectric field effect on the strained InGaN quantum wells [8]. In addition to the study of the optical properties of the AlInGaN, a follow up to the previous work on ordering in the InGaN system [9] was performed. The AlInGaN samples were prepared for cross-sectional TEM to study ordering effects in the AlInGaN system.

5.3 SASL Effect

Surprisingly, the cross-sectional TEM images showed the formation of a Self-Assembled Super-Lattice (SASL) structure, as shown in Figure 5-3. Figure 5-3 is a bright-field image taken under two beam conditions using the c-axis as the operating g vector ($g=0002$). SIMS was used to determine the composition of the superlattice, and the results are shown in Figure 5-4. The compositional determination from SIMS data was performed using several calibration standards obtained from thick films of InGaN and AlGaN. The InN and the AlN compositions for the standards varied from zero to about 40%, as determined from x-ray diffraction measurements. From Figure 5-3 and Figure 5-4, the periodicity of the superlattice can be observed. From the SIMS results, it can be determined that each period is made of two distinct layers of quaternary alloy with different compositions. The first layer is about 15 nm thick and consists of AlInGaN with In and Al compositions of approximately

6% and 8%, respectively. The second layer of AlInGaN is about 1.2 nm thick In and Al compositions of approximately 9% and 23% respectively.

Using the data from the SIMS results and using Vegards law to calculate the lattice parameters of the two AlInGaN alloys, it was determined that the two SASL layers have the same lattice constant, thereby resulting in no strain between the alternating SASL layers. However, the SASL as a whole was not lattice matched to the GaN buffer layer. It was calculated that a compressive strain of about 0.5% exists in the SASL films. In the superlattices, the Al and In increased in the ratio of approximately 5:1. This is very close (within experimental error) of the ~ 4.5:1 ratio of Al:In required for a-plane lattice matching to GaN in the AlInGaN alloy, even though the observed self assembled superlattices were not lattice matched.

The SASL behaviour was also observed in the AlInGaN used for the cladding layers of the InGaN quantum well structures. The cross-sectional TEM image of one of the quantum wells is shown in Figure 5-5. In these figures, the InGaN quantum well has a thickness of about 6 nm while the quaternary cladding layer is composed of a SASL structure. From the TEM, the SASL is made of a high Al and In region about 1.5 nm thick followed by a low Al and In region with thicknesses in the range of 5–7 nm. It should be noted that there is almost a monolayer abruptness at the interfaces between this self-assembled superlattice structure. SIMS was not carried out for this single quantum well sample, but the light and dark contrasts, both in the low- and high-resolution images for the sample, confirm that the intended quaternary barrier layers have formed a SASL. In addition, the periodicity of the SASL structures was confirmed from the separation of the satellite peaks in the high-resolution x-ray rocking curves of both samples.

PL measurement was also used to characterize the two samples. For the first sample, the PL emission was sharp and centered around 381 nm. Because the barriers of the SASL are fairly thin at approximately 1.2 nm and the wells were fairly thick at approximately 15

nm, this emission wavelength is close to the bulk properties of the quaternary alloy for the lower composition thicker layers 6% In and 8% Al.

The above results show that when AlInGaN quaternary alloys are grown under certain combinations of temperature and growth conditions, self-assembled superlattice structures can develop. The mechanism for the formation of the SASL is not clear. It can be argued that it is a result of fluctuations in the substrate temperature or the mass flow controllers carrying the precursors; however, such fluctuations were not observed during the growth process. Even if slight temperature fluctuations actually occurred, this cannot explain the monolayer abruptness between the different layers as observed by high-resolution TEM, or the periodic changes in the Al concentrations as observed by SIMS. It is also interesting that the InGaN films grown in the same reactor under similar conditions did not show any self-assembled superlattice behaviour when studied by TEM or SIMS.

5.4 Strain Equilibrium In incorporation Effect

In the original study of the quaternary alloys, a significant bowing parameter was observed in the x-ray results for several samples. During subsequent high resolution XRD, intended to search for superlattice peaks from ordering, it was discovered that the 0002 spacings were not consistent with Vegards law. Given that a bowing parameter for the lattice spacing would be highly unusual and has not been noted in the nitride system, another explanation was sought.

In the original work, it was assumed that the In incorporated at the same rate in the InGaN and AlInGaN samples. However, in the SASL, the In appears to incorporate at different rates depending on the Al percentage of the AlInGaN films. In induces compressive stress in the crystal and Al induces tensile stress. This means that with the right proportion of In and Al, the stresses can cancel. The proper proportion can be calculated by taking the lattice difference in the a-plane between Al and Ga and the lattice difference

between In and Ga and comparing them. The In to Ga mismatch is about 4.5 times the Al to Ga mismatch. If you started with GaN and incorporated In and Al in a 1:4.5 ratio, the resulting lattice parameter for the AlInGaN alloy would equal GaN. By assuming that the In in the AlInGaN alloys incorporates at the ~1:4.5 ratio for strain equilibrium to GaN as observed in the SASL, it is possible to explain the deviations in the XRD behaviour of the AlInGaN alloys.

For the AlInGaN runs, the actual lattice parameters determined by x-ray diffraction were compared to two theoretical curves, one assuming constant In incorporation with increasing Al% and the other assuming the 1:4.5 In:Al strain equilibrium In incorporation. These curves were generated and compared to the experimental data for the samples grown at temperatures of 790°C (Figure 5-6), 810°C (Figure 5-7), 830°C (Figure 5-8), 850°C, and 857°C (Figure 5-9). In the samples grown above 850°C, the experimental data follows the curves for constant In incorporation with increasing Al%. At temperatures below 850°C, however, the experimental data follows the curves for the strain equilibrium In incorporation. Results were consistent across all of the AlInGaN samples.

Several samples, grown at low temperatures and high Al (up to 50% AlN), exhibited secondary Al phases by x-ray diffraction. Samples grown at 810°C exhibited secondary phases at 15% and 20%, while samples grown at 790°C exhibited secondary phases at 51% Al. The samples with secondary Al phases separated into the Strain Equilibrium In Incorporation composition and a second higher Al composition. At lower Al concentrations, the secondary Al phases were not observed.

In addition to the Al segregation, several of the samples grown at higher temperatures (above 842°C), and higher (Ga+Al) fluxes, exhibited secondary In phases (Figure 5-10). In the AlInGaN samples grown at 857°C, secondary In phases were observed in the AlInGaN samples with 0% and 16% Al, but disappeared in the samples with higher Al concentrations (Table 1). This indicated that the addition of Al suppressed the formation of secondary In phases.

AllInGaN composition	Normalized counts 50%In
0% Al	790
16%Al	312
22%Al	0
26%Al	0

Table 5-1 Intensity of 50% InGaN peak with increasing Al

A similar effect was observed by Hirayama et al. in AlInGaN samples grown by MOCVD on AlGaN buffer layers [2, 10-12]. Only in the case of AlInGaN grown on AlGaN, the Al:In incorporation ratio was ~12:1 instead of the ~5:1 reported for AlInGaN on GaN. The 12:1 incorporation rate would be strain matched to the reported AlGaN compositions in the base layers. Hirayama et al. attribute the additional In incorporation with increasing Al composition to a partial pressure effect reported by Koukitu et. al.[13]. While this partial pressure effect does predict additional In incorporation with increasing Al, it does not explain the difference in Al:In ratios depending on the underlying base layers.

5.5 The Role of Strain in AlInGaN

Most models for phase separation in the AlInGaN quaternary system assume an even distribution of the constituent atoms [14]. Because the Al and In atoms are assumed to incorporate evenly, both the compressive strain introduced by the In and the tensile strain introduced by the Al contribute to the total crystal strain. This crystal strain is used to calculate the onset of phase separation. As a result, the phase diagrams show decreased In solubility with increasing Al. Given the predictions from the computer models, the experimental results showing both the self assembled superlattice and the Strain Equilibrium Indium Incorporation are surprising. They show that the In incorporation is increasing with increasing Al concentration. These results agree with the results from Cremades et al.[15].

They showed that in MBE grown AlInGaN the In and Al showed competitive incorporation behaviour around defects in the material. They found that the built in strain in the layer determines which species will incorporate. In the relaxed regions, the incorporation of In is preferred, whereas in the strained regions, the incorporation of Al is preferred.

The discrepancy between the random solubility models and the experimental results can be resolved by assuming that there is a clustering effect with the Al and In atoms in the growth film. Incorporating the In atoms in proximity to the Al atoms would allow the compressive and tensile strains introduced by the Al and In atoms to cancel out. This assumption can also explain the suppression of the secondary In phases with additional Al incorporation. Because the additional Al atoms would reduce the compressive strain from the In atoms, adding Al would reduce the driving force for phase separation. In atoms are much more mobile on the growth surface than the Al atoms, and the In is flux much higher, so it is likely that the mechanism involved is an increased In incorporation in areas of higher Al composition.

5.6 The composition pulling effect in InGaN and its relation to the Strain Equilibrium In incorporation effect

Clues to the behaviour of In incorporation in strained crystals under similar conditions to the AlInGaN study can be gleaned from the InGaN critical layer thickness study [16]. The critical layer thickness study was grown using similar growth structures (Figure 5-11) and buffer layer conditions to the AlInGaN study but at lower temperatures and in the InGaN system. The study was performed to determine the critical layer thickness of InGaN films (Figure 5-12). During the study, some of the higher composition films were sent off for additional analysis [17]. The thicker films of 28% and 40% InGaN, which were used for XRD calibration of alloy composition, were analyzed using a reciprocal lattice map (Figure 5-13). It is possible to determine from the plots in **Figure 5-13** that there are two separate layers of InGaN in the samples. Using the method from Pereira et al.[18], the first

layer is calculated to be the relaxed bulk crystal and the second layer is calculated to be a lower In percentage layer. The reduced In layers were calculated to be 16% In for the 28% InGaN and 20% In for the 40% InGaN film, respectively. The lower In percentage layers were biaxially strained to GaN. The third layer was the underlying GaN layer. These results indicated that the InGaN compositions were lower in the strained layers than in the relaxed layers.

This is not a new discovery, as Hiramatsu et al.[19] first published the composition pulling effect in 1997. They showed an increase in the composition of InGaN films as the films grew above the critical layer thickness. However, these results are important since they show that the composition pulling effect occurs in our reactor with our growth conditions. Additional instances of composition pulling are shown in Figure 5-14 and Figure 5-15 for layers that are closer to the critical layer thickness. These samples show a decrease in In incorporation from 6.2% In in the relaxed film to 4.2% In for the strained film. Using similar thin InGaN films, Pereira et al.[20] performed Rutherford backscattering and cathodoluminescence. They discovered that the composition of the InGaN layer decreased from 20% near the surface of the film, down to 14% near the GaN/InGaN interface. Using tetragonal distortion, they determined that the layers near the surface were relaxed and the layers near the interface with GaN were strained. In addition to the underlying bulk layer affecting the In composition, the buffer layer used can also affect the In incorporation rate in InGaN [21].

The Composition pulling effect is not limited to InGaN. Tsai et al.[22] reported lower Al incorporation in strained films grown on sapphire compared to films grown on AlN buffer layers. Chang, et al.[23] reported that MOCVD grown AlGaN exhibited Al segregation near edge dislocations. They suggested that the Al segregation is due to the strain fields near the dislocations. Figure 5-16 shows the results from Gong et al.[24] showing that Al incorporation in AlGaN films is dependent on the biaxial strain in the film from the underlying layer. The films grown on the AlN underlayers have much greater Al compositions for the same gas conditions compared to films grown on the GaN underlayers.

5.7 Initial two-dimensional VFF model

If the strain from defects in the crystal and the underlying growth layers can affect both the incorporation of In and the incorporation of Al, is it possible that the strain fields from the Al and In atoms would effect each other? To test this hypothesis, a simple two-dimensional Valence Force Field (VFF) model was constructed using the method outlined by Ho et al.[25]. The idea was to test how the compressive strain field surrounding the In atom and the tensile strain field surrounding the Al atom would interact and what effect this interaction would have on the energy of the crystal. The results of the model for the In and Al atoms placed far apart in the crystal are given in Figure 5-17. Looking at the figure, it is apparent that the strain fields from the In and the Al atoms extend well beyond their nearest neighbours. The total strain energy for the crystal is calculated by summing the strain from each of the unit cells in the two-dimensional lattice. In the case with the In and Al atoms spaced far apart, the total strain is 20.01 units. Figure 5-18 shows what happens when the In and the Al atoms are moved closer together. In this case, the strain in the vicinity of the In and Al atoms is much higher than before. However, looking at lattice farther away from the In and Al atoms, the crystal is almost relaxed. This is because the compressive strain field from the In atom and the tensile strain field from the Al atom are cancelling, resulting in much lower strain away from the In and Al atoms. While the strain is much higher near the In and Al atoms, the total strain for all of the cells in the crystal is now 15.32, which is a significant reduction from the previous case.

While the initial two-dimensional model is not physically realistic, the underlying principle is sound. If the In and Al can cluster to relax their respective strain fields, then the overall energy of the crystal will be reduced. A more realistic model to describe these effects is presented in Chapters 6 and 7.

5.8 References

1. Kawakami, Y., et al., *Recombination dynamics of localized excitons in self-formed InGaN quantum dots*. Materials Science and Engineering B-Solid State Materials for Advanced Technology, 1997. **50**(1-3): p. 256-263.
2. Hirayama, H., et al., *Room-temperature intense 320 nm band ultraviolet emission from quaternary InAlGaN-based multiple-quantum wells*. Applied Physics Letters, 2002. **80**(9): p. 1589-1591.
3. Chen, C.H., et al., *Mechanism of enhanced luminescence in $In_xAl_{1-x}N$ quaternary alloys*. Applied Physics Letters, 2002. **80**(8): p. 1397-1399.
4. Koukitu, A. and H. Seki, *Unstable region of solid composition in ternary nitride alloys grown by metalorganic vapor-phase epitaxy*. Japanese Journal of Applied Physics Part 2-Letters, 1996. **35**(12B): p. L1638-L1640.
5. Keller, S., et al., *Growth and characterization of bulk InGaN films and quantum wells*. Applied Physics Letters, 1996. **68**(22): p. 3147-3149.
6. Aumer, M.E., S.F. LeBoeuf, and F.G. McIntosh, *High optical quality AlInGaN by metalorganic chemical vapor deposition*. Applied Physics Letters, 1999. **75**: p. 3315-17.
7. Aumer, M.E., S.F. LeBoeuf, and S.M. Bedair, *Effects of tensile and compressive strain on the luminescence properties of AlInGaN/InGaN quantum well structures*. Applied Physics Letters, 2000. **77**: p. 821-3.
8. Aumer, M.E., S.F. LeBoeuf, and B.F. Moody, *Strain-induced piezoelectric field effects on light emission energy and intensity from AlInGaN/InGaN quantum wells*. Applied Physics Letters, 2001. **79**: p. 3803-5.
9. Behbehani, M.K., et al., *Phase separation and ordering coexisting in $In_xAl_{1-x}N$ grown by metal organic chemical vapor deposition*. Applied Physics Letters, 1999. **75**(15): p. 2202-2204.

10. Hirayama, H., et al., *Fabrication of a low-threading-dislocation-density Al_xGa_{1-x}N buffer on SiC using highly Si-doped Al_xGa_{1-x}N superlattices*. Applied Physics Letters, 2002. **80**(12): p. 2057-2059.
11. Hirayama, H., et al., *Efficient 230-280 nm emission from high-Al-content AlGaN-based multiquantum wells*. Applied Physics Letters, 2002. **80**(1): p. 37-39.
12. Hirayama, H., et al., *Marked enhancement of 320-360 nm ultraviolet emission in quaternary In_xAl_yGa_{1-x-y}N with In-segregation effect*. Applied Physics Letters, 2002. **80**(2): p. 207-209.
13. Koukitu, A., Y. Kumagai, and H. Seki, *Thermodynamic analysis of the MOVPE growth of InGaAlN quaternary alloy*. Journal of Crystal Growth, 2000. **221**: p. 743-750.
14. Matsuoka, T., *Calculation of unstable mixing region in wurtzite In_{1-x}yGa_xAl_yN*. Applied Physics Letters, 1997. **71**(1): p. 105-106.
15. Cremades, A., et al., *Inhomogeneous incorporation of In and Al in molecular beam epitaxial AlInGaN films*. Journal of Applied Physics, 2001. **90**(9): p. 4868-4870.
16. Parker, C.A., et al., *Determination of the critical layer thickness in the InGaN/GaN heterostructures*. Applied Physics Letters, 1999. **75**(18): p. 2776-2778.
17. Robins, L.H., et al., *Optical absorption, Raman, and photoluminescence excitation spectroscopy of inhomogeneous InGaN films*. Mrs Internet Journal of Nitride Semiconductor Research, 1999. **4**: p. U226-U231.
18. Pereira, S., et al., *Interpretation of double x-ray diffraction peaks from InGaN layers*. Applied Physics Letters, 2001. **79**(10): p. 1432-1434.
19. Hiramatsu, K., et al., *The composition pulling effect in MOVPE grown InGaN on GaN and AlGaN and its TEM characterization*. Mrs Internet Journal of Nitride Semiconductor Research, 1997. **2**(6).
20. Pereira, S., et al., *Compositional pulling effects in In_xGa_{1-x}/GaN layers: A combined depth-resolved cathodoluminescence and Rutherford backscattering/channeling study*. Physical Review B, 2001. **64**(20): p. art. no.-205311.

21. Scholz, F., et al., *Influence of strain and buffer layer type on In incorporation during GaInN MOVPE*. Materials Science and Engineering B-Solid State Materials for Advanced Technology, 1999. **59**(1-3): p. 268-273.
22. Tsai, Y.L., et al., *Observation of compositional pulling phenomenon in Al_xGa_{1-x}N (0.4 < x < 1.0) films grown on (0001) sapphire substrates*. Applied Physics Letters, 2003. **82**(1): p. 31-33.
23. Chang, L., et al., *Observations of Al segregation around dislocations in AlGaN*. Applied Physics Letters, 2001. **79**(7): p. 928-930.
24. Gong, J.R., et al., *Strain-induced effect on the Al incorporation in AlGaN films and the properties of AlGaN/GaN heterostructures grown by metalorganic chemical vapor deposition*. Journal of Crystal Growth, 2003. **249**(1-2): p. 28-36.
25. Ho, I.H. and G.B. Stringfellow, *Solid phase immiscibility in GaInN*. Applied Physics Letters, 1996. **69**(18): p. 2701-2703.

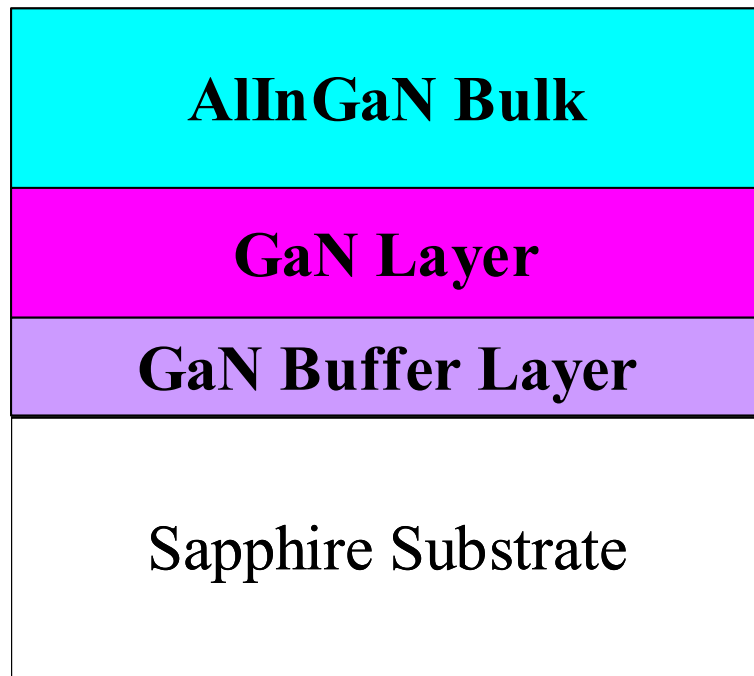


Figure 5-1 Structure for AlInGaN Growth using GaN buffer layer

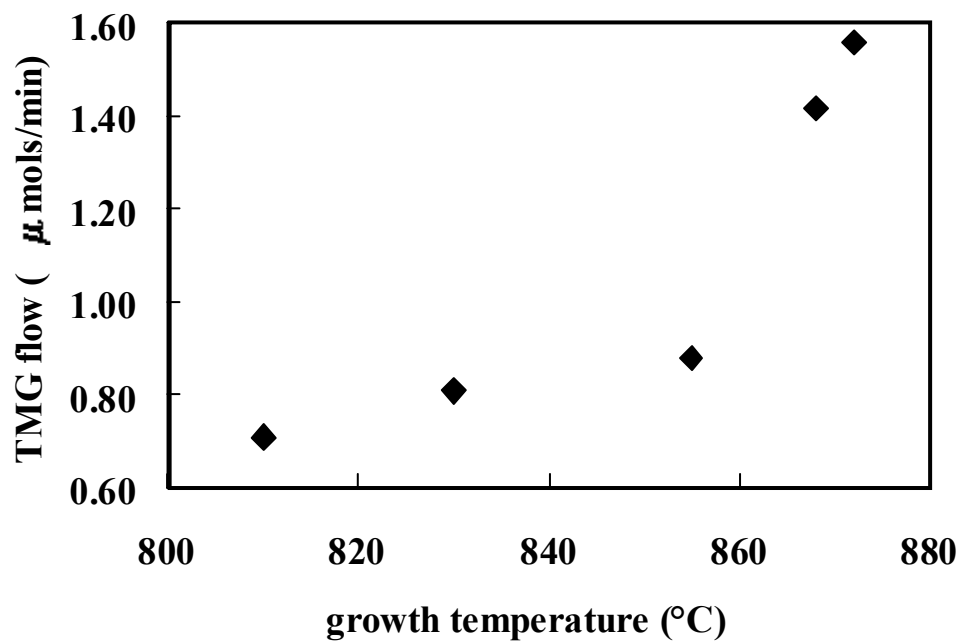


Figure 5-2 Plot of growth flux required for 10% InGaN at various temperatures. In:Ga ratio was held constant at 10:1 while V/III ratio was 100,000:1 (Aumer)

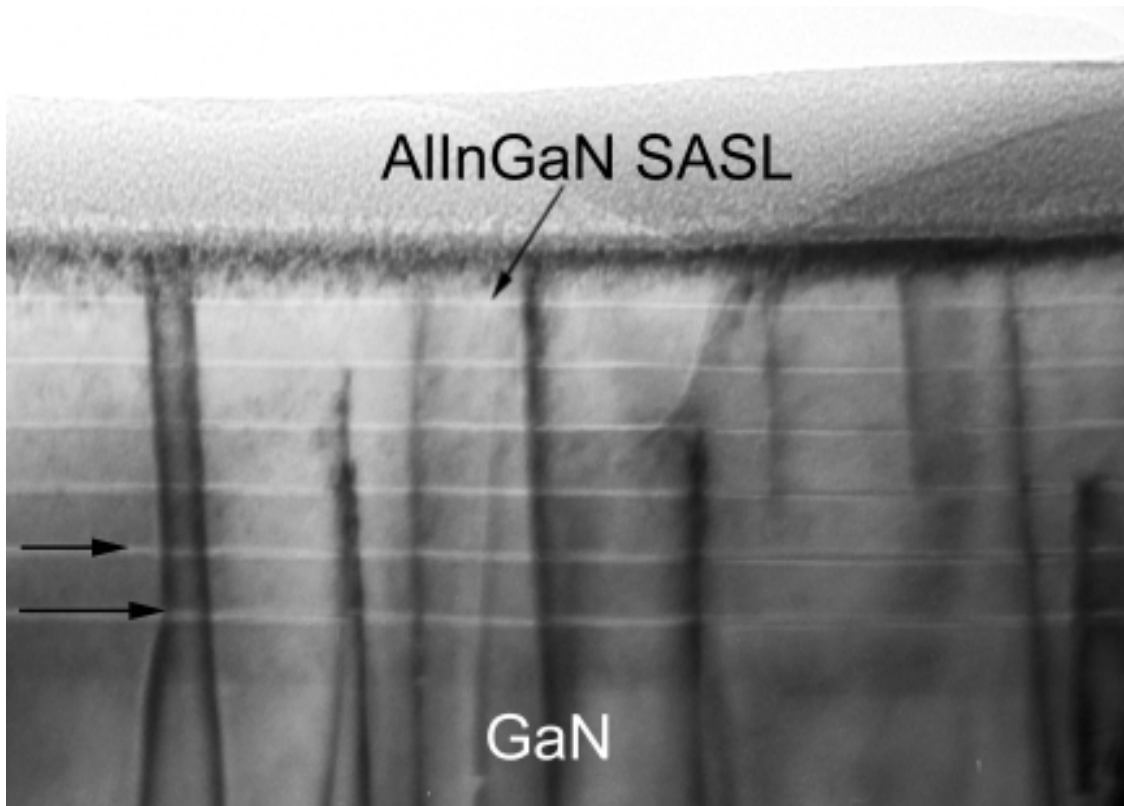


Figure 5-3 Cross-sectional TEM of the self-assembled superlattice (SASL) in AlInGaN. The SASL consists of high-In, high-Al regions alternating with lower-Al, lower-In regions. The arrows are pointing to the bright layers with high-Al and high-In content.

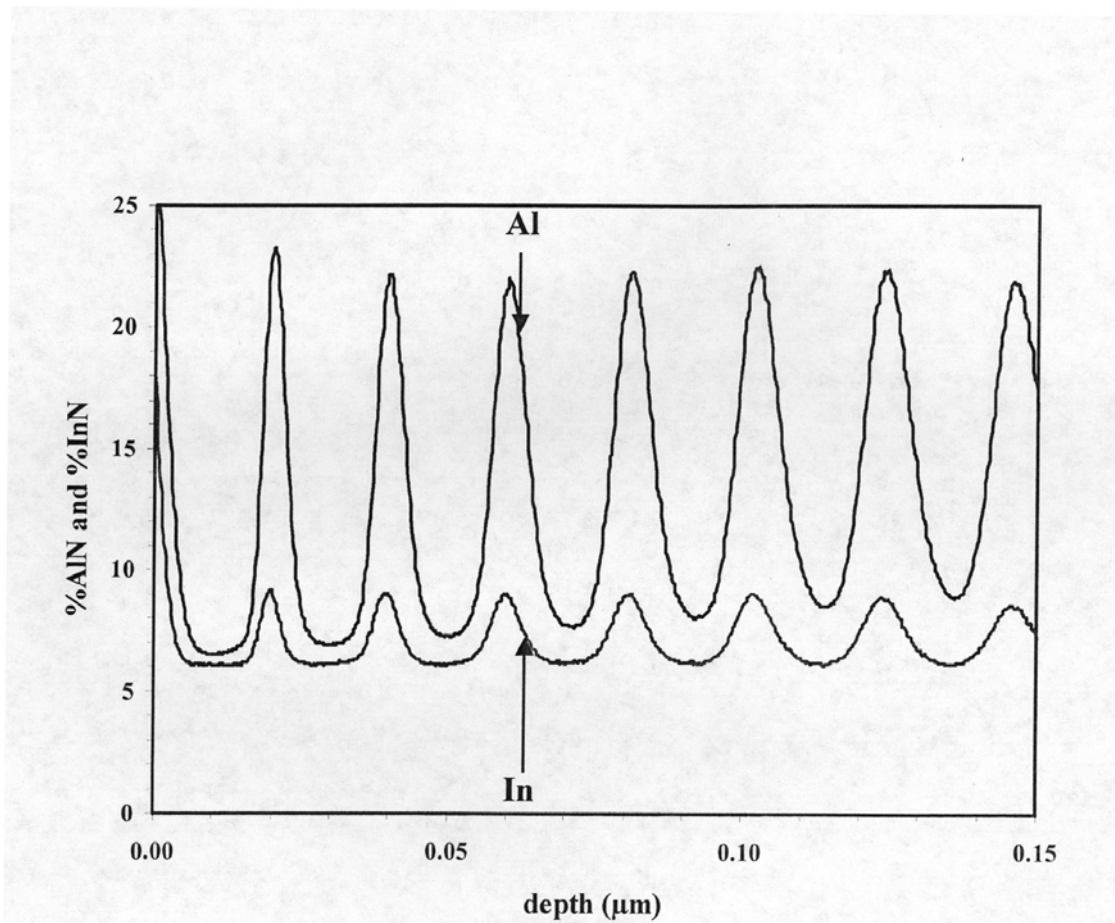


Figure 5-4 SIMS data for SASL shows increase in both In and Al during SASL effect. In increases from 6-9% while Al increases from 8-23%. Temperature and Growth conditions are constant.

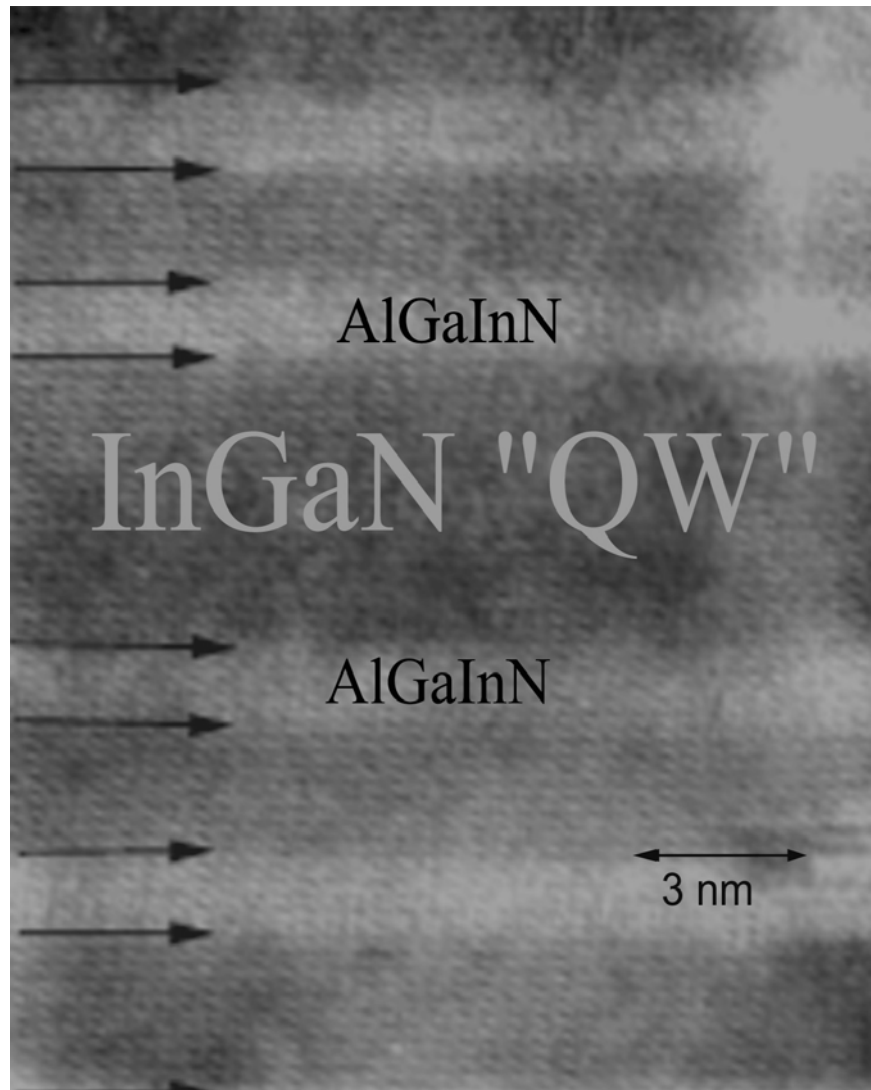


Figure 5-5 Quantum well structure exhibiting SASL effect. Quantum well is 6nm InGaN while cladding layers are AlInGaN with SASL.

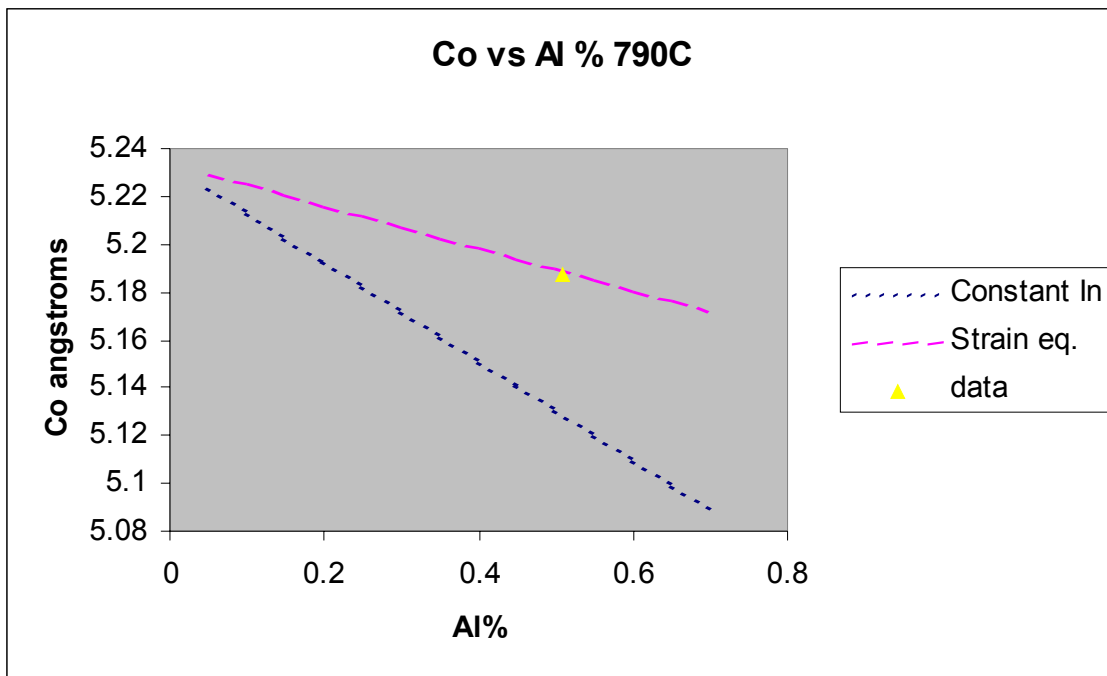


Figure 5-6 Graph shows actual and predicted 0002 lattice spacing for constant In incorporation and Strain Equilibrium In incorporation at 790°C. In:Al ratio for Strain Equilibrium. Effect is approximately 1:4.5 for growth on GaN. The datapoint closely follows Strain Equilibrium Effect curve.

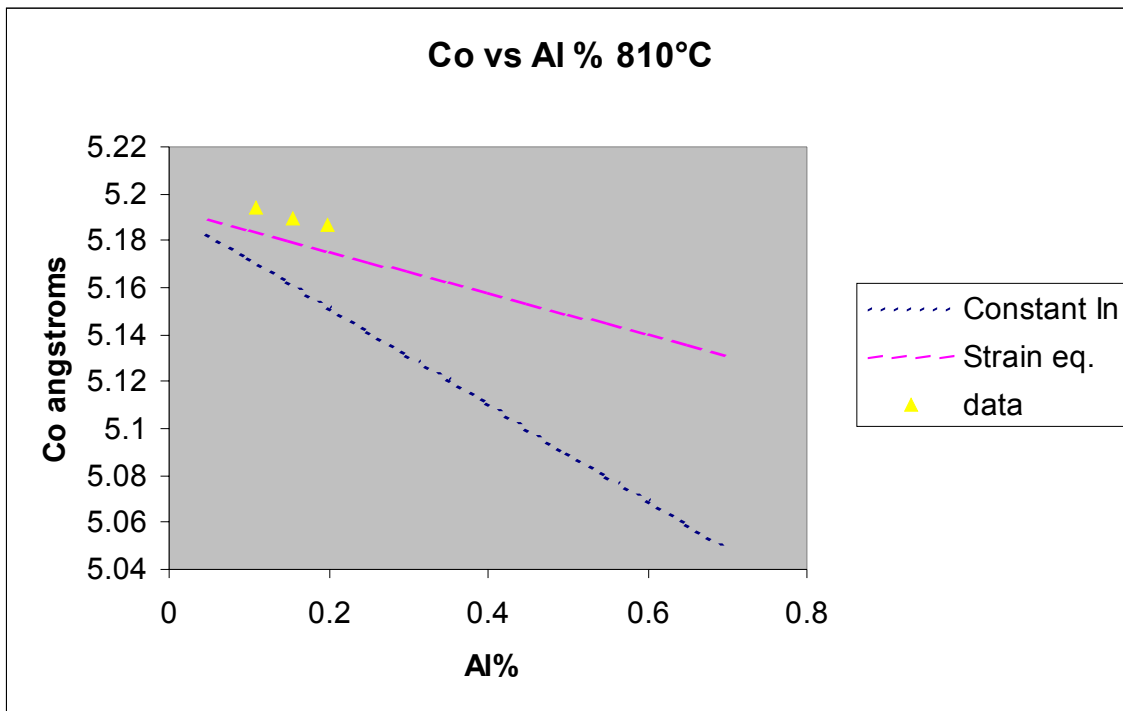


Figure 5-7 Graph shows actual and predicted 0002 lattice spacing for constant In incorporation and Strain Equilibrium In incorporation at 810°C. In:Al ratio for Strain Equilibrium Effect is approximately 1: 4.5 for growth on GaN. The datapoints closely follow Strain Equilibrium Effect curve.

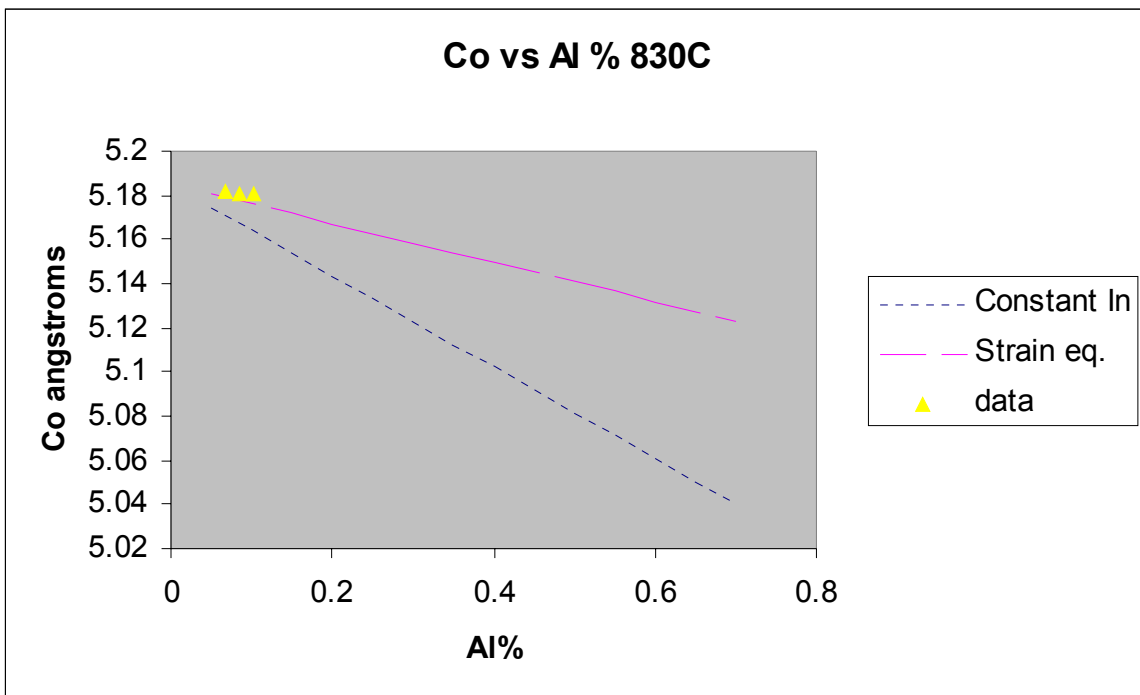


Figure 5-8 Graph shows actual and predicted 0002 lattice spacing for constant In incorporation and Strain Equilibrium In incorporation at 830°C. In:Al ratio for Strain Equilibrium Effect is approximately 1: 4.5 for growth on GaN. The datapoints closely follow Strain Equilibrium Effect curve

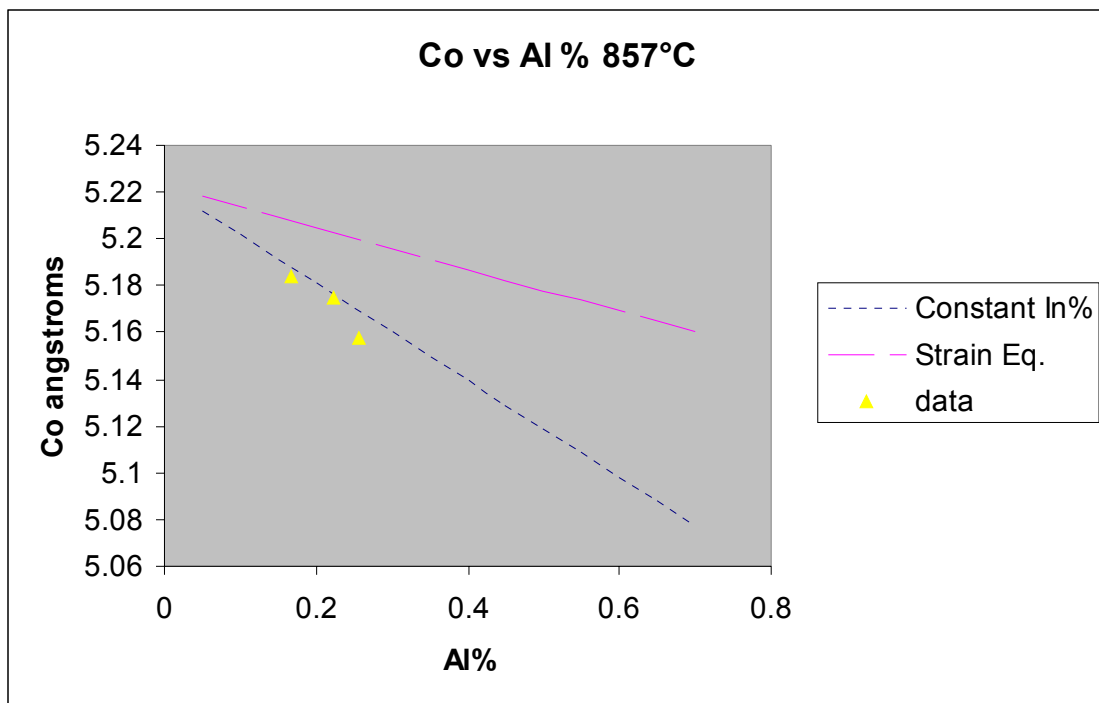


Figure 5-9 Graph shows actual and predicted 0002 lattice spacing for constant In incorporation and Strain Equilibrium In incorporation for 857°C. In:Al ratio for Strain Equilibrium Effect is approximately 1: 4.5 for growth on GaN. The datapoints closely follow Constant In incorporation curve.

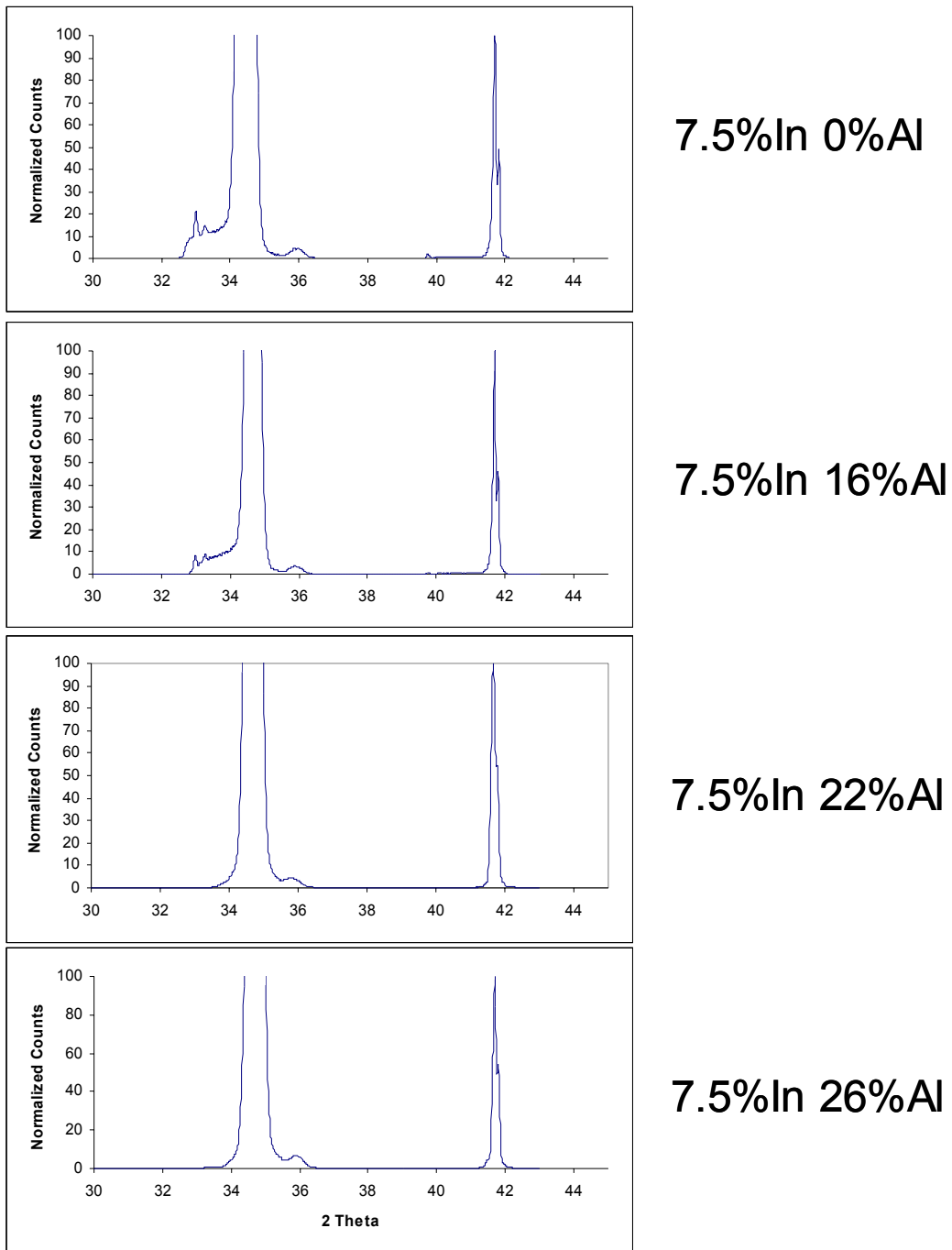


Figure 5-10 Plot shows suppression of phase separation with increasing Al content. The strain from Al cancels strain from In reducing the strain and the driving force for phase separation.

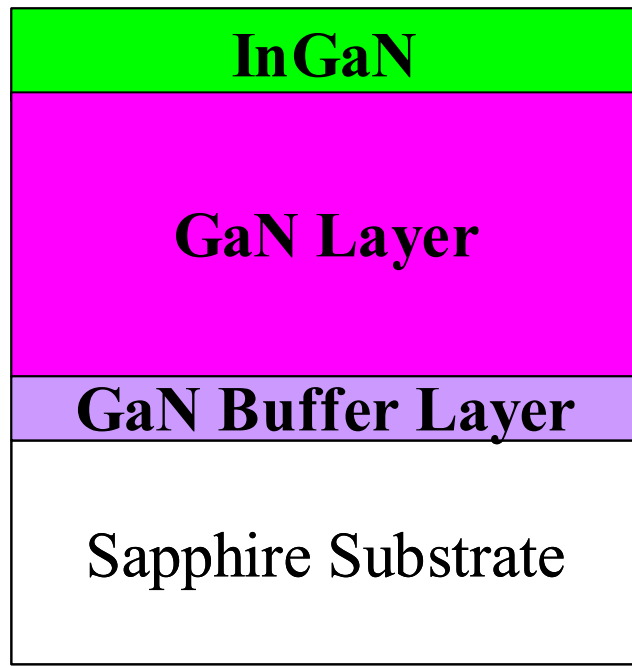


Figure 5-11 Structure for critical layer thickness study. Thin InGaN layers are grown on 1 μ m GaN bulk layer. Buffer layer is GaN buffer layer.

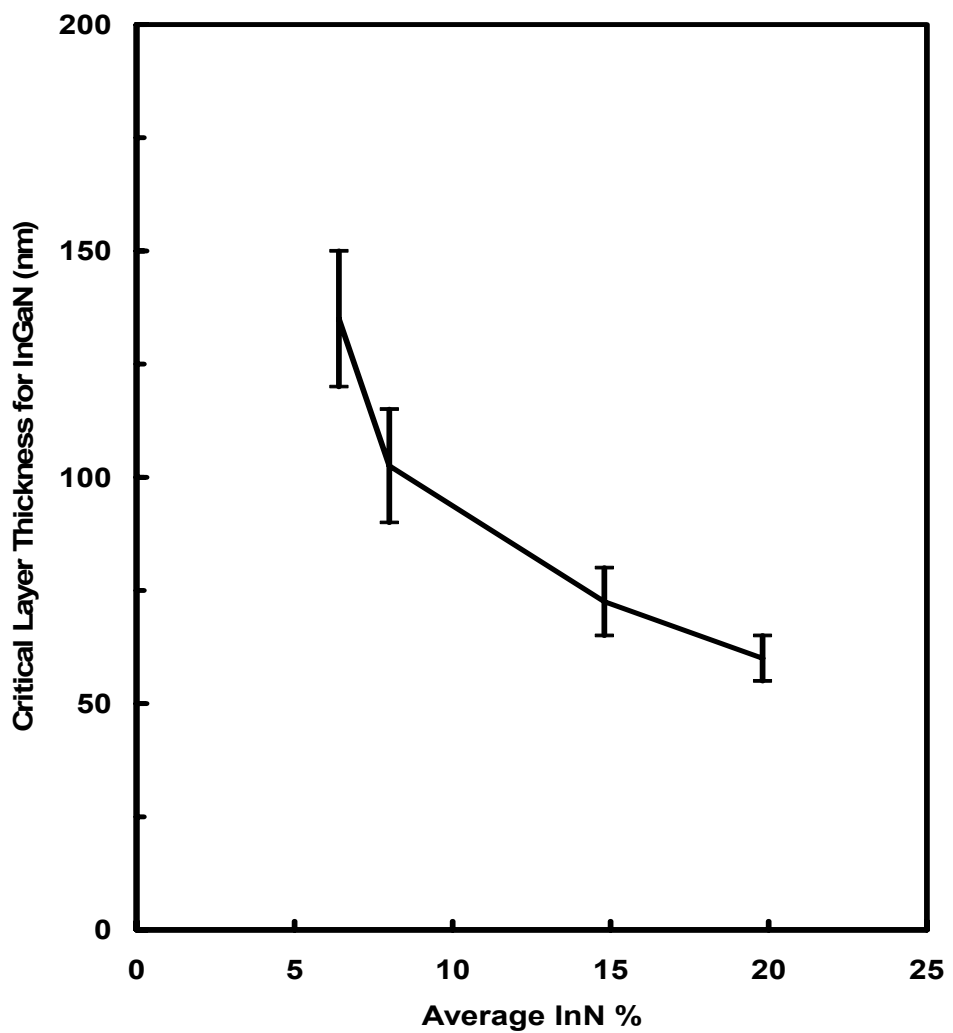


Figure 5-12 Results for critical layer study showing the critical layer thickness for different InGaN compositions.

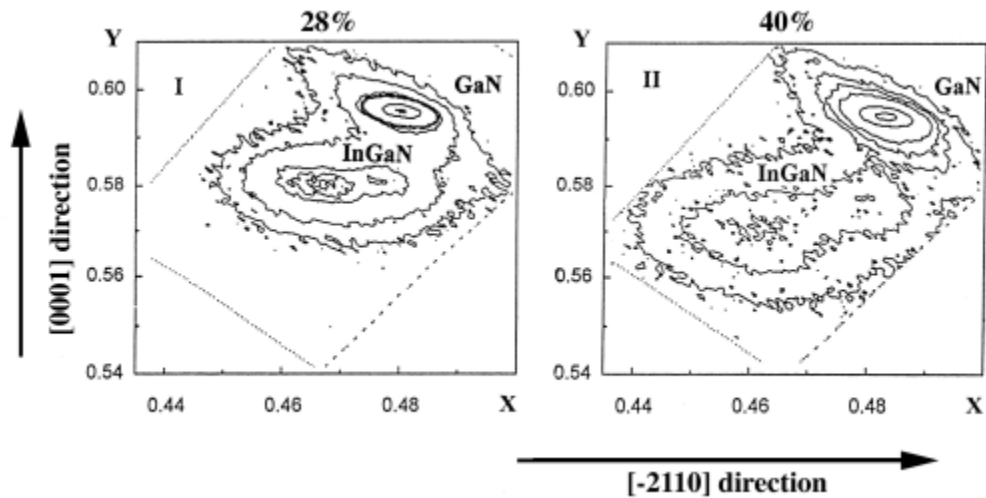


Figure 5-13 Reciprocal lattice maps for InGaN samples. Maps show main layers at 28% and 40% InGaN respectively plus strained layers of different composition. Initial strained layers are 16% for 28% InGaN and 20% for 40% InGaN (Robbins)

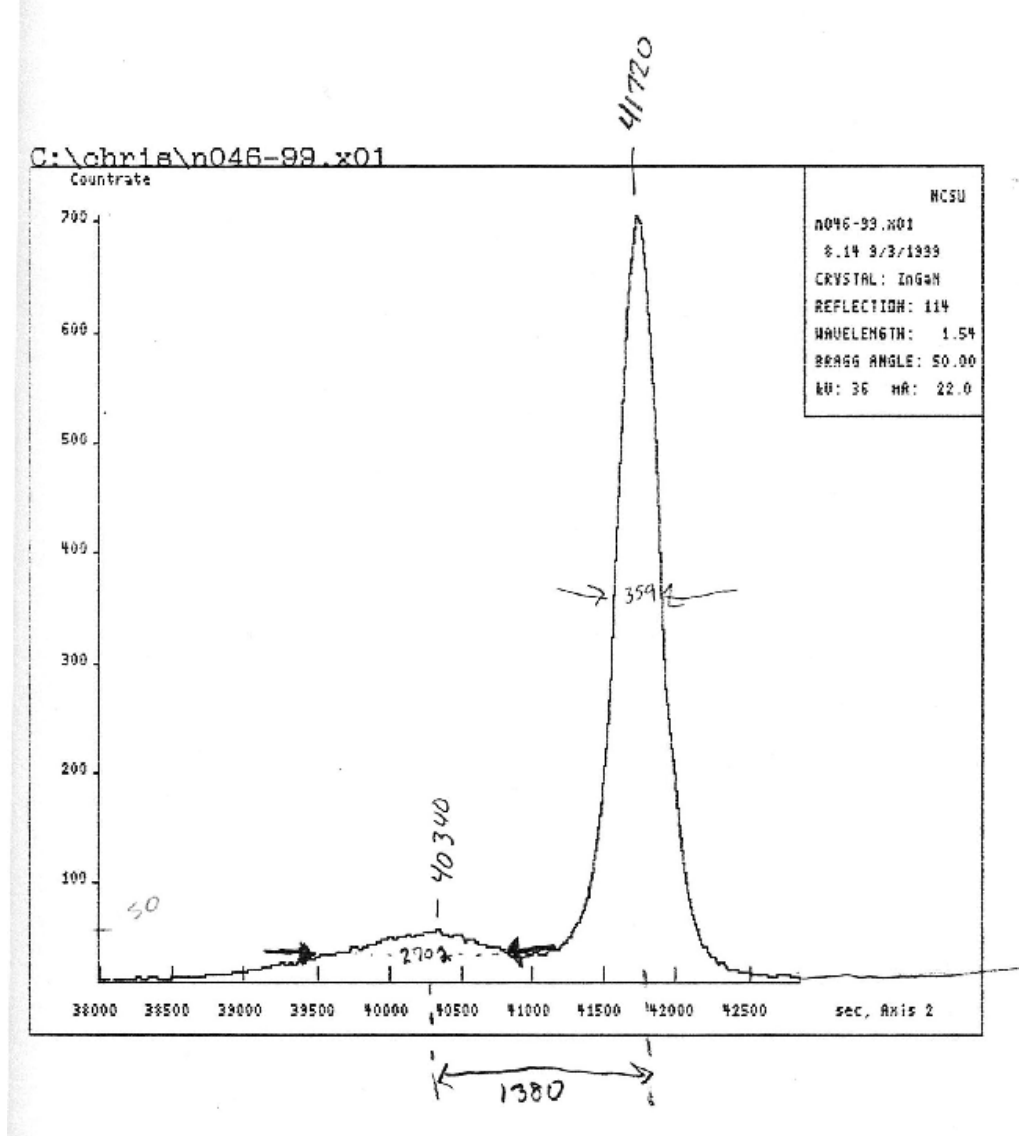


Figure 5-14 Double crystal X-ray analysis of 11-24 off axis peak to determine composition.
 25 minute film shows composition of 4.2% InGaN (Reed)

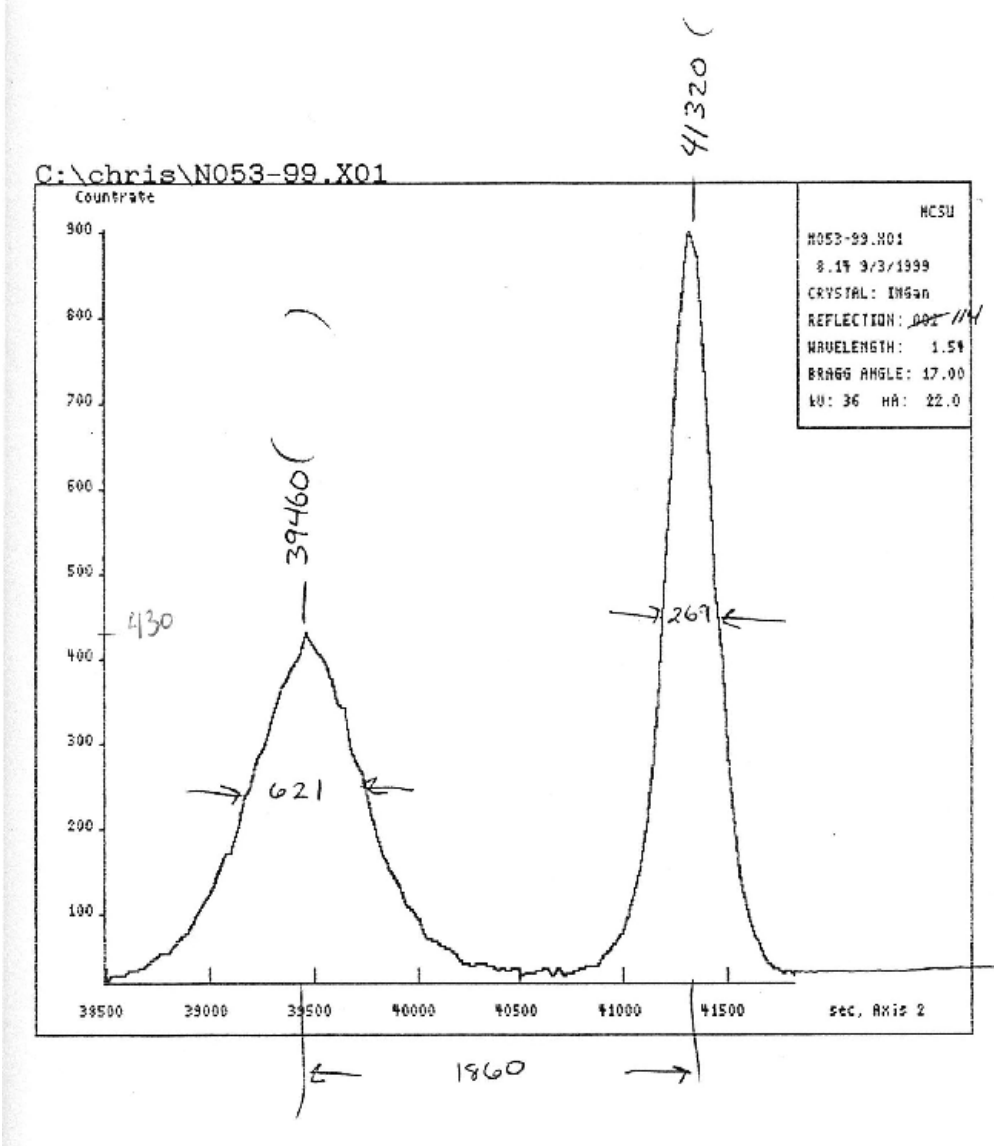


Figure 5-15 Double crystal X-ray analysis of 11-24 off axis peak to determine composition.
105 minute film shows composition of 6.2% InGaN(Reed)

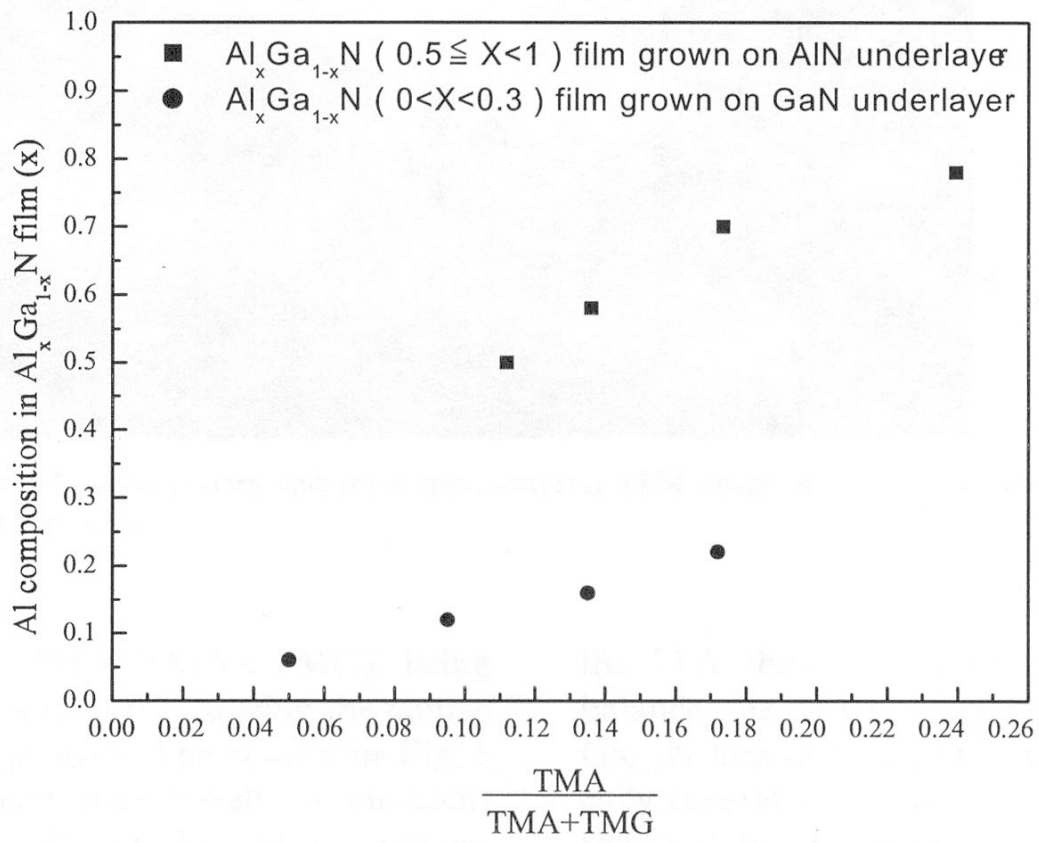


Figure 5-16 Results from Gong, et al., showing the increase of Al composition for AlGaN grown on AlN layer compared with AlGaN grown on a GaN layer. Shows similar composition pulling effect in AlGaN (Gong)

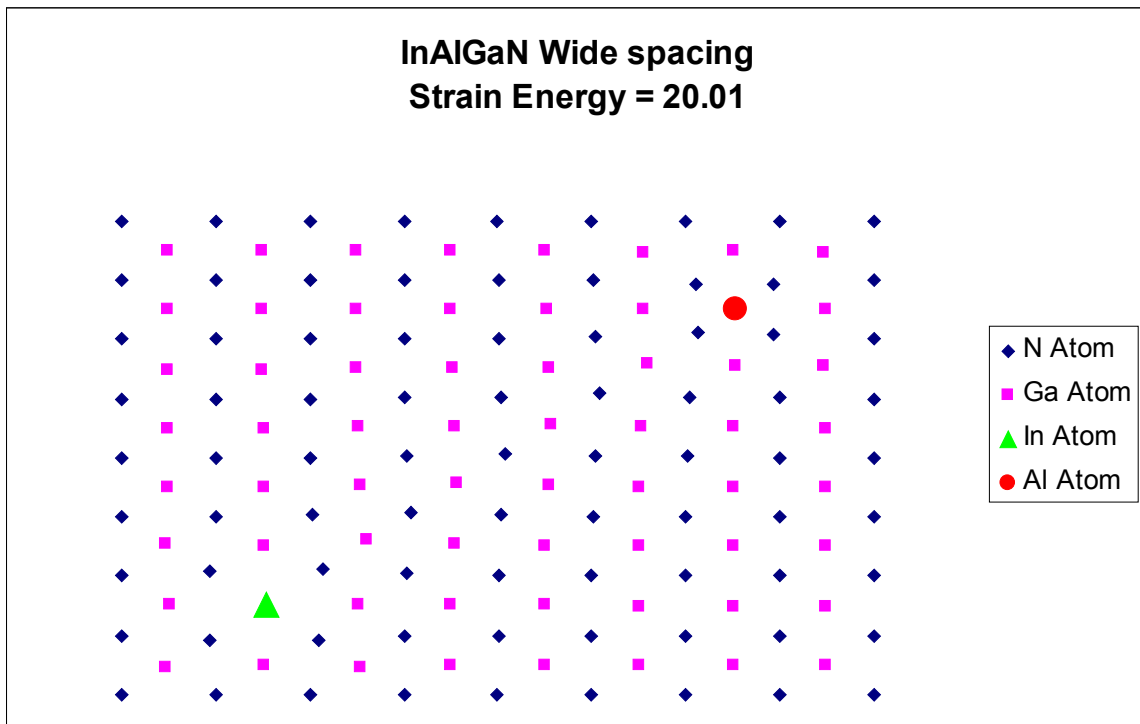


Figure 5-17 Two-dimensional Valence Force Field Model showing $\text{In}_1\text{Al}_1\text{Ga}_{62}\text{N}$ crystal atom positions are distorted by the strain fields surrounding the In and Al atoms. The total strain Energy of the crystal is 20.01 arbitrary units.

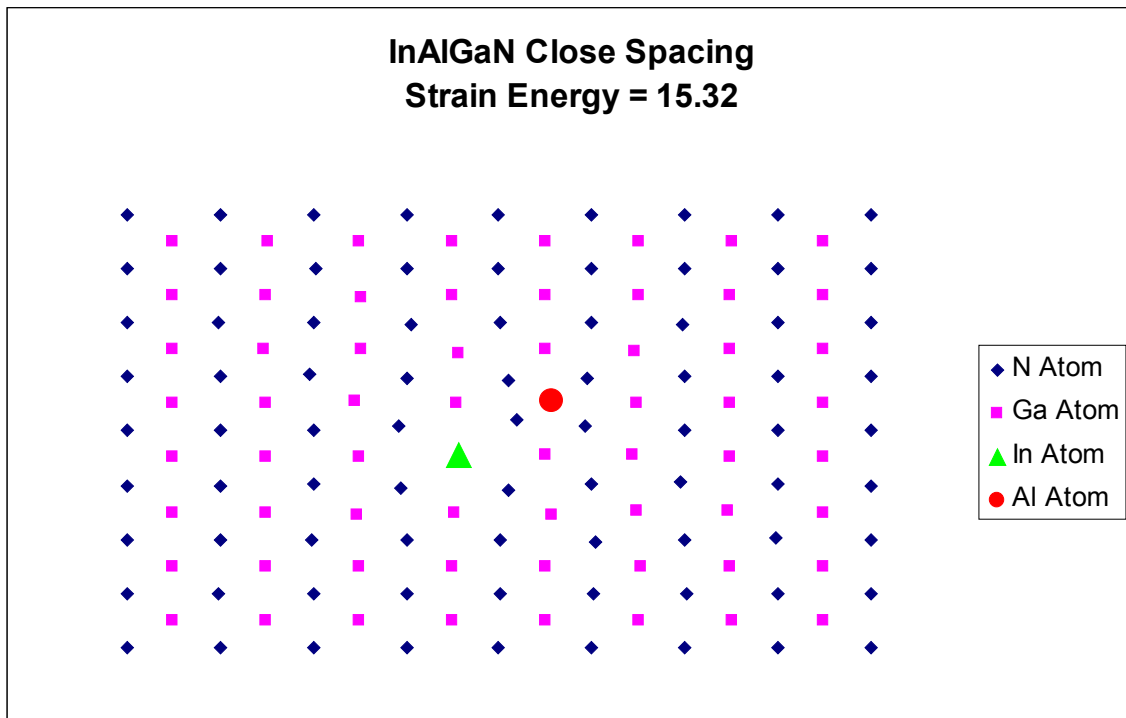


Figure 5-18 Two-dimensional VFF model of same $\text{In}_1\text{Al}_1\text{Ga}_{62}\text{N}$ crystal as before but with the In and Al atoms moved closer together. The strain fields from the In and Al atoms cancel out leaving the surrounding atoms relatively undistorted. The total strain for the crystal is 15.32 arbitrary units.

Chapter Six: Modeling Introduction and Background

The most convenient way to measure energy in phase systems is the Gibbs free energy. The Gibbs free energy is normally written as

$$G = H - TS$$

for a fixed energy and

$$dG = dH - TdS$$

for a free energy change. In the free energy change formula, TdS term is the change in entropy for the reaction and the dH term is the change in internal energy. Technically dH includes the work from volume changes PdV , but in dealing with solids this term is usually neglected. The Gibbs free energy for a phase can be calculated by various methods ranging from simple to very complex.

From the Gibbs free energy curve, it is possible to generate the phase diagram for a given system. In the case where the entropy term is large compared to the enthalpy term, or the enthalpy term is negative, there is complete miscibility, making the phase diagram trivial. In the case where the enthalpy is larger than the entropy, the phase diagram is determined by the shape of the free energy curve. The minima of the free energy curves show the minimum energy, or equilibrium, compositions. To have an equilibrium mixture of the two phases, you need to have the chemical potential of the two phases equal. Chemical potential is given by the change in free energy G with composition or dG/dN . This is shown on the free energy curve as the slope of the free energy line. To determine the equilibrium between the two phases, you just have to draw a tangent to the two minima on the curve. The endpoints of

this tangent line will be near, but not equal to, the energy minimums. For most crystals, the error between tangent and minima is small.

Any composition within the region between the two equilibrium points defined by the tangents of equal chemical potential is considered to be non-equilibrium. Near the equilibrium points the compositions are non-equilibrium and metastable. However, if you move too far from the endpoints you can enter the spinodal region, where the composition is unstable. The spinodal region is defined where the free energy curve has an inflection point. Within the spinodal region, any microscopic fluctuations (which are impossible to prevent) are sufficient to set up a chain reaction decomposing the composition into its equilibrium phases. Both the equilibrium compositions and the spinodal region are defined by the free energy vs. composition curve.

The simplest model for Gibbs free energy of a phase is the perfect solution model where the atoms are indistinguishable. In this case, there are no entropy or enthalpy effects. This can only apply to mixtures of ideal gasses.

The next level of complexity is the Ideal Mixture model, where there are no interactions between the different atoms. This results in the enthalpy of mixing being zero. In this case the only energy in the system is the entropy of mixing. The entropy calculation S arises from the approximation for the Boltzmann equation,

$$S = k \ln W$$

where k is the Boltzmann constant and W is the number of configurations. The value for S can be approximated by the expression

$$S = X_a \ln X_a + (1-X_a) \ln(1-X_a).$$

This case applies where the atoms of type A and type B have no preference for either A or B. Because the entropy of a mixture is always larger than the entropy of a pure component, the ideal mixture model always results in complete miscibility between the two components.

In most solutions, however, there is a preference between nearest neighbours. If A prefers to be next to B, you will have good mixing. When the A atoms prefer to be next to A atoms and B atoms next to B atoms you will get segregation if the effect is strong enough. The strictly regular mixture expression takes this into account by using a term Ω as the mixing interaction parameter. In the regular mixture, the mixing enthalpy can be calculated by

$$H = \Omega X_a(1-X_a).$$

If Ω is strongly positive, then A atoms prefer A atoms and B atoms prefer B atoms. A positive Ω does not always mean segregation. Depending on whether the entropy term or the enthalpy term is dominant, you can get varying degrees of segregation. The effect from the Ω term is strongest at $X_a = 0.5$. At lower concentrations near pure A or pure B, the entropy term dominates. The entropy term also dominates at high temperatures due to the T in the equation TdS . If the temperature is high enough, then there will be no segregation regardless of Ω . This critical temperature is given by

$$T = \Omega / 2k.$$

To determine whether a phase is stable using the regular solution model, you need to know the composition, the temperature, and the interaction parameter Ω . The first two are easy, but Ω is not always simple to calculate. In the strictly regular solution model Ω is calculated by assuming that only nearest neighbour interactions are important. This gives a simple formula

$$\Omega = E_{ab} - \frac{1}{2} (E_{aa} + E_{bb}).$$

In real materials systems, the energy of AB bonds is influenced by internal distortions in the crystal. Because these distortions extend farther than the single AA or AB bond, the simplified formula for Ω is not sufficient for representing real behaviour.

To calculate the phase diagram for a material, you need the free energy curve. To calculate the free energy curve for a material you must first calculate the enthalpy curve H using the ideal solution model, the regular solution model or a direct calculation of the strain energy. The entropy curve can be calculated by simply knowing the composition and temperature. These curves are shown in Figure 6-1. Combining these values for each composition at a given temperature gives the free energy curve for that temperature Figure 6-2. The minima (or tangents to the minima) represent the equilibrium composition at that temperature and the inflection points (represented by the peak of the derivative) represent the spinodal point. If you repeat these calculations for each temperature you will get a curve that looks like Figure 6-3. The calculations are very straight forward, if you have the strain energy.

6.1 Development of strain energy modeling

One of the early methods to estimate this was Keating's Valence Force Field (VFF) [1] model. By taking into account the stretching and bending forces on zinc-blende crystals, he came up with a formula for Ω in terms of the bond stretching coefficients α and the bond bending coefficients β and the difference in lattice parameters. In the original VFF model Ω is given by the formula

$$\Omega \approx 2 \alpha \beta / (\alpha + \beta).$$

Although the VFF model was accurate for some materials systems, it was not as accurate for others. To correct this, Stringfellow et al. developed the Delta Lattice Parameter (DLP) model which modified the VFF model to include a fitting parameter to allow for a better fit to experimental data[2, 3]. The DLP model used the difference in lattice parameters plus a fitting parameter to calculate the strain of the material. Figure 6-4 gives the DLP equation along with fitting parameter for some common materials systems.

The VFF model is generated using a single tetrahedron in the zinc-blende structure. One simplification of the VFF model was to assume that the atom positions are constant, in which case the bond angles remain undistorted and the bonds stretch and extend to make up the mismatch. This is called the Virtual Crystal Approximation (Figure 6-5). Another simplification is to assume that the bonds remain the same length and the center atom position changes, distorting the bond angles to make up for the mismatch, while keeping the bond distances the same. This is called the Covalent Radius Approximation (Figure 6-5) What actually happens in the crystal is a mixture of both. As you can see from Figure 6-6,

the actual bond lengths from x-ray adsorption fine structure are closer to the CRA model than the VCA model. Allowing both the bond length and bond angle to change will result in the general VFF model (Figure 6-7). In the general VFF model, the atom positions are varied to get the lowest overall strain energy using the VFF formula given in Figure 6-8.

By keeping the composition of the center atom constant and changing the composition of the four corners you can generate 5 different compositions of tetrahedra (Figure 6-9). Taking into account the different configurational combinations of these 5 tetrahedra, it is possible to calculate the entropy of the crystal. By combining the elastic strains in the bonds with the entropy factors from the tetrahedral configurations, it is possible to calculate the free energy directly. This is known as the cluster variation model and is the basis for the DLP model. While the DLP model improved on the original VFF model it still had the artificial restriction of keeping the corners of the tetrahedra fixed. This causes extra strain from the difference in composition between the different tetrahedra (Figure 6-10).

In 1996, Ho and Stringfellow [4] extended the Valence Force Field model introduced by Keating. By allowing the lattice to relax beyond the first set of nearest neighbours, the strain energy calculated is reduced and brought closer into agreement with experimental data. The modified VFF model was originally developed to study the solubility of N in GaAsN and GaPN systems [5]. The modified VFF model utilized a zinc-blend approximation to the wurtzite GaN structure and allowed the crystal to relax out to the sixth nearest neighbour. When the Modified VFF approximation was applied to InGaN [4], it reduced the interaction parameter Ω , at 50% InGaN, from 9.60 kcal/mol with the DLP model to 5.98 kcal/mol with

the modified VFF. Using the modified VFF, the interaction parameter Ω varied from 5.63 on the In rich side to 6.32 on the Ga rich side. Ho and Stringfellow took the average of these two values for Ω to create a theoretical phase diagram for the InGaN system.

Matsuoka's model [6] started with the zinc-blende approximation for the GaN crystal and used the DLP model to study the behaviour of the AlInGaN system. Matsuoka generated both the ternary phase diagram and spinodal curves (Figure 6-11). Work by Wakahara et al.[7] also utilized the DLP model for the zinc-blende approximation of InGaN to match experimental data of the miscibility gap. Elyukhin et al.[8] applied the cluster variation method to the wurtzite structure to study the miscibility gap in the ternary wurtzite crystal system.

Up to this point all modeling, except for Elyukhin, was done assuming the zinc-blende structure of GaN. There are several reasons for this. The zinc-blende structure is cubic and has orthogonal axis, greatly simplifying calculations of bond angles and bond lengths. When you work in the wurtzite crystal structure, all of the bond angles are referenced to the hexagonal unit cell, which has 60-degree angles. Because the crystal structures were very similar, other than stacking sequence, the error from using the zinc-blende structure was assumed to be small.

In 2000, Takayama et al.[9] developed a modified VFF model that utilized the wurtzite structure. GaN, like most hexagonal based materials, has a c/a ratio that deviates from the ideal of 1.633, resulting in a distorted tetrahedra. Due to the asymmetry in the GaN

wurtzite crystal, the mathematics involved for the hexagonal VFF model are more complex and computer intensive than the VFF model for the zinc-blende structure. In the wurtzite model, the lengths of the three a -axis bonds are different than the c -axis bond and the $a\text{-}c$ bond angles are different than the $a\text{-}a$ bond angles. Because the wurtzite crystal system is not orthogonal, dot and cross products cannot be used for the wurtzite system. This requires $\text{Sin}\theta$ and $\text{Cos}\theta$ to be used instead at much greater computational expense. To keep computation time reasonable, randomly generated 20x20x20 atom crystals with periodic boundary conditions were used in the hexagonal VFF calculations.

Using the strictly regular approximation, Takayama et al. estimated the interaction parameter using the wurtzite VFF model using the formula $\Omega X_a(1 - X_a) = \text{sum of VFF energies}$. For the InGaN system, the interaction parameter is calculated to be 7.81 kcal/mol compared to 5.98 kcal/mol from previous studies. This increase in interaction parameter results in a larger unstable mixing region in InGaN. In addition, the wurtzite VFF model was able to accurately calculate equilibrium atom positions on a microscopic level. The bond length data from Takayama's VFF model fitted closely to the experimental data from Hughes et al.[10] using extended x-ray absorption fine structure (EXAFS) in Figure 6-6. Takayama's later work extended the VFF model to the AlInGaN, BGaN, BAlGaN, and BGaInN systems.

6.2 References

1. Keating, p.n., *Effect of invariance requirements on the elastic strain energy of crystals*. Physical Review Letters, 1966. **145**: p. 637.
2. Stringfellow, G.B., *Calculation of Ternary-III-V and Quaternary-III-V Phase-Diagrams*. Journal of Crystal Growth, 1974. **27**(DEC): p. 21-34.
3. Stringfellow, G.B., *Calculation of Solubility and Solid-Gas Distribution Coefficient of N in Gap*. Journal of the Electrochemical Society, 1972. **119**(12): p. 1780.
4. Ho, I.H. and G.B. Stringfellow, *Solid phase immiscibility in GaInN*. Applied Physics Letters, 1996. **69**(18): p. 2701-2703.
5. Ho, I.H. and G.B. Stringfellow, *Solubility of nitrogen in binary III-V systems*. Journal of Crystal Growth, 1997. **178**(1-2): p. 1-7.
6. Matsuoka, T., *Calculation of unstable mixing region in wurtzite In_{1-x}-yGa_xAl_yN*. Applied Physics Letters, 1997. **71**(1): p. 105-106.
7. Wakahara, A., et al., *Compositional inhomogeneity and immiscibility of a GaInN ternary alloy*. Applied Physics Letters, 1997. **71**(7): p. 906-908.
8. Elyukhin, V.A., et al., *Miscibility gap of ternary alloys of binary compounds with zinc-blende and wurtzite structures using the cluster variation method*. Journal of Crystal Growth, 1997. **173**(1-2): p. 69-72.
9. Takayama, T., et al., *Theoretical analysis of unstable two-phase region and microscopic structure in wurtzite and zinc-blende InGaN using modified valence force field model*. Journal of Applied Physics, 2000. **88**(2): p. 1104-1110.

10. Hughes, O.H., et al., *Reflection high-energy electron diffraction studies of wurtzite GaN grown by molecular beam epitaxy*. Journal of Vacuum Science & Technology B, 1998. **16**(4): p. 2237-2241.

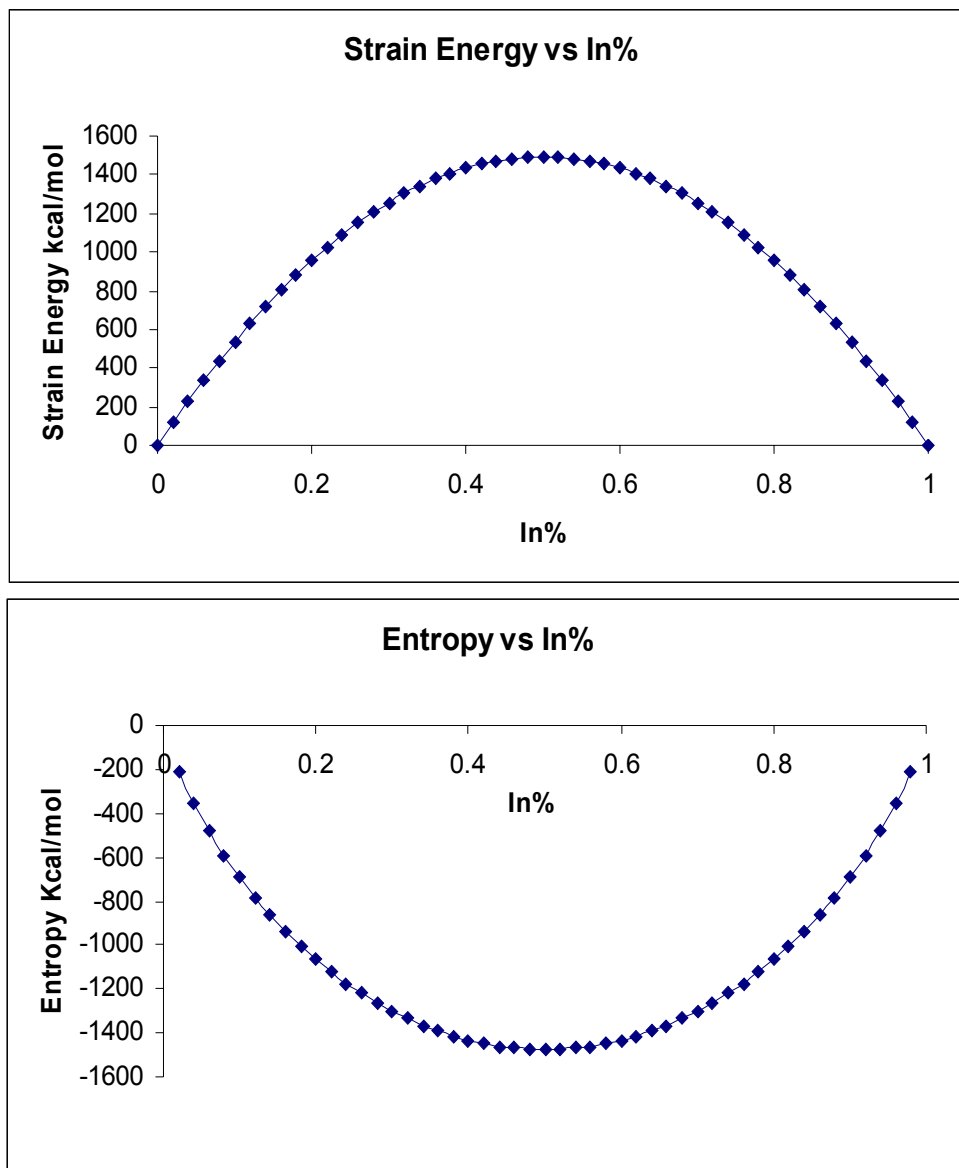


Figure 6-1 Calculation of phase diagram using the regular solution model. Ω used is Stringfellow's value of 5.98 kcal/mol. Upper curve represents the strain energy H . Lower curve represents the entropy term TS .

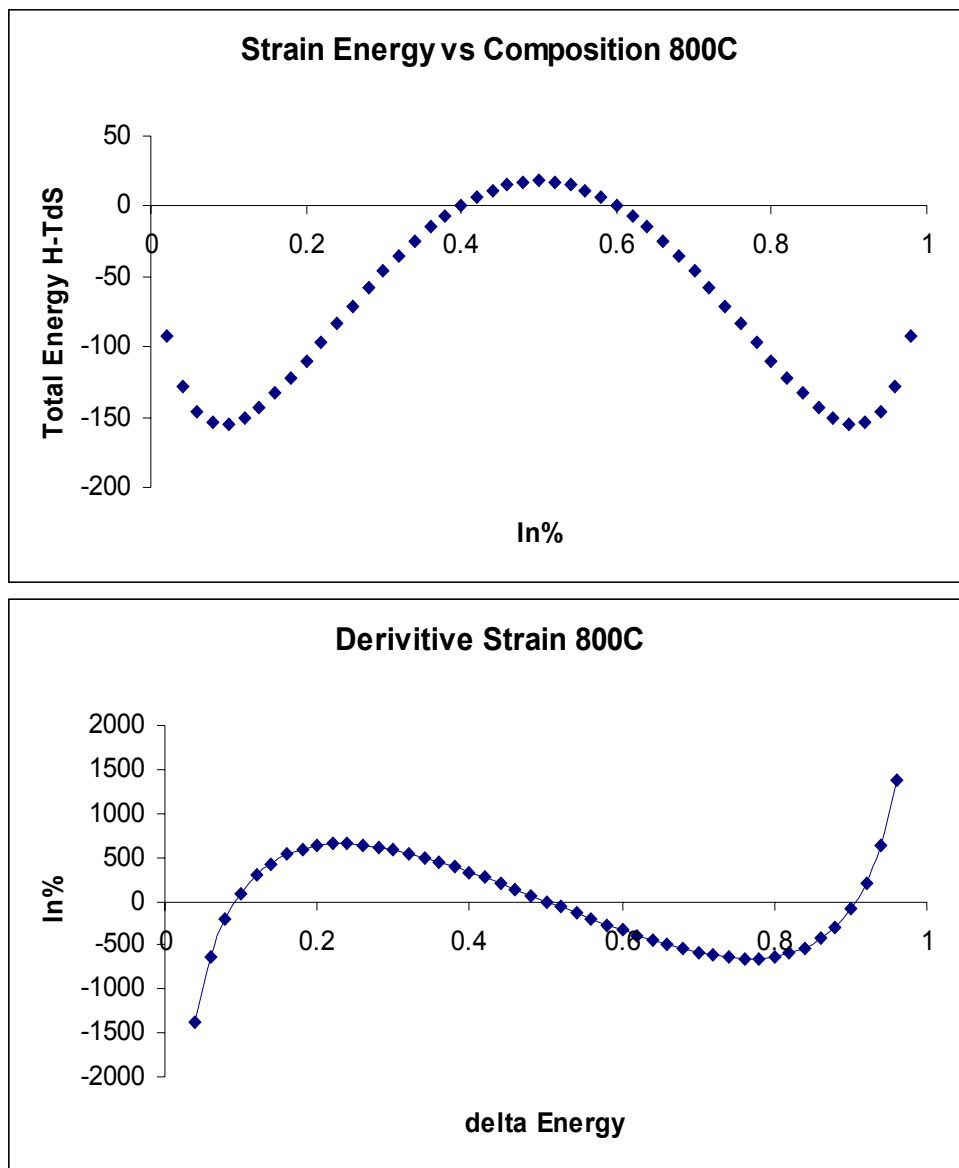


Figure 6-2 Calculation of phase diagram using the regular solution model. Ω used is Stringfellow's value of 5.98 kcal/mol. Upper curve is the free energy diagram. Lower curve is the derivative of the free energy.

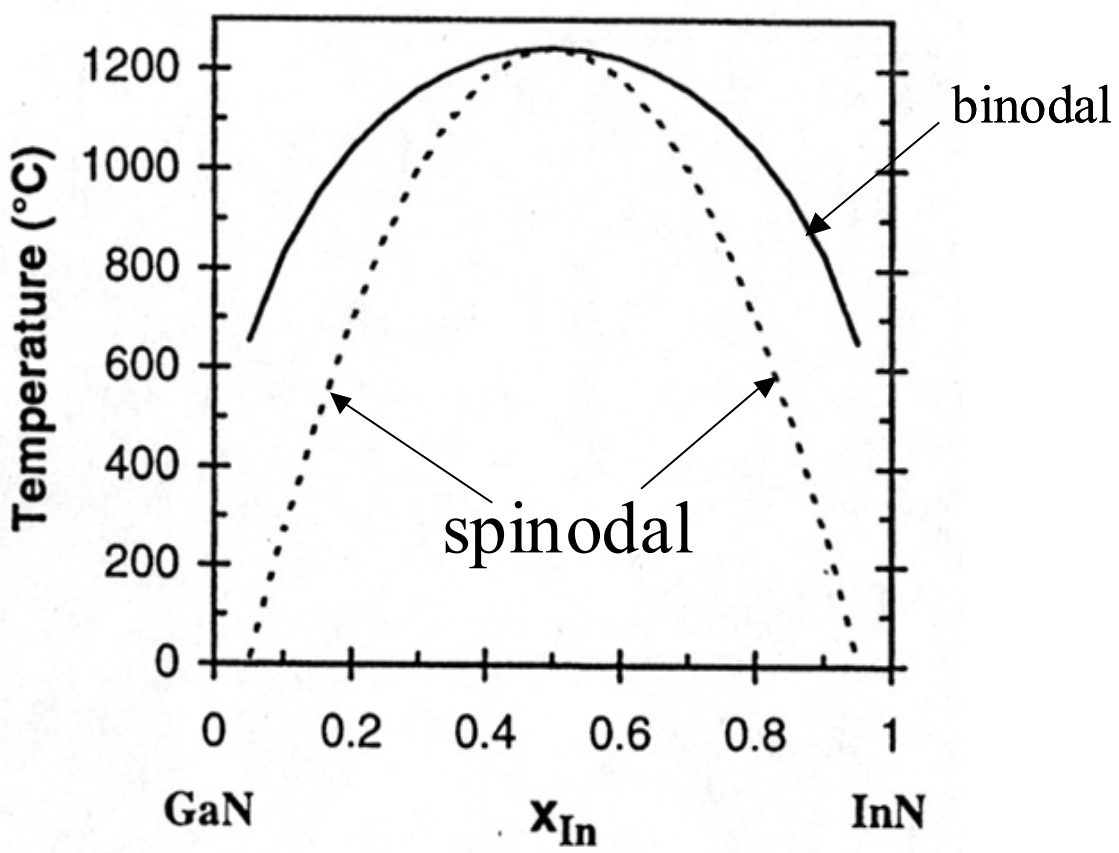


Figure 6-3 Predicted phase diagram for InGaN from Ho and Stringfellow (APL 69 1996)

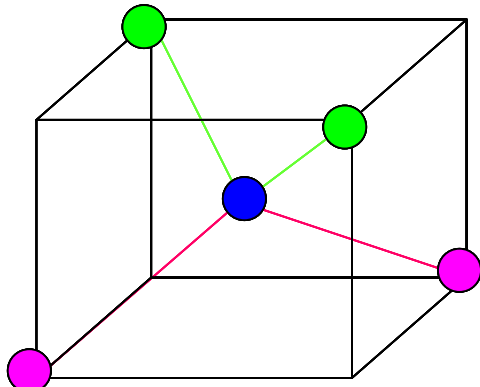
III-V ternary alloy system	Lattice mismatching $\Delta a/a$ (%)	Interaction parameter α (DLP model) (cal/mol)	Critical temperature T_c (K)
AlAs-GaAs	0.159	0	0
GaAs-InAs	6.92	2815	709
AlP-GaP	0.239	0	0
GaP-InP	7.39	3630	914
GaP-GaN	18.9	28 900	7276
AlN-GaN	2.93	931	233
AlN-InN	13.38	17 300	4338
GaN-InN	10.46	10 300	2583

$$\alpha_{i-j} = 4.375K \frac{(a_i - a_j)^2}{\left(\frac{a_i + a_j}{2}\right)^{4.5}}.$$

Figure 6-4 Formula for Delta Lattice Parameter model with table of interaction parameters for III-V alloys.

VCA

Bonds lengths stretched



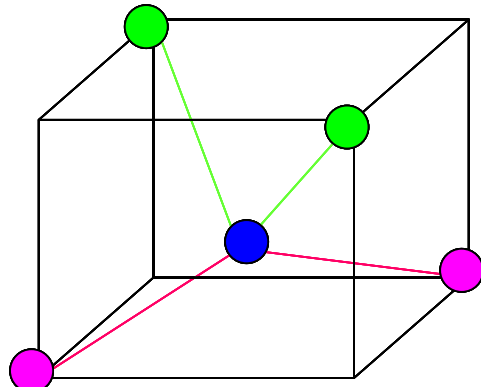
Bonds angles relaxed

● N Atom

● Ga Atom

CRA

Bonds lengths relaxed



Bonds angles distorted

● In Atom

Figure 6-5 Limiting cases for the VFF model. The VCA approximation represents fixed bond angles, while the CRA approximation represents fixed bond lengths. The minimum energy VFF model is a combination of the two but is closer to the CRA model.

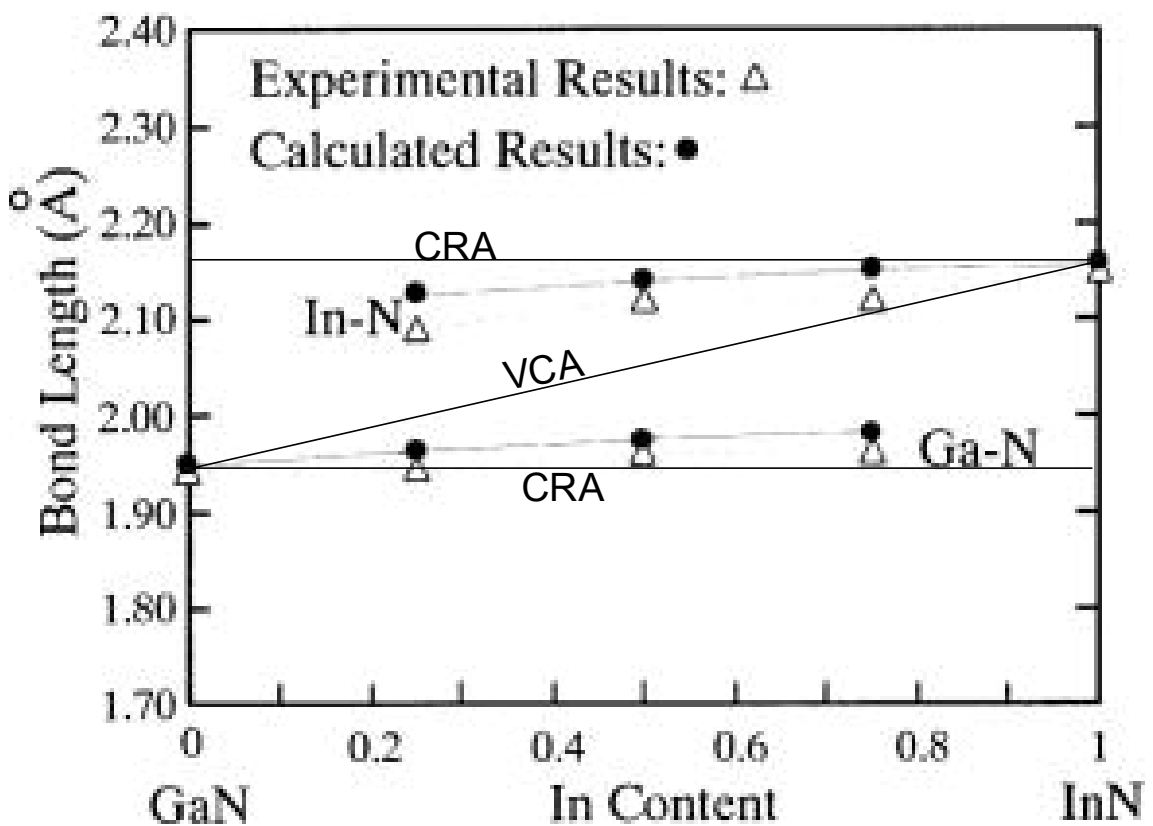


Figure 6-6 Figure showing the actual bond lengths for the InGaN crystal system. The upper and lower lines represent the CRA crystal approximation and the middle line represents the VCA approximation. Figure from Jeffs N.J., Mater. Res. Soc. Symp. Proc. No 512, p.519.

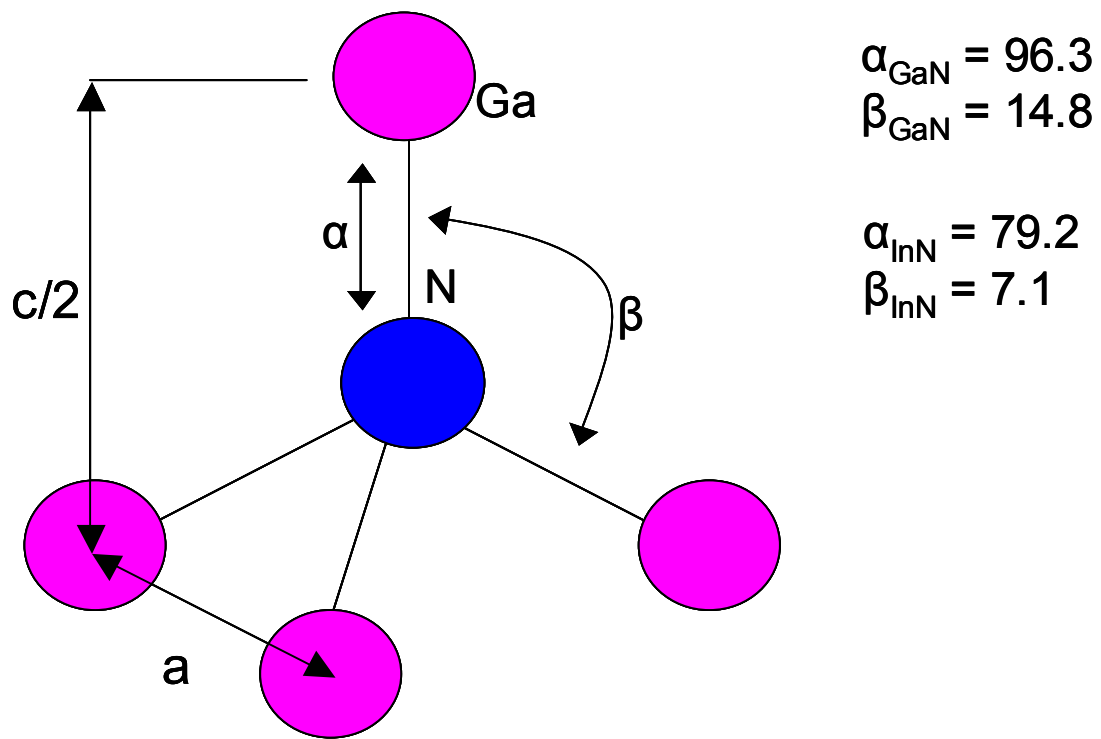


Figure 6-7 Diagram of the stretching and bending moments for the GaN tetrahedra used in the VFF model. α represents the bond stretching energy and β represents the bond angle distortion

$$U_j = \sum_{i=1}^4 (3\alpha_{ij}/8r_{ij_0}^2)(r_{ij}^2 - r_{ij_0}^2)^2 +$$

$$2 \sum_i \sum_{k>1}^4 (3\beta_{ijk}/8r_{ji_0}r_{jk_0})(r_{ij}r_{jk} - r_{ij_0}r_{jk_0})^2$$

Move atom(s) until U_j is minimum

Figure 6-8 Formula for the VFF model in the zinc-blende crystal system. The r_{ij} represent the vectors between the pairs of atoms in the tetrahedra. The atom position is relocated to get a minimum total energy U

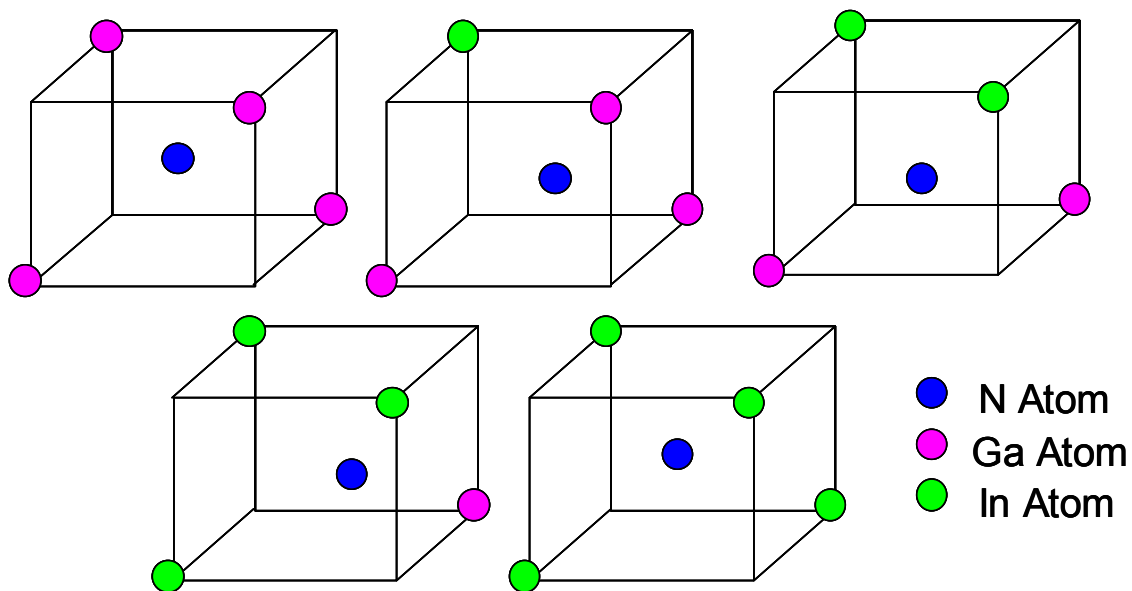


Figure 6-9 Elemental clusters used for the CVM method. The cluster variation method statistically combines the elemental clusters and was used extensively in the zinc-blende crystal structure as the basis for the DLP model

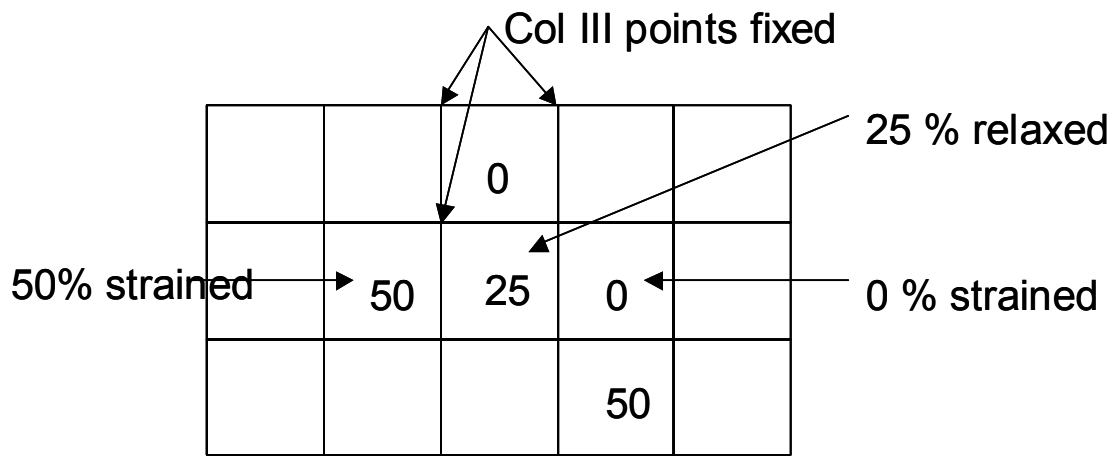


Figure 6-10 The cluster variation method has drawbacks however. If alloy is 25% overall, 0%, 50%, 75% and 100% tetrahedral will all be strained leaving only 25% relaxed. This error tends to overestimate the strain in the crystal.

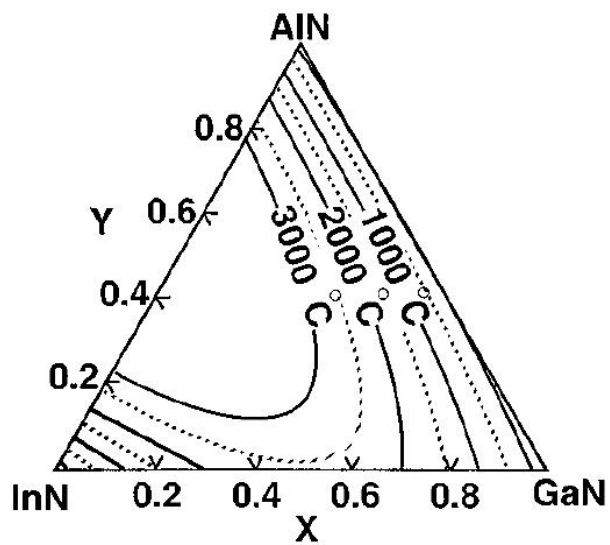


Figure 6-11 Phase diagram for the AlInGaN system showing isotherms from 0-3000C.
Figure from Matsuoka T., App. Phy. Lett. 71(1) 1997.

Chapter Seven: Description of Model and Results

7.1 Development of Model from Takayama

The model described here is an extension of the wurtzite VFF model developed by Takayama et al. (**Figure 7-1**). The formula used by Takayama for the strain energy made use of $\text{Cos}\theta$ terms to calculate the strain (**Figure 7-2**). To improve computational performance, a hybrid crystal structure is used. The atoms are indexed as the wurtzite structure, but the equilibrium positions are calculated in a Cartesian xyz coordinate system. This allows the use of ordinary dot products and cross products to calculate stretching and bending energies with only a single conversion at the beginning of the calculations. Considering that a dot product can be calculated dozens of times faster than a $\text{Sin}\theta$ or $\text{Cos}\theta$, this leads to a considerable speedup.

While the Poisson's ratio from the VFF model is not consistent with published values for the Poisson's ratio of GaN, this is not unexpected. The VFF model has a limitation in that the VFF model tends to overestimate the Poisson's ratio. The Keating parameters α and β are determined by C_{11} and C_{12} , while the actual crystal is described by four elastic constants C_{11} , C_{12} , C_{44} and the lattice constant. The missing bulk shear C_{44} could explain the inconsistency[1]. If the C_{44} elastic shear constant were accounted for in the VFF model, it would limit the Poisson's ratio for large shear strains. Regardless of this limitation, VFF models have been used to study strained systems successfully, including InAs/GaAs heterointerfaces[2], initial growth of CdTe/GaAs[3] and Si[4].

The estimated Ga diffusion lengths are on the order of 2nm - 20nm[5]. This would give a possible range for the crystal size of 6 - 60 atoms. Because the growth conditions for the AlInGaN study use a high V/III ratio and no H₂ (both conditions reduce surface

mobility), the diffusion lengths would be on the low end of the range given. Therefore, a crystal size of 8x8 should not be unrealistically small.

7.2 Development of Computer Model

The model utilizes an N terminated surface convention for indexing. Both Ga and N surface polarities can be modeled by considering either the top surface or the bottom surface of the model to be the film surface. Indexing of the Ga and In atoms is relative to the 120 degree wurtzite basis vectors. By using a coordinate conversion, these indices are converted to the Cartesian system for calculation of bending and stretching energies. Each atom is an instance of an Atom() class, which keeps track of the properties of that particular atom. The Atom() class keeps track of whether or not the atom is on the edge of the crystal and whether it has a periodic boundary or a free surface. This allows both bulk and thin films to be modeled.

Data for the initial atom positions can be created on the fly for different atom configurations that are either randomly generated or ordered. There are three different ways that data can be entered into the simulation. One is to have a separate program create the crystal and output the atom positions, type of atom at that position (In, Ga, Al, N), and the initial position of the atoms. This approach has problems with rounding error due to the limited precision of the x,y,z position values in the data file. Another approach is to generate the atoms internally within the simulation program. This approach gives full precision to all data associated with the crystal. By keeping full precision, the strain energy for a GaN 8x8x8 cell containing 256 total atoms was reduced from 10^{-7} J/mol of energy with the external file down to 10^{-28} J/mol. (The ideal value for a pure GaN cell should be zero, while a 50% InGaN crystal is approximately 8,000 J/mol). The new functions allow for the creation of patterns and the creation of random alloys.

While the internally generated random crystals have far less error than ones read from a datafile, by their nature they are not perfectly repeatable. To fix this a new datafile format needed to be created that will keep track of the overall composition of the crystal and the atom type at each of the crystal indexes. When the datafile is read into the simulation, the position of the individual atoms are calculated internally. This method allows for repeatable runs by using the same dataset, but with the accuracy of having all data calculated internally with almost no roundoff error. Finally, the function WriteDataTypes() was written to output the final state of the model to a file with the correct syntax to be read in again. This allows running a series of simulations with each simulation depending on the output of the previous run. This proves to be invaluable for setting up checkpoints for longer runs.

After the initial atom positions are setup, the neighbour types and equilibrium distances are initialized. The function AtomInit() sets up the Atom() class for each atom in the crystal to keep track of the type and position of the atom, equilibrium distance, and stretching and bending coefficients of each neighbour. Finally, the values for the stretching and bending coefficients are entered based on the atom types. As soon as the crystal is set up and the initial positions and values are entered, an initial strain value is calculated. This value represents the Virtual Crystal Approximation strain value for the crystal with all of the atoms are in their Vegards law predicted positions. As a result, this initial value is unrealistically large.

To allow the crystal to relax, an iterative process is used. The function OptStrain() optimizes the strain energy for a single tetrahedral by allowing the atoms to rearrange into the lowest energy configuration. The model uses a black–white ordering scheme to relax the crystal lattice. It first allows the 0,0,0 Ga atoms to relax, then the 2/3 1/3 ½ Ga atoms, then the 0,0,5/8 N, and finally the 2/3 1/3 1/8 N. While this order is not optimal from a memory access perspective, it is necessary to enhance the convergence. If you were to relax all atoms from one side of the crystal to the other, the crystal would be displaced overall in the direction of your selections. These “waves” in the atom position would relocate the entire

crystal and prevent the crystal from converging to a minimum value in a reasonable period of time.

Each time OptStrain() is called the central atom in the tetrahedral is allowed to move in each of the six available directions in the Cartesian space and the energy is calculated. If the new energy is lower, the atom stays; if the new energy is higher, it moves back. This process is repeated 50 times for each atom. In the first version of the model, there was no limit to the movement per iteration and there were problems with local minima tricking the relaxation step.

In the initial crystal, certain atom positions are inherently unstable. Imagine three atoms perfectly aligned in a vertical row spaced closer than the equilibrium value. If you fix the two end atoms and let the center atom move, it will be unstable. If it moves one step right or left, it will end up permanently right or left of its original position. The problem is that it might move in the wrong direction on that first step. If its movement was not limited, it could end up completely outside the tetrahedral. Once that atom has reached its lowest energy with the corners fixed, OptStrain() is finished with that atom position. Once all of the atom positions in a lattice site have been optimized, OptStrain() moves on to the next lattice site. A full iteration consists of OptStrain() minimizing all the atom positions for all four lattice sites. The program continues iterations until the total change in strain energy for the entire crystal (total relaxation for that iteration) falls below a certain threshold value.

7.3 Implementing Strain

There are two possible ways to implement strain in the model. The first method is to have a setting within that Atom() class for a “none” nearest neighbour type. When the strain for that tetrahedra is calculated, the “none” atoms do not contribute any strain. This allows the atoms on the surface to move up or down with no restraint from above. The problem with this approach is that it allows the surface layers of atoms to form very unevenly. In

most actual thin films there are hundreds of layers of atoms, yet the model is limited for computational reasons to at most 32 layers (in most cases less than 16). To give a more accurate representation of the strain in a thin film, a biaxial strain method was used. In this case, the *a*-axis lattice parameter is fixed while the *c*-axis lattice parameter is varied to give the minimum energy. This should be a more accurate representation of the bulk of the thin film, rather than just the atoms near the surface. This method was initially performed by hand, which took many runs to get a value for the *c*-axis to the nearest 0.001Å.

In the Metropolis Monte Carlo simulations that took many days, it was infeasible to manually optimize the *c*-axis for each composition in the simulation. A method was needed to automatically relax the *c*-axis to its minimum strain value. The brute force method to simply try all the possible combinations proved to be computationally infeasible. For large strain differences in the *a*-axis, you would need to try thousands of possible *c*-axis values to find the minimum. A method was needed to speed the estimation up. The initial runs were for the InGaN system only and involved a simple linear estimation formula to guess a good starting point for the *c*-axis lattice parameter. From that starting point, a limited range was tried using brute force. The better the initial estimation, the less time it took to find the minimum *c*-axis value.

A simple polynomial regression was used to calculate the *c*-axis for the InGaN system. However, this approach did not work at all for the quaternary alloys. Because even the smallest runs had hundreds of possible compositions, a more general method for estimating the *c*-axis was needed. After significant trial and error, the method devised was to separately calculate the Poisson's ratio (according to the VFF model) for AlN GaN and InN and to apply a weighting function to determine a weighted average Poisson's ratio for the composition. This weighted average Poisson's ratio is used, along with the *a*-axis strain, to determine the initial estimate for the *c*-axis lattice parameter. The *c*-axis lattice parameter is adjusted over a small range to find the minimum strain energy. This method was incorporated in the VFF Monte Carlo model to allow batch calculation for an entire series of In compositions.

7.4 Debugging the VFF Computer Model

Because the correct function of the model was not obvious, a rigorous debugging process was used. The initial stages of debugging were done by hand to insure that the results being returned from the simulation were correct. The debugging process started with the most basic functions of the simulation. The data generation and reading functions are the easiest to test, as incorrect results are readily visible. The next tests looked at the AtomInit() function. Starting with simple data structures such as one In atom in a crystal of Ga atoms, all aspects of the Atom() structure were checked to make sure that the proper values were stored. Crystals with one In atom were checked in all possible locations to make sure that the neighbouring atoms' types, distances, and strain coefficients were correctly set across all boundaries in the periodic boundary condition.

The next step in the debugging process involved confirming that all of the calculations on the crystal were performed correctly. The initial tests were performed on a small crystal with an ordered structure. This made all of the spacings along the *c*-plane the same for all the atoms on that *c*-plane. The spacing of the *c*-planes was found to be consistent with the literature reported values of approximately 80% relaxation from bending with 20% relaxation from stretching. Next, using a single In atom in the GaN crystal, the strain calculation for the tetrahedral centered on the In atom was calculated by hand and found to agree with the function results. The atom was moved from its equilibrium value to confirm that it was, in fact, the minimum strain location. The strain was then calculated for the In atom in all of the 128 possible column III locations to make sure that the energy was consistent when crossing the periodic boundary condition.

Modifications to the OptStrain() function were helpful during the debugging process. The function was written to include a debugging mode to print out all calculations for one atom in the crystal. This debugging mode output all of the data from each move in the

optimization process. This allowed the discovery of the unstable atom positions and the fix of limiting total movement for each optimization step. The function also returned the total energy of the tetrahedral along with the stretching and bending components. The PrintAtomFull() function also aided debugging by allowing all information in the Atom() class to be printed out and checked at critical points in the code.

The final debugging step in the code involved insuring that the results were consistent for different crystal sizes. The code was written from the beginning with different crystal sizes in mind. However, it was necessary to test all of the same parts that were tested previously using different crystal sizes. The problem was that the data was inherently random, making it not always possible to directly compare. The final results were derived statistically from multiple runs. The runs were repeated until the new runs were considered statistically insignificant compared to the average using a t-test. As the total crystal size increased, these statistics also changed, which added uncertainty. In addition, the datasets themselves were not completely compatible because they were different sizes. This was solved by looking at patterns that could be relatively consistent between crystals of different sizes. Finally, the strain effect was fairly long-range. Although it became negligible at eight spacings away, it was not zero. This meant that for a single In atom in the center of the crystal (it actually did not matter exactly where due to the periodic boundary), the larger crystals had a lower calculated energy. This was because the calculation for the smaller crystal assumed that the strain at the edge of the 8x8x8 continued to infinity. The difference between the 16x16x16 and 32x32x32 was not as large as the difference between the 8x8x8 and the 16x16x16. Table 7-1 gives the calculated strain energies for different size crystals:

Crystal Size	8x8x8	16x16x16	32x32x32
Strain Energy 50%	1.90 kcal/mol	1.821	1.814

Table 7-1 Strain energies for various crystal sizes.

7.5 Comparison to Published Values

As soon as the bugs were worked out of the model, a series of runs calculating the VFF interaction energy for InGaN, AlGaN, and AlInN were generated. The model is closely based on Takayama's wurtzite VFF model; therefore, the values were compared to his results. Because both models were utilizing randomly generated crystals, the results were not expected to be exact, but in this case, they were very satisfactory. The results for crystal strain for InGaN are listed in Table 7-2:

	25% InGaN	50% InGaN	75% InGaN
Current Model	1.52 kcal/mol	1.90 kcal/mol	1.25 kcal/mol
Takayama W VFF	1.55 kcal/mol	1.95 kcal/mol	1.30 kcal/mol

Table 7-2 Comparison of Current Model to Published Results.

A full set of data points for all of the curves for the AlInGaN system are given in **Figure 7-3**. Given the random factors in both models, the results are close enough to confirm that the model is calculating the strain energy properly.

7.6 Optimizing performance of VFF model

Because the VFF algorithm will be run hundreds of thousands of times in the course of this study, the next logical step is to optimize the performance of the VFF calculation. The main setting that determines how long a given VFF run will take is the threshold strain change from iteration to iteration. When the strain change falls below the threshold, the simulation terminates. As can be seen in **Figure 7-4**, the strain energy of the VFF model starts out at a very high number and then rapidly decreases to a final value. A set of VFF runs using the same crystal was done for a different number of iterations and different threshold values. The plot of the VFF energies vs. the number of iterations is given in **Figure 7-5**. The values for the final energy are given for various threshold values in **Figure 7-6**.

It is interesting to note that for some crystals the minimum strain is reached at less than the maximum number of iterations. This is due to the fact that the VFF algorithm is a greedy algorithm and only looks at its immediate tetrahedral to determine the optimum positions. It is possible that the true optimal solution for the overall crystal is not the same positions as the optimal solution for the individual tetrahedra. This effect can be seen in **Figure 7-5**, where the minimum strain energy is achieved at 90 iterations and is lower than the steady value for 120-1000 iterations. The difference between the minima and the final steady state value is very small. In the example of **Figure 7-6**, the difference between the minimum value and the steady state value is 0.08 out of a total strain of 1308 (internal units). Based on this data, the threshold for convergence of the VFF model was set at 0.00001 units. The effects from the non-optimal solution, due to the greedy algorithm were never more than 0.01% of the total value and were ignored.

7.7 Calculating Phase Diagrams with the VFF Model

Using the results from the VFF computer model, it is possible to generate a theoretical phase diagram for the InGaN system. The VFF model can be used to generate a value of H for the regular solution model. The value for H can be calculated from the formula $H = \Omega x(1-x)$ and entropy term S can be calculated from the equation

$$S = X_a \ln(X_a) + X_b \ln(X_b).$$

The equation for Gibbs free energy

$$G = H - TS$$

can be calculated from these values. The strain energy H can be calculated either directly from the VFF model or by an approximation using the interaction parameter Ω . Because Ω varies over the composition range there are two methods to approximate H from Ω . The first method utilized by Ho and Stringfellow, Matsuoka and others is to calculate Ω from the VFF calculation for several compositions and apply the average Ω value over the whole InGaN phase diagram.

This method is not entirely accurate though, as Ω varies significantly with composition. Because Ga bonds are much stiffer than In bonds, it is much harder to strain a Ga crystal by adding an In atom than it is to strain a In crystal by adding a Ga atom. This effect can be seen clearly in the plot of Ω vs. composition as calculated from the VFF model. The free energy vs. composition curve calculated from the Ω value for each composition is given in **Figure 7-7**. These values of Ω were used to generate a free energy curve **Figure 7-8**. In this curve, the solubility for the In incorporation is significantly reduced while the solubility for the Ga incorporation is significantly increased from the curves generated using the average Ω value **Figure 7-9**. The resulting free energy curve for InGaN at 800°C shows an equilibrium solubility of In of around 2% with a spinodal point of 13%. Additional calculations at 1000°C showed the spinodal to be around 17%. These numbers are consistent with the published spinodal values from Takayama of 20% In at 1000°C **Figure 7-10**.

Another, more accurate, method that can be employed is to determine the value for H directly from the VFF model at every composition. This yields a phase diagram that shows less In incorporation on the Ga rich side than the 50% approximation method and more Ga incorporation on the In rich side. While this does not agree as well with experimental data, the spinodal point, which represents the upper limit on In incorporation is relatively unchanged.

When applying the VFF model to the quaternary system, the Al atoms are substituted in the crystal along with the proper α and β coefficients for the Atom() class. In this case, the calculation for the free energy curve is slightly different. The H value is taken from the VFF model as before, but the entropy is higher because of the additional configurations possible using the Al atoms. The Al contribution to the entropy is represented by an additional term of $X \ln(X)$ for the Al composition. For the curves used in this study, the Al composition is fixed for each curve and the In composition is varied. The $X \ln(X)$ contribution from the Al is significant and puts the curves on different scales. The expanded scale needed for the Al entropy factor makes the details of the individual curves impossible

to see. To make the curves more readable, they have been generated neglecting the Al contribution. This does not affect the conclusions from the graphs for two reasons. First, the $X \ln(X)$ component of the entropy is a constant value so it does not change the shape of the free energy curve; it merely shifts the curve by a constant value. Second, the absolute value of the free energy does not determine the phase behaviour, only the relative values. The equilibrium composition and spinodal are given by the first and second derivatives. Because the constant term from the $X \ln(X)$ factor disappears when taking the derivative, the equilibrium composition and the spinodal are unaffected by the Al entropy contribution.

Takayama et al. studied the AlInGaN crystal system [6] using a randomly generated VFF model. Takayama's experiments indicated that the spinodal limit for solubility of In in the AlInGaN crystal system ranged from 20% at 0% Al to less than 10% for 100% Al (**Figure 7-10**). Matsuoka [7] also reported a decrease in the solubility of In with the addition of Al in the AlInGaN system. Matsuoka calculated the spinodal limit to be 17% In for 0% Al decreasing to less than 10% for 100% Al (**Figure 7-11**). Neither Takayama or Matsuoka published the estimated equilibrium compositions for the AlInGaN system, but the equilibrium concentrations of In should be significantly below the spinodal limit.

Using the current VFF model, the spinodal limit at 800°C (which is a much more reasonable growth temperature for AlInGaN) is found to be approximately 13% In, decreasing slightly with increasing Al. The free energy curves for the AlInGaN system calculated using a randomly generated crystal are given in **Figure 7-12** and **Figure 7-13**. The equilibrium concentration decreases from 2% to 1% with the addition of 20% Al. The results for 1000°C are in agreement with Takayama, with solubilities of approximately 3% In. While these numbers are in agreement with other VFF work done previously, they do not agree completely with experimentally observed equilibrium solubilities and would seem to contradict the Strain Equilibrium In Incorporation Effect. However, all of these results are based from random crystals, where all configurations of atoms are considered equally likely.

The free energy curves for the randomly generated, strained VFF crystals are shown in **Figure 7-14** and **Figure 7-15**. It is interesting to note that while the overall free energy of the strained crystal is higher than for the relaxed crystal, the addition of the Al increases the equilibrium composition of In compared to the relaxed free energy curve. In the curves, the equilibrium In composition is slightly higher with additional Al, compared to reduced In with increasing Al in the relaxed curves. Another interesting effect is that in the strained crystals the spinodal point is not present. This is because the strain effect dominates the overall energy at higher In compositions. Assuming coherent strain, the strain energy for all compositions will always be higher for the separated phases due to the strain in the high In phase. This behaviour provides an explanation for the experimental data from Tabata and Teles [8] by showing that phase separation in the InGaN system is suppressed by the presence of biaxial strain.

Because MOCVD growth is a non-equilibrium process, it is not unusual to be able to grow InGaN with In compositions above the equilibrium composition. In the GaPN system, it has been shown that local surface conditions can enhance solubility by up to five times[9]. While it is extremely difficult to grow In compositions above the spinodal point, given enough additional energy from the gas phase, it is possible to grow compositions above the equilibrium. The hypothesis behind the Strain Equilibrium In Incorporation Effect is that the incorporation rate is affected by the strain. To test this hypothesis, the VFF model is applied to InGaN samples that are grown on GaN. Many of the proposed explanations for the additional In incorporation with increasing Al are based on the interaction, either in the gas phase, or on the surface, between the In and Al species. By simulating the In incorporation during the growth of InGaN, the gas conditions are identical for the layers with different In compositions. This means that the strain of the layers is the only difference.

7.8 Using VFF to Study the Compositional Pulling Effect

Experimental results have shown, both in the literature and in our own growth chamber, that the composition of InGaN when growing on a GaN or AlGaN substrate is not constant with growth time. The composition is lower initially and then increases to the bulk value when the growth exceeds the critical layer thickness. Because the InGaN samples on GaN are only affected by strain and the gas chemistry is constant, this effect cannot be from gas thermodynamics as has been suggested by Koukitu et al.[10] for the AlInGaN system. By comparing the strained and unstrained layers of the film, it is possible to isolate the strain effect on the growth of InGaN.

Data from Hiramatsu et al.[11] (Figure 7-16) for 20% InGaN grown on a layer of GaN shows that the InGaN film has a composition of 7% In below the critical layer thickness (**Figure 7-17**). Above the critical layer thickness, the composition of the InGaN is 20% In. Using the VFF model, it is possible to estimate the In composition from the change in strain per incorporated In atom (**Figure 4-18**). Starting with the 20% InGaN film that is fully relaxed, the Ω value was calculated to be 8.29 Kcal/mol. By using the formula for H from Ω , the differential strain energy was estimated at 6.54 Kcal/mol. The same calculation was made for the strain energy of the 7% layer strained to GaN. The differential strain energy for the 7% layer was found to be 9.42 Kcal/mol. Assuming the growth conditions are the same for each layer (which is a reasonable assumption because the layers are from the same run conditions), then the difference in composition is a direct result of reduced incorporation. To calculate the reduction in In incorporation, the Boltzmann probability is used. The Boltzmann distribution gives the probability of incorporation to be

$$I/I_0 = \exp(-dE/kT).$$

Assuming the rate of incorporation for the 20% bulk film is the base incorporation rate, the Boltzmann distribution predicts 7.0% InGaN for the initial strained layer based on the strain energies from the VFF model (**Figure 7-19**).

Using data from our lab taken during the critical layer study, the In composition for two runs with different growth times were analyzed. **Figure 7-20** and **Figure 7-21** show the off axis x-ray scans for 25 minutes and 105 minutes of growth, respectively. [12]. In this

data, the initial strained InGaN was 4.2% In strained to GaN. The InGaN layer relaxed to 6.2% In above the critical layer thickness. Using the VFF model to predict the strained composition **Figure 7-22**, the model predicts 4.3% In which is in excellent agreement with the experimental value.

7.9 Monte Carlo Method

The next step is to apply the Monte Carlo algorithm to the AlInGaN crystal system. Using the same method as the composition pulling study, the AlInGaN alloys were formed by adding In atoms using the Boltzmann probability. The In atoms were substituted for Ga atoms and the Monte Carlo algorithm was run until the desired number of In atoms for the crystal were generated. However, there were problems with this approach. The worst – and, as it turned out, fatal -- problem was that the deviation from one run to the next was extremely large. The deviations were much larger than for the randomly generated alloys even though they all started from an identical starting crystal. In **Figure 7-23** you can see the standard deviation from ten runs with increasing numbers of Al atoms. All ten crystals started with the same $\text{Al}_{25}\text{Ga}_{103}\text{N}$ crystal, yet had dramatically different energies after the addition of 30 In atoms. The strain energy difference was on the order of 1000 J/mol, which dwarfed the free energy minimum, which was on the order of several hundred J/mol.

The reason for such a large variation is that the sequential addition method follows just one path out of the billions of possible paths for the In atoms to be added. The same problem happens if the InGaN alloys are generated by randomly adding In atoms in sequence. Because the effects of each In atom are additive, one very poor choice (which is possible because the Monte Carlo is probabilistic) will affect all subsequent choices. In the randomly generated crystals, each atom has a probability that is independent of the others. While this gives a higher overall energy than the Monte Carlo algorithm, the energies for the individual atoms tend to even out and give a lower variation between runs.

The solution to this problem is to try to average all of the possible paths together. This will allow the higher and lower energy paths to even out. This is what effectively happens with a pure random crystal. However, in a pure random crystal, the different paths are all equally likely. A basic Monte Carlo algorithm randomly generates crystal configurations (or states), but it averages them using a probability distribution function. Typically, the distribution function is a Boltzmann distribution, but not always. By summing the contributions of the randomly generated states using the probability distribution function, it is possible to get highly accurate and repeatable results.

While the basic Monte Carlo algorithm can give good results, it is not very efficient. At low temperatures, the Boltzmann distribution will result in a small subset of states that will contribute the majority of the energy, while a large number of unfavourable states will contribute very little to the final result. Randomly selecting the states means that the majority of the algorithm's time is spent generating states that do not contribute significantly to the final result. To get around this problem, improved Monte Carlo algorithms have been developed. In the improved Monte Carlo algorithms, the system is allowed to transition between states, depending on the energy between the states. Instead of averaging all of the generated states, the system is sampled at various times. With the transition probabilities dependent on the energies, this should result in the lower energy states being sampled more often than the higher energy states. The idea behind the improved Monte Carlo algorithms is that the system will spend more of its time in the lower energy states where the contribution is largest.

The wurtzite VFF models, as originally developed, rely on randomly generated crystals for the starting point. Although this is a reasonable approximation, it does not take into account that some crystal configurations are more energetically favourable than others and hence more likely to occur. The cluster variation model uses statistical methods to estimate the contribution from the differently strained tetrahedra, but the overestimation of the strain energy from the lack of relaxation mitigates the improvement in the overall strain. An extension to the wurtzite VFF model to account for the relative probabilities of each

configuration can be implemented using the Monte Carlo Method. The Monte Carlo method has been used successfully with the VFF model to study the effects of interstitial atoms[4], initial growth [3], high mismatch heteroepitaxy[13], and mismatch relaxation[14].

The Monte Carlo algorithm used in the current model is the Metropolis Monte Carlo. The Metropolis Monte Carlo is implemented in the current model by allowing atoms to switch positions and calculating the strain energy. The atom types for two random atom positions will be swapped and the new distances and constants for the new neighbours will be calculated. After the crystal is initialized with the swapped atoms, the relaxation process is started all over. When the crystal is relaxed, the energy is compared with the energy for the previous relaxed configuration. If the new strain energy is less than the old strain energy, the swap is kept. If the new strain energy is greater, the Metropolis Monte Carlo method calculates the probability of the swap occurring based on the energy change using the Boltzmann distribution. A random number is generated and compared to this probability. If the random number is smaller than the probability, then the atoms stay put, if it is larger the atoms are swapped back (**Figure 7-24**,**Figure 7-25**,**Figure 7-26**,**Figure 7-27**). After a certain number of iterations, the resulting energy converges on an equilibrium value that includes the entropy factor from the Metropolis Monte Carlo method.

In this case, the quantity that we are trying to study is the energy contribution to the system arising from the strain of the bonds of the crystal. Viewing this energy as a sum of its parts, each subpart of the total energy would be the strain of a single configuration of the atoms in the crystal, multiplied by its probability. Each different crystal arrangement or configuration is considered a separate state. In the case of the smallest crystal with 128 total column III atoms, the total number of possible states is $128!/64!64!$ This is a very large number of possible states and it would be impossible to check them all. The goal of a Metropolis Monte Carlo algorithm is to sample a subset of the total number of states in order to obtain a representative value for the whole.

For a Metropolis Monte Carlo method to be valid, it must sample the proper states. If the simulation is not set up properly, it will not yield valid results. The first thing needed for a Metropolis Monte Carlo simulation is an estimator. In the case of the current model, the estimator is the strain energy of the crystal. The estimator must have the property that the more states that are sampled, the more accurate the result. Second, the probability of a transition from one state to another can only depend on the final and starting state. Third, starting with any given state it must be possible (given enough transitions) to reach another state in the system. Finally, the probability of a given final state must depend on the probabilities of the other states transitioning to it. This last condition is called detailed balance.

The Metropolis Monte Carlo algorithm was originally developed for use with spin states. In the case of spins, each state is the collection of spins for every atom in the crystal and each transition represents the flipping of a spin. The energy of the system is a function of the states of the spins at each location in the crystal. The states with identical spin states are indistinguishable which satisfies the requirement that the transitions depend on the initial and final states. It is easy to show that it is possible to get from any set of spins to any other set by flipping one spin at a time. Because the transition from and to each state is a clearly defined event, it is also possible to prove the final condition of detailed balance.

The Metropolis Monte Carlo algorithm can be applied to atoms in a crystal. In the case of the current model, the different atom configurations represent the states. Because the crystal in the VFF model is fully relaxed, two crystals with identical atom configurations should have the same energy and be indistinguishable. Modifying the composition of one atom at a time would change the composition of the alloy. To get around this problem, a pair of atoms is swapped. By swapping atoms, the composition of the crystal is unaffected. It is possible to generate every possible configuration of a given composition by swapping two atoms at a time. Because the energy of the crystal is dependent on the configuration of the atoms in the crystal, regardless of how they got there, the transition energy (and probability)

only depend on the initial and final configurations. In the Metropolis Monte Carlo algorithm, transition probabilities are given by the equation:

$$P_{1-2} = \exp(-(E_2 - E_1)/kT); \text{ when the new energy is greater than the old energy}$$

$$P_{1-2} = 1.0; \quad \text{when the new energy is less than the old energy}$$

Transitions from low to high energy are less likely than transitions from high to low energy, which always occur. A low energy configuration will have higher probabilities of neighbouring configurations (neighbouring meaning that the configurations can be reached with a single swap of atoms) transitioning to it. Because the probability of transitioning away from a low energy configuration is lower, there will be a higher probability for the atom to be there. If a configuration has a high energy, the probability of neighbouring configurations transitioning to it will be lower, resulting in a lower probability of finding the crystal in that configuration. Because each configuration has a clearly defined energy, the overall probability of that configuration occurring depends on the energy of that configuration.

7.10 Testing Metropolis Monte Carlo Simulation for Correctness

Once the theoretical basis for the Metropolis Monte Carlo algorithm using atom positions is established, the final conditions for a valid model can be tested. This condition is called importance sampling and in short, it means that the final probabilities of each state follow a Boltzmann distribution depending on the energy of that state. While, in theory, the Boltzmann probability guarantees that the final result will follow a Boltzmann distribution, it would be beneficial to insure that the VFF Metropolis Monte Carlo behaves appropriately.

To test the VFF Metropolis Monte Carlo algorithm, a dedicated simulation was run. The first part was to generate a crystal with all Ga atoms except for one Al in the center of the crystal and one In atom that was moved from site to site. The VFF program was run with

the In atom in each of the 127 possible sites (not including the Al site) and the relaxed strain energy of the crystal was recorded. These result represented the number of possible states of the system with the Al in the center atom. The VFF model has a periodic boundary condition. This means that the strain energy of a state with the Al near the center and another state with the Al near an edge would be identical (this was tested in debugging). For a given relative In and Al position pair, there are 128 possible states with this same pairing, all of which will have the same overall energy. Therefore, as long as the relative positions of the In and Al atoms are the same, all 128 possibilities of this arrangement can be considered indistinguishable.

This data was pulled into another program, which was designed to test the Metropolis Monte Carlo implementation in the VFF Metropolis Monte Carlo model. The model operated by starting the In atom at a random column III lattice site within the crystal. Beginning with the current lattice site, the In atom was swapped with another randomly generated site. The current strain energy of the crystal was saved, the atoms were swapped, and the energy was recalculated. The old and new energies were compared and a transition probability was assigned. If the new energy was lower, the swap was kept. If the new energy was higher then the transition probability was given by the formula:

$$P_{1-2} = \exp(-(E_2 - E_1)/kT)$$

The In atom was swapped 128 times (although some of those swaps were energetically unfeasible and were reversed). This number represented the possible number of In configurations, thereby giving each one a chance to occur. This method of swapping gave the probability that the In atom would test against every possible atom site once on average and was called a sweep of the crystal lattice. The number of sweeps was increased from 1-32 and a long series of 256k sweeps was performed to represent the long-term equilibrium. While performing these experiments, several problems came up. While they might seem simple, they were actually quite critical when using the Metropolis Monte Carlo method.

The first problem involved generating good random numbers. The built in random number generator in the compiler used a linear congruential algorithm. This is a popular

algorithm because it is simple to use and gives a good distribution over its output range. Its main drawback is that from a given seed you will get the same series of numbers (this is more of a problem for cryptography). The standard way of seeding a random number generator is to get the value of the timestamp from the operating system. In the Windows XP machine that the experiments were run on, the timestamp is the lower 32 bits of the total system time (in ms). (As an aside, in the Windows 95 and 98 operating systems the counter only had 32 bits total, guaranteeing a crash every 49.7 days). The problem was that seeding the random number generator every time it was used resulted in the program running so fast that there was a chance it might generate repeat cycles if the program were to finish before the operating system timestamp got renewed. The solution to this was to have a unique seed for every sweep and depend on the distribution of the random number generator. Long runs of 16 million swaps (purely random with no calculations) were performed to check the accuracy of the random number generator. These tests resulted in an even distribution among the various states with no statistically significant deviations.

The next problem that came up was with the formula for the transition probabilities in the Metropolis Monte Carlo algorithm. When adding atoms to a strained crystal, almost all of the possible sites for addition of the In atom result in an increased strain energy. As a result, the majority of the probabilities for the state changes were very low. While having low probabilities does not violate the requirements of a Monte Carlo simulation, it does hurt the performance. If, for example, the probabilities were on the order of 1/1000, then 99.9% percent of the time, the model would be making swaps that got reversed. The ideal situation is one where the maximum probability is close to 1 and all other probabilities are lower. This will give the maximum efficiency for the simulation while still maintaining the requirements of the Metropolis Monte Carlo algorithm.

In the test run, there were only 127 possible energy values. This meant that the maximum energy change could be known beforehand. This allowed the Boltzmann distribution to be calculated beforehand. The results of the experiments are shown in **Figure 7-28**, **Figure 7-29**, **Figure 7-30**, and **Figure 7-31** showing the distribution of the states that

the final system was in for 4096 sweeps at a temperature of 300K. During the simulation, snapshots were taken at the end of each sweep and the location of the In atom was noted. The plots show the distribution of the In atoms vs. strain energy of the different crystal sites. As can clearly be seen in the 2048 sweep simulation, the distribution of the final states followed the expected Boltzmann distribution with a high degree of correlation. The simulation was run using two different swapping algorithms. The initial swapping algorithm used a correlated jumping method that only allowed swaps between nearest neighbours. The second swapping algorithm allowed random swaps between all column III sites. Because the data was consistent between the two methods and the random method converged slightly faster than the correlated method, the rest of the simulations used the random jumping method.

Once all of these conditions were met, the Metropolis Monte Carlo simulation was running properly. However, because the goal of the Metropolis Monte Carlo is not to test every possibility, there needed to be a way to determine how long the model needed to run. In the test run, this was made significantly easier by knowing in advance all of the possible energy states. The results of the $\text{Al}_1\text{In}_1\text{Ga}_{126}\text{N}$ Metropolis Monte Carlo simulation did not change for more than 2048 sweeps. Therefore, it was assumed that at 2048 sweeps, the simulation had converged. With the assumption that the 2048 sweep run had reached equilibrium, runs with less than 2048 sweeps were compared to the results for the 2048 sweeps. From the results in **Figure 7-32**, it would appear that somewhere between 24 and 32 sweeps were needed for the $\text{Al}_1\text{In}_1\text{Ga}_{126}\text{N}$ Metropolis Monte Carlo simulation to converge. Although it would be expected that crystals with more atoms and more configurations would take longer to converge, 25 sweeps should be considered a minimum for convergence. Therefore, all subsequent experiments the simulations were run for at least 25 sweeps.

7.11 Preferential Lattice Sites for In and Al

In addition to determining the number of sweeps necessary for the convergence of the simulation, the $\text{Al}_1\text{In}_1\text{Ga}_{126}\text{N}$ Metropolis Monte Carlo simulation gave interesting information regarding the strain between the atoms. The VFF model used to generate the data for the $\text{Al}_1\text{In}_1\text{Ga}_{126}\text{N}$ Metropolis Monte Carlo simulation was also used to explore the least and most favourable sites for In incorporation. According to the VFF model, the minimum energy site for In incorporation with the Al atom at position 4 4 4 are the next immediate column III sites. There was a slight preference for those column III sites adjacent to the *c*-axis N (bonded to the Al) vs. the *a*-axis N. This is what was initially expected from the preliminary two-dimensional modeling. The most energetically unfavourable In site was the 2 4 4 and 6 4 4 site which were directly above and below the Al atom along the *c*-plane

Figure 7-33.

This was not the result expected from the two-dimensional preliminary modeling. In the two-dimensional modeling, the overall energy of the crystal was directly proportional to the distance of separation between the Al and In atoms. However, in the hexagonal model, the energy was determined not by distance of separation, but by the number of bonds. The minimum energy lattice sites represented the shortest path along the crystal bonds between the Al atom and the In atom. The 2 4 4 and 6 4 4 sites did not represent the longest path; however they did represent the maximum number of bonds along the shorter path. The path between the 4 4 4 and 2 4 4 atom location traveled along three identical length paths. Assuming that the strain was transferred evenly along the three paths, this represented the maximum number of distorted bonds. The conclusion that the strain in the crystal was dependent on the number of distorted bonds is consistent with the operation of the VFF model.

7.12 Temperature Effects on the Metropolis Monte Carlo Simulation

The data used to determine the convergence of the Metropolis Monte Carlo method for the $\text{Al}_1\text{In}_1\text{Ga}_{126}\text{N}$ alloy were all taken at 300K, as the Boltzmann distribution was most

pronounced at that temperature. Additional runs were performed at 300°C, 500°C, 700°C, 800°C, 900°C, 1000°C, 1200°C, and 1400°C. The data from those runs is presented in **Figure 7-34**, **Figure 7-35**, **Figure 7-36**, **Figure 7-37**, and **Figure 7-38**. As the temperatures increased, the curves became less correlated and more random due to the increase in thermal energy available for transitions to less energetically favourable states. Exponential trendlines for the Boltzmann distribution were plotted for each curve. The trendlines for low temperature showed a strong correlation factor of approximately 0.95.

If the correlation coefficient is plotted vs. temperature, an interesting effect is noted. The plot of correlation coefficient vs. temperature is gradually decreasing as temperature increases. However, there is a discontinuity in the plot at approximately 900°C (**Figure 7-39**). The Metropolis Monte Carlo simulation was repeated numerous times with both random and correlated jumps and the discontinuity was present in all of the datasets.

Regardless of whether or not the discontinuity in the correlation coefficient represents a second order effect, it is interesting nonetheless. The temperature of the discontinuity corresponds to the disappearance of the Strain Equilibrium In Incorporation Effect seen at temperatures above 850°C. The origin of the discontinuity is not completely clear from the model. The thermal energy available at 900°C does not correspond to any of the individual jumps between neighbouring sites. It is likely that the thermal energy at 900°C is sufficient to allow the In atom to jump “uphill” towards the higher energy sites. At lower energies the In atoms would be limited to moving “downhill” in strain from their current positions, therefore limiting the number of possible sites for the In atoms to be found in the snapshots that are taken at the end of each sweep. One possibility is that the thermal energy available at 900°C allows the probability of the In atoms to jump over the “activation barrier” of the higher energy sites to become a significant portion of the total number of jumps. In any case, the data represents an interesting correlation with the experimental data of the Strain Equilibrium In Incorporation Effect, disappearing above 850°C.

It is possible to accurately predict the convergence of the $\text{Al}_1\text{In}_1\text{Ga}_{126}\text{N}$ Metropolis Monte Carlo simulation, but this is only because all of the possible states are known. In cases where the number of possible states is impossible to calculate beforehand, it is necessary to come up with an alternative method to determine convergence. For systems with a large number of possibilities, a modified version of the autocorrelation function is used. The basic idea is that the changes in the strain energy for each transition are integrated numerically and the result is plotted. When the Metropolis Monte Carlo simulation has not converged, the integrated changes in strain are primarily in the same direction. When the function converges, then the mass balance equation should be in equilibrium and the energies of the atoms transitioning should even out to zero. This can be seen in **Figure 7-40** for $\text{Al}_{25}\text{In}_{25}\text{Ga}_{78}\text{N}$ crystal as it converges. The top plot shows the absolute value of the strain energy as a function of the number of sweeps. The bottom plot shows the integrated value for the energies of all of the transitions made in the crystal per sweep. As can be seen in **Figure 7-40**, the value of the integrated differential strain is initially negative and oscillating. After about ten sweeps, the value of the integrated differential strain oscillates between positive and negative values but spends roughly even amounts of time positive and negative. When the area above zero and below zero is roughly equal, there are no more long-term changes in the strain energy. The results from sampling the energy of the crystal will be valid from this point on. For smaller compositions such as $\text{Al}_5\text{In}_5\text{Ga}_{118}\text{N}$, the sample converges almost immediately (**Figure 7-41**). The plot of integrated differential strain is very useful for determining where to start sampling for each crystal composition.

7.13 VFF Metropolis Monte Carlo Method for AlInGaN

For the Metropolis Monte Carlo implementation, the program starts with an initial crystal and then adds In atoms one at a time using a Boltzmann probability. The initial crystal can either be randomly generated or read in from a file. In most cases, the crystal is read in from a file to allow for more consistent runs, even though experiments showed that once the crystal had converged, there was almost no difference in the final result. Once the

initial crystal is either read in or generated, the a -axis and c -axis values are calculated. For relaxed crystals, this is simply done using Vegards law. However, for strained crystals, the Poisson's estimation as described above is used. The crystal can be strained to any a -axis (or even c -axis) value desired.

Once the a -axis and c -axis values have been calculated, the bulk of the Metropolis Monte Carlo simulation is executed. The crystal is sampled for a number of sweeps with datapoints being taken at the end of each sweep and an integrated differential being calculated during each sweep. These numbers are output to a file such that there is a listing of values for each composition datapoint with separate files for the integrated differential strain and total strain values. These datapoints for each sweep are necessary to determine when the crystal is converged and which datapoints to average to get the final value for that composition.

During each sweep, the program is looped either 128 or 1024 times, depending on the crystal size. For each loop, random atoms are swapped (making sure that the atoms swapped are not the same type). After the atoms are swapped the function SingleAtomInit() is used to reset all of the nearest neighbour information in the Atom() class. Once the Atom() class is configured properly, the new strain is calculated. The Metropolis Monte Carlo algorithm is then applied using the energy difference to calculate a swap probability for the atoms. Finally, a random number is generated and compared with the swap probability. If the random number is more, the atoms are swapped back. Otherwise, the swap is left in place. In the initial simulation runs, there was an error in the Metropolis Monte Carlo implementation. This error resulted in the predicted swap probability being divided by a small constant. Further testing showed that the results were not significantly changed by this mistake. Because the mistake had the greatest effect on the higher energy transitions, the contribution of the mistake to the final result was negligible.

At the end of the desired number of sweeps, one or more In atoms is added to the crystal to change the composition. The In atoms are added using the Boltzmann probability.

The In atom is substituted for a Ga atom and the resulting Boltzmann probability is calculated. This is repeated until there is a successful addition. Unlike in the previous VFF Metropolis Monte Carlo loop, the addition of In atoms is almost always energetically unfavourable. The algorithm used in the VFF Metropolis Monte Carlo loop is not at all sufficient here, as the energy is so unfavourable that the program effectively stops because the probability is so low that the event will almost never occur.

In order to solve this problem, a method from my car's fuel injection computer was used. The method is to have both a short- and long-term trim. One advantage here is that since the strain is increasing, all of the probabilities are too low rather than too high. This means material balance of the Monte Carlo algorithm is not an issue, only the model's computing performance. The short-term trim is activated whenever the probability is less than 0.05 and multiplies the SwapProbShortMod number by a small fixed correction factor. At the end of ten attempts the SwapProbLongMod number is calculated to make the average swap probability fall around 0.10. This gives sufficient buffer so that the swap probability does not exceed 1.0 and violate the material balance. The long-term SwapProbLongMod is kept between cycles, whereas the short term SwapProbShortMod is reset each time. While not the most elegant solution, it is effective and gets the probability down to a reasonable number quickly. This is not a general solution, however, as it is only designed to correct for low probabilities. This calculation is not strictly necessary, because the atom is run through many sweeps of the Metropolis Monte Carlo algorithm before the data is sampled. However, by applying the Boltzmann probability to the addition process, the additional In atom is placed into a low energy configuration from the beginning. This allows for much faster convergence of the simulation with the new composition.

The amount of computation involved to calculate the Metropolis Monte Carlo VFF algorithm for a series of compositions is significant. For the smaller crystal size, the runs consisted of 20 compositions. For each composition, the Metropolis Monte Carlo algorithm was run for 50 sweeps. In each of the 50 sweeps, the crystal was swapped 128 times. The number 128 comes from the number of column III sites. While there are 256 atoms total in

the smaller crystal, the column V sites are all identical, so there is no change in state from swapping them. There is also no mechanism for swapping a column III atom for a column V atom, as it would be extremely unfavourable. For each swap, the crystal was optimized, atoms were swapped, the crystal was optimized again and the Metropolis Monte Carlo calculation was performed. The optimization step involves typically around 100 iterations, with each iteration performing several hundred calculations for each of the 256 atoms in the crystal. Typical runtimes were on the order of a day. For larger crystals, the problem is even worse. These consisted of 80 compositions with each composition limited to 10 sweeps. Each of the sweeps involved 1024 swaps and each swap running hundreds of iterations over 2048 atom sites. The number of sweeps was limited by computational power and did not achieve full convergence. Even with this limited number of sweeps, the larger crystal runs took approximately 20 days on a 3.2 GHz machine.

The AlInGaN simulations were run to test the Strain Equilibrium In Incorporation Effect. Under those same conditions, the temperature was approximately 800°C and the Al composition varied from 8% to 23% AlN while the In incorporation increased from 6% to 9% InN. To simulate the same conditions, a set of runs was made with 0 Al, 10 Al and 25 Al atoms, respectively. The 0 Al atom run would represent the pure InGaN system and was included as a baseline. The 10 Al atom run would represent approximately 8% AlN while the 25 Al atom run would represent approximately 20% AlN. The theory was that, if the strain equilibrium effect was present in the model results, then the In incorporation should increase by 2 atoms and 5 atoms, respectively, for the 10 Al atom and 25 Al atom curves.

The Metropolis Monte Carlo simulation was run for 25 sweeps at compositions of 0 Al, 10 Al and 25 Al. The number of In atoms was varied from 1 to 20 and the strain energies were recorded. The total size of the crystal was 128 atoms. The strain energies were converted into free energy curves using the method described in Chapter 6. The results are shown in **Figure 7-42** and **Figure 7-43**. The baseline 0 Al curve shows an equilibrium In composition of approximately 2.5 In atoms with the free energy increasing rapidly above that composition. For the 10 Al atoms run, the free energy curve shows a composition slightly

greater than 3 In atoms with a lower slope than the 0 Al curve. The 25 Al atoms run shows a free energy curve with an equilibrium In composition of 7 In atoms. The equilibrium In concentration increased from 2.5 atoms to 7 atoms with the additional 25 Al atoms. This is in good agreement with the SIMS data showing a 5:1 Al:In incorporation ratio.

Figure 7-44 and **Figure 7-45** show the results for the Metropolis Monte Carlo simulation for the larger crystal size of 16x16x16, or 1024 column III (2048 total atoms). The simulation was run at 800°C for only 10 sweeps. Although this is less than the minimum number for convergence, each of the curves was “pre relaxed,” allowing the initial AlInGaN composition to be relaxed for 10 sweeps. This allows some of the crystal to relax prior to the addition of the In, thereby limiting the necessary relaxation of the crystal with each additional In atom. The curves show the Strain Equilibrium In Incorporation Effect, but it is not as large as the 128 atom crystals. The equilibrium In composition for the 0 Al case is approximately 22 In atoms, while the 200 Al curve shows an equilibrium composition of 44 In atoms. This is only about half of the expected 1:5 ratio. The cause of this is incomplete relaxation of the crystal given the limited number of sweeps. Each run took approximately 20 days on a 3.2GHz machine.

To test that the discrepancy between the 1024 atom data and the Strain Equilibrium In Incorporation Effect is, in fact, due to the limited number of sweeps, an additional set of simulations was performed on the 25 Al curve. The simulation took the same data from the 25 Al run with 128 atoms, but ran the simulation for different numbers of sweeps. The simulation was run with the algorithm only applied to the addition of In atoms, the Metropolis Monte Carlo applied for five sweeps and the Metropolis Monte Carlo algorithm applied for 25 sweeps. As it can be seen in **Figure 7-46** and **Figure 7-47**, the curve for the algorithm on In addition only was very close to the random InAlGaN curve for 25 Al, while the 25 sweep Metropolis Monte Carlo was identical to the previous Metropolis Monte Carlo simulation. However, the five sweep Metropolis Monte Carlo algorithm had a significantly lower equilibrium In composition than the 25 sweep simulations. The addition only curve had an equilibrium composition of 2.5 In atoms, while the five sweep Metropolis Monte

Carlo simulation had an equilibrium composition of 5.0 atoms. The 25 sweep Metropolis Monte Carlo simulation had an equilibrium composition of 7.0 In atoms. This shows that, with a limited number of sweeps, the Strain Equilibrium In Incorporation Effect is reduced. This is consistent with the differences in equilibrium In compositions between the 128 atom simulations and the 1024 atom simulations.

Another interesting property of the Strain Equilibrium In Incorporation Effect is its disappearance at temperatures above 850°C. To study whether the model can predict the disappearance of the effect, additional simulations were run at higher temperatures. The Metropolis Monte Carlo simulation was run for 128 atoms at 1000°C for 25 sweeps. The compositions and number of sweeps were identical to the previous set of simulation runs. The results for the simulations can be seen in **Figure 7-48** and **Figure 7-49**. The curves for zero Al, 10 Al, and 25 Al atoms all show increased equilibrium In incorporation from the previous simulations at 800°C. The equilibrium composition for zero Al is 5.0 In atoms at 1000°C compared with 2.5 at 800°C. For the 25 Al atom simulation, the equilibrium In composition is now at 10 In compared to 7 In at 800°C. While the equilibrium In composition for all of the alloys has increased, the Strain Equilibrium Effect is relatively constant to slightly higher (4.5 In atoms to 5 In atoms). This would indicate that the model is unable to predict the disappearance of the Strain Equilibrium Effect from the strain in the crystal.

The Metropolis Monte Carlo simulation is based on real events in the crystal. The strain energy for incorporation is based on the elastic constants of the real material, while the swapping events represent diffusion in the alloy. While the strain in the crystal is relatively unchanged with higher temperatures, the diffusion of the atoms almost certainly is. In the AlInGaN crystal, the surface behaviour of the crystal is dominated by the high desorption coefficient. At higher temperatures, the atoms will have a shorter residence time on the surface. The desorption rate for the In atoms on the surface can be calculated using the In composition data from the InGaN runs performed in Chapter 4. Given the growth rate, gas composition and final In composition, the desorption rate for the In atoms can be calculated.

The residence time for Ga atoms on the surface of GaN has been calculated to be anywhere from 0.6 - 5 seconds for normal growth temperatures[15]. Assuming a similar time for In atoms on the surface of 1 second, it is possible to get actual numbers for the desorption rate. While these numbers are probably too low, the following comparison is still valid. From the desorption rate curve given in **Figure 7-50**, the activation energy for desorption of In from InGaN for 0 sccm H₂ conditions is approximately 2.6eV. This agrees closely with published values[16]. Taking the activation energy for In of 0.7eV from the literature[17], it is possible to compare the relative diffusion rates and desorption rates of In with temperature. Given the absence of an absolute value for In surface diffusion, a ratio of 1000 diffusion events per desorption events at 800°C is set. Using these boundary conditions, the plot of the ratio of diffusion events to desorption events is given in **Figure 7-51**. The ratio of diffusion to desorption events decreases from 1000:1 at 800°C to 140:1 at 900°C. This represents almost an order of magnitude decrease in the number of diffusion events per atom. While these numbers may be suspect (the ratio might be 200,000 at 800°C), the trend with temperature depends only on the activation ratios so the relative effect should be the same for any starting point.

Applying this decrease to the Metropolis Monte Carlo simulation would be equivalent to reducing the number of sweeps for each In addition event. As it was shown in **Figure 7-46** and **Figure 7-47**, this reduces the Strain Equilibrium In Incorporation Effect. Given the dramatic decrease in the diffusion to desorption ratio, it would be equivalent to reducing the number of sweeps from 20 to 3. According to the simulation results, this would result in a strong decrease in the In Incorporation Effect.

In conclusion, the Metropolis Monte Carlo simulation has shown that the Strain Equilibrium In Incorporation Effect can be explained by the increase in In incorporation due to the strain in the system. It can also be concluded that the relative ratio of surface diffusion to desorption can have a strong effect on the Strain Equilibrium In incorporation effect.

7.14 References

1. Grosse, F. and J. Neugebauer, *Limits and accuracy of valence force field models for In_xGa_{1-x}N alloys*. Physical Review B, 2001. **6308**(8): p. art. no.-085207.
2. Maroudas, D., L.A. Zepeda-Ruiz, and W.H. Weinberg, *Interfacial stability and misfit dislocation formation in InAs/GaAs(110) heteroepitaxy*. Surface Science, 1998. **411**(3): p. L865-L871.
3. Rouhani, M.D., et al., *Strained Semiconductor Structures - Simulation of the 1st-Stages of the Growth*. Surface Science, 1992. **276**(1-3): p. 109-121.
4. Rouhani, M.D., et al., *Monte Carlo simulation of the effect of interstitial atoms interaction on the heteroepitaxial growth of compound semiconductors*. Materials Science and Engineering B-Solid State Materials for Advanced Technology, 1997. **44**(1-3): p. 82-86.
5. Koleske, D.D., et al., *Growth model for GaN with comparison to structural, optical, and electrical properties*. Journal of Applied Physics, 1998. **84**(4): p. 1998-2010.
6. Takayama, T., et al., *Analysis of phase-separation region in wurtzite group III nitride quaternary material system using modified valence force field model*. Journal of Crystal Growth, 2001. **222**(1-2): p. 29-37.
7. Matsuoka, T., *Calculation of unstable mixing region in wurtzite In_{1-x-y}Ga_xAl_yN*. Applied Physics Letters, 1997. **71**(1): p. 105-106.
8. Tabata, A., et al., *Phase separation suppression in InGaN epitaxial layers due to biaxial strain*. Applied Physics Letters, 2002. **80**(5): p. 769-771.
9. Zhang, S.B. and A. Zunger, *Surface-reconstruction-enhanced solubility of N, P, As, and Sb in III-V semiconductors*. Applied Physics Letters, 1997. **71**(5): p. 677-679.
10. Koukitu, A., Y. Kumagai, and H. Seki, *Thermodynamic analysis of the MOVPE growth of InGaAlN quaternary alloy*. Journal of Crystal Growth, 2000. **221**: p. 743-750.
11. Hiramatsu, K., et al., *The composition pulling effect in MOVPE grown InGaN on GaN and AlGaN and its TEM characterization*. Mrs Internet Journal of Nitride Semiconductor Research, 1997. **2**(6).

12. Reed, M.J., et al., *Critical layer thickness determination of GaN/InGaN/GaN double heterostructures*. Applied Physics Letters, 2000. **77**(25): p. 4121-4123.
13. Rouhani, M.D., et al., *Surface morphology due to enhanced migration in heteroepitaxial growth of compound semiconductors*. Materials Science and Engineering B-Solid State Materials for Advanced Technology, 1996. **37**(1-3): p. 25-29.
14. Rouhani, M.D., R. Malek, and D. Esteve, *Monte Carlo simulation of mismatch relaxation and island coalescence during heteroepitaxial growth*. Thin Solid Films, 1998. **318**(1-2): p. 61-64.
15. Guha, S., N.A. Bojarczuk, and D.W. Kisker, *Surface lifetimes of Ga and growth behavior on GaN(0001) surfaces during molecular beam epitaxy*. Applied Physics Letters, 1996. **69**(19): p. 2879-2881.
16. Stanley, I., G. Coleiny, and R. Venkat, *Theoretical study of In desorption and segregation kinetics in MBE growth of InGaAs and InGaN*. Journal of Crystal Growth, 2003. **251**(1-4): p. 23-28.
17. Neugebauer, J., et al., *Adatom kinetics on and below the surface: The existence of a new diffusion channel*. Physical Review Letters, 2003. **90**(5).

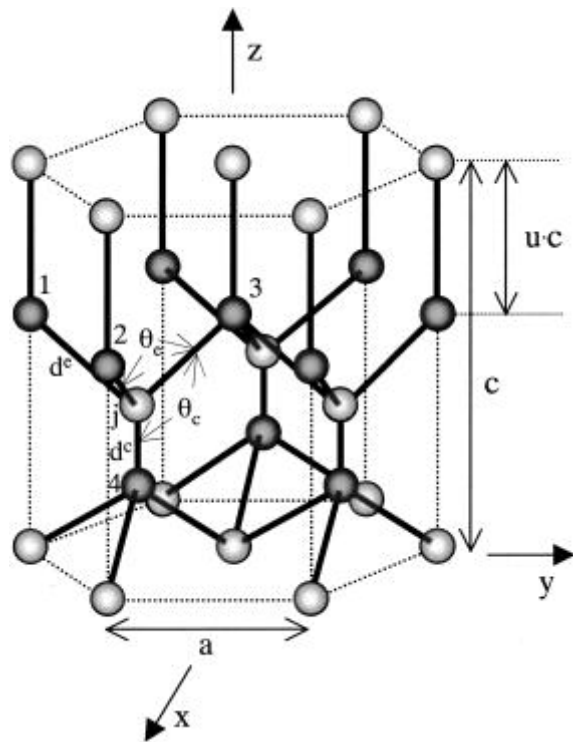


Figure 7-1 Diagram of the stretching and bending moments for the wurtzite GaN tetrahedra. Note that the distances in the a and c directions are not equal. Likewise, the angles between the a - a and a - c bonds are not equal either. This makes the calculations more difficult. Figure from Takayama.

$$\begin{aligned}
U_j = & \sum_{i=1}^3 (3\alpha_{ji}/8d^3_{ji}{}^2) (\mathbf{r}_{ji}{}^2 - d^e_{ji}{}^2) + (3\alpha_{j4}/8d^c_{j4}{}^2) (\mathbf{r}_{j4}{}^2 - d^c_{j4}{}^2)^2 + \\
& 2 \sum_{i=1}^3 \left\{ \sum_{k>i}^3 (3\beta_{ijk}/8d^e_{ji}d^e_{jk}) (\mathbf{r}_{ji}\mathbf{r}_{jk} - d^e_{ji}d^e_{jk} \cos \theta^e_{ijk})^2 \right\} + \\
& 2 \sum_{i=1}^3 (3\beta_{ij4}/8d^e_{ji}d^c_{j4}) (\mathbf{r}_{ji}\mathbf{r}_{j4} - d^e_{ji}d^c_{j4} \cos \theta^c_{ij4})^2.
\end{aligned}$$

Figure 7-2 Formula for the total energy for the wurtzite VFF model. Notice that the c axis components and a axis components have been calculated separately. This is essentially the algorithm used for the current model; however, the axes have been transformed to a orthogonal axis system to allow the use of dot products instead of the slower $\cos()$ functions. Figure from Takayama.

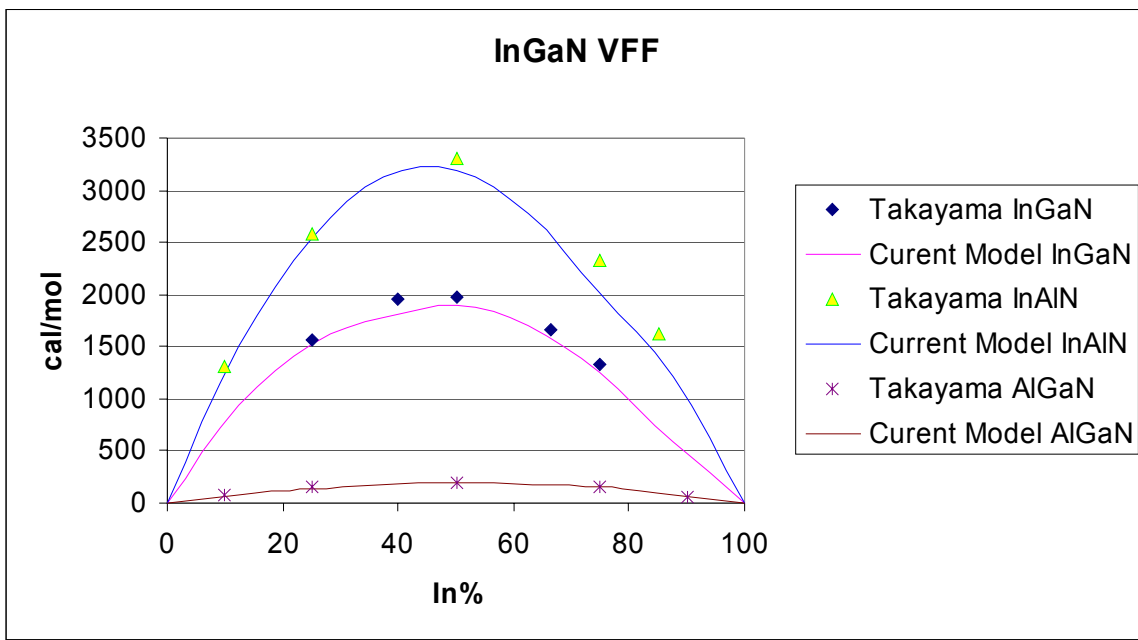


Figure 7-3 Comparison of the current model to the data from Takayama. The values are in agreement to less than 5%. Because both models are randomly generated, perfect agreement is unlikely

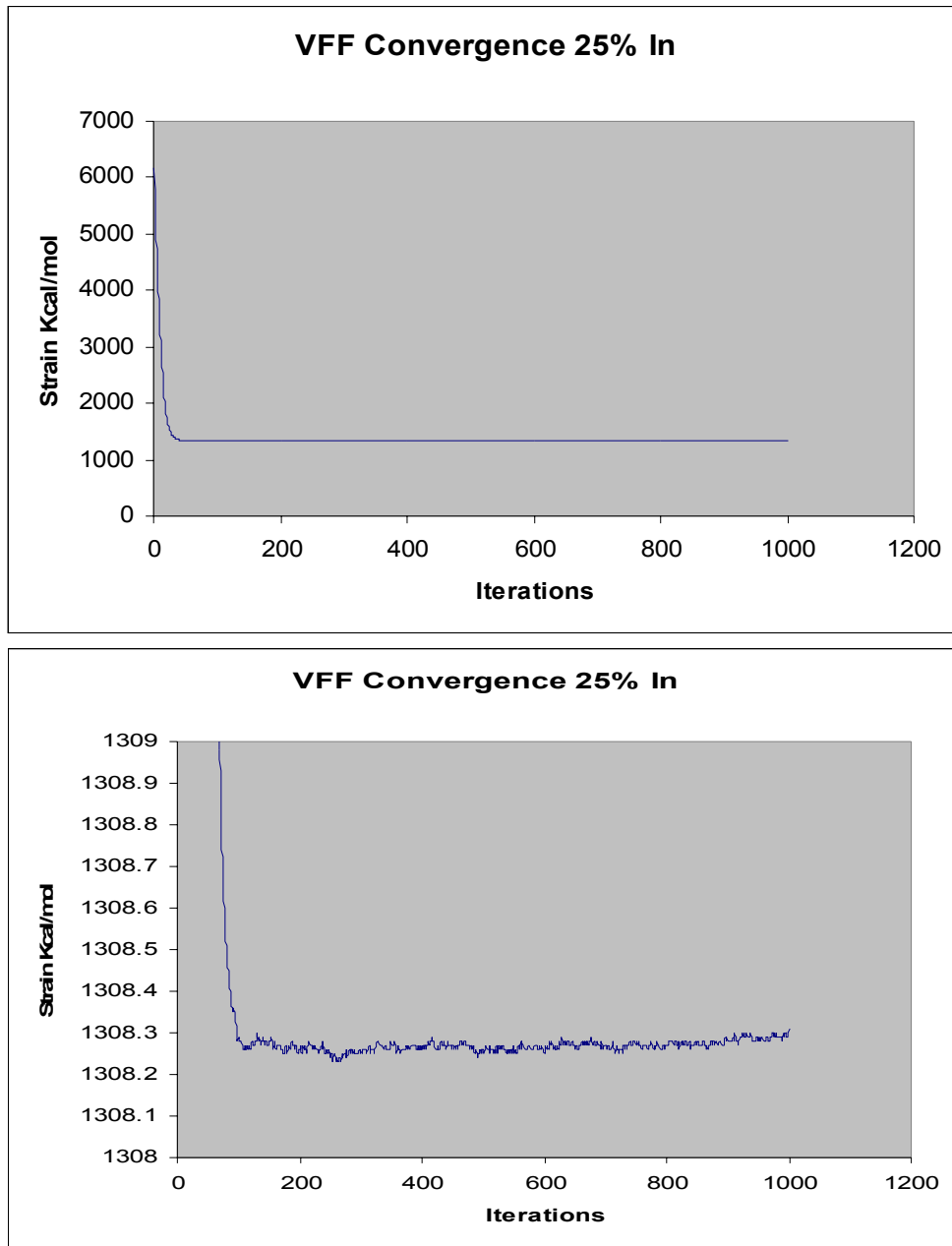


Figure 7-4 Showing the convergence of the strain energy with iterations for 25% InGaN alloy using the VFF model. Bottom plot is same curve on a magnified scale.

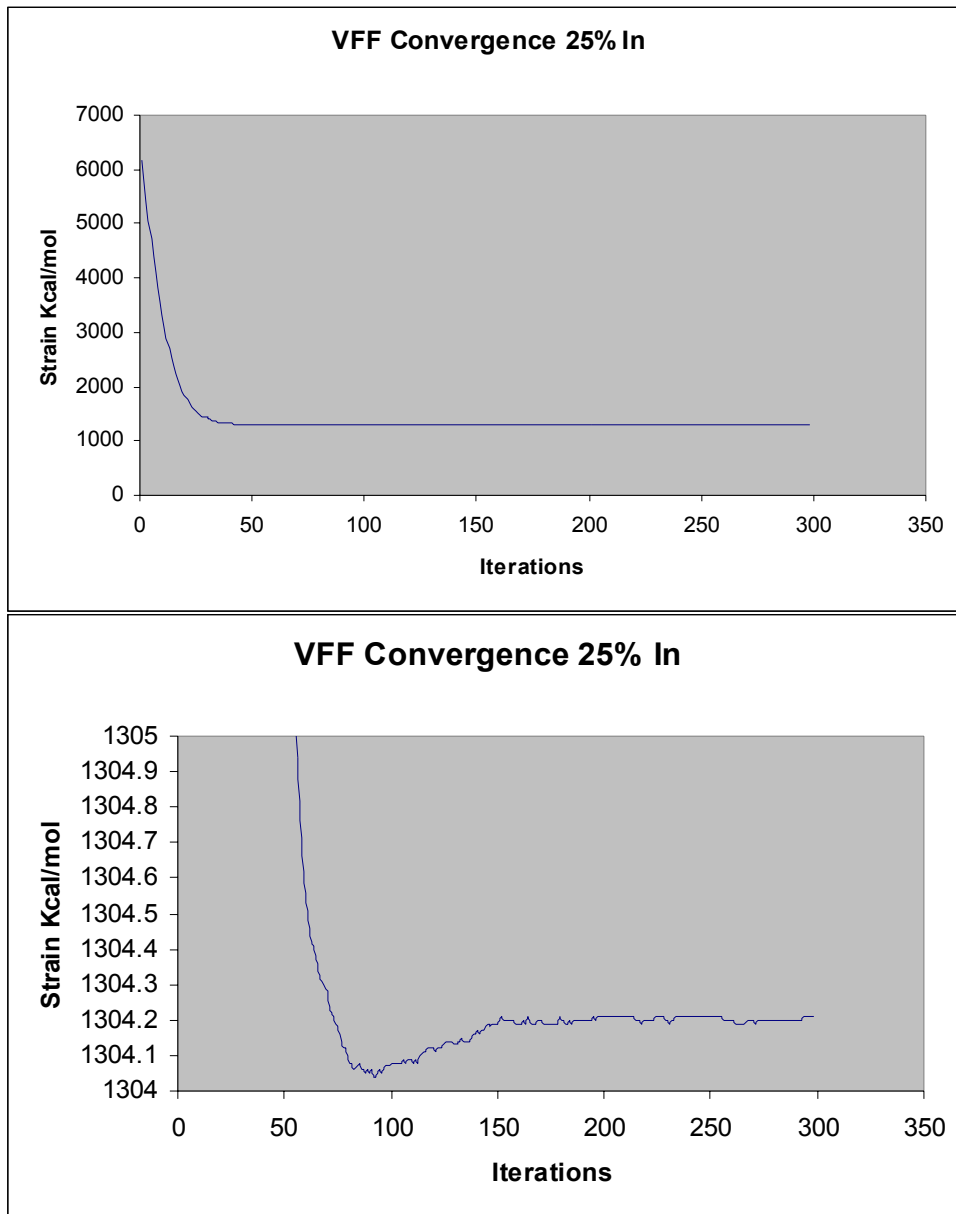


Figure 7-5 Showing strain energy vs. number of iterations for 25% InGaN alloy. Notice that the final converged value is not the minimum. This is due to the greedy algorithm being non-optimal.

limit	final value	iterations	delt sol	min value	final 1k
0.001		76	1308.64	1308.23	1308.31
0.0001		85	1308.41	1308.23	1308.31
0.00001		92	1308.36	1308.23	1308.31
0.000001		101	1308.29	1308.23	1308.31
1E-07		101	1308.29	1308.23	1308.31
1E-08		229	1308.26	1308.23	1308.31
1E-09		577	1308.27	1308.23	1308.31
1E-10		702	1308.27	1308.23	1308.31
1E-11				1308.23	1308.31
1E-12				1308.23	1308.31

Figure 7-6 Table showing the final values of strain energy for different threshold values.

Notice the slight difference between the final converged value and the minimum.

Threshold for all simulations was set at 1E-5.

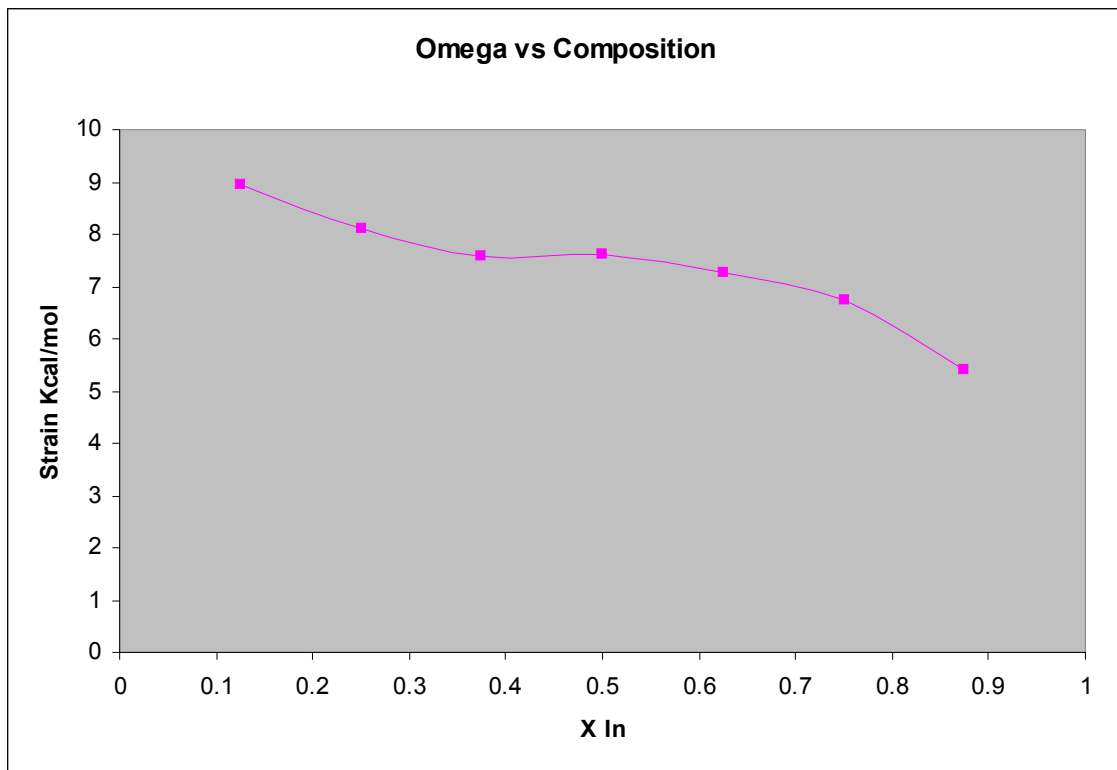


Figure 7-7 Plot of Ω vs. composition for the wurtzite VFF model. Adding In to a GaN matrix is more difficult than adding Ga to an InN matrix due to the larger strain energy for GaN.

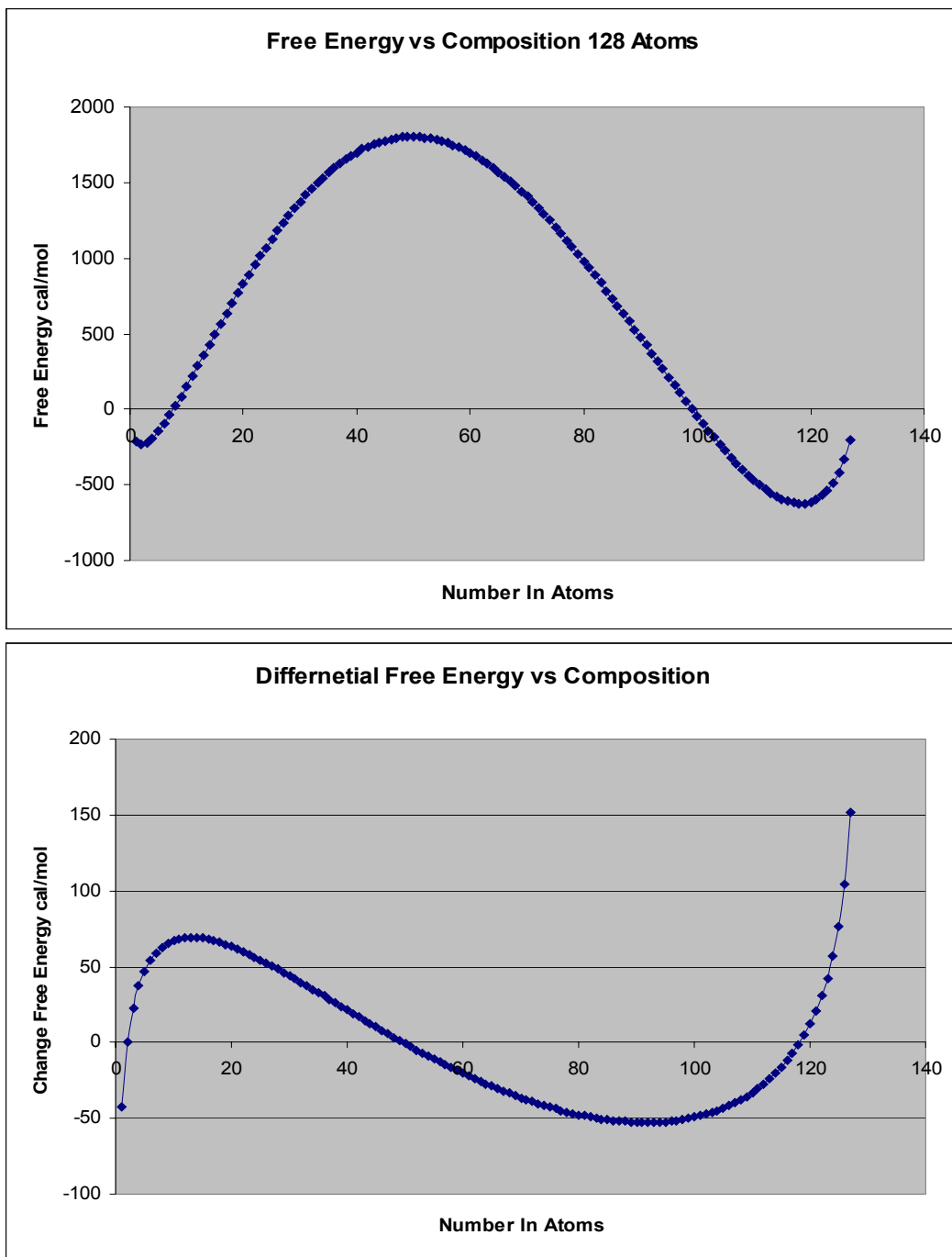


Figure 7-8 Free energy curves using variable Ω . Notice once again the lower solubility of In in the GaN matrix.

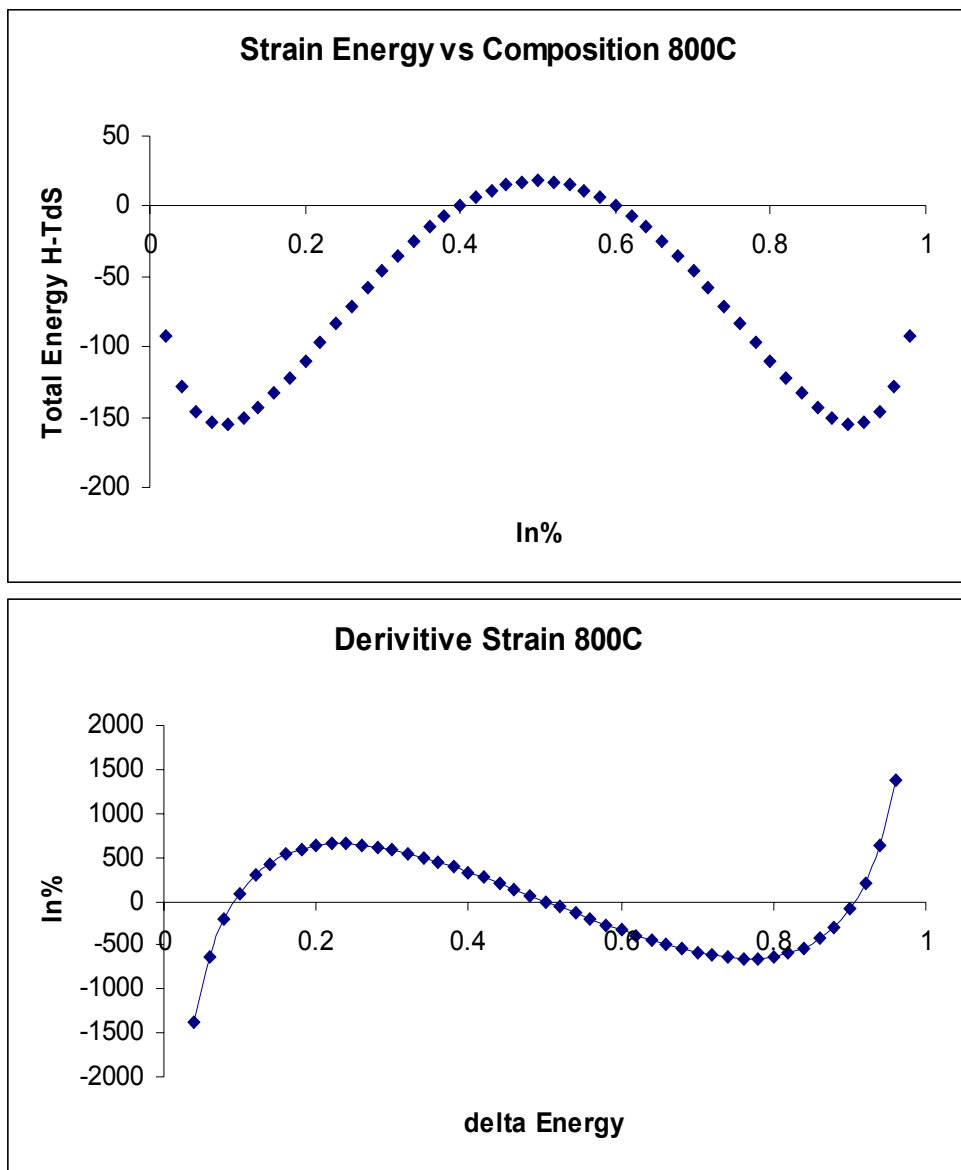


Figure 7-9 Calculation of phase diagram using the regular solution model. Stringfellow's value for Ω of 5.98 kcal/mol is used. Upper curve is the free energy diagram. Lower curve is the derivative of the free energy.

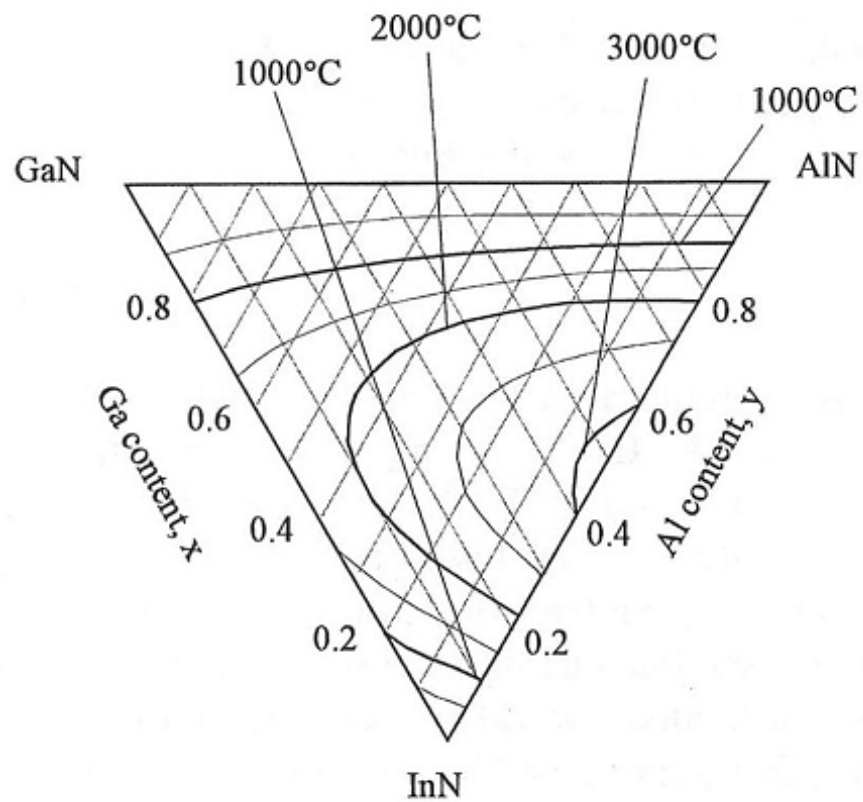


Figure 7-10 Unstable mixing region calculation for AlInGaN from Takayama.

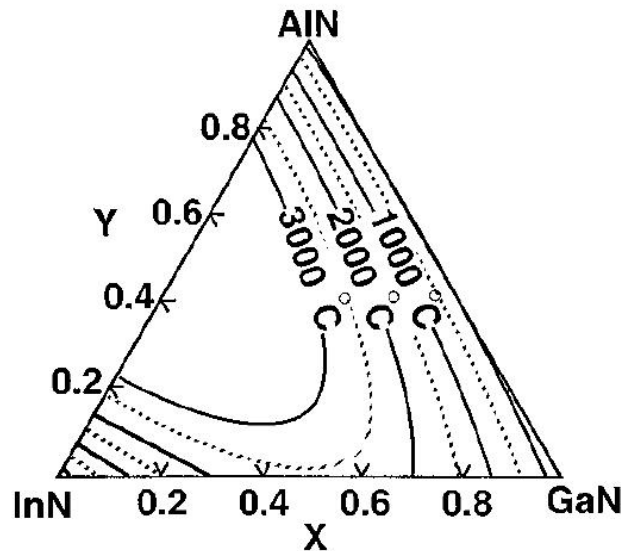


Figure 7-11 Calculated Spinodal for AlInGaN from Matsuoka

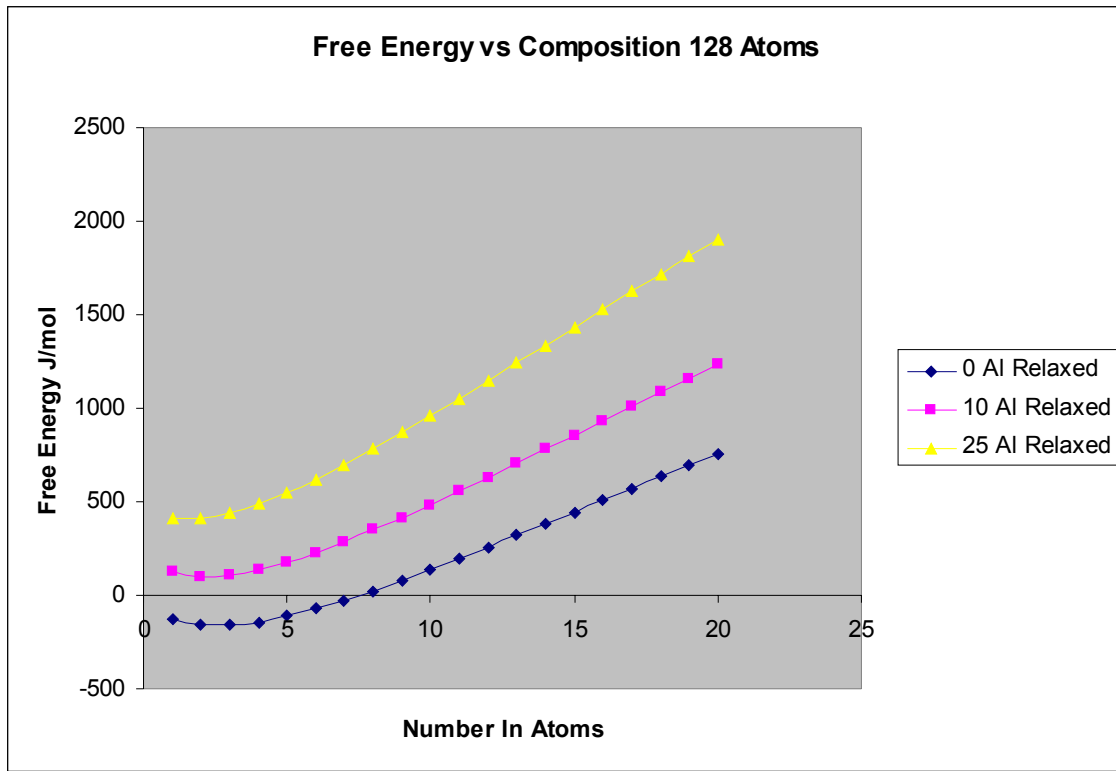


Figure 7-12 Free energy curves, for the relaxed crystal, generated using the VFF calculation at every point. Model used code from Monte Carlo algorithm, but with random swaps. Values for InGaN (0 Al) curve are consistent with Ω calculations.

Notice the decrease in In solubility with increasing Al.

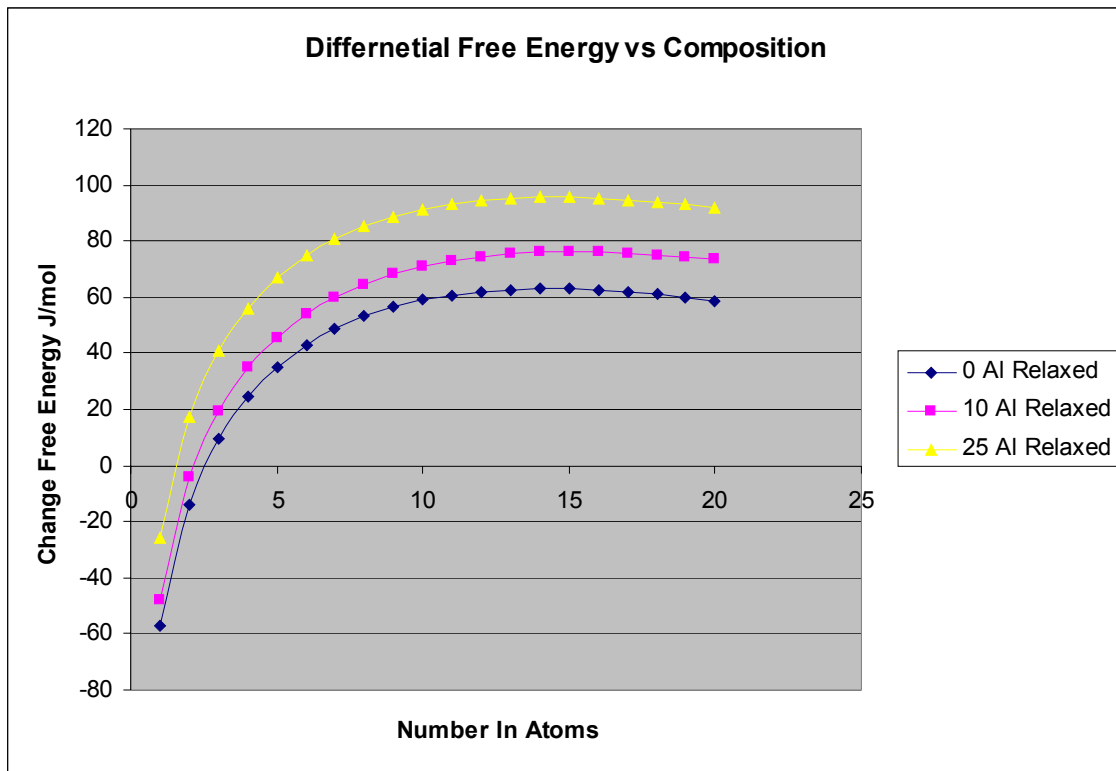


Figure 7-13 Derivative of the free energy curve for relaxed crystal. Notice the decrease (x axis intercept) of the equilibrium In composition. Spinodal point (maximum) is relatively unaffected.

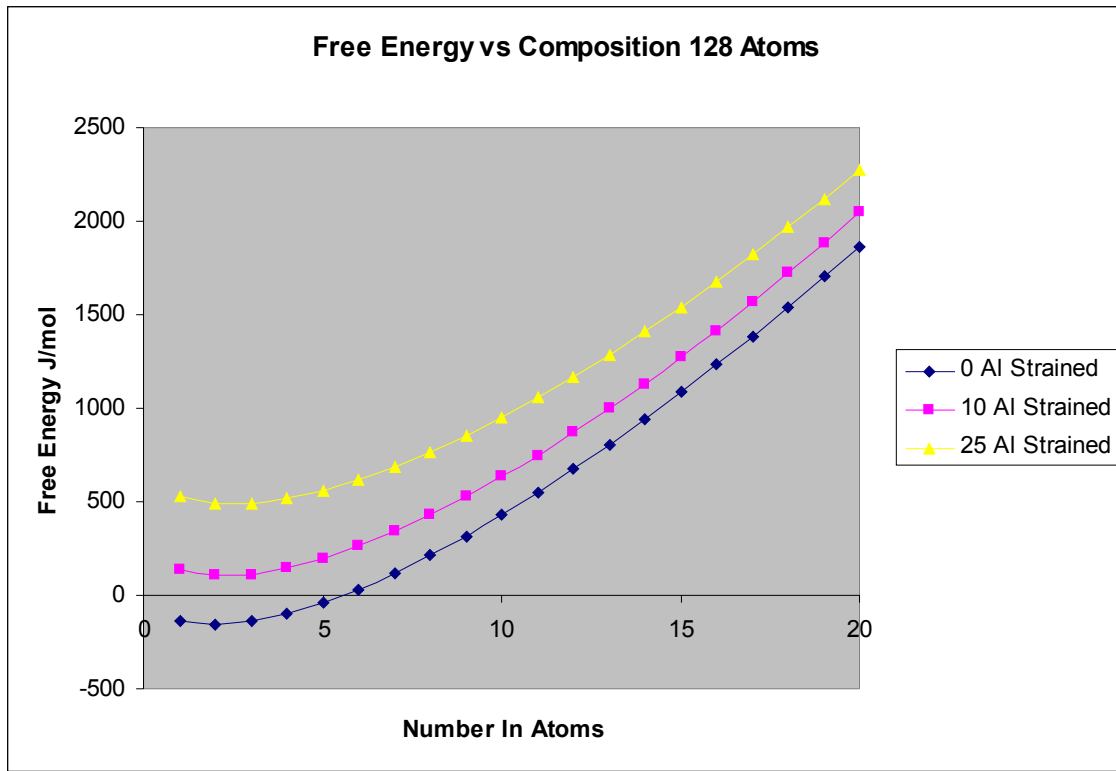


Figure 7-14 Free energy curves for strained InGaN and AlInGaN on GaN generated using the VFF calculation for every point. Model used code from Monte Carlo algorithm, but with random swaps. Notice that unlike the relaxed curves the solubility of In is not affected by the increasing Al.

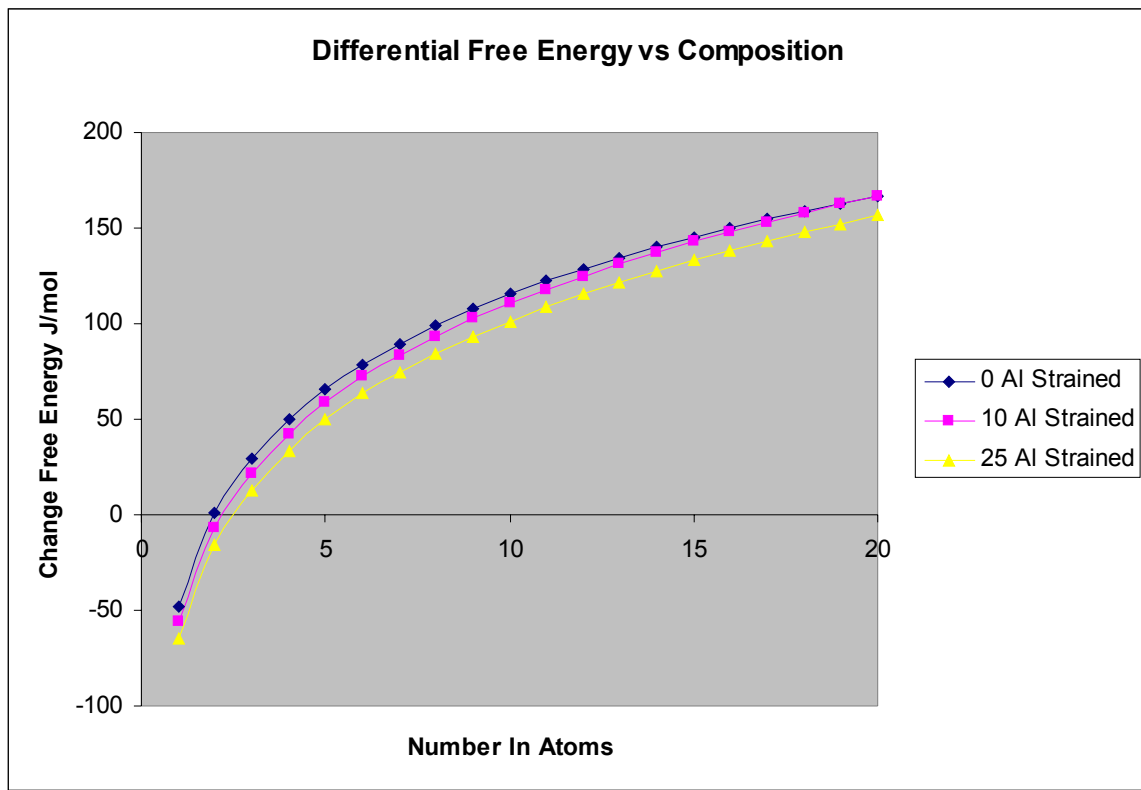


Figure 7-15 Derivative of the free energy curve for strained InGaN and AlInGaN alloys. The equilibrium In composition increases slightly with increasing Al. The spinodal point is no longer present.

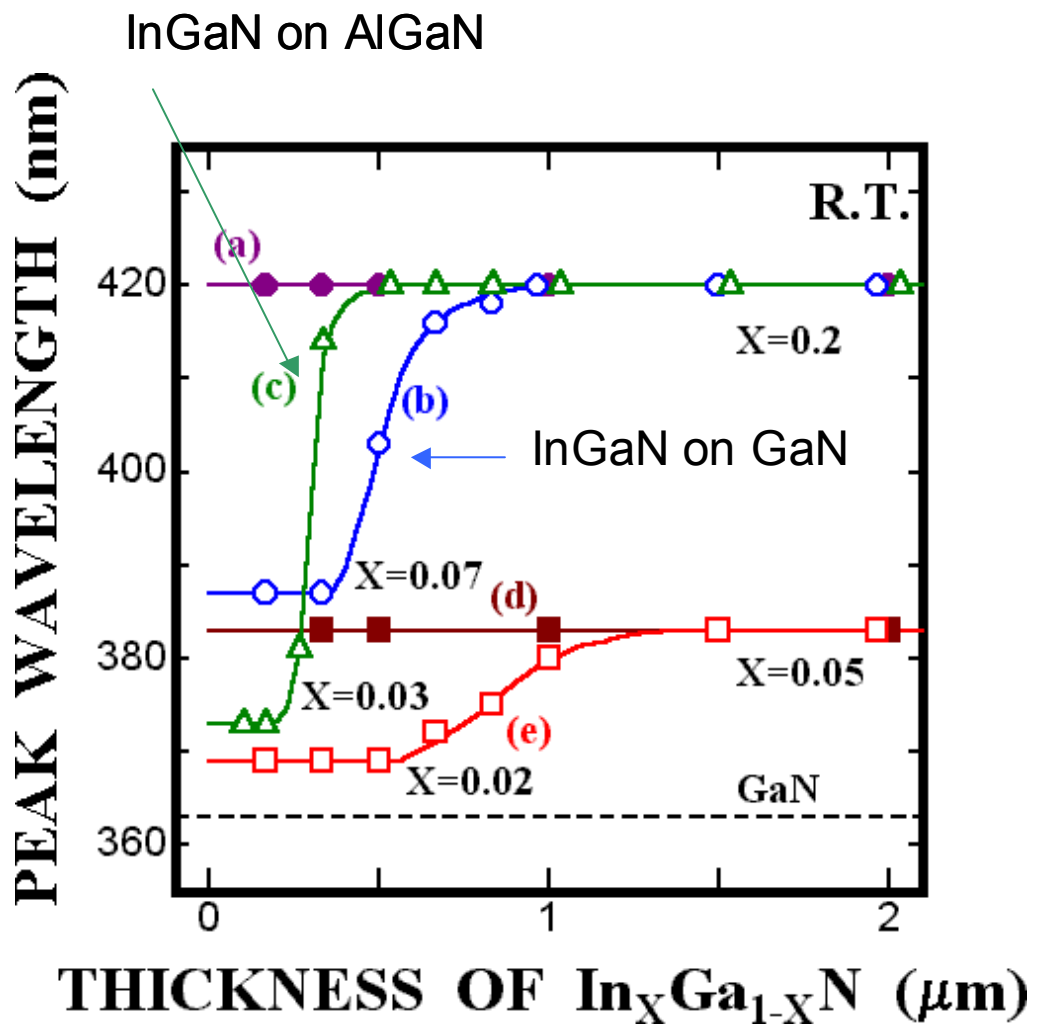


Figure 7-16 Data from Hiramatsu showing the increase in In composition with layer thickness.

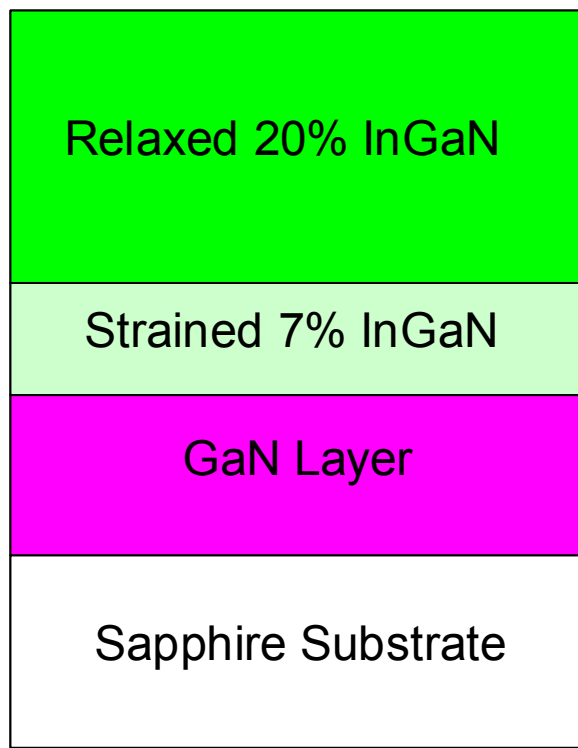


Figure 7-17 Diagram of the growth of 20% InGaN on a AlGaN layer. The initial layers are strained to the underlying substrate and are of lower composition than the relaxed bulk film.

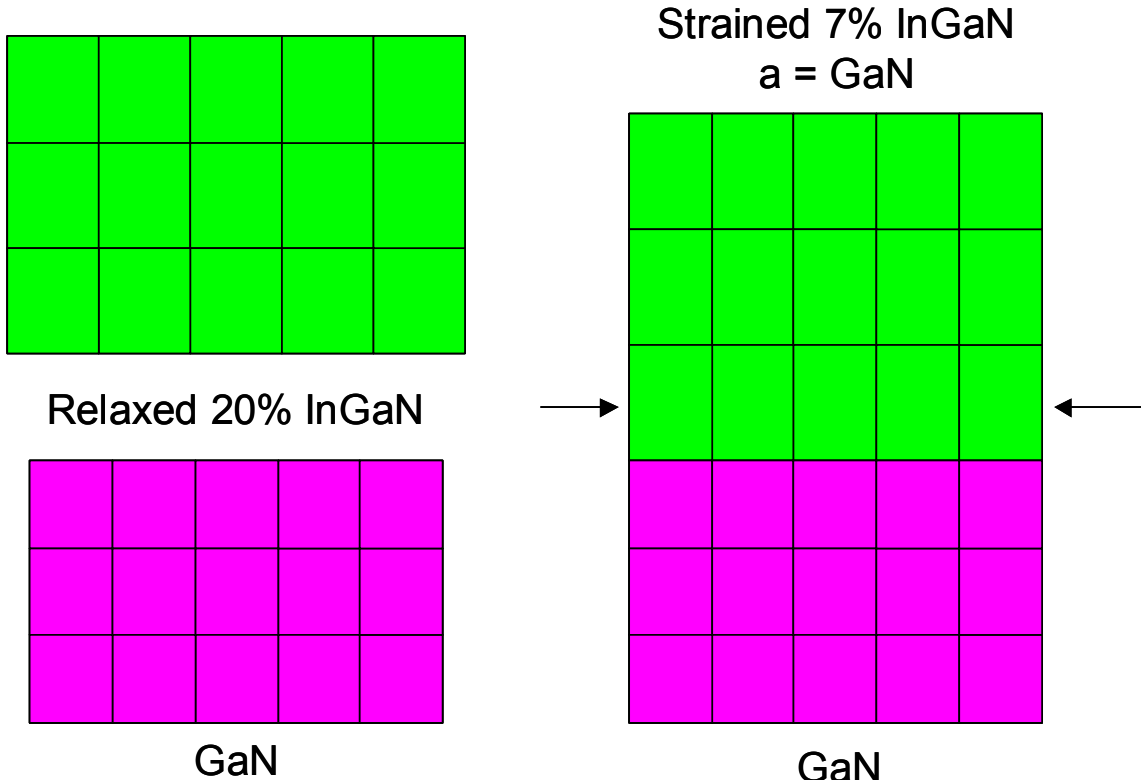


Figure 7-18 Method for testing the Monte Carlo In incorporation hypothesis. The two films are compared using the VFF model. The model compares the energy to add an In atom into each film using the relationship

$$I/I_0 = \text{Exp}(dE/kT)$$

For relaxed 20%
InGaN

$$\Omega_{\text{avg}} = 8.29 \text{ kcal/mol}$$

$$d \Omega/dx \approx 8.29(1-x) \quad d \Omega/dx \approx 6.54$$
$$d \Omega/dx \approx 9.42 \text{ kcal/mol}$$
$$d \Omega/dx \approx 8.76$$

For 7% InGaN
strained to GaN

$$\Delta E_{7\% \text{str}-20\%\text{relax}} = 2.22 \text{ kcal/mol}$$

$$\frac{Inc \ 7 \%}{Inc \ 20 \%} = \text{EXP} \frac{\Delta E}{kT} = 0.353$$

$$20\% * 0.353 = 7.0\%$$

Figure 7-19 Calculations for composition pulling of 20% InGaN on GaN

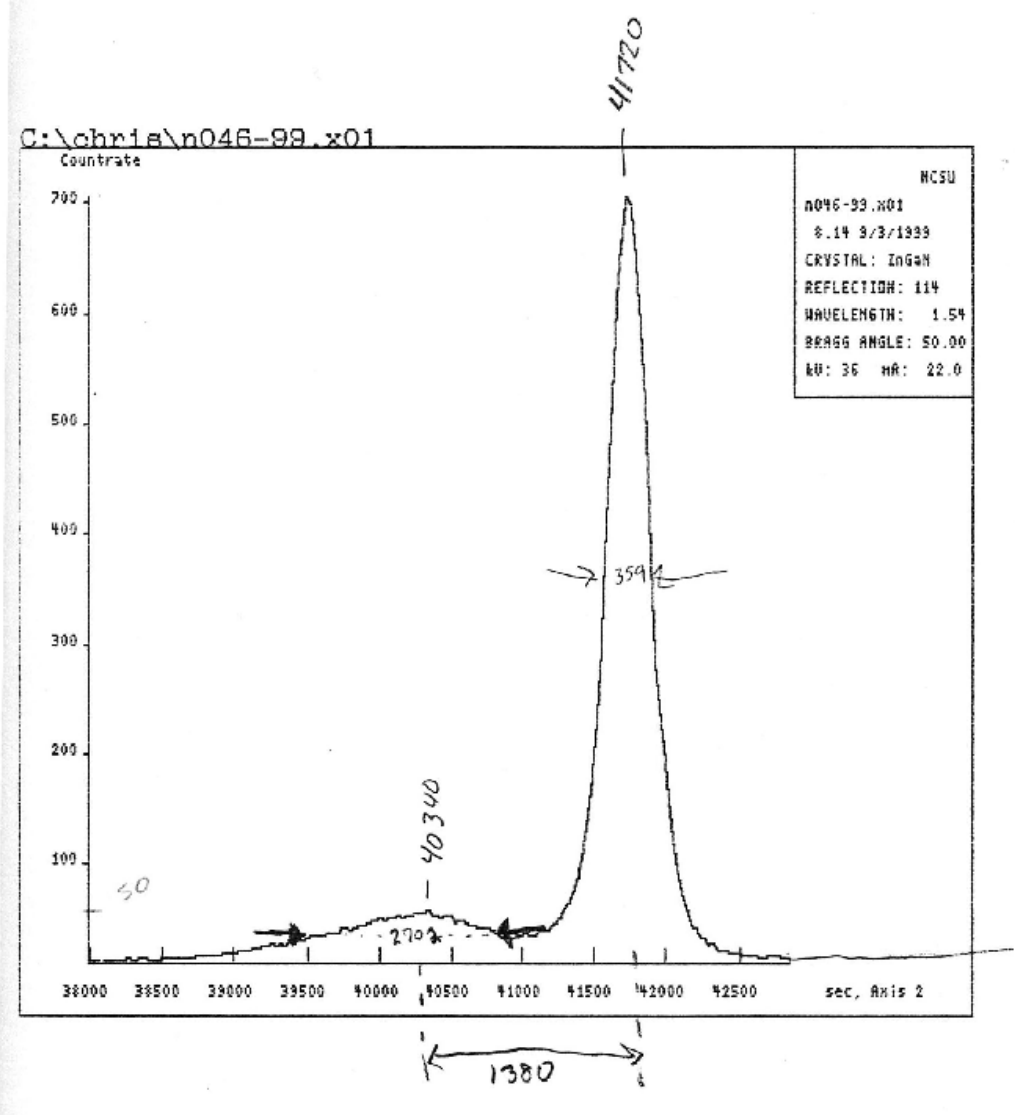


Figure 7-20 11-24 off-axis DCXRD scan of InGaN Showing 4.2% In

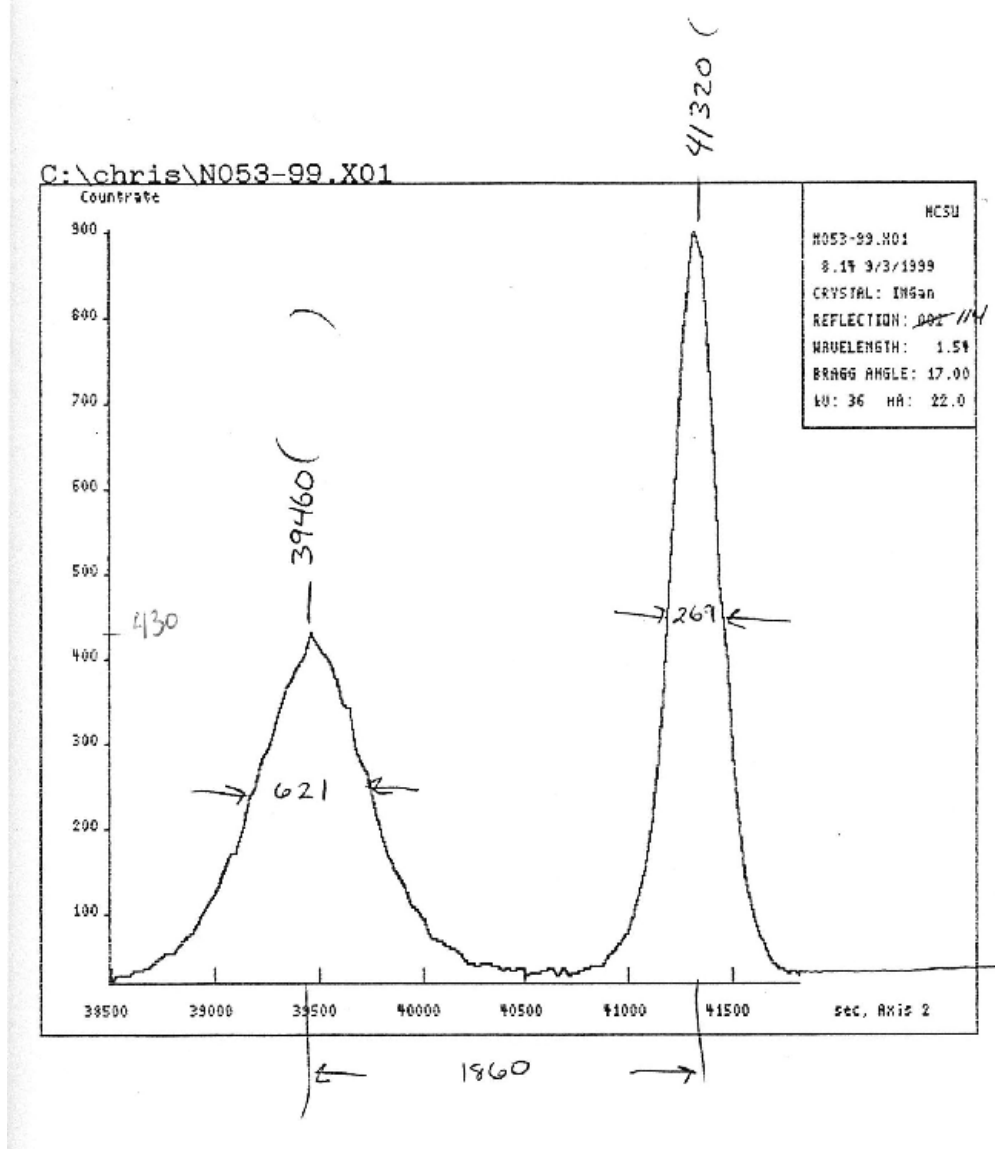


Figure 7-21 11-24 off-axis DCXRD scan of InGaN Showing 6.2% In

For relaxed 6.2% InGaN	For 4.2% InGaN strained to GaN
$\Omega_{\text{avg}} = 8.5 \text{ kcal/mol}$	$\Omega_{\text{avg}} = 9.0 \text{ kcal/mol}$
$d \Omega/dx \approx 8.5(1-x)$	$d \Omega/dx \approx 9.0(1-x)$
$d \Omega/dx \approx 7.45$	$d \Omega/dx \approx 8.24$

$$\Delta E_{4.2\% \text{str}-6.2\%\text{relax}} = 0.789 \text{ kcal/mol}$$

$$\frac{Inc\ 4.2\%}{Inc\ 6.2\%} = EXP \frac{\Delta E}{kT} = 0.69$$

$$6.2\% * 0.69 = 4.3\%$$

Figure 7-22 Composition pulling calculations of 6.2% InGaN on GaN

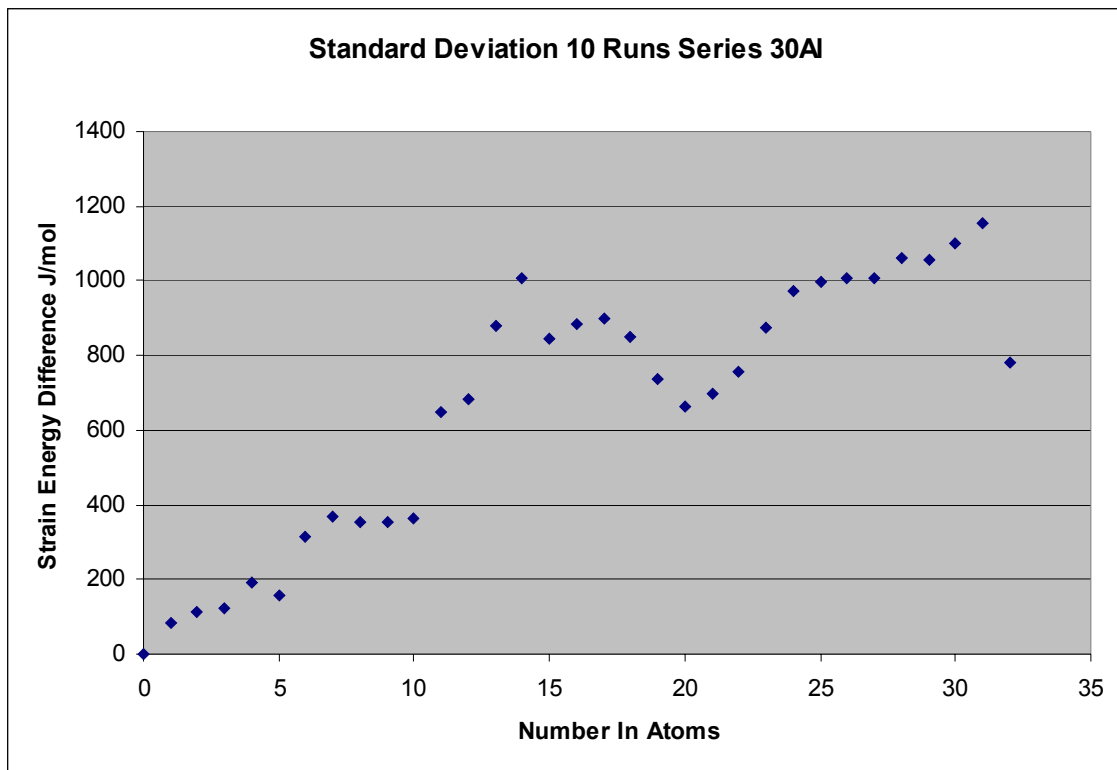


Figure 7-23 Showing the standard deviation for ten runs with the Boltzmann probability applied to the addition of In atoms only. The deviations using this method are large enough to mask the Strain equilibrium In incorporation effect.

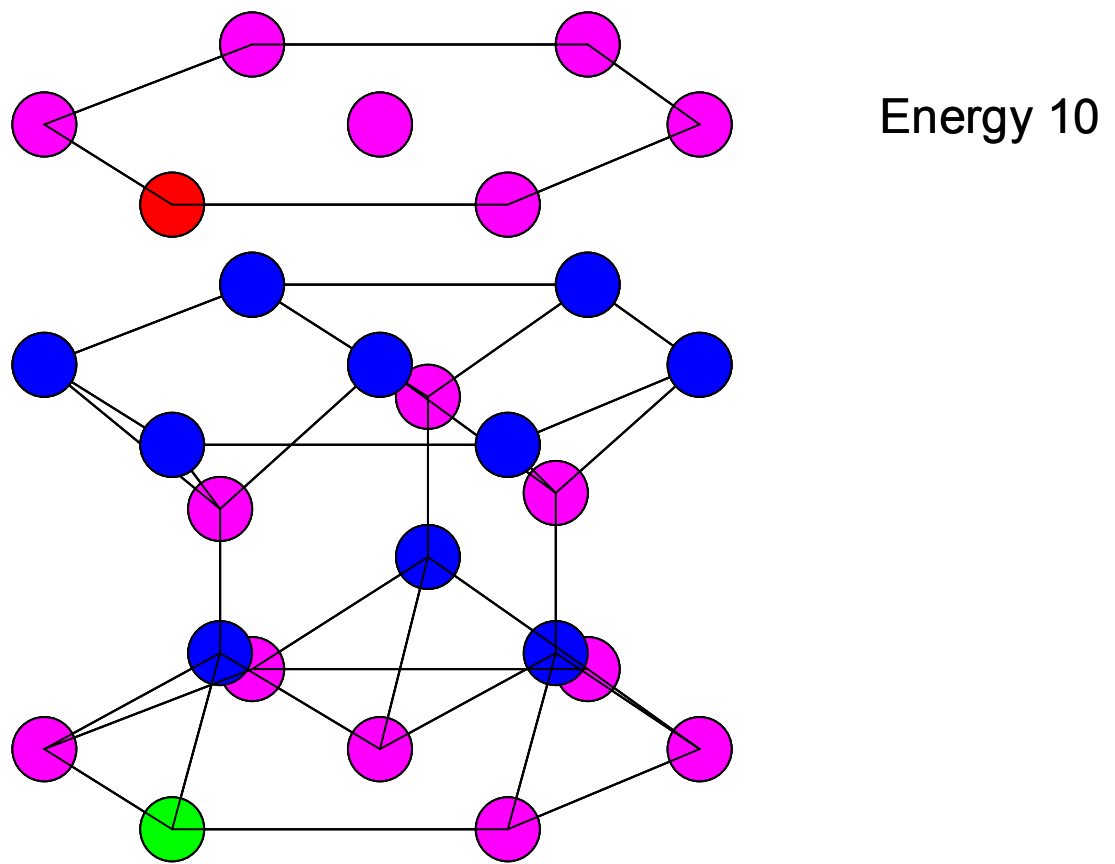


Figure 7-24 Start the Monte Carlo algorithm by calculating the strain energy of the crystal.

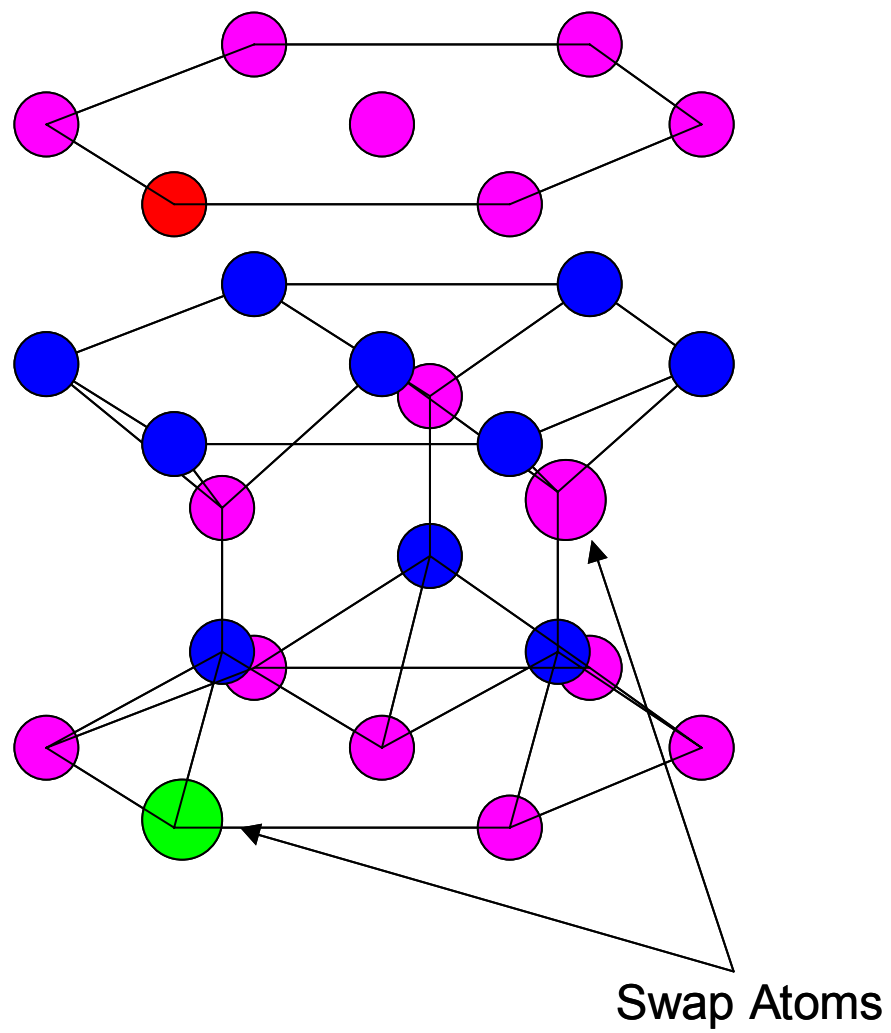


Figure 7-25 Select two random column III sites that are different atoms and exchange positions.

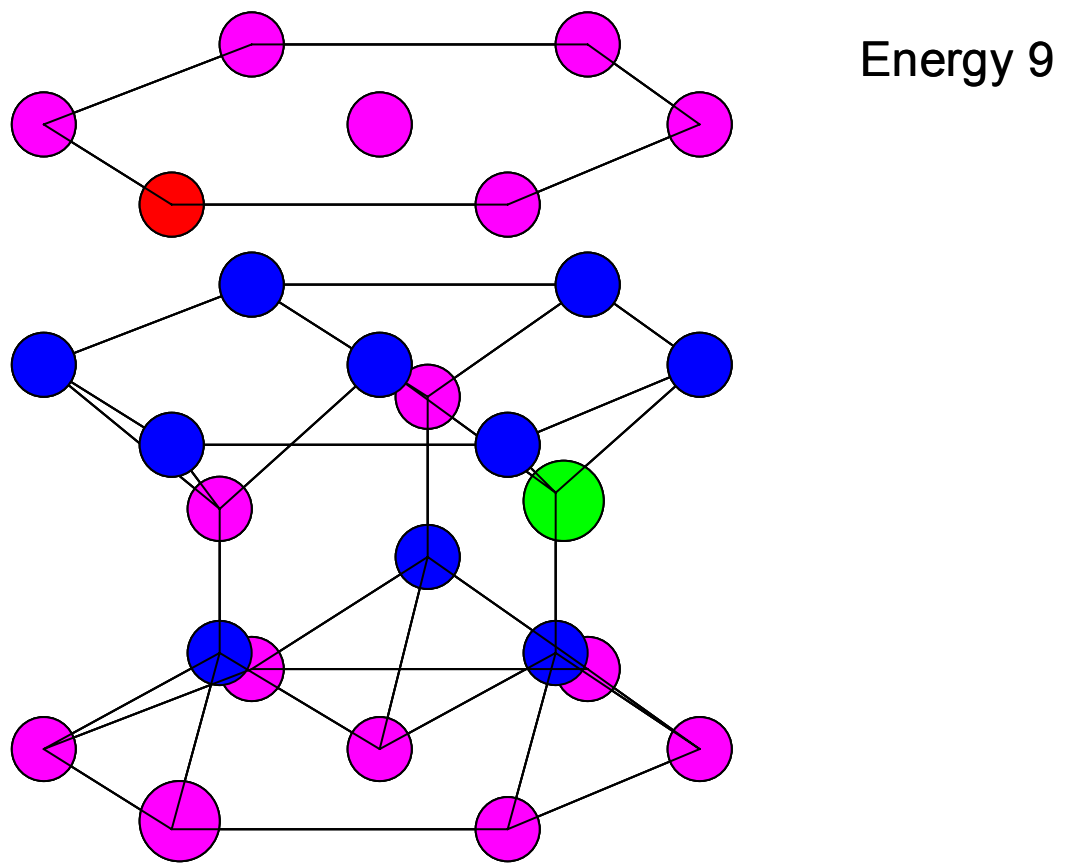


Figure 7-26 Recalculate strain energy with the new atom positions.

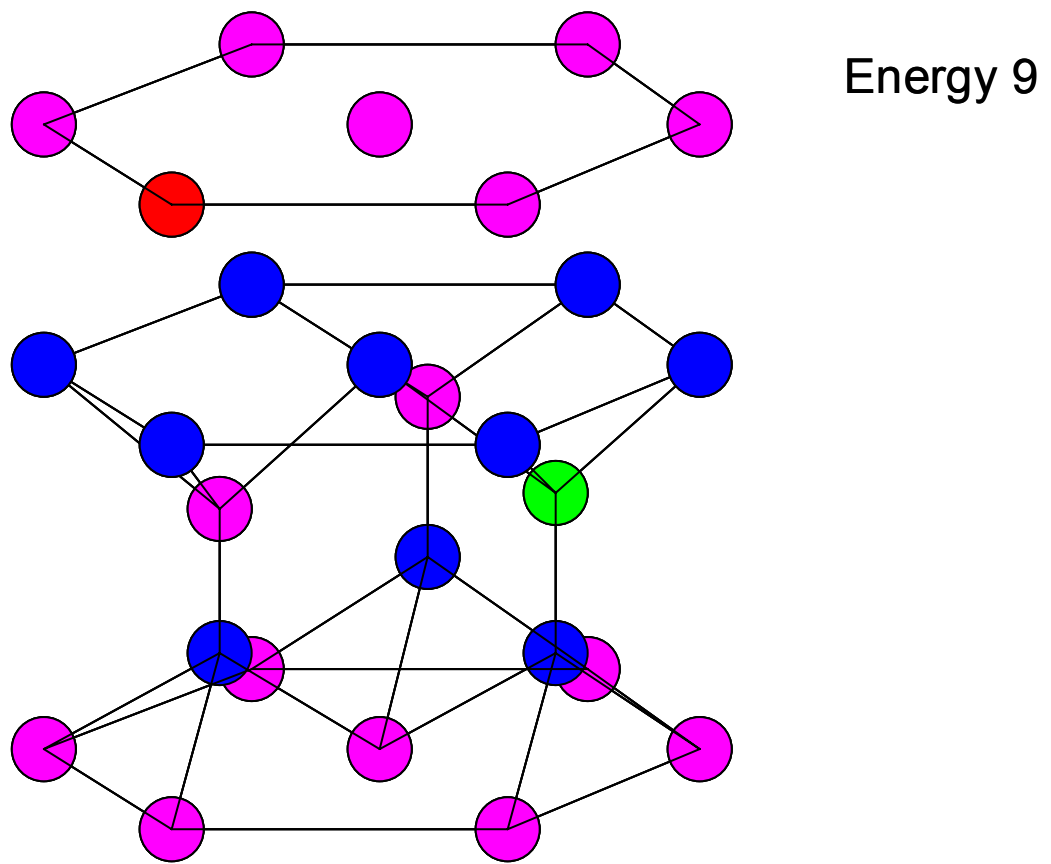


Figure 7-27 If the energy is less, the swap always occurs. If the energy is greater then the probability is given by the formula $P = \text{Exp}(-(\text{Energy change})/kT)$. Unfavourable transitions are still possible but with a Boltzmann distribution of probability.

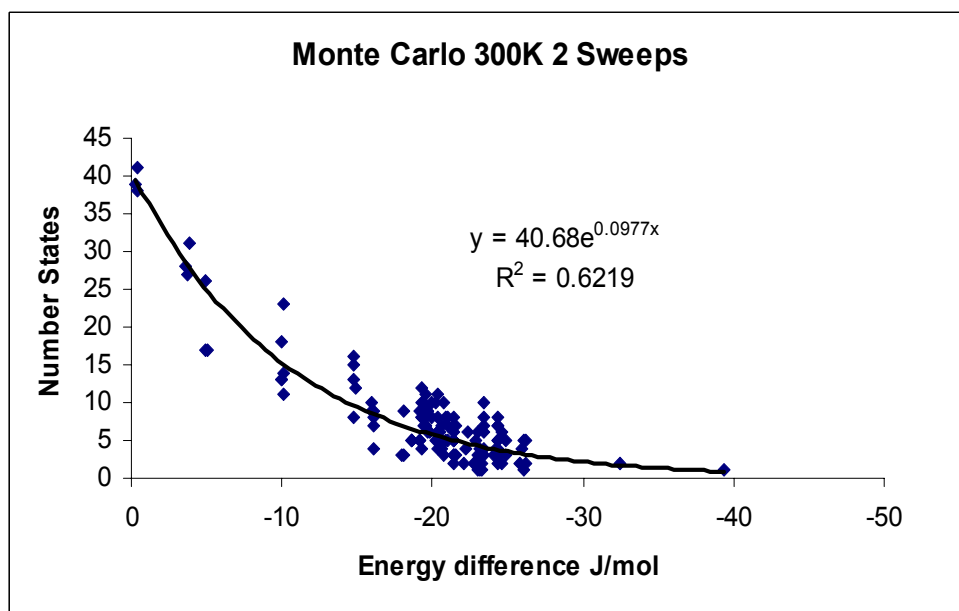
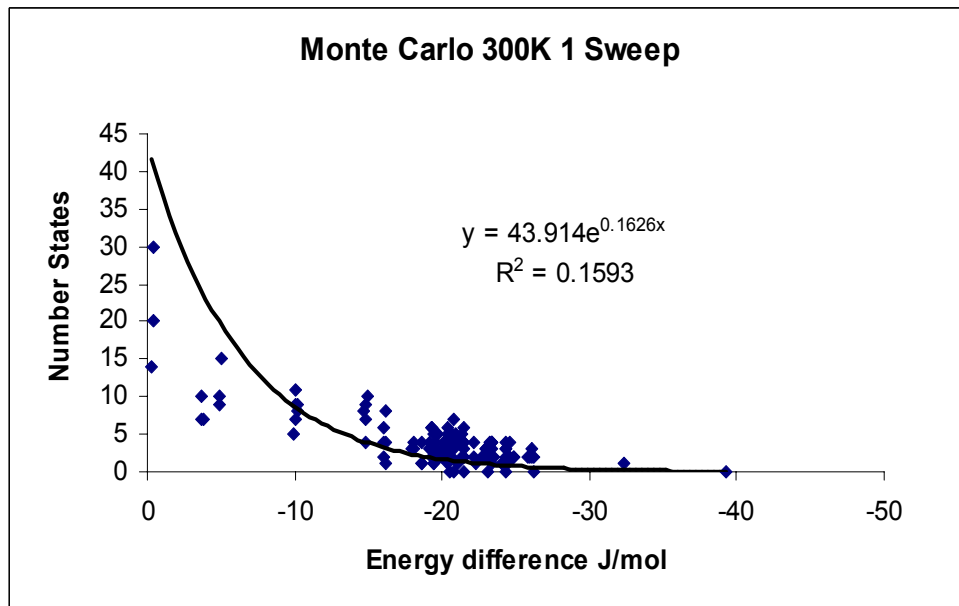


Figure 7-28 Monte Carlo simulation for $\text{Al}_1\text{In}_1\text{Ga}_{126}\text{N}$ showing the final number of atoms per lattice site vs. strain energy of that lattice site. Simulations are run for various numbers of sweeps.

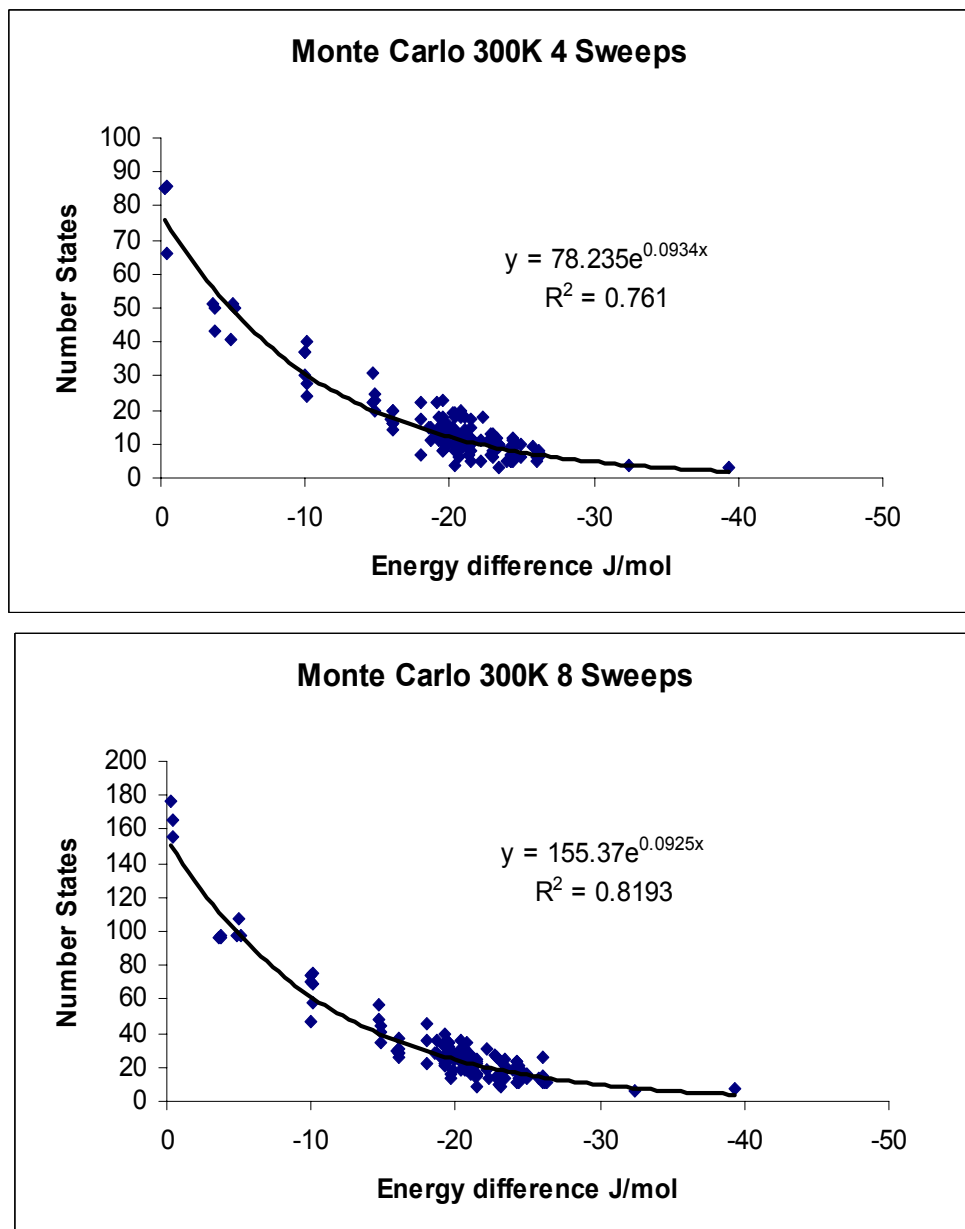


Figure 7-29 Monte Carlo simulation showing the final number of atoms per lattice site vs. strain energy of that lattice site. Simulations are run for various numbers of sweeps.

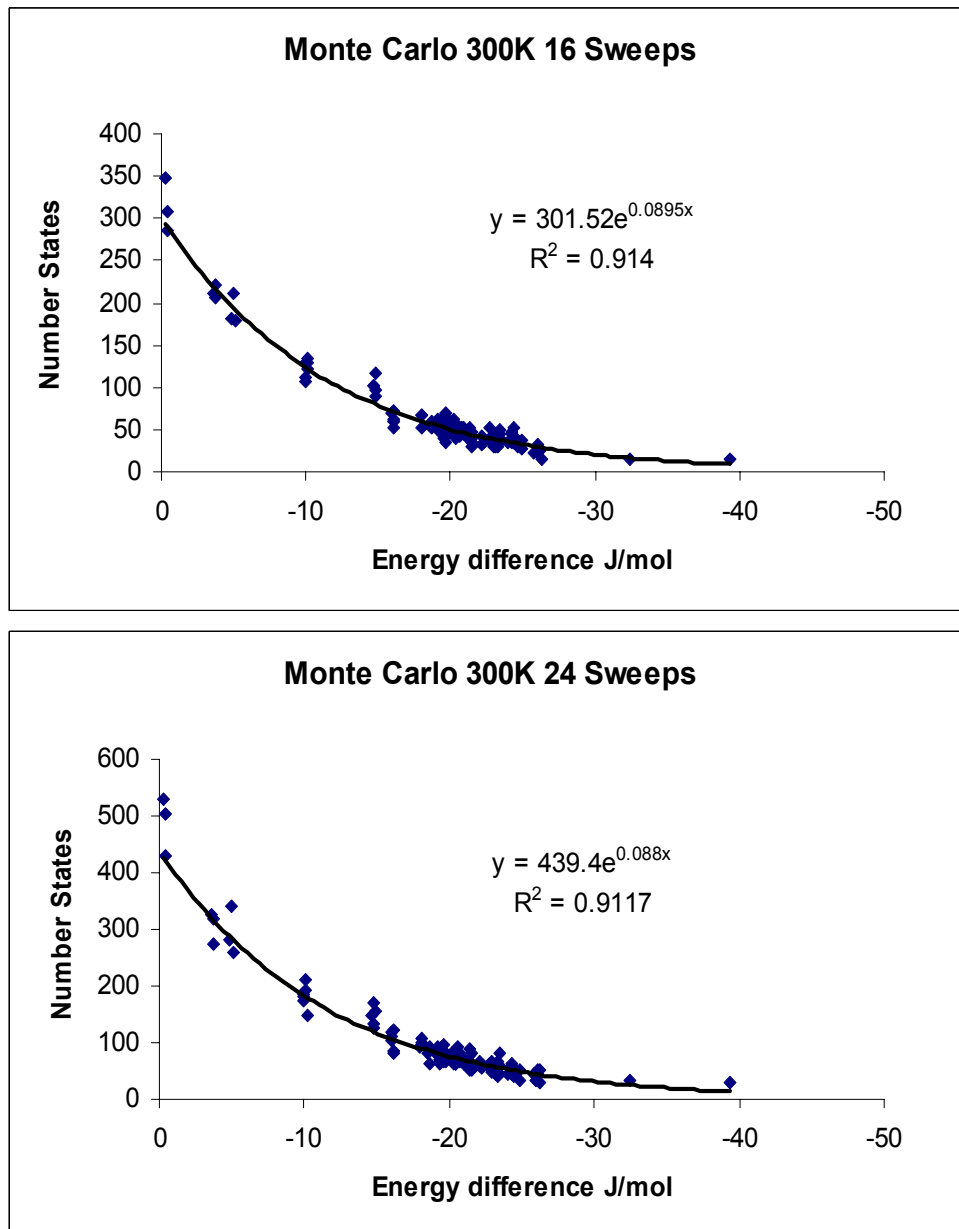


Figure 7-30 Monte Carlo simulation showing the final number of atoms per lattice site vs. strain energy of that lattice site. Simulations are run for various numbers of sweeps.

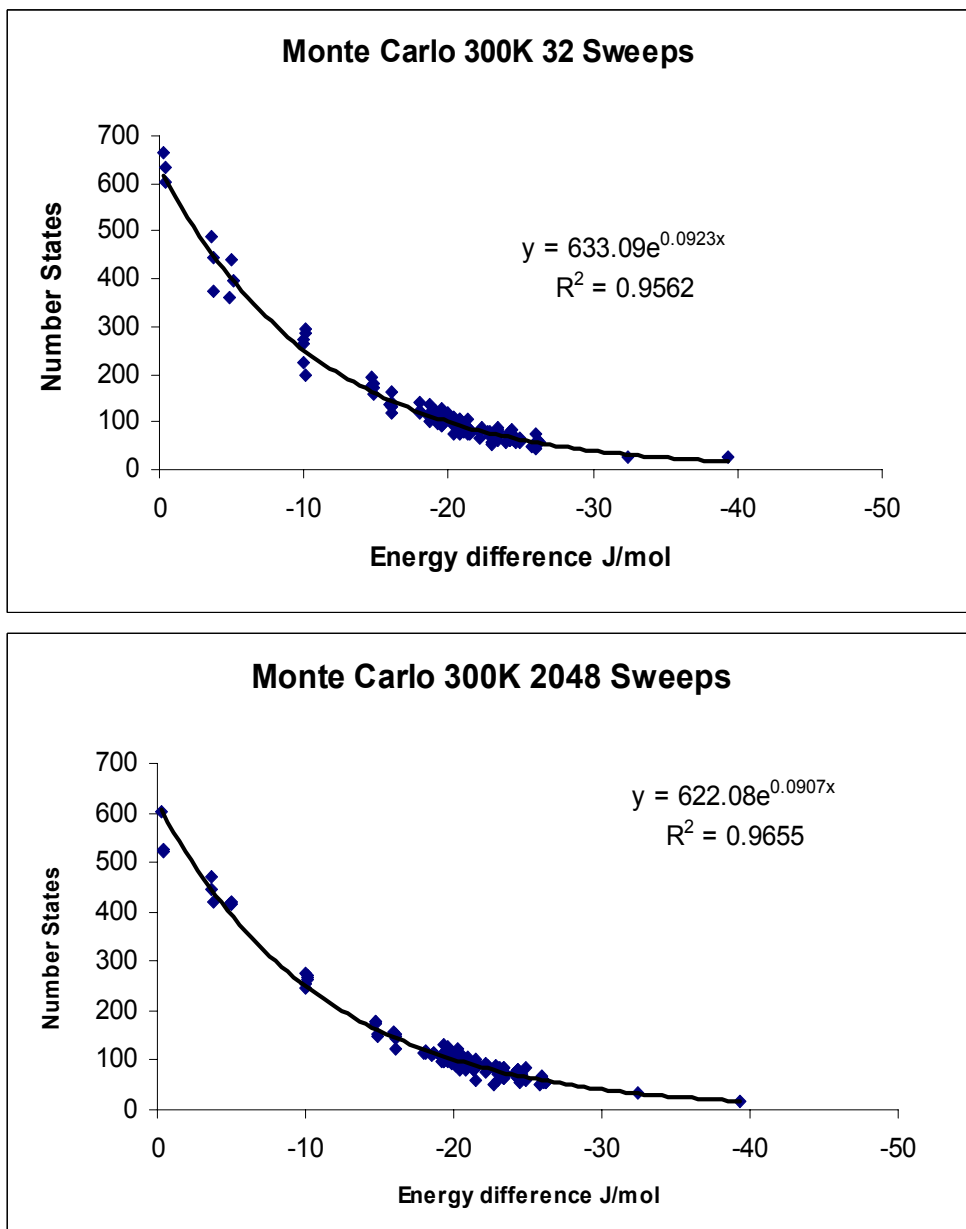


Figure 7-31 Monte Carlo simulation showing the final number of atoms per lattice site vs. strain energy of that lattice site. Simulations are run for various numbers of sweeps.

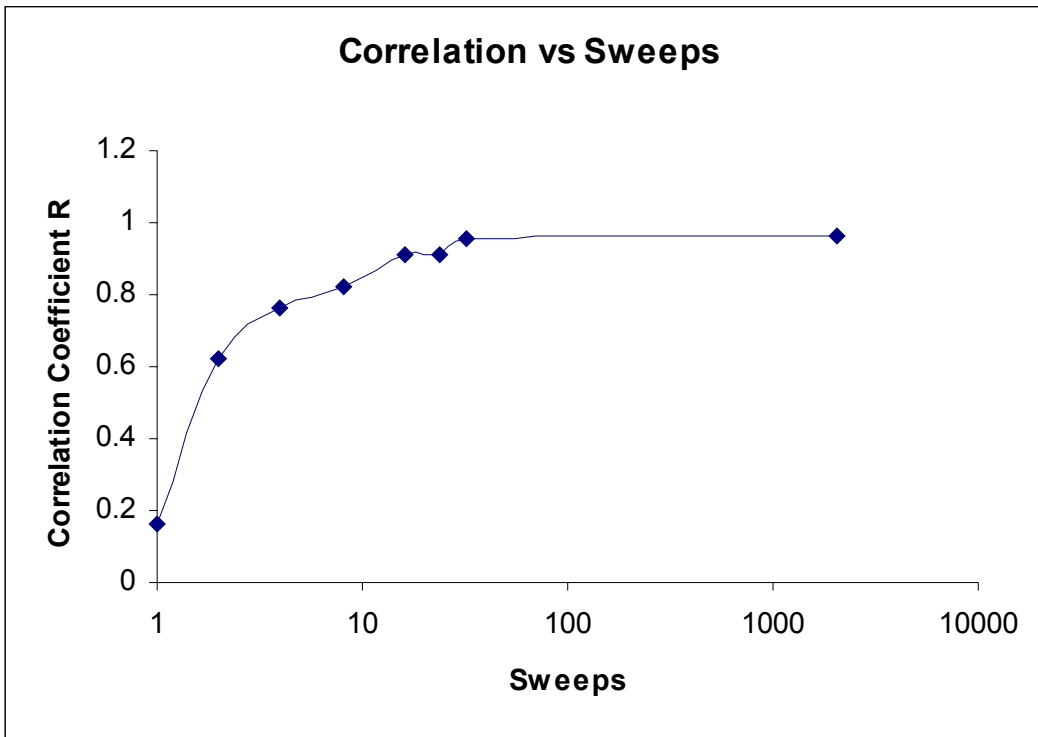


Figure 7-32 Plot of the correlation coefficient R to the ideal Boltzmann distribution. Curve is essentially flat above 32 sweeps. Curve bends over between 16 and 32 sweeps. Therefore all simulations will be run at least 25 sweeps.

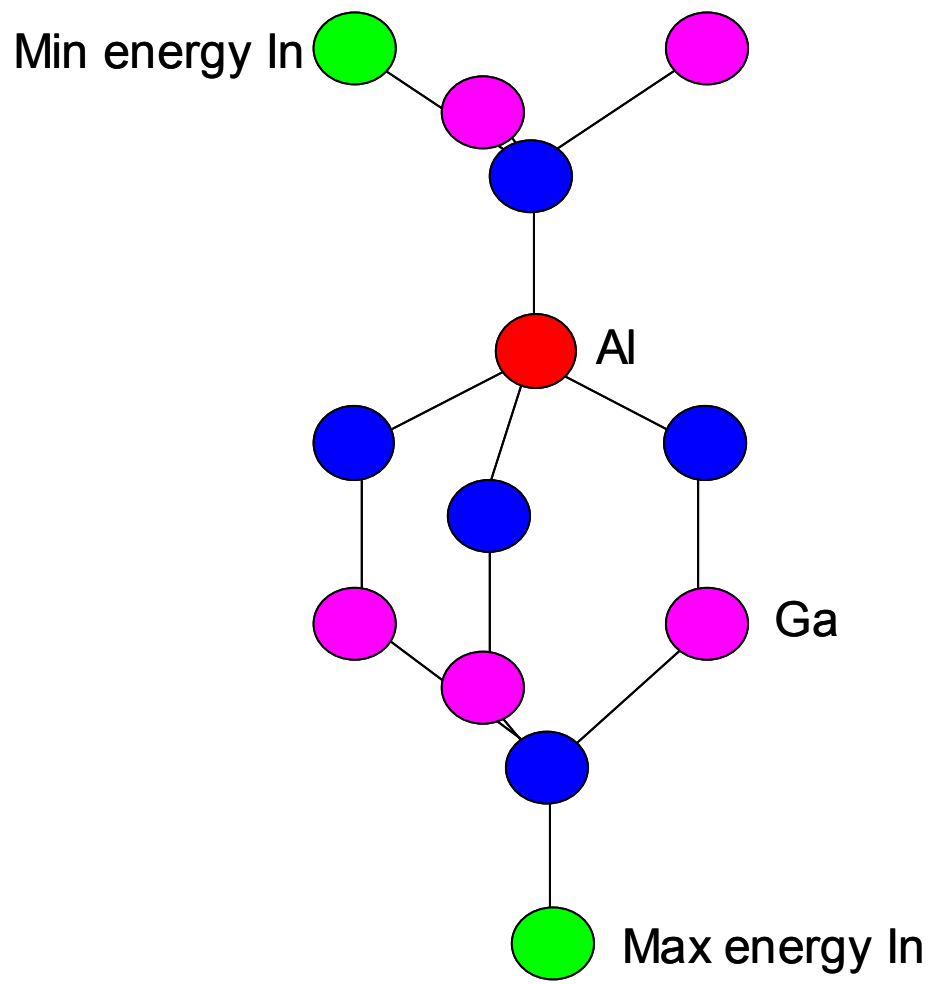


Figure 7-33 The minimum energy location has a path of two bonds between the In and Al atoms. The maximum energy locations have three paths of three bonds each for a total of ten bonds.

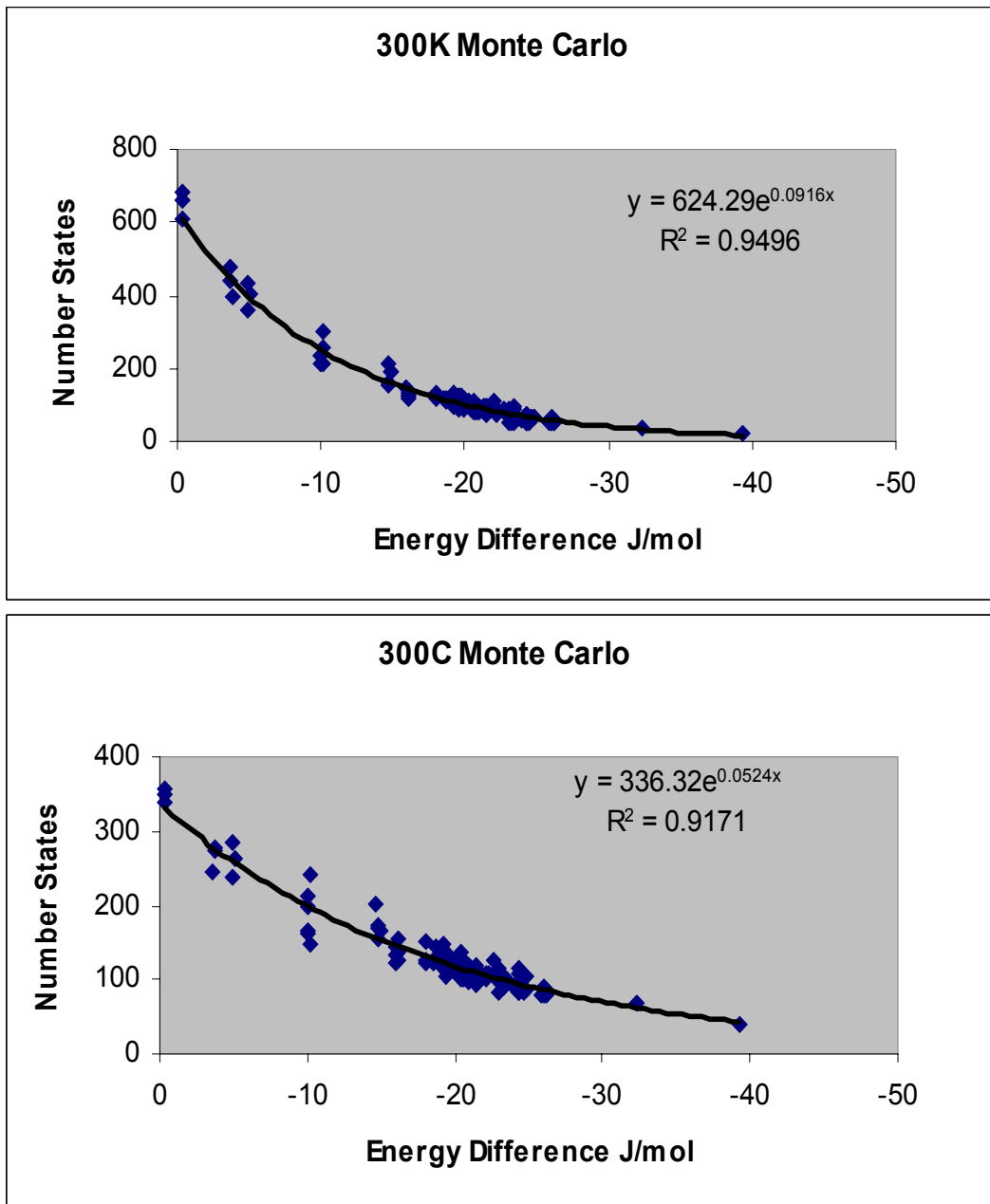


Figure 7-34 Curves showing Monte Carlo simulation of $\text{Al}_1\text{In}_1\text{Ga}_{126}\text{N}$ crystal at 300K and 300°C. The number of atoms per lattice site is plotted vs. strain energy of lattice site.

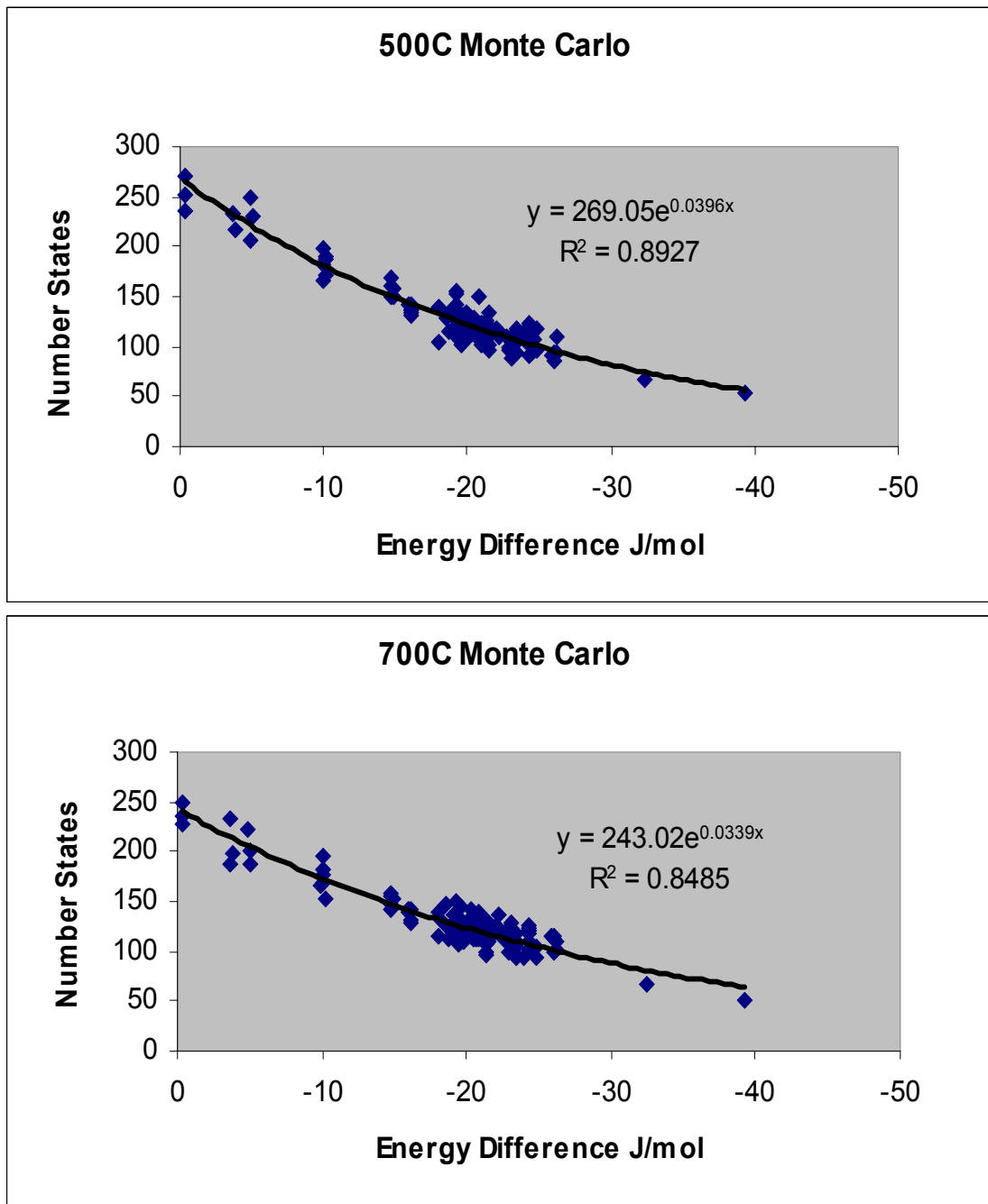


Figure 7-35 Curves showing Monte Carlo simulation of $\text{Al}_1\text{In}_1\text{Ga}_{126}\text{N}$ crystal at 500°C and 700°C. The number of atoms per lattice site is plotted vs. strain energy of lattice site.

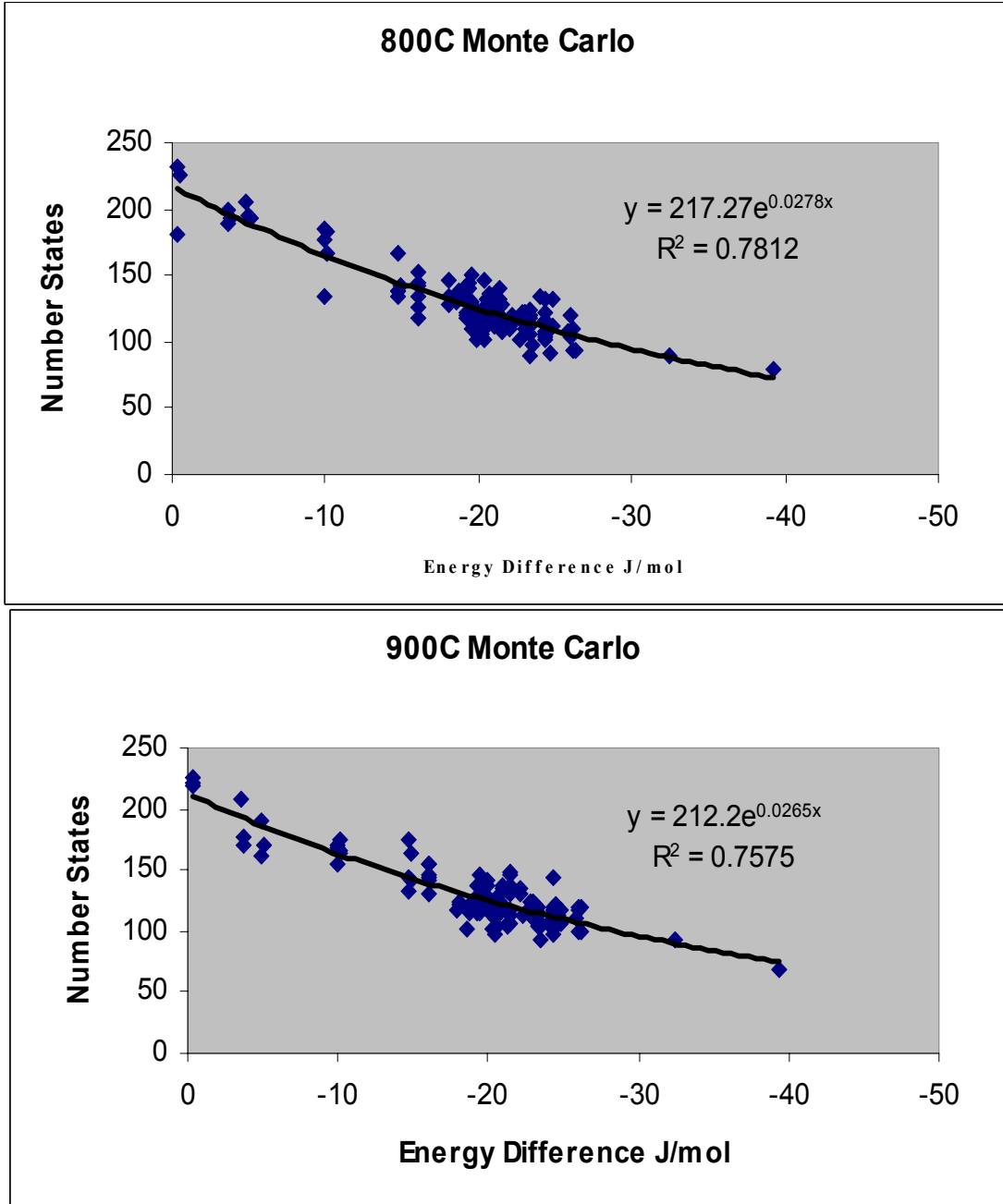


Figure 7-36 Curves showing Monte Carlo simulation of Al₁In₁Ga₁₂₆N crystal at 800°C and 900°C. The number of atoms per lattice site is plotted vs. strain energy of lattice site.

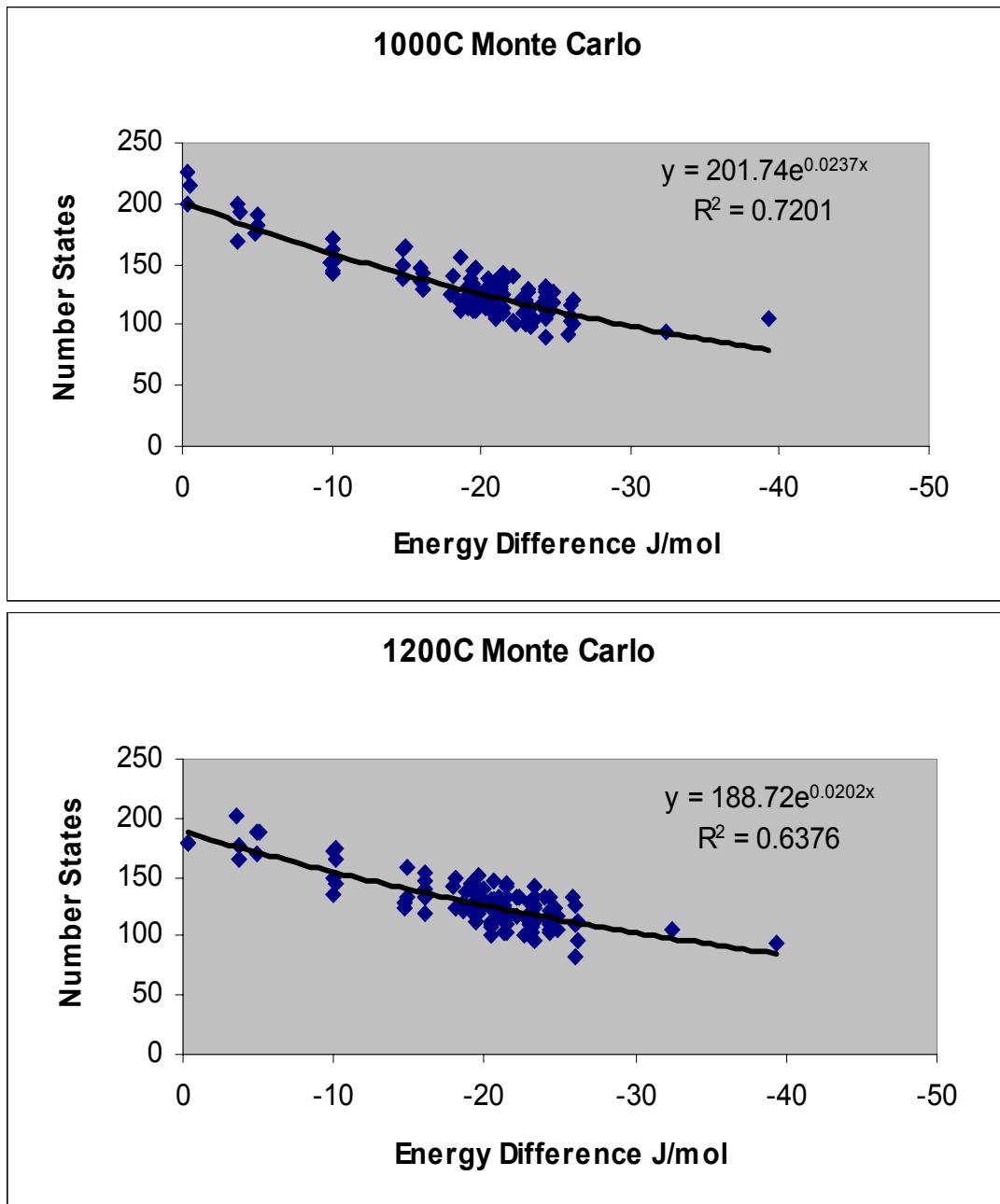


Figure 7-37Curves showing Monte Carlo simulation of $\text{Al}_1\text{In}_1\text{Ga}_{126}\text{N}$ crystal at 1000°C and 1200°C. The number of atoms per lattice site is plotted vs. strain energy of lattice site.

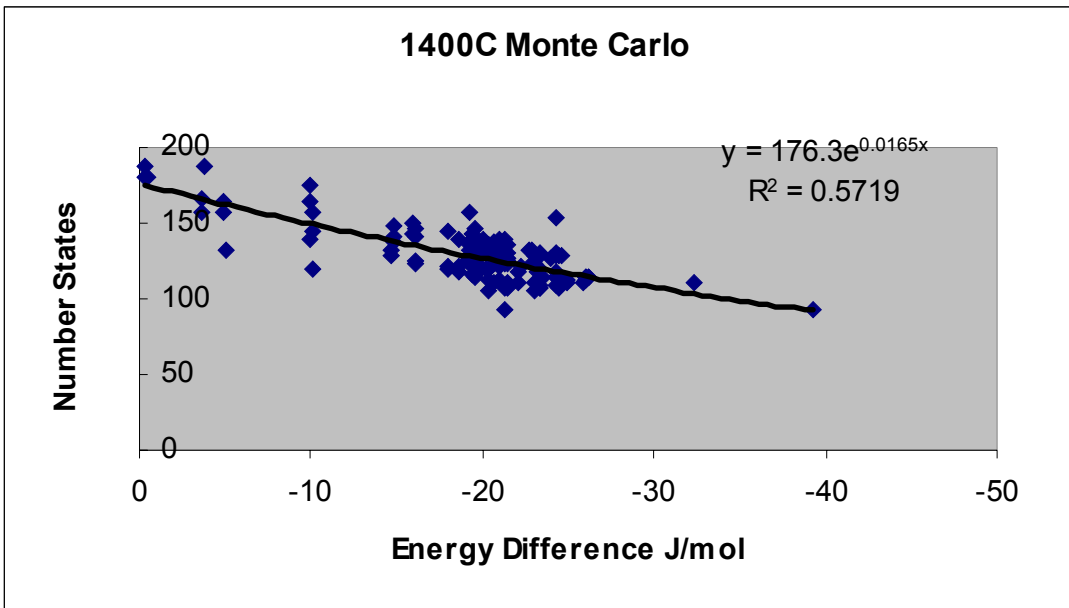


Figure 7-38 Curves showing Monte Carlo simulation of $\text{Al}_1\text{In}_1\text{Ga}_{126}\text{N}$ crystal at 1400°C. The number of atoms per lattice site is plotted vs. strain energy of lattice site. Notice how the curve fits the Boltzmann less and less at high temperatures.

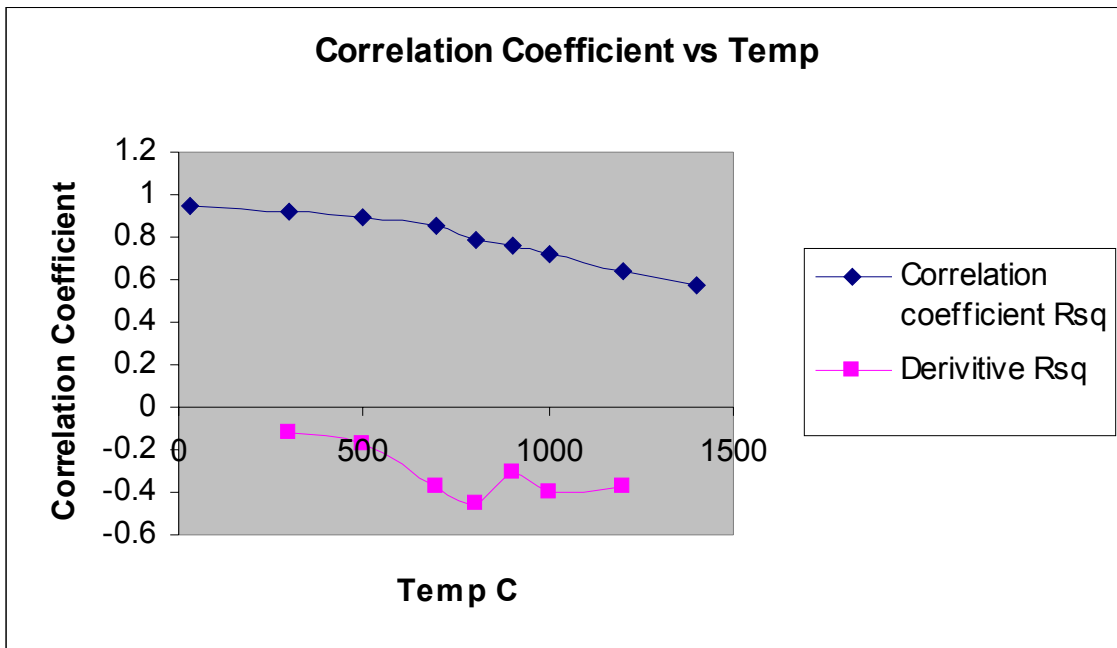


Figure 7-39 Plot of correlation coefficient of the data to the ideal Boltzmann distribution. Note the second order transformation between 800°C – 900°C. This is most likely due to the increase in thermal energy allowing the atoms to hop “uphill” against the strain field.

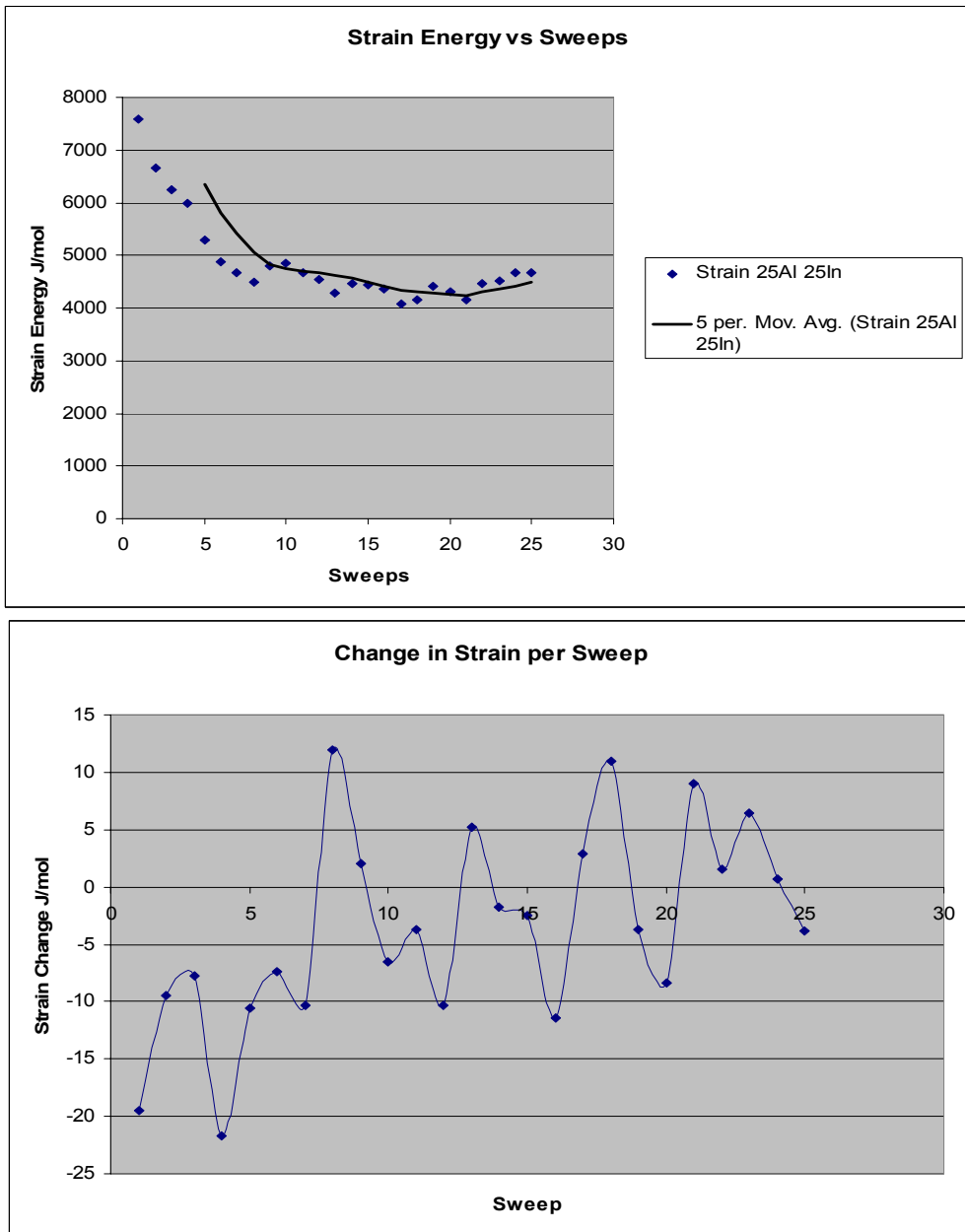


Figure 7-40 Curve showing strain energy and integrated differential strain energy for the Monte Carlo simulation of a 25In 25Al 78Ga N alloy. Convergence is indicated when the integrated differential strain oscillates around zero.

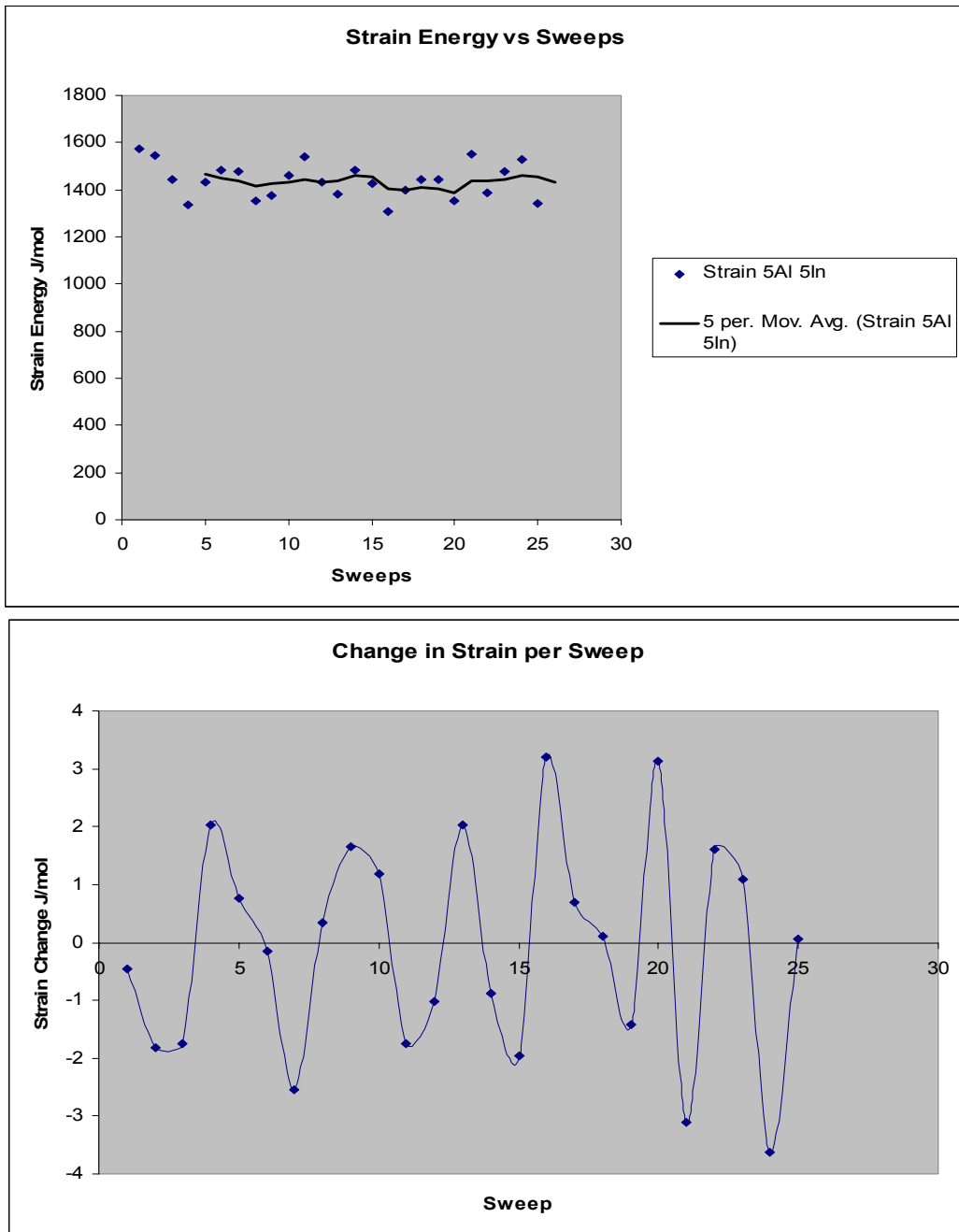


Figure 7-41 Curve showing strain energy and integrated differential strain energy for 5In 5Al 118Ga N alloy. Notice the much faster convergence than the 25In 25Al alloy.

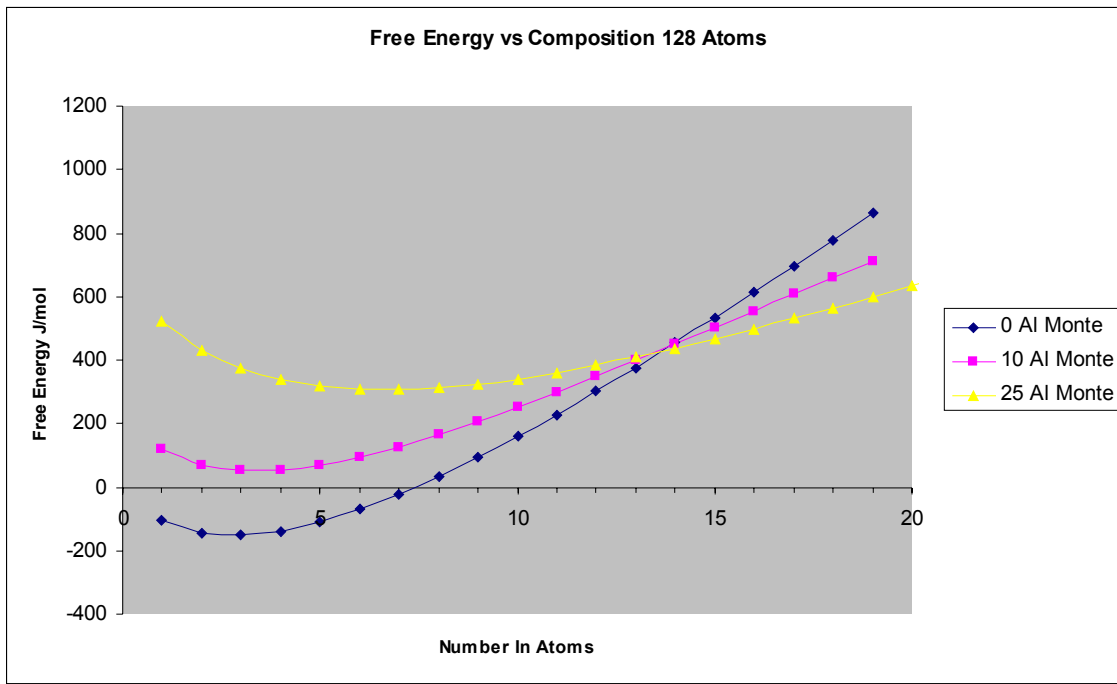


Figure 7-42 Free energy curve for Monte Carlo simulation for 128 atom AlInGaN crystal strained to GaN at three different compositions of Al. Simulation was run at 800C for 25 sweeps. The equilibrium In composition increases with increasing Al. Simulation runs took approx. 20hr.

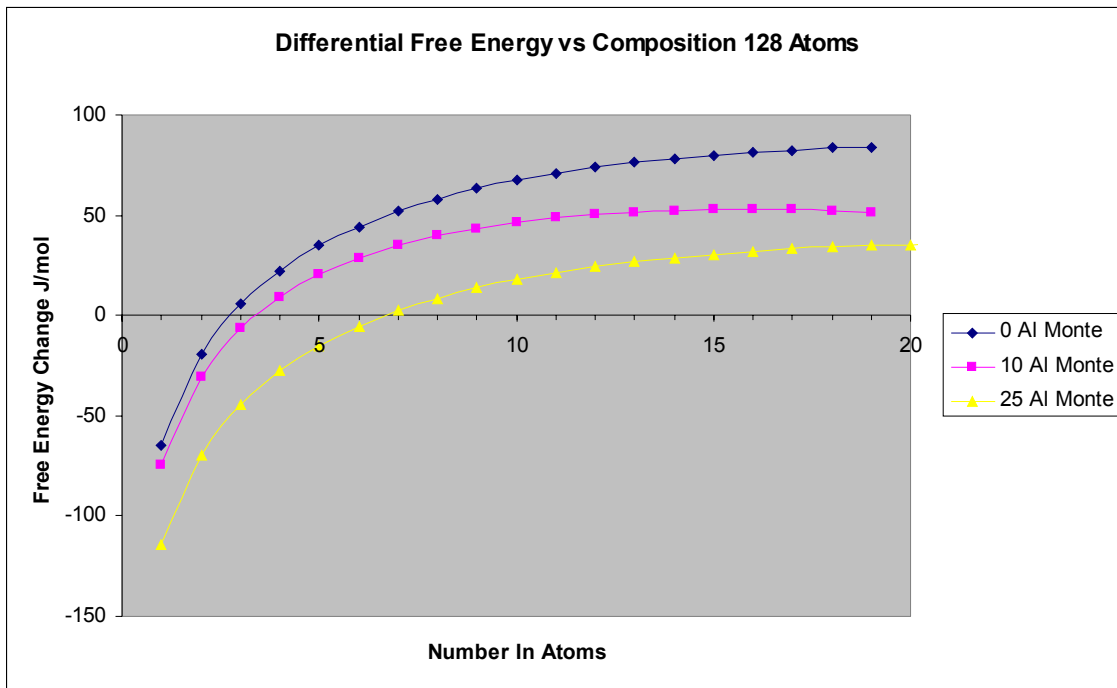


Figure 7-43 Derivative free energy for Monte Carlo simulation of 128 atom AlInGaN crystal strained to GaN. Equilibrium In composition shifts from 2.5In to 7In with the addition of 25Al atoms. This is in complete agreement with the strain equilibrium In incorporation effect.

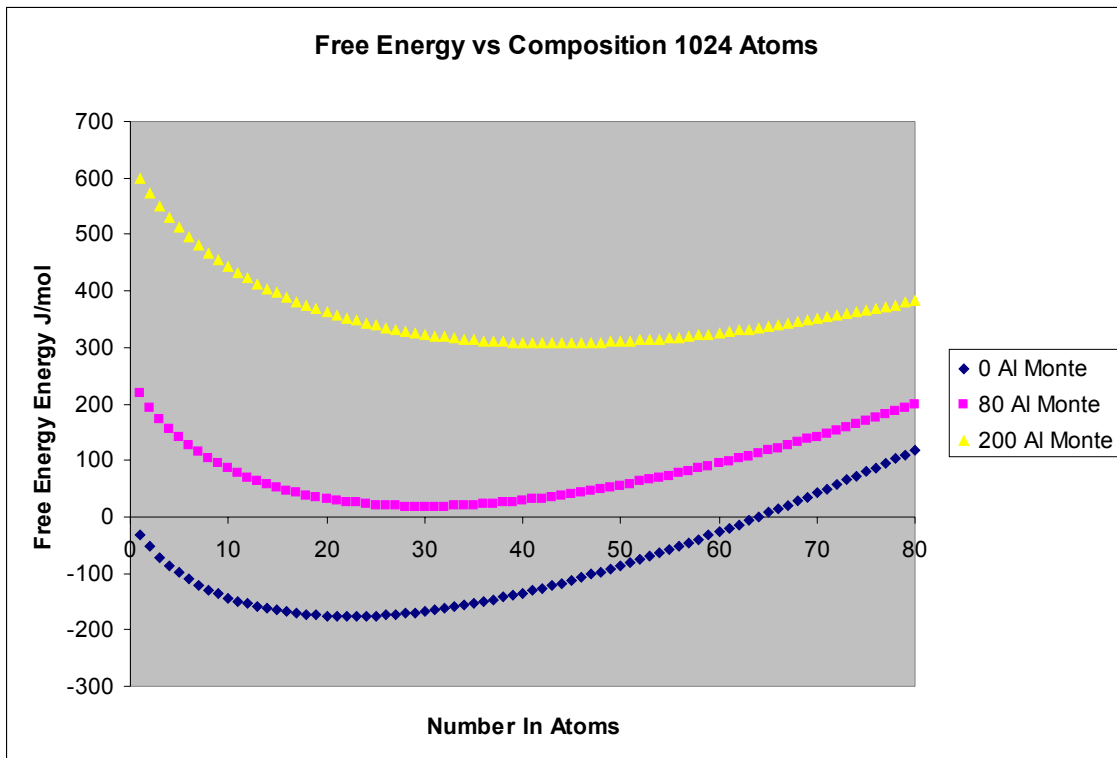


Figure 7-44 Monte Carlo simulation for 1024 atom crystal strained to GaN at three different compositions of Al. Simulation was run at 800C for 10 sweeps. The equilibrium In composition increases with increasing Al, but not as large an effect as for 128 atoms. Simulation runs took approx. 20 days.

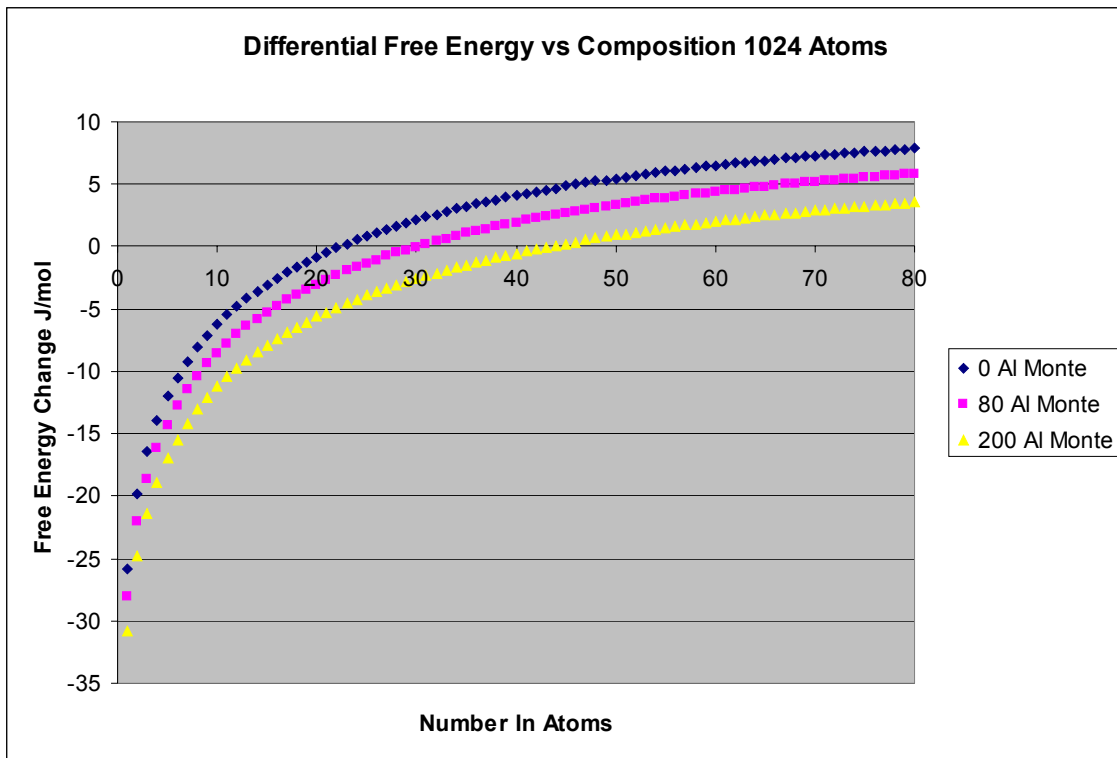


Figure 7-45 Derivative free energy for Monte Carlo simulation for 1024 atoms strained to GaN. Equilibrium In composition shifts from 22In to 44In with the addition of 200Al atoms. The expected shift would be 40In. The discrepancy between the actual and expected shift is due to the limited number of sweeps.

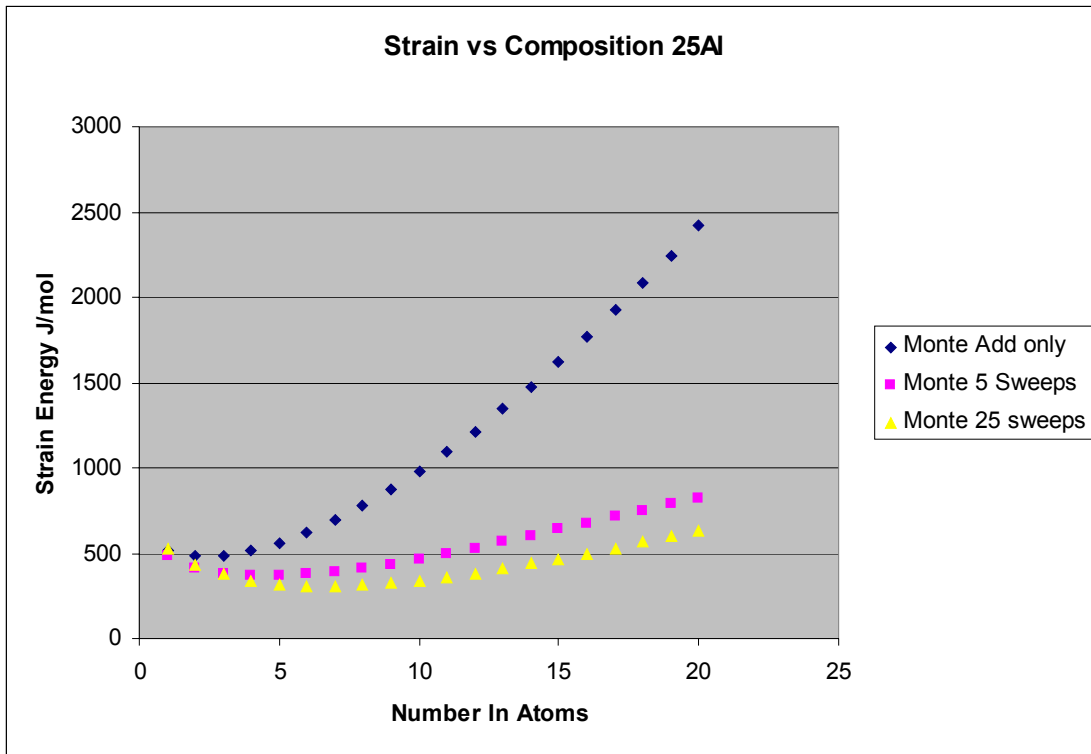


Figure 7-46 Set of Monte Carlo runs for 25Al curve. Monte Carlo simulations were performed using Boltzmann probability addition only, 5 sweeps and 25sweeps. The 25 sweep curve matches the result for the 128 atom simulation while the 5 sweep is closer to the results from the 1024 atom crystal. This would indicate that the discrepancies for the 1024 atom crystal are from an insufficient number of sweeps.

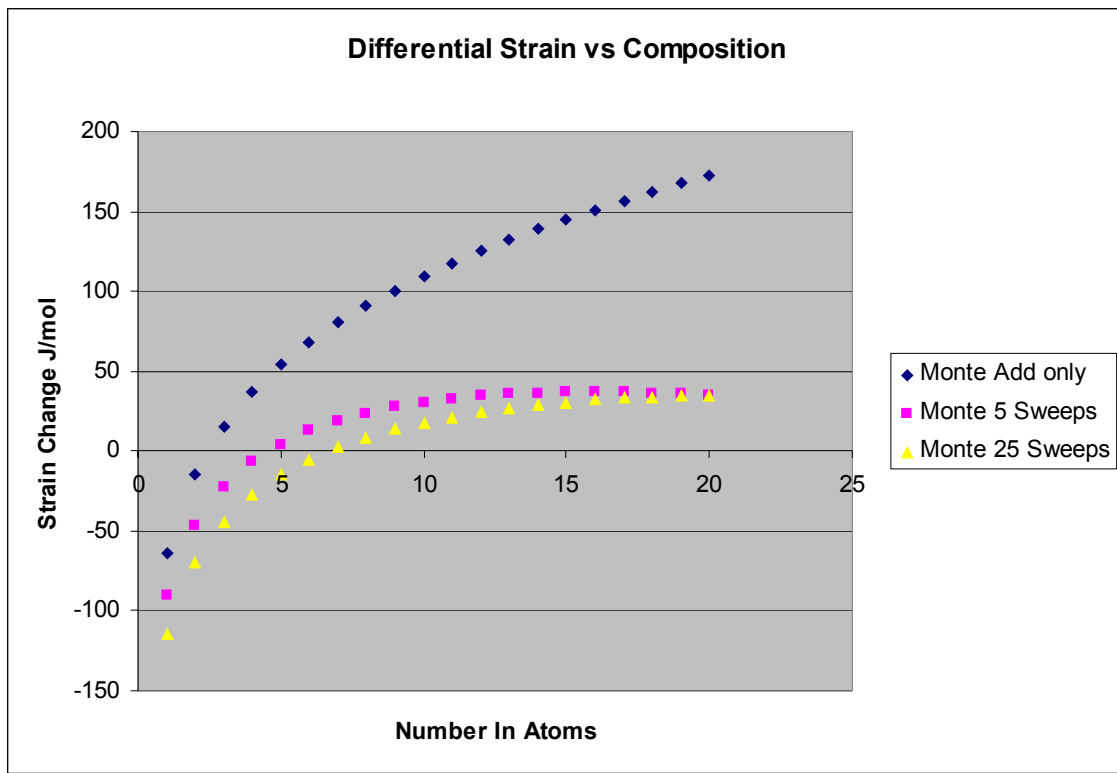


Figure 7-47 Derivative free energy for Monte Carlo simulation for 25Al curve. The 25 sweep curve matches the results for the 128 atom simulation while the 5 sweep is in close agreement with the 1024. This would indicate that the discrepancies for the 1024 atom crystal are from an insufficient number of sweeps.

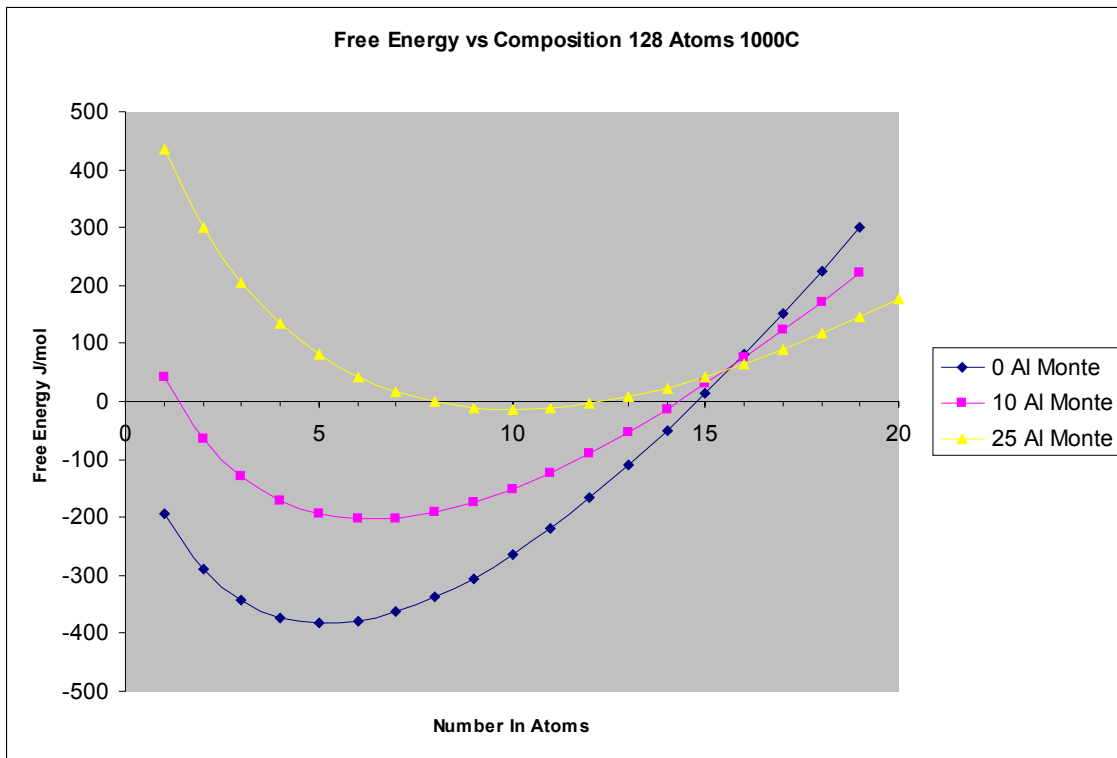


Figure 7-48 Free energy curves from Monte Carlo simulation for 128 atoms strained to GaN at 1000°C and 25 sweeps. The equilibrium In composition changes from 5In to 10In. While the equilibrium In compositions are higher, the strain equilibrium effect is unchanged.

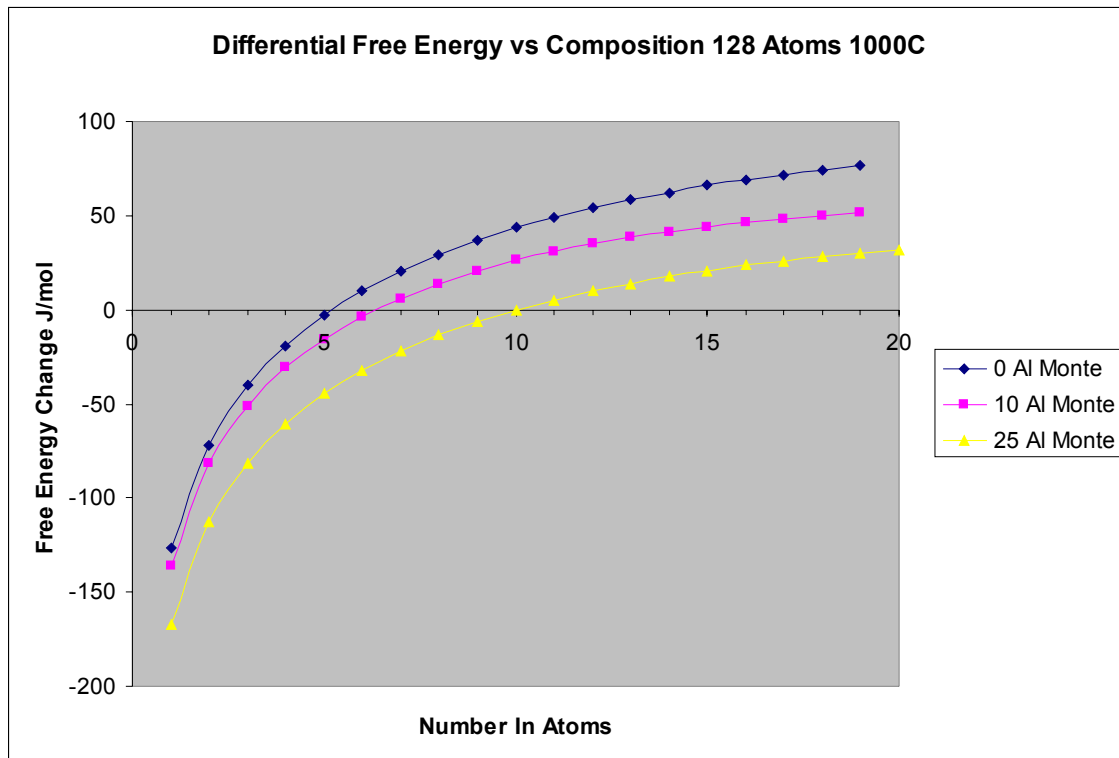


Figure 7-49 Derivative free energy for Monte Carlo simulation at 1000°C. Equilibrium In composition shifts from 5In to 10In. All equilibrium In compositions are shifted higher.

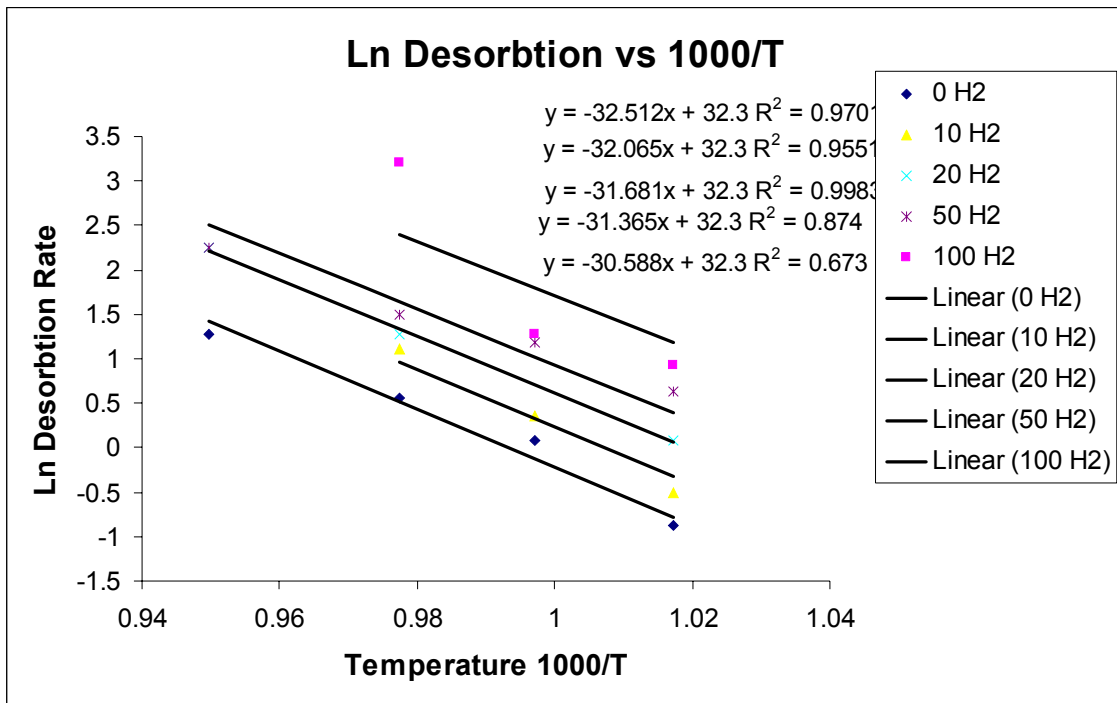


Figure 7-50 Plot of desorption rate vs. temperature for different H₂ flows using the data from the InGaN runs for the H₂ study. All fitting curves are normalized to a Do value corresponding to the Debye frequency for GaN. Resulting activation energy for 0 sccm H₂ is 2.6eV.

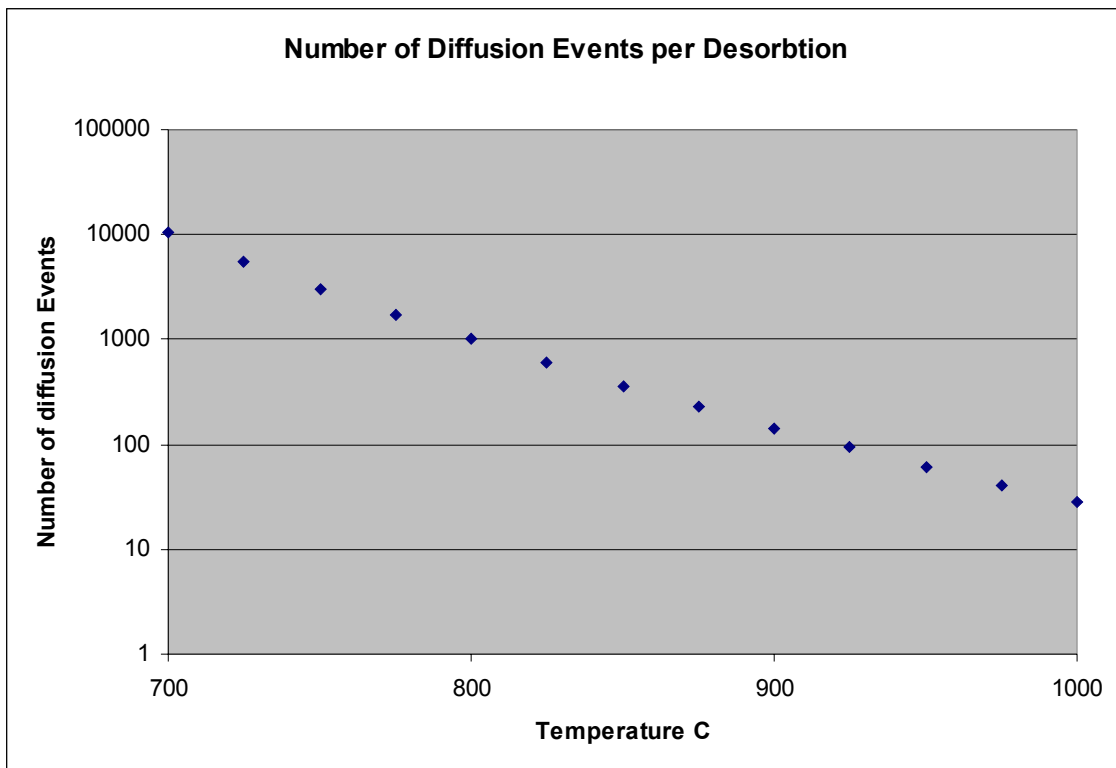


Figure 7-51 The ratio of diffusion events to desorption events is plotted using the activation energy for desorption combined with the activation energy for In surface diffusion from Neugebauer. The curve is normalized for 1000 diffusion events/desorption event at 800°C. The number of diffusion events per desorption decreases from 1000 to 140 from 800°C – 900°C.

Chapter Eight: Conclusions

A comprehensive study of the phase behavior of InGaN and AlInGaN including growth characterization and computer modeling was performed. InGaN alloys were grown with up to 50% InN and studied for phase separation and ordering. The AlInGaN system has been studied with the discovery of the Self Assembled Super-Lattice and the Strain Equilibrium In Incorporation Effect. Computer modeling was performed using a strain-based Valence Force Field (VFF) model combined with the Metropolis Monte Carlo method to study both the composition pulling and the Strain Equilibrium In Incorporation Effect

In the InGaN system, both phase separation and ordering behavior in the InGaN system was studied extensively. Using Transmission Electron Microscopy (TEM), the presence of simultaneous phase separation and (0002) ordering was confirmed. The Composition Pulling effect was also studied in the InGaN system. VFF computer modeling was successfully used to predict the composition of highly strained InGaN films based on the bulk composition.

In the AlInGaN system, the SASL effect was discovered using TEM. In addition, the Strain Equilibrium In Incorporation Effect was discovered and studied using a combination of TEM and X-ray diffraction. The computer model has been able to predict the In incorporation behavior of highly strained films in the AlInGaN system and has confirmed that the strain energy is the primary factor determining the In composition in strained AlInGaN films. As a result, the successful implementation of the VFF Metropolis Monte Carlo simulation has confirmed the origin of the Strain Equilibrium In Incorporation Effect.

Chapter Nine: Future Work

To simplify the implementation of the Valence Force Field Metropolis Monte Carlo simulation, the growth conditions studied were artificially limited to the conditions for the Self Assembled Superlattice Structures. This allowed for a very controlled environment to model. It also had the advantage of excellent data for the real system under those conditions. Now that the computer model has proven to be successful, it could be expanded to include other growth variables so that it can become a generalized computer model rather than studying one set of conditions.

Previous work in the InGaN system has shown that the composition of In in the final InGaN film can be modeled by the delivery rate of the In precursors to the growth surface offset by the desorption rate of In from the growth surface. The desorption rate is strongly influenced by the temperature and the presence of H₂.

The InGaN growth model assumes a constant In incorporation rate regardless of the strain in the crystal either locally or globally. By combining the incorporation / desorption model with the incorporation vs. strain model, it should be possible to accurately estimate the incorporation of In under strained conditions. This would allow you to predict the composition of the crystal on both a global and local level. This can have the advantage of accurately estimating the composition of thin, highly strained films such as quantum wells, from the composition attained in the bulk material under similar conditions.

In the AlInGaN alloys, you have another set of interactions. In addition to the Al and In atoms affecting the free energy of the GaN matrix, you also have the Al and In atoms interacting with each other. In films that were grown by MOCVD at relatively high temperatures and high In/(Ga+Al) ratios, an interesting effect was seen. As the Al composition was increased, the In composition in the film increased as well. This change

in In incorporation under identical growth conditions cannot be explained by the InGaN growth model. The In increase was proportional to the amount of In needed to offset the tensile strain generated by the Al incorporation. In other studies, the ratio of In/Al incorporation was a different ratio corresponding to the zero strain ratio for the AlGaN underlying film.

In the first generation, the model will only consider strain for the probability of incorporation into the growing film. Other probabilities such as desorption and surface diffusion to a neighboring site will be represented by constant probabilities. The desorption probability will be based on temperature. With probabilities for incorporation, surface diffusion, and desorption, it will be possible to model the MOCVD process using a statistical Monte Carlo method. The atom hits the surface and for each slice of time the atom has a probability of moving to another site, desorbing, or incorporating.

The effect of growth rate can also be included by considering a Grow-in time. If the atom is on the surface and has not incorporated or desorbed by the Grow-in time, then it assumed that that atom will be incorporated into the growing film at its current location. This effect can be used to simulate the effect of high growth rates on the incorporation of In. By reducing the grow-in time, you can simulate a high growth rate, by increasing the Grow-in time you can simulate a low growth rate.

The InGaN growth model estimates the relative rates of incorporation vs. desorption but does not estimate the surface coverage of atoms that have not desorbed and not incorporated. The Grow-in time is one method to get around this as it “freezes” the atoms from moving any further. In the real crystal, atoms are coming on to the crystal surface simultaneously. In the real crystal, you have a rate incorporating into the film, a rate of desorption, and a population of adsorbed atoms that balances the two. If an atom hangs around too long it is incorporated into the film, which grows around it. In the current model, the atoms will be added to the surface one at a time, at a random location. The grow-in method is a way to simulate the effects of simultaneous atoms hitting the

surface without the complexity of simultaneously modeling thousands of atoms. In addition, it eliminates the need to know the surface coverage.

Since this model does not include a chemical equilibrium component, it cannot estimate the effect of V/III ratio, H₂ partial pressure or system pressure. In the coarsest sense, it is possible to estimate these effects by changing some of the parameters such as probability for surface diffusion, but these experiments are beyond the scope of this model. Changes in the desorption and surface diffusion probabilities based on surface atoms nearby could be modeled, but the mechanism does not appear to be strain, so again it is beyond the scope of this model.

The model is also capable of studying large-scale properties such as the critical layer thickness. By generating successively larger crystals consisting of the base GaN layer with different thickness films of InGaN on top, it is possible to calculate the strain generated in both the crystal and the underlying layer of GaN. This is more accurate than current methods that take into account only the strain in the InGaN layer. By combining the strain estimates from the model and the actual data from experiments with critical layer thicknesses, it is possible to determine the strain energy needed to generate the misfit dislocations for different compositions of InGaN

With the energy required for the formation of misfit dislocations in the strained layers, it is possible to predict the maximum stable size of coherent separated phases. For applications such as quantum dots, the quantum dot region is typically coherently strained with respect to the crystal lattice. The point at which it is energetically favorable for the phase-separated region to become incoherent depends on the interface energy between the two phases vs. the strain energy of the coherent structure. By taking the strain energy for the phase separated region from the wurtzite VFF model, and combining it with the energy for misfit dislocations in the strained thin films, it is possible to predict the maximum stable size for coherent phases.